

Growth and morphology evolution of semiconducting oxides and sulfides prepared by magnetron sputtering

vorgelegt von
M.Sc. Man Nie
aus Hubei, P.R. China

von der Fakultät IV – Elektrotechnik und Informatik
der Technischen Universität Berlin
zur Erlangung des akademischen Grades

Doktorin der Naturwissenschaften

-Dr.rer.nat.-

genehmigte Dissertation

Promotionsausschuss:

Vorsitzender: Prof. Dr. Bernd Rech

Gutachter: Prof. Dr. Bernd Szyszka

Prof. Dr. Norbert Kaiser

Dr. Klaus Ellmer

Tag der wissenschaftlichen Aussprache: 24. November 2014

Berlin 2014

Abstract

Tin-doped indium oxide (ITO) and Al-doped zinc oxide (AZO) belong to the material class of transparent conductive oxides (TCOs) which exhibit both low electrical resistivity and high optical transmittance. These superior properties make them widely used in different flat panel displays, thin film solar cells, multi-functional windows and flexible electronics as n-type materials. Polycrystalline Cu(In,Ga)S_2 (CIGS) thin films are very promising p-type absorbers in highly efficient thin film solar cells. The wide variety of the materials assembled into these devices, which consist of semiconductors, molecular or polymer organics, metal, glass or plastic, require the development of TCO and CIGS materials with new properties, a good processibility and even tailored morphology.

The objective of this work was to investigate the influence of different deposition conditions on the structure and morphology evolution of different semiconducting oxides (ITO and AZO), and semiconducting sulfides (CIGS) grown by a one-step magnetron sputtering process, which is a cost effective and widely used efficient technology for large scale production. This was achieved by depositing thin films over a wide range of conditions, i.e. varying sputtering atmosphere, plasma excitation mode, sputtering pressure and substrate temperature, and analyzing the roughness scaling properties, in order to understand the growth mechanism of ITO, AZO and CIGS in sputtering process. The main techniques which were employed to characterize the structure and morphology of the films are X-ray diffraction and atomic force microscopy.

The first part is focused on the growth and morphology evolution of ITO films sputtered from a ceramic target under different sputtering atmospheres, excitation modes and substrate temperatures. The investigation showed that, for room temperature deposition, additional O_2 in sputtering atmosphere smoothen the surface of ITO films, and H_2 roughens the surface. It was the other way around in AZO films. The growth exponent of ITO films increases from 0.35 via 0.65 to 0.98 with changing sputtering atmospheres from $\text{Ar}/10\%\text{O}_2$ via pure Ar to $\text{Ar}/10\%\text{H}_2$ mixture, respectively, indicating that nonlocal mechanisms such as shadowing roughening dominate the growth. Discharge modes (i.e. with different plasma excitation frequencies in the range of DC to 27.12 MHz) have a very different influence of structure and roughness evolution for ITO films at low temperature and high temperature. A crossover of roughness evolution can be clearly observed due to the competition between surface diffusion and crystallite growth enhanced shadowing effect.

The second part of the thesis deals with the growth and morphology evolution of AZO films grown under different sputtering atmospheres and substrate temperatures. For room temperature deposition, abnormal growth exponents larger than 1 were found for pure Ar and Ar/1%O₂ deposition, and 0.73 for Ar/10%H₂ deposition, respectively, corresponding to different growth types. For high temperature deposition, the surface becomes smoother and the growth exponent decreases due to high adatom mobility and a faster relaxation of the compressive stress. The effect of film thickness on the microstructure, surface morphology and electrical properties of AZO and ITO films deposited in pure Ar at 300 °C was also compared in detail.

The final part of the thesis, the growth and morphology of CIGS films deposited by one-step DC reactive magnetron co-sputtering from CuGa and In targets in argon-hydrogen sulfide gas mixtures was investigated for different sputtering pressures and temperatures. For room temperature deposition, the roughness evolution can be also divided into two growth stages as a result of the change of the surface diffusion dominating in the initial growth stage (growth exponent ~ 0.13) to crystallite growth enhanced shadowing dominating in the latter growth stage (growth exponent ~ 0.56). With increasing surface diffusion effect, the surface becomes smoother with an even smaller growth exponent close to 0. For high temperature depositions, the surface becomes rougher than that at low temperature. A combination of local and nonlocal growth mechanism is used to explain the growth behavior.

Through a comparison of the scaling behaviors of ITO, AZO and CIGS films grown under different deposition conditions, it can be conclude that abnormal roughness scaling of polycrystalline films is not uncommon in magnetron sputtering process due to the unavoidable nonlocal effect.

Kurzfassung

Zinndotiertes Indiumoxid (ITO) und aluminiumdotiertes Zinkoxid (AZO) gehören zur Materialklasse der transparenten leitfähigen Oxide (TCOs). Diese Materialien weisen eine geringe elektrische Leitfähigkeit bei gleichzeitig hoher optischer Transparenz auf. Diese besonderen Eigenschaften führen zu einer Reihe verschiedener Anwendungsgebiete, wie zum Beispiel Flachbildschirme, Dünnschichtsolarzellen, funktionelle Verglasungen und flexible elektronische Bauelemente. Im Bereich der Dünnschichtsolarzellen gelten dünne Schichten aus polykristallinem Cu(In,Ga)S_2 (CIGS) als vielversprechendes Absorbermaterial, um hohe Effizienzen zu erreichen. Generell wird in den verschiedenen Anwendungsgebieten eine Vielzahl von unterschiedlichen Materialien, wie z.B. Halbleiter, molekulare oder polymere organische Verbindungen, Metalle, Gläser oder Plastiken, verwendet. Dies macht die Entwicklung von TCO- und CIGS-Schichten mit neuartigen Eigenschaften, guter Prozessierbarkeit und maßgeschneiderter Morphologie notwendig.

Das Ziel dieser Arbeit war es, den Einfluss verschiedener Abscheidungsbedingungen auf die Struktur und die Morphologie verschiedener halbleitender Oxide (ITO und AZO) und halbleitender Sulfide (CIGS) zu untersuchen. Die Schichten wurden in einem einzigen Prozessschritt mittels Magnetronsputters hergestellt. Diese Methode erlaubt eine kosteneffiziente Herstellung und wird bereits in der industriellen Produktion eingesetzt. Um die Wachstumsmechanismen von gesputterten ITO-, AZO- und CIGS-Schichten zu verstehen, wurden dünne Schichten unter stark variierenden Prozessbedingungen, das heißt unter verschiedenen Sputteratmosphären und -drücken, mit unterschiedlichen Plasmaanregungsfrequenzen sowie bei verschiedenen Substrattemperaturen, hergestellt und anschließend deren Rauigkeit untersucht. Dabei wurden hauptsächlich Röntgendiffraktometrie und Rasterkraftmikroskopie eingesetzt.

Der erste Teil der Arbeit fokussiert sich auf das Wachstum und die zeitliche Entwicklung der Rauigkeit von ITO-Schichten, die von einem keramischen Target in verschiedenen Sputteratmosphären, mit unterschiedlichen Plasmaanregungsmodi und bei verschiedenen Substrattemperaturen, abgeschieden wurden. Die Untersuchungen an Schichten, die bei Raumtemperatur abgeschieden wurden, haben gezeigt, dass die Zugabe von O_2 zur Sputteratmosphäre zu einer Glättung der ITO-Schichtoberfläche führt, während die Zugabe von H_2 zu einer Vergrößerung der Rauigkeit führt. Die AZO-Schichten zeigen ein entgegengesetztes Verhalten. Wird die Sputteratmosphäre von $\text{Ar}/10\% \text{O}_2$ über reines Ar zu $\text{Ar}/10\% \text{H}_2$ geändert, steigt der Wachstums-Exponent der ITO-Schichten von 0.35

über 0.65 bis 0.98 an. Das deutet auf einen Einfluss nicht-lokaler Mechanismen, wie zum Beispiel die Verstärkung der Rauigkeit durch Abschattungseffekte, hin. Der Einfluss des Plasmaanregungsmodus‘ (das heißt der Einfluss verschiedener Plasmaanregungsfrequenzen im Bereich von Gleichspannung bis 27.12 MHz) auf die Struktur und die zeitliche Entwicklung der Rauigkeiten hängt sehr stark von der Abscheidungstemperatur ab. Dabei wird ein Übergang in der zeitlichen Entwicklung der Schichtrauigkeit beobachtet, der durch die Konkurrenz zwischen Oberflächendiffusion und der verstärkten Verschattung durch das Wachstum von Kristalliten verursacht wird.

Der zweite der Teil der Arbeit widmet sich dem Wachstum und der zeitlichen Entwicklung der Morphologie von AZO-Schichten, die in verschiedenen Sputteratmosphären und bei verschiedenen Temperaturen abgeschieden wurden. Scheidet man bei Raumtemperatur ab, werden außergewöhnlich hohe Wachstums-Exponenten von über 1 für eine Abscheidung in reinem Ar und Ar/1% O₂ und 0.73 für eine Abscheidung in Ar/10% H₂ gemessen, die auf verschiedene Wachstumsmechanismen hindeuten. Wenn die Schichten bei hohen Temperaturen abgeschieden werden, werden die Schichten glatter und der Wachstums-Exponent sinkt aufgrund einer hohen Adatom-Mobilität und einer schnelleren Relaxation von kompressiven Verspannungen. Der Einfluss der Schichtdicke auf die Mikrostruktur, die Oberflächenmorphologie und die elektrischen Eigenschaften von AZO- und ITO-Schichten, die in reinem Ar bei 300 °C abgeschieden wurden, wurde ebenfalls systematisch untersucht.

Im letzten Abschnitt der Arbeit wurden das Wachstum und die Morphologie von CIGS-Schichten untersucht. Diese Schichten wurden mittels eines einstufigen DC-Kosputterprozesses in Reaktivgasatmosphäre, die aus einer Mischung von Argon, Wasserstoff und Schwefel besteht, von einem CuGa- und In-Target bei verschiedenen Drücken und Temperaturen abgeschieden. Es zeigte sich, dass die zeitliche Entwicklung der Rauigkeit für die Schichten, die bei Raumtemperatur abgeschieden wurden, wieder in zwei verschiedene Abschnitte eingeteilt werden kann. Der Übergang wird durch einen Wechsel von der anfänglichen Dominanz der Oberflächendiffusion (Wachstums-Exponent ~0.13) zu einer Dominanz der verstärkten Verschattung durch das Wachstum von Kristalliten (Wachstums-Exponent ~0.56) verursacht. Steigt die Oberflächendiffusion an, wird die Oberfläche glatter und der Wachstums-Exponent sinkt weiter bis zu Werten nahe 0. Wenn die Schichten bei hohen Temperaturen abgeschieden werden, ist die Oberfläche rauer als bei niedrigen Abscheidungstemperaturen. Das Wachstum der Schichten wird auf eine Kombination aus lokalen und nicht-lokalen Wachstumsmechanismen zurückgeführt.

Mit Hilfe eines Vergleichs der zeitlichen und räumlichen Entwicklung der Rauigkeit beim Wachstum von ITO-, AZO- und CIGS-Schichten unter verschiedenen Prozessbedingungen konnte geschlussfolgert werden, dass das anormale Skalieren der Rauigkeit wegen der unvermeidbaren nicht-lokalen Effekte für magnetrongesputterte polykristalline Schichten nicht unüblich ist.

List of Important Symbols and Abbreviations

| | | | |
|------------|---|------------------------------|---|
| α | Roughness exponent | Ar | Argon |
| β | Growth exponent | O | Oxygen |
| ξ | Correlation length | H | Hydrogen |
| ρ | Resistivity | $CuGa$ | Copper gallium |
| μ_n | Hall mobility of the electrons | In | Indium |
| n | Carrier concentration of the electrons | S | Sulfur |
| k_B | Boltzmanns constant (1.381×10^{23} J/K) | AZO | Al-doped zinc oxide (ZnO:Al) |
| γ^* | Interface energy | ITO | Tin-doped indium oxide ($In_2O_3: Sn$) |
| c | c-axis lattice parameter | TCO | Transparent conductive oxide |
| c_{ij} | Elastic constants | $CIGS$ | $Cu(In,Ga)S_2$ |
| D' | Diffusion coefficient | $CIGSe$ | $Cu(In,Ga)Se_2$ |
| d_f | Film thickness | F_{Ar+O_2} or F_{Ar+H_2} | Reactive gas flow Ar with O_2 or H_2 (supply in sccm) |
| $d_g(AFM)$ | Particle size obtained from AFM | AFM | Atomic force microscopy |
| $d_g(XRD)$ | Crystallite size obtained from XRD | $CAFM$ | Conductive atomic force microscopy |
| E_a | Activation energy for diffusion | SEM | Scanning electron microscopy |
| E_g | Band gap | RBS | Rutherford backscattering spectrometry |
| t | Time | XRD | X-ray diffraction |
| T | Absolute temperature | XRF | X-ray fluorescence |
| T_S | Substrate temperature | $FWHM$ | Full width at half maximum |
| T_M | Melting temperature | $JCPDS$ | Joint Committee on Powder Diffraction Standards |
| T_S/T_M | Homologous temperature | DC | Direct current |
| $at. \%$ | Atomic percentage | RF | Radio frequency |
| $wt. \%$ | Weight percentage | RT | Room temperature |
| k | Wave vector | rms | Root-mean- square |
| s | Sticking coefficient | RMS | Reactive magnetron sputtering |
| w | Root mean square surface roughness, interface width | $HHCF$ | Height-height correlation function, $H(r)$ |
| $h(r)$ | Height profile | HZB | Helmholtz-Zentrum Berlin für Materialien und Energie GmbH |
| $R_{cur.}$ | Root-mean- square current | $1DPSD$ | One-dimension power spectral density function |
| V_{dis} | Discharge voltage | | |

Table of Content

| | |
|--|------------|
| Abstract | i |
| Kurzfassung | iii |
| List of Important Symbols and Abbreviations | vi |
| 1 Introduction..... | 1 |
| 2 Thin Film Growth Models | 4 |
| 2.1 Growth mechanisms | 4 |
| 2.2 Deposition parameters affecting the microstructural evolution | 8 |
| 2.3 Structure zone models for physical vapor deposited films..... | 11 |
| 2.4 Scaling and correlations of rough surfaces..... | 14 |
| 2.5 Models for growth-induced roughening..... | 20 |
| 2.5.1 Discrete surface growth models | 20 |
| 2.5.2 Local continuum growth models | 22 |
| 2.5.3 Nonlocal continuum growth models | 27 |
| 2.6 Experimental scaling behavior of surface roughness for sputtered films | 29 |
| 3 Deposition and Characterization of Thin Films..... | 34 |
| 3.1 Magnetron sputtering deposition: DC and RF | 34 |
| 3.2 Structure and Morphology characterization methods | 37 |
| 3.2.1 X-ray diffraction (XRD)..... | 37 |
| 3.2.2 X-ray Fluorescence (XRF) | 39 |
| 3.2.3 Atomic force microscopy (AFM)..... | 41 |
| 3.2.4 Conductive atomic force microscopy (CAFM)..... | 44 |
| 3.2.5 Scanning electron microscopy (SEM)..... | 45 |
| 3.2.6 Rutherford backscattering spectrometry (RBS) | 45 |
| 3.2.7 Hall-Effect measurement..... | 46 |
| 4 Transparent conductive oxides by DC/RF magnetron sputtering | 48 |
| 4.1 Nucleation and growth of tin-doped indium oxide films | 48 |

Table of Content

| | | |
|----------|---|------------|
| 4.1.1 | Introduction..... | 48 |
| 4.1.2 | Experimental details..... | 51 |
| 4.1.3 | Growth of ITO films in different sputtering atmospheres | 52 |
| 4.1.4 | Influence of different discharge modes on the growth of ITO films | 66 |
| 4.1.5 | Conclusions..... | 77 |
| 4.2 | Nucleation and growth of Al-doped zinc oxide films..... | 78 |
| 4.2.1 | Introduction..... | 78 |
| 4.2.2 | Experimental details..... | 80 |
| 4.2.3 | Growth of AZO films in different sputtering atmospheres..... | 80 |
| 4.2.4 | Temperature effect of the growth of AZO films..... | 91 |
| 4.2.5 | Conclusions..... | 96 |
| 5 | One-stage deposition of Cu(In,Ga)S₂ films by dc reactive magnetron sputtering | 97 |
| 5.1 | Experiments details..... | 99 |
| 5.2 | Influence of sputtering parameters on the nucleation and growth of CIGS films ... | 100 |
| 5.2.1 | Influence of deposition pressure | 100 |
| 5.2.2 | Influence of deposition time | 102 |
| 5.2.3 | Effect of substrate temperature | 108 |
| 5.2.4 | Intrinsic electrical properties: CAFM | 110 |
| 5.3 | Conclusions..... | 113 |
| 6 | Summary and Outlook..... | 114 |
| 6.1 | Main Conclusions of this Thesis..... | 114 |
| 6.2 | Outlook | 121 |
| | References | 122 |
| | Publications..... | 137 |
| | Acknowledgments | 138 |

1 Introduction

Rough surfaces exist everywhere in the natural world. Roughness develops intrinsically from the growth process on a pristine surface, even at the atomic scale. The surface morphology plays an important role for many physical and chemical properties of thin films. For example, a low roughness is required for various thin film applications, such as wear-resistant coatings, quantum well multilayer structures, and thin film transistors.^{1,2} On the other hand, rough surfaces can be very helpful in applications such as catalysis, adhesion enhancement between materials, or increasing the effective area for advanced charge storage devices.^{3,4} To achieve or better control film properties, it is necessary to gain knowledge of the principal mechanisms that determine the roughness of growing films. In the last decades, particular scientific research interest has been focused on studying kinetic roughening of thin film surfaces grown under non-equilibrium conditions.^{2,3} The kinetic roughening mechanism depends on the local and nonlocal effects in different preparation processes, and describes spatial and temporal correlations of the surface roughness. Numerous experimental studies^{4, 31-35} have been performed relating to this topic, i.e. creating/growing thin films, characterizing the surfaces, and testing their properties, which reveals the existence of the kinetic roughening in thin films and found scaling relations between roughness and growth time and measurement scale on the basis of dynamic scaling theory. Different classes of scaling exponents (i.e. growth exponent β and roughness exponent α) correspond to different dominant processes involved in the growing process, which will be discussed in Chapter 2. The existing theoretical models cannot explain all the experimental results due to the complexity of the experimental conditions which are hard to simulate. A detailed analysis of the growth dynamics for such systems has to include the determination of the complete set of experimental data in order to better compare them to the existing models and simulations.

In this work, the kinetic roughening of semiconductor oxides including tin-doped indium oxide (ITO) and Al-doped zinc oxide (AZO), and semiconductor sulfides including Cu(In, Ga)S₂ (CIGS), grown by the magnetron sputtering process, was investigated. ITO and AZO films are well known as transparent conductive oxides which are widely used as the transparent electrodes in organic light emitting diodes (OLEDs), transparent window electrodes for light transmission and extraction of the photocurrent in thin film solar cells etc.⁵ CIGS films are very promising photovoltaic absorbers.⁶ More detailed information

about these three materials will be given in Chapters 4 and 5. To our knowledge, very little effort was devoted to systematic investigations of the growth dynamics of oxides and sulfides, not to mention all films are prepared by magnetron sputtering which has already used to prepare a variety of thin films in industry. Moreover, it would be also very interesting to understand the general kinetic roughening mechanism no matter prepared oxides or sulfides by this deposition technique.

The aim of this work is firstly to check the growth and morphology of these semiconducting oxides and sulfides under different sputtering conditions independently, and secondly to study the dynamic scaling exponents related to the influence of the processing conditions such as sputtering atmospheres, temperature and excitation modes. In the following, the structure of this thesis and its contents will be described briefly.

Chapter 2 starts with a brief introduction of the film growth mechanisms, the sputtering parameters which affect the microstructure and some structure zone models for physical-vapor deposited films. Furthermore, the parameters which are used to describe a rough surface and how to obtain these scaling parameters are introduced. Some important theoretical models related to film growth and a categorization of the scaling exponents is overviewed.

Chapter 3 introduces the principle of magnetron sputtering and the characterization methods for the sputtered films. X-ray diffraction (XRD), atomic force microscopy (AFM) and scanning electron microscopy (SEM) were used for structure and surface morphology characterization. X-ray fluorescence (XRF) and Rutherford backscattering spectrometry (RBS) were performed for determining the film composition, and Hall effect measurements for electrical properties.

Chapter 4 is divided into two parts: growth and morphology of ITO and Al-doped ZnO thin films. The first part describes the preparation of ITO thin films with a briefly introduction of this material and a literature review of growth investigations. The influence of different sputtering atmospheres on the structure and morphology of ITO thin films has been discussed. The influence of the excitation modes on the growth of ITO films at low and high temperature was also discussed. The second part of chapter 4 discusses the influence of different sputtering atmospheres and temperature on the growth and morphology of AZO films prepared by RF sputtering. These scaling exponents were compared with the models available in the literature and relative growth effects were proposed for the reasoning. The electrical properties such as resistivity, carrier

concentration, mobility of ITO and AZO films prepared under the same condition were also compared.

Chapter 5 describes the growth and morphology of $\text{Cu(In,Ga)}\text{S}_2$ film prepared by a one-step DC magnetron co-sputtering process. The influence of sputtering pressure, deposition time and temperature has been discussed. The intrinsic electrical properties of CIGS film were also investigated by conductive AFM.

Chapter 6 presents main conclusions on the structure and surface roughness evolution of ITO, AZO and CIGS films based on the results discussed in Chapter 4 and 5. And then an outlook is given.

2 Thin Film Growth Models

As mentioned in the introduction, in order to control and tailor the properties and performance of thin films, a detailed understanding of the growth mechanisms which determine the microstructural evolution of thin films is very important. In this chapter, some of the fundamental processes determining the microstructure of polycrystalline films will be discussed.

2.1 Growth mechanisms

When a flux of vapor atoms impinges onto a substrate, the strength and distribution of the flux plays a significant role in shaping the surface and noise in the flux also affects strongly the morphology. The film growth can be divided into several stages: condensation of the vapor on the growing surface (adsorption), desorption (re-evaporation or reemission) from the surface, diffusion of the atoms, form atoms of stable nuclei, followed by the coalescence of the reacted material into islands, and then the formation of a continuous film, as demonstrated in Fig. 2.1.

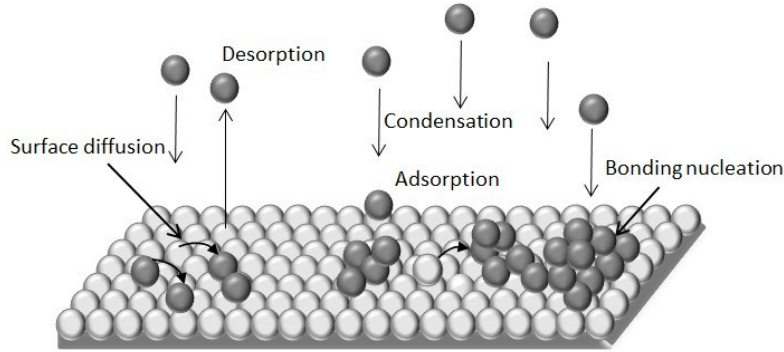


Fig. 2.1: Events in a typical vapor-phase thin film growth process.⁷

For vapor deposition, the condensation of material from the gas phase can be described by an impinging rate R_{im} (number of atoms per cm^2 per second) at the substrate is given by:

$$R_{im} = p(2\pi Mk_B T)^{-1/2} \quad (2.1)$$

where p is the vapor pressure, M is the molecular weight of the atoms, k_B is Boltzmann constant and T is the source temperature. The condensed atoms interact with the substrate surface either by van der Waals forces (≈ 0.25 eV; physisorption), or by chemical bonding ($\approx 1\sim 10$ eV; chemisorption) either through ionic or covalent bonding.⁷ Due to their own initial energy or by substrate-supplied energy or the energy they receive from the impinging

particles, they might immediately desorb or diffuse over the surface. Obviously, the desorption barrier in the physisorption state is much lower than that of the chemisorption state. To describe the desorption process, a sticking coefficient (s) is used to, which is the probability for a particle to remain adsorbed. It is the ratio between the particles that stick to the surface to the number of total impinging atoms upon that surface ($0 \leq s \leq 1$). For very low temperature deposition, the sticking coefficient is usually very close to 1, indicating no desorption. Through thermal effects or a knock-on event of an energetic impinging particle effect, s will decrease. For the adatoms moving over the surface, atoms move between energy minima on the substrate surface and diffuse to a position with the lowest potential. The diffusion coefficient is proportional to $\sim \exp(-E_a / k_B T)$, i.e., it obeys by Arrhenius-type exponential law, where E_a is the activation energy for diffusion. The diffusion process might lead to adsorption, particularly at special sites like edges or other defects, or the diffusing particle may re-evaporate if the characteristic activation barrier is overcome. Both, diffusion and desorption, are local processes since both are thermally activated and determined by bonds to the nearest neighbors.

In addition, due to the nature of some deposition process, the impinging atoms approach to substrate surface from different directions, e.g. as a result of scattering with background gases or oblique incidence. If the surface already has some degree of roughness, due to the geometrical shadowing, some of the incident atoms will be captured at high positions and may not reach the lower valleys of the surface. And then lower positions will be shadowed from the impinging flux by sites far from it, making the shadowing mechanism non-local. This process will result in an enhancement of the growth roughness. More details in terms of shadowing will be introduced later in section 2.5.3.

The initial growth modes determine the ultimate properties of the thin films deposited. Depending on the thermodynamic parameters of the deposition and the substrate surface interaction between the adatoms and the substrate material, three basic growth modes are used to explain thin film growth in non-equilibrium processes:

- (1) Frank-Van der Merwe model (FW), or layer- by- layer growth,
- (2) Volmer-Weber model (VW), or three- dimensional (3D) island growth,
- (3) Stranski-Krastanov model (SK), or 3D island on wetting- layer growth.

The schematic illustration of the three modes is displayed in Fig. 2.2. In the FM growth mode, the deposited atoms wet the substrate, and interatomic interactions between substrate and deposited materials are stronger and more attractive than those between the different

atomic species within the film itself. The opposite case, in which adatom-adatom interactions are stronger than those of the adatom with the substrate surface, leads to the formation of 3D adatom clusters or island growth in the VW model.⁸ SK growth is an intermediate case between FM and VW. Transition from the layer-by-layer FM growth to island-based VW growth occurs at a critical layer thickness which is strongly dependent on the chemical and physical properties, such as surface energies and lattice parameters of the substrate and film.⁹

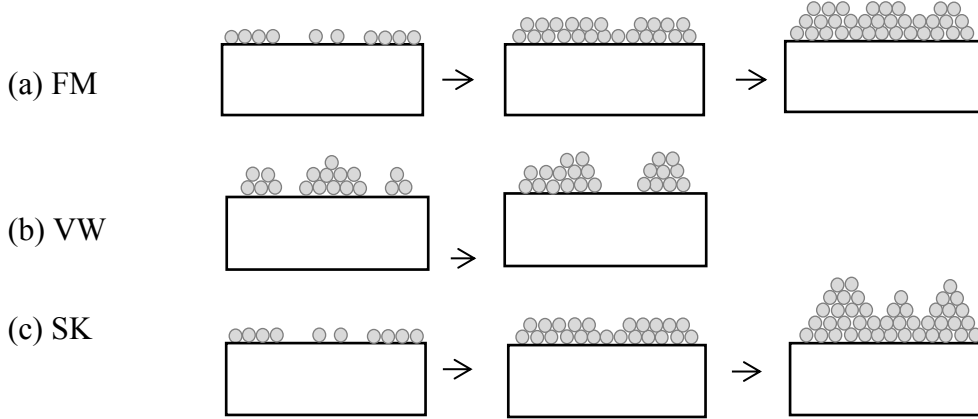


Fig. 2.2: Schematic representation of the three growth modes: (a) Frank-Van der Merwe layer growth (FM, 2D), (b) Volmer-Weber island growth (VW, 3D) and (c) Stranski-Krastanov layer plus island growth (SK, 2D+3D).⁹

A simple formal distinction between the conditions for the occurrence of the various growth modes can be made under the assumption of thermodynamic equilibrium in terms of surface or interface energy γ , i.e. the characteristic free energy to create an additional piece of surface or interface energy. Layer-by-layer FM growth of film A on substrate B is defined by

$$\gamma_A + \gamma_i \leq \gamma_B \quad (2.2)$$

where γ_A and γ_B are the surface free energy of film surface and substrate surface, respectively, and γ_i the interfacial free energy between film and substrate. Here the surface tension of the film does not exceed that of the substrate. Eq.(2.2) presents the effect that the total surface energy of the film surface energy and the interface energy is less than that of the substrate for wetting to occur. Alternatively, it becomes easier for FM growth to occur with increased substrate surface energy. However, strain energy which is a term in γ_i and increases linearly with the number of strained layers, plays a major role in determining the growth mode. At a certain thickness, $\gamma_A + \gamma_i$ exceeds γ_B and the FM growth mode shifts to SK model where a growing planar film begins to roughen resulting in 3D islands on the 2D

wetting layer. Moreover, γ_A may be sufficiently larger than γ_B that the Eq.(2.2) is never fulfilled even for a strong attractive interaction between atoms and substrate surface, then 3D islands nucleate from the onset resulting in VW growth. Deposition on amorphous or randomly textured polycrystalline substrates usually leads to Volmer-Weber growth.¹⁰

When considering the equilibrium condition for the whole system including the vapor phase above the deposited film, a minimum of the Gibbs free enthalpy G which determines the equilibrium needs to be considered. The change in Gibbs free energy when a particle is transferred from the vapor phase into the condensed phase of the deposited film is:⁷

$$\Delta G = n\Delta\mu = nk_B T \ln(p / p_0) \quad (2.3)$$

where n is the atom number, p_0 is the equilibrium vapor pressure, p/p_0 is the degree of supersaturation which is one of the driving forces for the formation of a thin film deposited from an ambient vapor phase. The conditions for layer or island growth is $\gamma_A + \gamma_i + Ck_B T \ln(p_0/p) \leq \gamma_B$ or $> \gamma_B$ (C is constant), respectively. It can be seen that the growth mode of a certain material on a substrate is not a constant material parameter, but can be changed by varying the supersaturation conditions, i.e. p/p_0 .

2.2 Deposition parameters affecting the microstructural evolution

The microstructure of thin films prepared by magnetron sputtering evolves as it nucleates and grows on the substrate surface depending on a number of factors including substrate surface quality, substrate temperature, energy of incidence particles, process gas pressure, sputtering power and deposition rate etc. Kinetic factors and process parameters that affect the microstructure evolution of thin films were reviewed by Thompson¹¹ (see Table 2.1.).

Table 2.1: Factors affecting the structure evolution of polycrystalline films.¹¹

| |
|---|
| ➤ Kinetic factors affecting structure evolution: |
| Adatom diffusivities on substrate surface |
| Adatom self-diffusivities on island surfaces |
| Self-diffusivities in grain boundaries |
| Grain boundary mobilities |
| Adatom cluster nucleation rates |
| Adatom desorption rates |
| ➤ Process parameters |
| Deposition rate (affects adatom arrival rate, adatom diffusion time before cluster nucleation or desorption, also affects film purity) |
| Substrate temperature (affects all kinetic processes, increasing rates with increasing temperature) |
| Background pressure (affects film and surface purity) |
| In sputter deposition: sputtering gas pressure and substrate bias (affect the angular distribution and energies of arriving adatoms) |
| ➤ Factors affecting zone models |
| Materials class, impurities incorporation, deposition technique |

It can be seen that all kinetic factors are related to diffusivities of adatoms on the surface or neighboring island surfaces. The nucleation rate depends on the substrate temperature and the deposition rate. The island growth rate also depends on the deposition rate as well as the adatom diffusivity on the substrate and the adatom desorption rate, both of which are strongly related to temperature. At low substrate temperatures, adatom mobilities are low and grain boundary mobilities are also low, the initial grain sizes are small and tend to change only through coarsening at the surface of the growing film. For example, Bruschi et al.¹² studied the Monte Carlo simulations of the nucleation and island growth of thin metal films on amorphous substrates, which aimed to investigate the role of diffusion and reevaporation in the determination of the microstructure of thin films. As can be seen from Fig. 2.3, surface diffusion of particles and clusters was restricted and the morphology was similar to random site percolation networks with high density of small islands at the lowest temperature ($T_s/T_M=0.027$). With increasing the substrate temperature up to the activation

of single adatom diffusion ($T_S/T_M=0.037$), surface diffusion was increased and caused the growth of cluster islands with dendritic shape. The higher of temperature ($T_S/T_M=0.04$), the stronger activates diffusion along the border of the clusters, the larger islands with more regularly shaped can be observed.

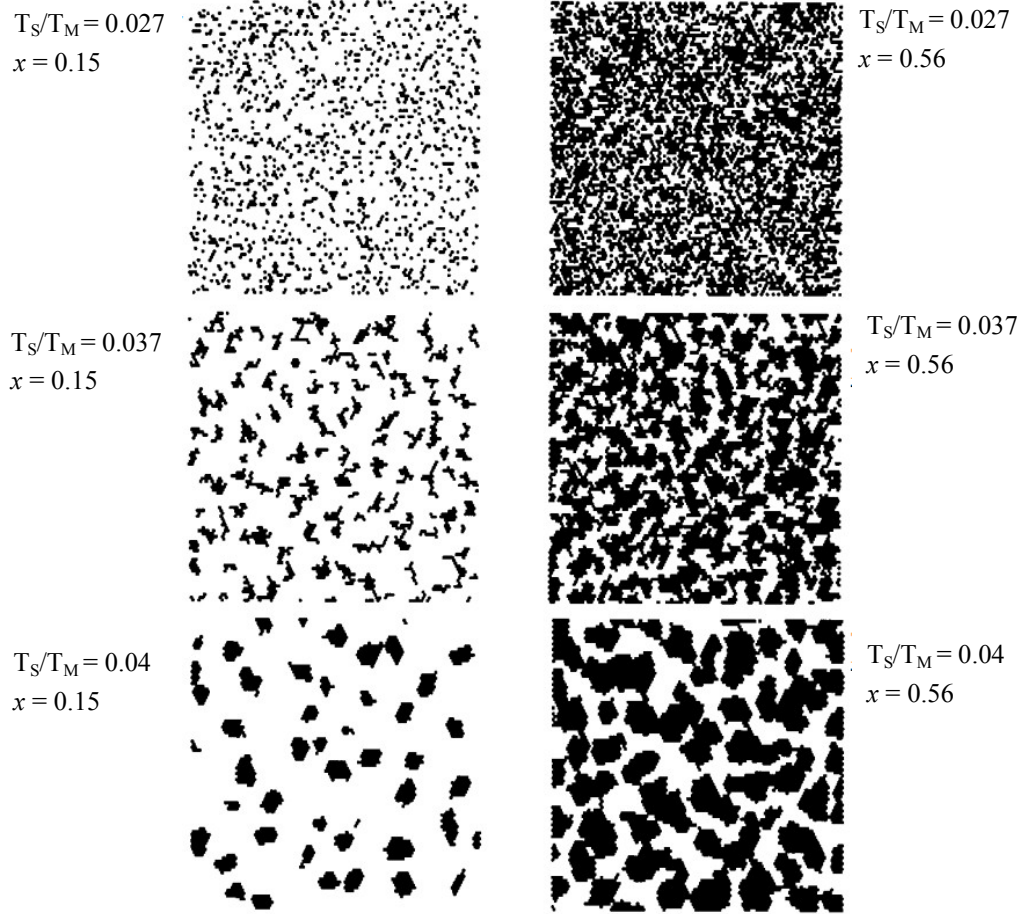


Fig. 2.3: Results of Monte Carlo simulated depositions of thin metal films performed at different homologous temperature (T_S/T_M) and final fractional coverages (x). The rate of reevaporation is set to zero. The figure shows 100×100 portions of 400×400 samples.¹²

Additionally, strain energy may easily build-up as a result of incorporation of defects in the crystal lattice, since the atoms cannot diffuse to low-energy sites. And then generally the island density is the same as the defect density, as demonstrated in Fig. 2.4 (shown in the next page).

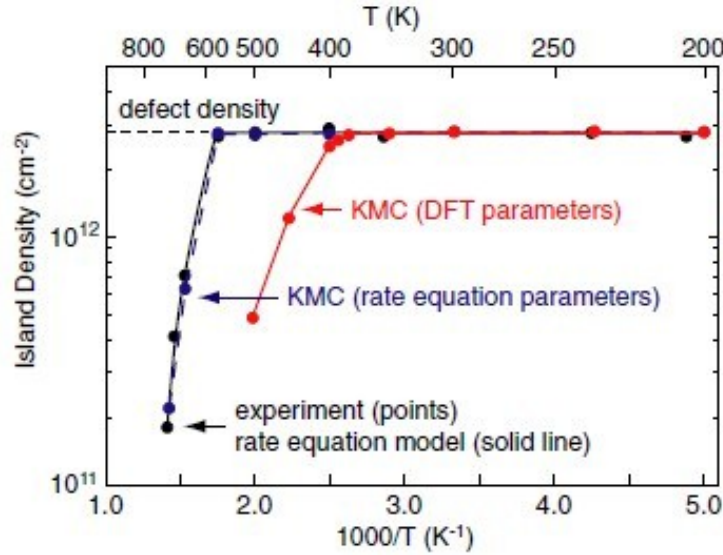


Fig. 2.4: Kinetic Monte Carlo (KMC) simulation of Pd island density on MgO(100) as a function of temperature. The diffusion barrier was set to 0.2 eV and 0.34 eV at rate equation model and density functional theory (DFT), respectively. KMC simulations using parameters calculated from DFT show that the island density is equal to the defect density at low T , matching the rate equation model (and experiment), which is due to a high monomer diffusivity in the later, and high cluster mobility in the former.¹³

In a magnetron sputter process, the substrate bias voltage plays an important role in controlling the effective adatom mobility and nucleation rates as well as the substrate temperature. When applying a substrate bias voltage, energetic ion bombardment will transfer kinetic energy to the film surface, thereby increasing the adatom mobility.¹⁴ However, too high ion bombardment energy can cause defects in the crystal lattice and induce compressive stress in the bulk of films as a result of the atomic peening effect.¹⁵ The energy of the impinging flux atoms is also affected by the sputtering gas pressure due to collisions between the sputtered atoms from the target and the gas atoms (such as Ar). By varying the sputtering power, the deposition rate can be controlled. High deposition rate reduces the adatom mobility since the adatoms have no time to move to low-energetic sites and are buried by newly arriving adatoms. And then nuclei formation rate increases. On the other hand, a very low deposition rate will introduce impurity incorporation on the film which depends on the background pressure of the chamber, due to a large relative flux of rest-gas particles. The relation between film structure and these deposition parameters is correlated by structure zone models which will be outlined briefly in next section.

2.3 Structure zone models for physical vapor deposited films

Film formation and the resulting microstructure are very crucial for their physical properties. Depending on the type of the material system, deposition process and chamber design etc, morphology and crystallographic orientation of thin films usually vary a lot. Over the past five decades, a number of models¹⁶⁻²¹ have been proposed to predict and explain correlation between film microstructure and deposition parameters for vapor deposited thin films. The first structure-zone model (SZM) was introduced by Movchan and Demchishin¹⁶ in 1969 for very thick evaporated metal films and oxides (0.3 mm to 2 mm) with high deposition rates ranging from 1200-1800 nm/min (see Fig. 2.5).

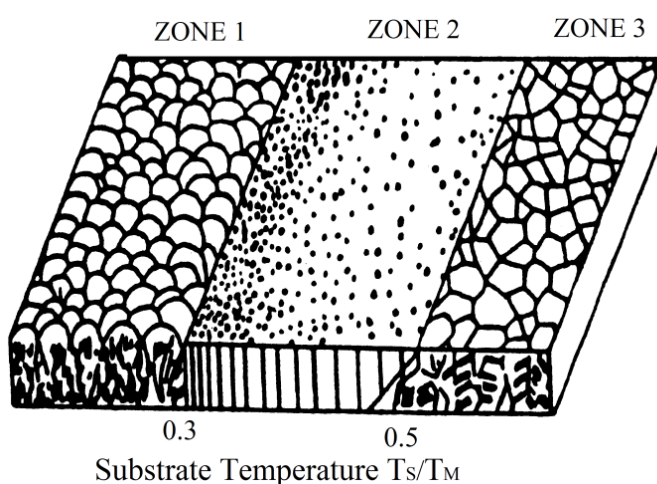


Fig. 2.5: Structure zone model for evaporated films proposed by Movchan and Demchishin.¹⁶

The model shown in Fig. 2.5 consists of three distinct structure zones (1, 2, 3) as a function of the ratio of substrate temperature to melting temperature (T_s/T_M). In this scheme, zone 1 structures ($T_s/T_M < 0.3$ for metals and $T_s/T_M < 0.26$ for oxides) are voided columns with domed tops due to self-shadowing effects and very limited adatom mobility at low temperature. The columns are generally consisting of amorphous-like structures. Zone 2 structures ($0.3 < T_s/T_M < 0.45$ for metals and $0.26 < T_s/T_M < 0.45$ for oxides) exhibit a dense columnar structure separated by grain boundaries. Surface and grain-boundary diffusion apparently becomes more important in the evolution of this structure, because the columnar grain size increases with T_s/T_M in accordance with the activation energies for these mass-transport mechanisms. Zone 3 structure ($T_s/T_M > 0.45$ for metals and oxides) is characterized by equiaxed polycrystalline grains that grow in size by bulk diffusion. Generally, the boundaries between these three zones are diffuse and the transition from one zone to another occurs gradually over a relatively wide range in T_s/T_M .

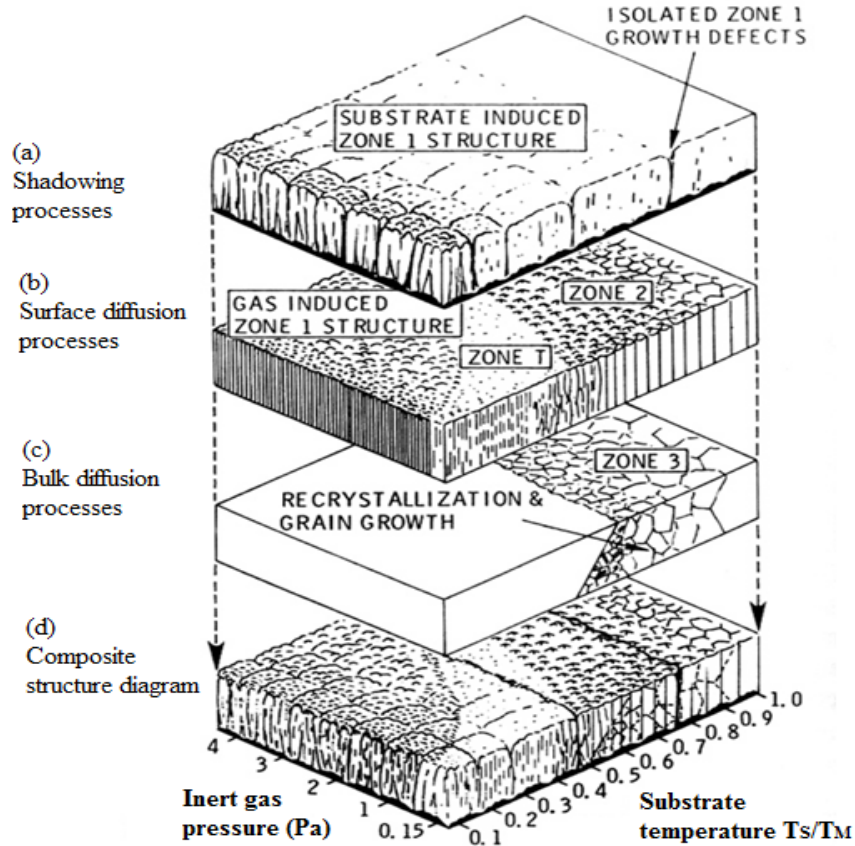


Fig. 2.6: Structure zone model for sputtered films proposed by Thornton.¹⁸

With the advent of magnetron sputtering, a similar SZM was developed by Thornton^{17,18} for metal films but with four zones (1, T, 2, 3), based on homologous temperature (T_s/T_m) and sputtering pressure. Since the inert gas induces collision with sputtered atoms, process pressure can change both the kinetic energy of the ions that arrive at substrate in random directions and the mean free path of the particles which allows an increase or decrease in the bombardment of the substrate surface, which in turn determines the adatoms mobility. Reduction of gas pressure increases the energy of the bombarding species which enhances adatom mobilities and makes the film denser. Furthermore, gas scattering also decreases the oblique component of the deposition flux, then self-shadowing increases the density at grain boundaries. The 4-zone SZ model dependent on the microstructure of cross-sectional view was shown in Fig. 2.6. In Zone 1 ($T_s/T_m < 0.1$ @ 0.15Pa to < 0.5 Pa @ 4Pa), the adatoms have little or no mobility since they cannot overcome the diffusion barrier E_d at very low T_s . Porous structure consists of tapered crystallites separated by voids which was promoted by substrate roughness and oblique deposition. Zone T ($0.1 < T_s/T_m < 0.4$ @ 0.15Pa, $0.4 < T_s/T_m < 0.5$ @ 4Pa) consisting of density packed fibrous grains is the transition region between zones 1 and 2. The surface of zone T is denser and less rough than the two surfaces around them. In Zone 2 ($0.4 < T_s/T_m < 0.7$), columnar grains with

dense grain boundaries are the result of surface diffusion controlled growth. Large equiaxed recrystallized grains are formed in zone 3 ($0.6 < T_s/T_M < 1$) due to lattice and grain-boundary diffusion processes at the highest T_s . Note that gas pressure only slightly affects the structure of zone 2 and 3 since the homologous temperature T_s/T_M is sufficiently high for substantial thermally activated surface diffusion and bulk diffusion.

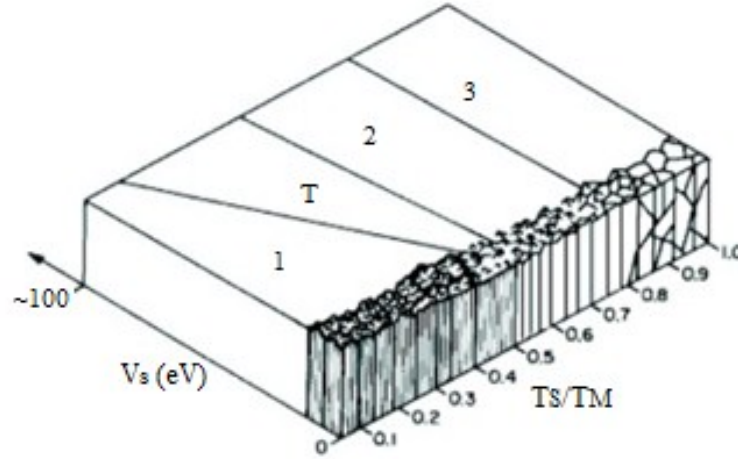


Fig. 2.7: Revised structure zone models for RF sputtering films, including ion bombardment effect.¹⁹

Messier et al.¹⁹ proposed a modified SZM for RF sputtering with zones 1, T, 2 and 3, shown in Fig. 2.7, where the ion energy axis replaces the pressure axis. Applying a negative substrate bias potential (V_s) enhances the ion bombardment, they found that there is a non-linear limit between zone 1 and zone T which is a function of the bias voltage applied to the substrate in some ceramic films (like TiB_2 , BN and SiC). The bias voltage of the substrate has the similar effect on the mobility and adsorption of the atoms as an increase in T_s . i.e. with increasing the bias voltage, zone T is widened compared to zone 1, which results in denser thin films and with a high degree of crystallinity due to increased ion bombardment enhancing adatom mobility. Moreover, the morphological evolution with increasing film thickness has been recognized at low mobility range ($T_s/T_M \leq 0.5$) in which dominant surface morphology size is nearly linear with the $\sim 3/4$ power of the film thickness.

In terms of SZMs for oxides related to the present work, Ellmer²⁰ proposed a complex structure-phase zone model for reactive sputtered Al-doped ZnO thin films with varying deposition parameters of oxygen partial pressure and the deposition rate. He established relations among phase composition, compressive stress, structure, grain size and optical properties to develop transparent conductive AZO films. Mirica et al.²¹ studied the morphological evolution of ZnO films deposited by reactive sputtering and proposed a

modified structure zone model, as shown in Fig. 2.8. In their model, the boundaries between zones with specific features were shifted toward lower homologous temperatures than in the classical models, which is due to the energetic ion bombardment during the sputtering process. They proposed two new subzones of zone II with pronounced faceting structure and smooth but pitted surface, respectively.

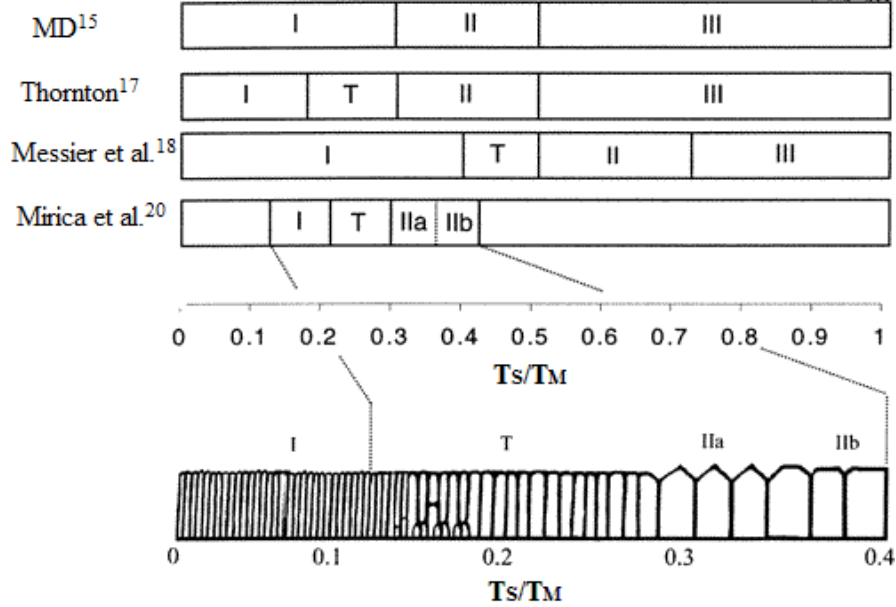


Fig. 2.8: Modified structure zone model ($0.13 \leq T_s/T_m \leq 0.43$) for reactive sputtered ZnO films from Mirica et al.²¹ compared with other SZMs.

Those extended structure zone models present a good qualitative guideline into which elementary processes or fundamental phenomena of structure formation occur during growth and give expectations for the structural evolution as a function of deposition variables for physical vapor deposited films. General features of extended SZMs have been found to be very universal based on those experimental investigations. There is also a lot of theoretical modeling for thin film growth in terms of noise (fluctuations), surface diffusion, shadowing and reemission effects, which will be described in the next chapter.

2.4 Scaling and correlations of rough surfaces

Since the morphology of the interface directly affects many physical and chemical properties of thin films, surface roughness as one of the most important features of morphology, needs to be considered carefully. For example, small roughness is desirable for many applications in microelectronic and optoelectronic devices in which surface roughness can generate additional scattering losses in optical waveguides through grain boundaries and decreases the electrical conductivity of polycrystalline thin films.²² On the other hand, rough surfaces are also demanded in some applications such as in catalysis and

adhesion improvement between different materials.²³ The growth of surfaces with certain roughness, especially the self-affinity of the surface roughness, is presently an active research topic. A self-affine surface has different scale-invariance properties and scaling relations along different growth directions, i.e. one perpendicular to the surface where the roughness is characterized by the height parameters, and the other along the surface. If the surface is rescaled by a factor of b in the surface dimension then the dimension in the direction of perpendicular growth must be magnified by a factor b^α in order to identify the similarities between the original and enlarged surfaces,² where α provides a quantitative measure of the imperfections of the surface morphology. For the special case $\alpha=1$, the surface shows self-similar properties.

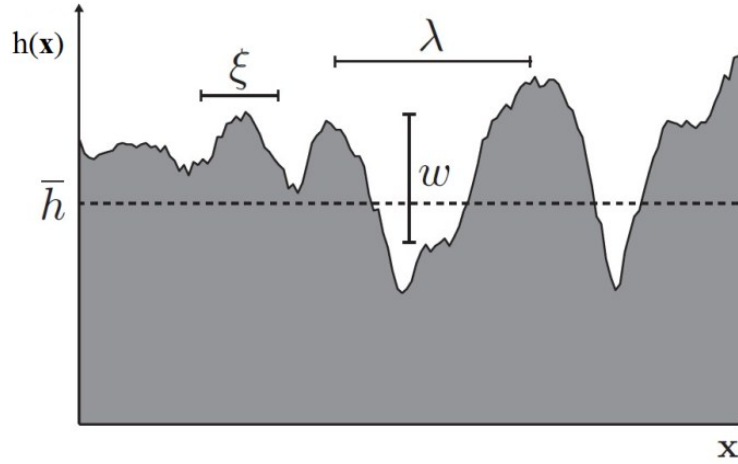


Fig. 2.9: Illustration of statistical parameters used to describe rough surfaces: the mean height \bar{h} , interface width w , lateral correlation length ξ , and wavelength λ .

The most commonly used statistical parameter to describe the roughness is the root-mean-square roughness (R_q or R_{rms} or w), as shown in Fig. 2.9, which is defined as the standard deviation of the surface heights:

$$w(L, t) = \sqrt{\langle (h(\mathbf{x}, t))^2 \rangle} = \sqrt{\frac{1}{L} \sum_{i=0}^L [h(i, t) - \bar{h}(t)]^2} \quad (2.4)$$

where $h(\mathbf{x}, t)$ is the relative surface height at a position \mathbf{x} at a deposition time t , corresponding to different film thicknesses depending on the deposition rate. L is the scan length of the measurement and the angular brackets mean configurational averages. Large values of root-mean-squared roughness indicate a rougher surface. It is well established that a large class of growth models follow the Family-Vicsek scaling relation²⁴:

$$w(L, t) \sim L^\alpha f(t/L^{\alpha/\beta}) \quad (2.5)$$

This equation reduces to $w(L, t) \sim t^\beta$ for very large values of L ($t/L^{\alpha/\beta} \ll 1$) and to $w(L, t) \sim L^\alpha$, for small values of L ($t/L^{\alpha/\beta} \gg 1$). β and α are the growth exponent and the roughness exponent, respectively. Therefore, the surface roughness increases with deposition time t (or thickness) at a rate determined by β value until a saturation value of the roughness is achieved. The saturation value depends on the scale length through α . This characteristic behavior of the roughness is the basis for dynamic scaling theory, widely used to describe the dynamic properties of self-affine thin films. It is known, that film growth by magnetron sputtering exhibits a linear time dependence of the film thickness $d_f(t)$.²⁵ This means, the surface roughness can also be scaled as $w \sim d_f^\beta$. Correlations along the surface can also be measured by the distance ξ over which surface fluctuations spread during deposition time t as $\xi \sim t^{1/z}$. These different exponents are not independent and are related by $z = \alpha/\beta$ in self-affine surface growth, where z is defined as the dynamic scaling exponent which depends on what kind of physical mechanisms are present in the growth process.

The exponents α and β can also be determined by analyzing surface correlation functions such as height-height correlation function $H(\mathbf{r}, t)$ of the surface, which measures the correlation of surface heights separated laterally by a vector \mathbf{r} in short range. $H(\mathbf{r}, t)$ is defined by:

$$\begin{aligned} H(\mathbf{r}, t) &= \langle (h(\mathbf{x} + \mathbf{r}, t) - h(\mathbf{x}, t))^2 \rangle \\ &= \langle [h(\mathbf{x} + \mathbf{r}, t)]^2 \rangle + \langle [h(\mathbf{x}, t)]^2 \rangle - 2 \langle h(\mathbf{x} + \mathbf{r}, t) h(\mathbf{x}, t) \rangle \\ &= 2w^2 - 2 \langle h(\mathbf{x} + \mathbf{r}, t) h(\mathbf{x}, t) \rangle \end{aligned} \quad (2.6)$$

For isotropic surfaces, the statistical behavior of the surface does not depend on the specific orientation of the surface which means that $H(\mathbf{r}, t)$ depends only on $|\mathbf{r}|$. Thus, $r = |\mathbf{r}|$ can be used to express $H(\mathbf{r}, t)$ as $H(r, t)$. This equation can be used to describe the statistical evolution of surfaces with self-affine fractal characteristics.³ For an isotropic self-affine surface, Sinha et al.²⁶ proposed the following functional form for the height-height correlation function:

$$H(r, t) = 2w^2 [1 - \exp[-(\frac{r}{\xi})^{2\alpha}]] \quad (2.7)$$

For $r \ll \xi$, $H(r, t) \approx 2w^2[1 - (1 - (\frac{r}{\xi})^{2\alpha})] \approx \frac{2w^2}{\xi^{2\alpha}} r^{2\alpha} \sim (mr)^{2\alpha}$, which m is the local slope and behaves as $m = \frac{(\sqrt{2}w)^{1/\alpha}}{\xi} \sim \frac{w^{1/\alpha}}{\xi}$. For $r \gg \xi$, $H(r, t) \sim 2w^2$, as shown in Fig. 2.10. Therefore, the height-height correlation function exhibits an asymptotic behavior as follows:

$$H(r, t) \sim \begin{cases} (mr)^{2\alpha}, & \text{for } r \ll \xi \\ 2w^2, & \text{for } r \gg \xi \end{cases} \quad (2.8)$$

Hence, the height-height correlation function $H(r, t)$ of a random self-affine fractal surface is described by three parameters: the vertical correlation length (surface width or roughness) w , the lateral correlation length ξ and the roughness exponent α . ξ is a length that gives an average measure of the lateral coarsening size at the deposition time t , i.e., it is the distance beyond which the surface height fluctuations are not correlated, indicating that there is no long-range characteristic length scale involved; the surface height fluctuation is random beyond ξ . The roughness exponent α characterizes the short-range roughness of a self-affine surface and how well the roughness can be described by a single lateral length scale.

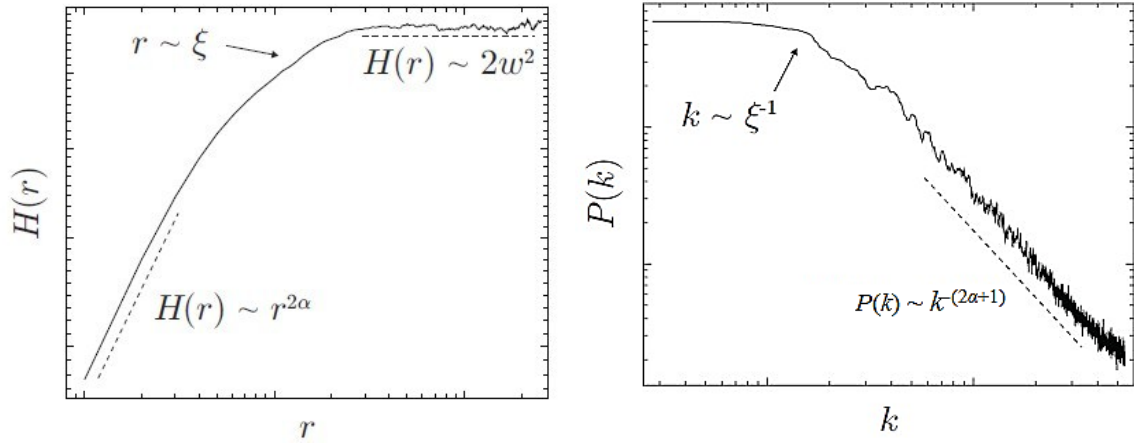


Fig. 2.10: Representative height-height correlation function $H(r)$ and one-dimensional power spectral density function $P(k)$ obtained from a self-affine surface. The plot is log-log scale.³

Note that for most thin film surfaces, height-height correlation function behaves as a power law only for small r in short range. The lateral correlation length also represents the short-range lateral behavior of a surface. But beyond ξ , a periodic behavior on a length scale larger than the ξ may be still presented even though surface heights are not

significantly correlated. To describe this long-range behavior, the power spectral density function (PSD) which is related to a d -dimensional Fourier transform of the surface heights, is used and defined in reciprocal space as:

$$\begin{aligned}
 P(\mathbf{k}, t) &= \frac{1}{(2\pi)^d} \left| \langle h(\mathbf{x}, t) e^{-i\mathbf{k} \cdot \mathbf{x}} \rangle \right|^2 \\
 &= \frac{1}{(2\pi)^d} \left[\int h(\mathbf{x}, t) e^{-i\mathbf{k} \cdot \mathbf{x}} d\mathbf{x} \right] \left[\int h(\mathbf{x}', t) e^{i\mathbf{k} \cdot \mathbf{x}'} d\mathbf{x}' \right] \\
 &= \frac{1}{(2\pi)^d} \iint h(\mathbf{x}, t) h(\mathbf{x}', t) e^{-i\mathbf{k} \cdot (\mathbf{x} - \mathbf{x}')} d\mathbf{x} d\mathbf{x}' \\
 &= \frac{1}{(2\pi)^d} \iint h(\mathbf{r}, t) h(\mathbf{r} + \mathbf{r}', t) e^{i\mathbf{k} \cdot \mathbf{r}'} d\mathbf{r} d\mathbf{r}' \\
 &= \frac{1}{(2\pi)^d} \int \left[\int h(\mathbf{r}, t) h(\mathbf{r} + \mathbf{r}', t) d\mathbf{r} \right] e^{i\mathbf{k} \cdot \mathbf{r}'} d\mathbf{r}'
 \end{aligned} \tag{2.9}$$

where the change of variables $\mathbf{x} = \mathbf{r}$ and $\mathbf{x}' = \mathbf{r} + \mathbf{r}'$ was used and the integration is over the entire domain of \mathbf{r} and \mathbf{r}' . Noting that the integral of PSD in \mathbf{k} -space is equal to w^2 . Recall from Eq.(2.6), the PSD can be expressed in terms of the height-height correlation function as:

$$P(\mathbf{k}, t) = \frac{1}{2(2\pi)^d} \int [2w^2 - H(\mathbf{r}, t)] e^{i\mathbf{k} \cdot \mathbf{r}} d\mathbf{r} \tag{2.10}$$

If the PSD spectrum exhibits a characteristic peak at a wavenumber k_C , the surface possesses a long-range periodic behavior and is said to be mounded and exhibit wavelength selection at a wavelength $\lambda = 2\pi k_C^{-1}$. Note that the lateral correlation length ξ is a measure of the size of the mounds and the wavelength λ is a measure of the average distance between mounds (as demonstrated at Fig. 2.9); therefore a relation of $\xi \leq \lambda$ should exist. For a self-affine surface in a scaling form, PSD spectrum has no characteristic peak:

$$\begin{aligned}
 P(k < \xi^{-1}) &\sim w^2 \xi^d \\
 P(k > \xi^{-1}) &\sim w^2 \xi^d (k\xi)^{-(2\alpha+d)}
 \end{aligned} \tag{2.11}$$

At lower wave number (longer length scale) the PSD magnitude is constant. At higher wave number (shorter length scale $k^{-1} < \xi$), the PSD function scales as $k^{-\gamma}$ and $\gamma = 2\alpha + d$. As shown in Fig. 2.10, for a line scan (dimension $d=1$), the long range roughness exponent α can be calculated from $\alpha = \frac{\gamma-1}{2}$.

In some cases, the dynamic scaling relation given by Eq.(2.5) cannot be applied and anomalous scaling²⁷⁻³⁰ has been proposed which is an extension of the dynamic scaling

relation. Anomalous scaling extends the local interface width which depends on both the scan length $l < L$ and the time t as:

$$w(l, t) \sim \begin{cases} t^\beta \\ t^\kappa l^{\alpha_{loc}} \end{cases} \quad (2.12)$$

where $\kappa = \beta - \alpha_{loc} / z$ and α_{loc} is a local roughness exponent that differs from the global α obtained from Eq.(2.5). This behavior of the interface width can be related to the local slope m which scales with growth time as t^κ . Note that when $\kappa = 0$, $\alpha_{loc} = \alpha$, and the Family-Vicsek scaling of Eq.(2.5) is recovered. Anomalous scaling occurs whenever $\kappa > 0$, leading to a local roughness exponent $\alpha_{loc} = \alpha - z\kappa$. On the one hand, there are intrinsically anomalous roughened processes induced surfaces. The local roughness presents as $0 < \alpha_{loc} < 1$ and α take values larger or smaller than 1 depending on the different systems, which is due to the disorder and/or nonlocal effects (such as shadowing or bulk diffusion). On the other hand, there exist superroughening processes with $\alpha > 1$ and $\alpha_{loc} = 1$ which occurs in local growth models.^{29,31}

In conventional dynamic scaling theory, the exponents α and β do not change with deposition time. However, in some systems^{32,33} the growth exponent β exhibited different values in different growth regions indicating that there is a transition between different growth modes and each region satisfies independently the Family-Vicsek scaling relation (Eq.(2.5)). For the roughness exponent α , it is hard to figure a relation with growth time. Some groups reported that α is time independent. For example, Jeffries et al.³⁴ have studied the kinetic roughening in the sputter deposition growth of Pt on glass at room temperature. They found that α with a value of 0.9 ± 0.02 was independent of the growth time. Huo et al.³⁵ found a similar behavior of α during Cu electrodeposition. But the fluctuation of the roughness exponent with time is an anomalous behavior. Some groups reported it is a time-dependent parameter. For example, Zhu et al.³⁶ have investigated the coarsening dynamics and surface instability during ion-beam-assisted growth of amorphous diamondlike carbon. They reported α varies with the growth time at the initial growth regime and then becomes time invariant. Yanguas-Gil et al.³³ reported similar behavior for local roughness exponent by studying the growth of SiO₂ films grown by plasma-enhanced chemical vapor deposition. The variation roughness exponent with time is less important for the obtained local roughness in their system.

2.5 Models for growth-induced roughening

In the universal classes in statistical physics, specific details of the growth, such as the nature of the substrate, the deposition material, the deposition pressure and temperature etc. do not contribute to the scaling exponents. Classifying growth processes according to these exponents has attracted huge interest in the statistical physics community during the past two decades.^{2,3} Since the morphological structure of a surface grown by deposition of atoms is relevant to the actual physical properties of thin films, here we will briefly outline some of the most important theoretical growth models based on discrete and continuum mathematics which are able to predict values for the exponents α , β and z analytically. It is interesting to compare experimental data with these predictions and capture essential physical mechanism to achieve a better understanding of the growth behavior of different materials prepared by sputtering technique.

2.5.1 Discrete surface growth models

Monte Carlo (MC) modeling is the most common type of discrete simulation used in thin film growth modeling. Generally speaking, MC models only model general morphological behavior and do not incorporate deposition details, such as the specific types of deposited atoms, or their nature or chemical state. Instead, MC models use more empirical parameters which can be easily implemented in the algorithm, such as the activation energy for diffusion or the sticking coefficient.³ General rules in MC models in thin film growth are:

- (1) A lattice (2D or 3D) has to be initialized where the deposition will take place.
- (2) A particle has to be created at a random lattice point, and the particle is related to time according to a specified trajectory: deterministic or stochastic type.
- (3) When the particle impinges the substrate surface, it can be deposited (condensation), or reflected (reemission), depending on deposition parameters.
- (4) Deposited particles can diffuse according to a specified model for diffusion.
- (5) New particles can be created and the deposition process can be repeated.

If a particle travels in a straight line from certain direction, the randomness is determined by the impinging angle and the initial position of the particle. This deterministic trajectory is used in the solid-on-solid and ballistic deposition models. The restricted solid-on-solid (SOS) model³⁷ introduces the first systematic investigation of growth exponents for higher dimensions. Particles travel ballistically on a random position at the substrate. If a particle is able to diffuse to any adjacent surface site with a lower height, it will continue to diffuse

until the energy for diffusion is very low, and then the particle will stop diffuse. This process will be repeated by other particles at certain times. Physically, this model presents an adsorption/desorption dynamics. Kim and Kosterlitz³⁷ proposed the exponents are $\beta = 1/(d+1)$ and $\alpha = 2/(d+2)$. In their simulation, without diffusion, a growth exponent β of 0.5 was found, in agreement with the value derived from the continuum random deposition model in 1+1 dimensions. Taking surface diffusion into account in 2+1 dimensions, a value of $\beta = 0.332 \pm 0.05$ was obtained. The ballistic deposition (BD)³⁸ is another discrete growth model which exhibits an interesting surface scaling behavior. Essentially, the model describes particles rain down onto the substrate following straight-line trajectories in the columns and stick to the aggregate or the substrate upon first contact. The host particle can be at the top of the same column or in one of the nearest neighbor columns. Overhangs can exist in the ballistic growth model. In contrast to random deposition and random deposition with surface diffusion leading to completely compact structures, ballistic deposition generates voids or holes in the bulk due to the lateral sticking rule. The formation of these voids or holes increases the growth velocity of the interface, because with the same number of deposited particles the average height increases faster. Ko and Seno³⁹ studied deposition growth by multi-dimensions Monte Carlo simulations of BD and restricted SOS model whether overhangs are present or not. They found that the presence of overhangs is an important factor in determining the scaling properties of film growth. Since the overhangs start to form, the surface does not grow on the direction of local surface gradient any more, but rather results anisotropic growth. The simulated exponents are listed in Table 2.2. Meakin et al.⁴⁰ and Baiode et al.⁴¹ reported that the scaling exponents of ballistic deposition are $\alpha \approx 0.3$ and $\beta \approx 0.22$ in 2+1 dimensions.

Table 2.2: Calculated scaling exponents involving nonlocal growth models for different simulations in 2+1 dimensions. s_0 is the first order sticking coefficient.

| Model | Model Type | α | β | 1/z | Reference |
|-------------------------|-------------|----------|-------------------------------|----------|-----------|
| Shadowing growth (SOS) | Monte Carlo | 0.40 | 0.25 | 0.625 | 39 |
| Shadowing growth (BD) | Monte Carlo | 0.26 | 0.21 | 0.81 | 39 |
| Shadowing growth | Monte Carlo | - | 1 | 0.93±0.1 | 61 |
| Shadowing vs reemission | Monte Carlo | - | 0.1~1, depending on the s_0 | - | 62 |
| Shadowing growth | Continuum | - | 1 | - | 61 |

The Eden model⁴² is a random growth process originally describing the formation of specific types of clusters such as bacteria or tissue cultures which follow a stochastic trajectory (no assigned direction). In the Eden model all surface sites are the nearest-neighbor perimeter sites of the cluster and can grow with equal probability. A new particle is added on any randomly-chosen perimeter site and then forms a two-site cluster. Its scaling properties can be described by the KPZ equation and $\alpha \approx 0.5$ and $\beta \approx 1/3$ can be estimated in 1+1 dimensions, close to the results of ballistic deposition. While in 2+1 dimensions, strong crossover effects generate scattered α values in the range of 0.2~0.4.²

2.5.2 Local continuum growth models

Instead of an algorithm for the deposition process, continuum modeling of the surface growth uses a partial differential equation. The general form of a stochastic continuum equation is:

$$\frac{\partial h(\mathbf{x}, t)}{\partial t} = \phi h(\mathbf{x}, t) + \eta(\mathbf{x}, t) \quad (2.13)$$

where $h(\mathbf{x}, t)$ represents the surface height with respect to the substrate at a position \mathbf{x} on the surface at time t , which is assumed to be a single-valued function. $\eta(\mathbf{x}, t)$ is the random noise that inherently exists during growth, often assumed to be a Gaussian distribution with $\langle \eta(\mathbf{x}, t) \rangle = 0$ and $\langle \eta(\mathbf{x}, t) \eta(\mathbf{x}', t') \rangle = 2C\delta^d(\mathbf{x} - \mathbf{x}')\delta(t - t')$, where C is the parameter of the model and d is the dimension of the vector \mathbf{x} . $\phi(h, \mathbf{x}, t)$ is some function of the height profile $h(\mathbf{x}, t)$ that reflects the growth processes to be modeled, which we will discuss below.

2.5.2.1 Random deposition model

The random deposition (RD) is the simplest known model, where each particle drops vertically along a single column on random positions until they reach the top of the column on the surface and stick there. In RD, the columns grow independently which means the height of the interface does not depend on the height of the neighboring columns. Therefore, lateral correlations among the deposited particles can be completely neglected, the continuous and discrete atomistic versions of the model have exact solutions. In local continuum models, the function ϕ depends on local interaction terms only. The simplest growth process is that the function ϕ equals to a constant, C_0 , implying there is no growth process active to correlate surface heights. Therefore the continuum growth equation can be described as

$$\begin{aligned}\frac{\partial h(\mathbf{x}, t)}{\partial t} &= C_0 + \eta(\mathbf{x}, t) \\ h(\mathbf{x}, t) &= \int_0^t \frac{\partial h(\mathbf{x}, t')}{\partial t'} dt' = \int_0^t C_0 dt' + \int_0^t \eta(\mathbf{x}, t') dt' \\ &= C_0 t + \int_0^t \eta(\mathbf{x}, t') dt'\end{aligned}\tag{2.14}$$

The interface can be expressed as $[w(t)]^2 = \langle [h(x, t)]^2 \rangle - \bar{h}^2 = 2C_0 t \sim t$, which gives $\beta=0.5$. The RD model allows the interface width to grow indefinitely with time, i.e., without reaching to a saturation stage. Since no correlations are considered in this model, the correlation length ξ is always zero, and the dynamic exponent z is not defined. Also, the interface width does not saturate due to the lack of correlation of surface height, α is also not defined, as a result, the surface is not self-affine. Therefore, RD model does not completely describe any realistic experiment, but can be used as an analytical solvable model with an exact prediction of $\beta=0.5$, which is often observed at very early times during growth from a flat substrate when noise is the most dominant growth mechanism.

2.5.2.2 Edwards- Wilkinson model

When the surface heights start to correlate, the RD model cannot be used, and $\phi(h, \mathbf{x}, t)$ has to be modified to include correlations between surface heights. A simple model of symmetry surface evolution in describing the fluctuations of an equilibrium interface governed by surface tension and noise is the Edwards-Wilkinson (EW) equation:^{43,44}

$$\frac{\partial h}{\partial t} = \nu \nabla^2 h + \eta \quad (2.15)$$

where the first term on the right-hand side describes relaxation of the interface by a surface tension ν , which smoothens the surface while maintaining the mean height unchanged through evaporation-condensation processes. The EW equation is a continuum equation used to study the sedimentation of granular particles under gravitation. The exponents α , β , and z characterizing the growth of a surface according to the EW equation are: $z=2$, $\alpha = \frac{2-d}{2}$, $\beta = \frac{\alpha}{z} = \frac{2-d}{4}$. The scaling exponents depend on the dimensions of the surface. For $d=1$, the predicted exponents are $\alpha=1/2$, $\beta=1/4$. And obviously, $d=2$ is the critical dimension of the EW equation which predicts $\alpha=\beta=0$, suggesting that the behavior of the roughness is more complicated than a power law. For $d>2$, the roughness exponent α and growth exponent β both become negative, implying that the surface is very flat. Every noise-induced irregularity which generates nonzero width is suppressed by the surface tension.

2.5.2.3 Mullins Diffusion model

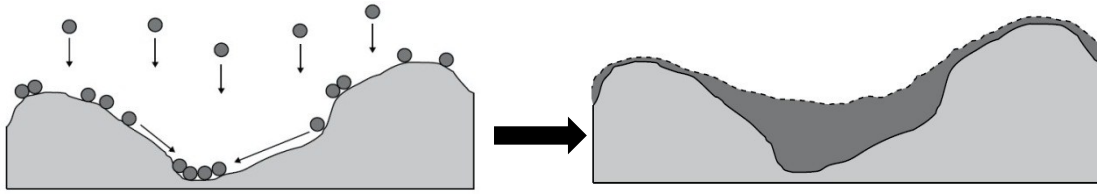


Fig. 2.11: The effect of the Mullins diffusion term $-D'\nabla^4 h$ on a surface profile.³

The Mullins diffusion (MD) model⁴⁵ describes a growth process where surface diffusion to highly coordinated surface sites constitutes the relaxation mechanism, as shown in Fig. 2.11. The growth equation is:

$$\frac{\partial h}{\partial t} = -D'\nabla^4 h + \eta \quad (2.16)$$

where the ∇^4 term represents the linear diffusion, with the diffusion coefficient D' determined by the Arrhenius law $\exp[-(E_a + n_n E_n)/k_B T]$, where E_a is the activation energy for diffusion, E_n is the bonding energy with a nearest neighbor, n_n is the number of nearest neighbors.^{46,47} It can be seen that higher activation energy and bonding energy of a particle leads to a smaller diffusion probability. The calculated scaling exponents in the MD model

are $z=4$, $\alpha = \frac{4-d}{2}$, $\beta = \frac{4-d}{8}$. In 2+1 dimensions, $\alpha=1$ and $\beta=1/4$ are obtained, which could in principle be used for growth process in which surface diffusion dominates. Experimental investigations^{34,48} in terms of growth dominated by surface diffusion show that the local slope m changes with growth time, indicating that the growth is nonstationary.

2.5.2.4 Kardar-Parisi-Zhang model

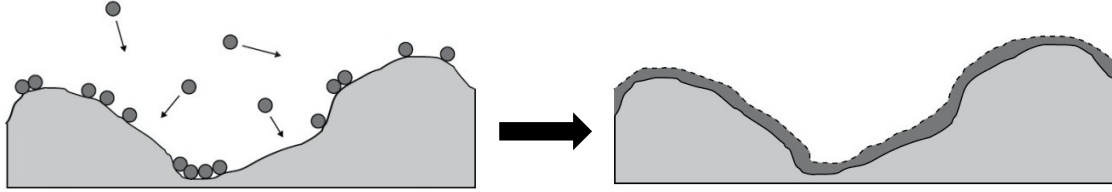


Fig. 2.12: The effect of the KPZ term $|\nabla h|^2$ on a surface profile.³

The surface height symmetries presented in the EW equation will break when the surface not only grows perpendicular to the local surface, but also develops along the local surface. By considering the growth along the local surface, Kardar, Parisi and Zhang (KPZ)⁴⁹ extend EW model and suggested a nonlinear stochastic partial differential equation widely used in the literature as a model of randomly growing interfaces. Fig. 2.12 shows a diagram of the growth dynamics modeled by the KPZ equation, which can be described as:

$$\frac{\partial h}{\partial t} = \nu \nabla^2 h + \frac{\lambda}{2} |\nabla h|^2 + \eta \quad (2.17)$$

where the first term represents surface relaxation as in the EW equation. The second term $\frac{\lambda}{2} |\nabla h|^2$ is the lowest-order nonlinear term reflecting the presence of lateral growth that can appear in the interface growth equation. Renormalization group theory² was used to obtain the exponents, which gives analytical values only in 1+1 dimensions: $z=3/2$; $\alpha=1/2$, $\beta=\alpha/z=1/3$. These exponent are in agreement with the numerical studies of Plischke and Racz⁵⁰ on the Eden model giving $z=1.55 \pm 0.15$, very close to the predicted value of $z=3/2$, and also some simulations confirm that for a strip geometry the roughness exponent is $\alpha=1/2$. The two exponents α and z are related by the ‘scaling law’ $\alpha+z=2$ which follows from the rotational invariance of the equations underling the KPZ model. The exponents in 2+1 dimensions have only been investigated using large scale simulations with the results²: $z=1.58$; $\alpha=0.38$, $\beta=0.24$.

2 Thin Film Growth Models

In order to better understand growth under chemical-bonding conditions, Wolf and Villain⁵¹ and Lai and Sarma⁵² proposed a kinetic growth model ($\frac{\partial h}{\partial t} = -D'\nabla^4 h + \frac{\lambda}{2}\nabla^2 |\nabla h|^2 + \eta$) in which the particles are randomly deposited onto a substrate and subsequently relax to nearby kink sites maximizing the number of saturated bonds. Drotar et al.⁵³ solved the noisy Kuramoto-Sivashinsky (KS) equation ($\frac{\partial h}{\partial t} = -v\nabla^2 h - D'\nabla^4 h + \frac{\lambda}{2}|\nabla h|^2 + \eta$) numerically in 2+1 dimensions which reflects the effect of particles being knocked out of the surface by ion bombardment (combination of the $\nabla^2 h$ and $|\nabla h|^2$ terms), surface diffusion and noise. The simulation scaling exponents are listed in Table 2.3.

Table 2.3: The predicted scaling exponents in various local growth models for different continuum equations in 2+1 dimensions: involving the random noise (η), surface relaxation (including the term v), surface diffusion (with the term D') and the presence of lateral growth (with a nonlinear term $\frac{\lambda}{2}|\nabla h|^2$).

| Differential equation $\partial h / \partial t =$ | Name | α | β | z | $1/z$ | Reference |
|--|-------------------------|---------------|---------------|----------------|----------------|-----------|
| η | Random deposition | - | 0.5 | - | - | 61 |
| $v\nabla^2 h + \eta$ | Edwards-Wilkinson | 0 | 0 | 2 | 0.5 | 44 |
| $-D'\nabla^4 h + \eta$ | Mullins diffusion | 1 | 0.25 | 4 | 0.25 | 2 |
| $v\nabla^2 h - D'\nabla^4 h + \eta$ | General linear equation | 0~1 | 0~0.25 | 2~4 | 0.25~0.5 | 54 |
| $v\nabla^2 h + \frac{\lambda}{2} \nabla h ^2 + \eta$ | KPZ | 0.38 | 0.24 | 1.58 | 0.63 | 49 |
| $-D'\nabla^4 h + \frac{\lambda}{2}\nabla^2 \nabla h ^2 + \eta$ | Lai-Das Sarma | $\frac{2}{3}$ | $\frac{1}{5}$ | $\frac{10}{3}$ | $\frac{3}{10}$ | 52 |
| $-v\nabla^2 h - D'\nabla^4 h + \frac{\lambda}{2} \nabla h ^2 + \eta$ | KS(early time) | 0.75~0.80 | 0.22~0.25 | 3~4 | 0.25~0.33 | 53 |
| | KS(late time) | 0.25~0.28 | 0.16~0.21 | - | - | |

2.5.3 Nonlocal continuum growth models

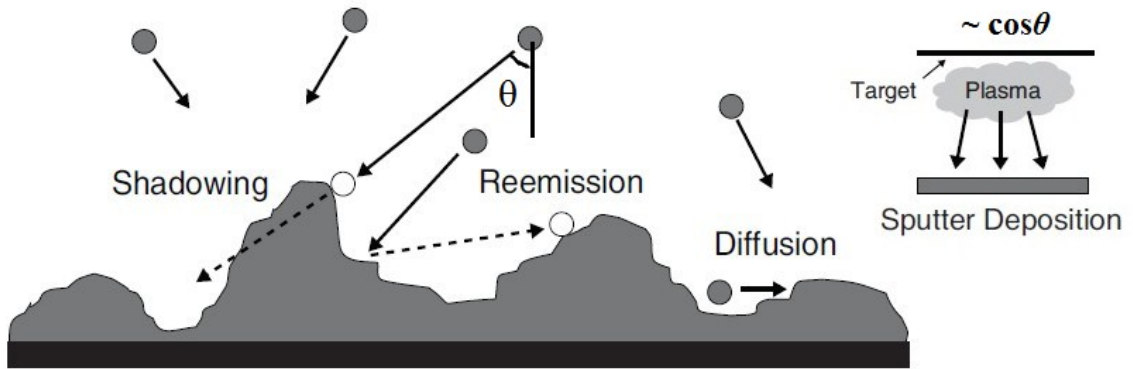


Fig. 2.13: Illustration of the growth effects including shadowing, reemission and surface diffusion. The incident flux has a distribution of $\sim \cos\theta$.³

In practical deposition techniques such as sputtering and chemical vapor deposition, nonlocal effects such as shadowing^{56,57,60}, along with the redistribution of atoms reflected from the surface due to a nonunity sticking coefficient⁵⁵ can play an important role for the surface morphology during film growth. In sputtering processes where the incident flux normally has an angular distribution, the ejected particles from the target have a long mean free path and can be assumed to move ballistically to the substrate surface. Those particles originated either under random angles or under a fixed angle depending on the experimental setup. In a random incidence deposition process, particles arrive from all directions and the local growth rate is proportional to the probability that its top receive particles which follows a ballistic trajectory with randomly-selected direction. In the oblique incidence deposition process, particles arrive ballistically with all trajectories forming an incidence angle. Obviously, more deposition atoms arrive on higher surfaces (hills) and fewer in lower positions (valleys) which are shadowed by the hills, as shown in Fig. 2.13. Therefore, the higher surface features grow at the expense of lower ones, leading to a competition among different surface features for particle flux. Since the shadowing of a surface feature does not only count on the close-by surface heights, but also depends on the heights of all other far-off surfaces, shadowing is an inherently nonlocal process. A simple continuous growth model for deposition of thin amorphous films in 1+1 dimensions by sputtering was proposed by Karunasiri et al.⁵⁶ and Bales et al.⁵⁷ by considering the shadowing instability together with surface diffusion during the growth process. Their growth equation is:

$$\frac{\partial h}{\partial t} = -D'\nabla^4 h + R\theta(\mathbf{x}, t) + \eta \quad (2.18)$$

where the first term on the right-hand side describes surface diffusion with diffusion coefficient D' as described at Mullins diffusion model. The second term denotes the deposition rate R with the exposure angle $\theta(\mathbf{x}, t)$ measuring the amount of particle flux that each point receives, which incorporates the shadowing effect. Due to the shadowing effect, the interface of the sputtered film has a columnar structure. If diffusion is limited, extremely rough surface structures with deep grooves between neighboring columns will form as a result of the shadowing. While broad tops structure growing with constant velocity along the surface normal does not account for the shadowing in the sputtering process but due to the Huygens principle, similar with geometric optics.^{58, 59} If the deposition rate R is negative in Eq.(2.18) it corresponds to the erosion of the surface. In contrast to growth processes, shadowing effect will smooth the surface during erosion.

If condensation/evaporation dynamics is a dominant annealing mechanism, then a surface relaxation term $\nu\nabla^2 h$ should substitute the first diffusion term, which was investigated by Yao and Guo⁶⁰. They observed shadowing instability develops the interface into a mountain landscape or columnar structure, which coarsens in time with a growth exponent β of 1 and dynamic exponent z of 0.33 in 2+1 dimensions from a 96×96 lattice simulation. Drotar et al.⁶¹ modeled the growth of a surface under both shadowing and reemission effects and proposed a stochastic continuum growth equation:

$$\frac{\partial h}{\partial t} = \nu\nabla^2 h - D'\nabla^4 h \mp \sqrt{1+|\nabla h|^2} \left[\sum_{i=0}^{\infty} s_i F_i(\mathbf{x}, t) \right] + \eta \quad (2.19)$$

In this equation, the third term is a nonlinear term corresponding to flux reemission which allows impinging particles bounce around before settling at appropriate sites on the surface which can reduce shadowing effect. s_i is the i th-order sticking coefficient, and $F_i(\mathbf{x}, t)$ is the i th-order flux incident on the surface due to reemission. Smaller values of the sticking coefficient indicates a larger percentage of incident particles that can be reemitted which consequently smoothes the surface. $\mp \sqrt{1+|\nabla h|^2}$ represents the growth (+) and etching (-) normal to the local surface. They calculated a growth exponent $\beta=1$ for growth under perfect shadowing (no reemission $s_0=1$) and $\beta=0$ for etching in 2+1 dimensional system. The correlation length followed a relationship $\xi \propto (t-t_0)^{1/z}$ with $1/z=0.93\pm0.1$ for growth and $1/z=0$ for etching. Lu et al.⁶² performed solid-on-solid Monte Carlo simulation for film

growth with different sticking coefficients s_0 and different diffusion lengths D/F . The result is shown in Fig. 2.14. They observed the growth exponent β is changed significantly by varying the value of s_0 , but slightly affected by changing the strength of surface diffusion. Pelliccione et al.⁶³ reported similar results that exponent $\beta=1$ occurs under strong shadowing and low reemission ($s_0 < 0.7$). When $s_0 \approx 0.625$, reemission begins to become significant and tends to smooth the surface, thereby decrease the β value to 0.58. When $0.125 < s_0 < 0.5$, reemission becomes the dominant growth effect and $0.11 < \beta < 0.25$.

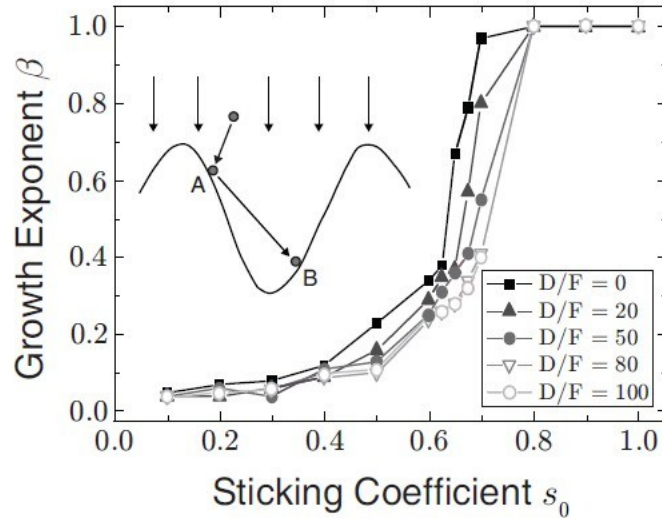


Fig. 2.14 Monte Carlo simulation of the growth exponent β as a function of the sticking coefficient s_0 with different diffusion lengths D/F for flux proportional to $\cos\theta$. The second order sticking coefficient s_1 is assuming to 1.⁶²

2.6 Experimental scaling behavior of surface roughness for sputtered films

Many reports on experimental dynamic scaling exponents for different materials prepared by sputtering deposition can be found in the literature. It is believed that also sputtered films exhibit the features of both local and nonlocal growth which were already discussed in the previous chapters.³ Fig. 2.15 summarizes the range of reported scaling exponents for sputter deposition together with thermal evaporation, chemical vapor deposition (CVD), and oblique angle deposition, displaying a significant variation of the β values. For comparison, the range of β values predicted by both local and nonlocal models is shown, too. Obviously, non-local models play a very important role in thin film growth and can be used to describe many experimental observations. But still some experimental results are above the predicted range pointing to the fact that the theory of surface growth has to be modified to describe the wide range of experiment results. Below, some

experimental scaling of surface roughness for thin films including metal, nitrides and oxides deposited by magnetron sputtering are discussed in detail.

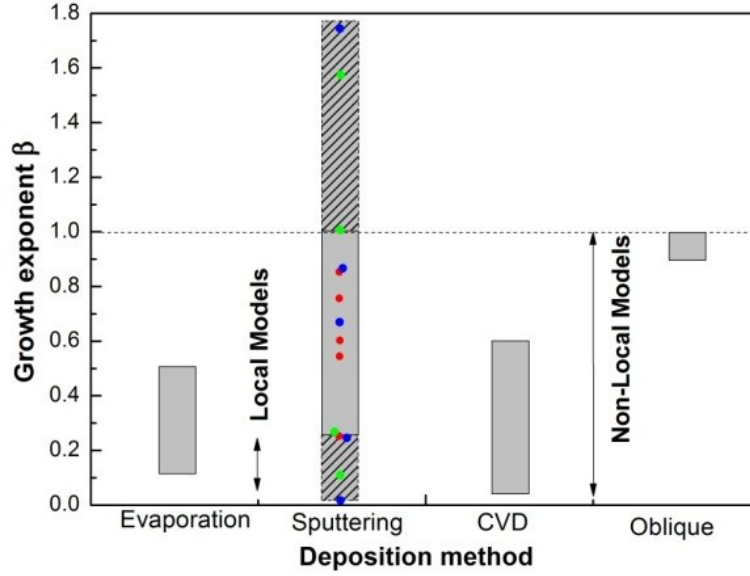


Fig. 2.15: Overview of the growth exponent β based on Ref.22, double-headed arrow indicate the range of β values predicted from both local (0~0.25) and nonlocal models (0~1). Shaded areas represent a range of the majority of experimentally measured values for β reported in the literature for different deposition techniques from Ref.22. We extended it to larger range by adding the slash area. Inserting symbols \bullet , \bullet , and \bullet represents some β values for metal^{34,64-67}, nitrides⁶⁹⁻⁷¹ and oxides films^{72,73,167,207}, respectively.

For metal films, Jeffries et al.³⁴ studied the kinetic roughening for the growth of sputter deposited Pt films on glass at room temperature by scanning tunneling microscopy. They observed irregularly growing mound morphology where the local surface slope increases with growth time. The obtained scaling exponents were $\beta \sim 0.26$ and $\alpha \sim 0.9$. Due to the spinning and planetary rotation of the sample holder during deposition, shadowing effects for the random and oblique incidence did not exist in their system. The Schwoebel barrier effect was excluded because the large-scale pyramids of regular size were not observed and it is unlikely in polycrystalline systems with randomly orientated small grains. Therefore, the growth of Pt films was governed by a linear diffusion process.

Lita et al.⁶⁴ investigated the dynamic scaling for sputtered polycrystalline Al films on thermally oxidized Si (100) substrates at room temperature. They found a temporal growth regime dominated by surface diffusion smoothing effect with β_1 of 0 and α_1 of 1.17~1.36, and followed by a growth stage of larger length scales by a roughening mechanism attributed to the effects of grain boundary grooves and grain growth which result in β_2 of 0.55 and α_2 of 0.30~0.38. Yang et al.⁶⁵ reported a β of 0.85 and α of 0.83 in the dynamic evolution of surface fluctuations for RF sputtered polycrystalline Cu thin films on Ta-

covered Si (111) substrates at 427 °C. They excluded the shadowing effect as a result of the rotation of the sample holder during film growth³⁴, but included the presence of nonlocal bulk diffusion which leads to grain growth and increases the height undulation of the grains for the anomalous scaling behavior.

Santamaria et al.⁶⁶ studied by energy-filtered transmission electron microscopy the scaling of the interface roughness in DC-sputtered Fe-Cr superlattices. They found very similar scaling of short-range roughness at different sputtering pressures and supposed that the growth processes are similar on the atomic scale. For the long-range case, the growth exponents β of 0.76 and 0.25 at high and low sputtering pressure, respectively, were obtained which was explained by a nonlocal shadowing effects. The correlation length increases with film thickness with a power law $1/z=0.7$ at high pressure, but showed an almost thickness independent relation at low pressure, indicating that kinetic roughening might be more complicated in superlattices than at single surfaces.

Schlomka et al.⁶⁷ studied the growth behavior of argon-ion sputtered, magnetic NiMnSb films on MgO (001) and Si(001) by *in situ* X-ray scattering. Growth exponents β of 0.6, 0.6 and 0.75 for NiMnSb films on MgO (001) were obtained at 100 °C, 250 °C and 300 °C deposition temperature, respectively. For NiMnSb films on Si (001), the β values of 0.4 for a 150 °C deposition was smaller than the β of 0.55 for the 250 °C deposition. The growth exponent is larger at high temperature than that of low temperature, which was explained by the thermally activated crystallization roughening mechanism.

For nitride films, Auger et al.⁶⁸ investigated by atomic force microscope the surface kinetic roughening of TiN films on Si (100) substrates grown at low temperature by DC reactive sputtering from a metallic target. They characterized the film kinetic roughening with β of 0.67 and α of 1.7 and argued that the intrinsic anomalous surface roughening behavior is probably due to the nonlocal shadowing effect in the sputtering process.

Karr et al.⁶⁹ studied the evolution of the surface morphology and microstructure for reactively magnetron sputtered epitaxial TiN (001) film on MgO (001) substrate at $650 \leq T_s \leq 750$ °C. They obtained a smaller $\beta=0.25\pm0.07$ than that of Auger's result as a result of stronger surface diffusion at the high deposition temperature.

Xu et al.⁷⁰ investigated comparatively the surface evolution of amorphous-Si₃N₄ films and of nanocrystalline CrN on boron-doped Si(100) substrates deposited by RF reactive magnetron sputtering in Ar/N₂ atmosphere at room temperature. It was found that the

growth exponents β of both nitrides can be divided into two regions of $\beta_1=0.09\pm0.01$ and $\beta_2=0.24\pm0.03$ for Si_3N_4 films and $\beta_1=0.22\pm0.08$ and $\beta_2=0.87\pm0.1$ for CrN films, respectively. For Si_3N_4 films, the very low exponent of 0.09 ± 0.01 was explained by the hopping rate of impinging particles far exceeding the deposition rate in the initial growth region. Shadowing effect generated a larger β than that of the surface diffusion for later growth region. For polycrystalline CrN films, oriented grain growth not only played an important role for the surface roughening, but also enhancing the shadowing effect, which induced rough surfaces with larger growth exponents than that of amorphous Si_3N_4 films. Lee et al.⁷¹ even determined three regions of dynamic scaling in the $\text{InN}/\text{Al}_2\text{O}_3(0001)$ deposited by DC sputtering in Ar/N_2 gases at 460 °C: $\beta_1=0.025$, $\beta_2=1.754\pm0.071$ and $\beta_3=0.236\pm0.022$, which corresponds to an initial stage of highly strained planar film growth, crossing over to the intermediate island growth, and then to 3D island growth.

For oxide films, Li et al.⁷² studied the growth of the amorphous SiO_2 films on n-type Si wafers grown by RF magnetron sputtering at 440 °C. They obtained $\alpha_1=0.53$ and $\beta_1=0.26$ for the initial growth stage and $\alpha_1=0.86$ and $\beta_1=0.56$ for the later growth. The surface diffusion smoothing and shadowing roughening effects were the two main competing mechanisms which determined the morphological evolution of the SiO_2 films.

Qi et al.⁷³ reported $\alpha=0.7\sim0.9$ and $\beta=0.4$ for ZrO_2 films on borosilicate glass substrates thicker than 60 nm grown by reactive ion beam sputtering at a low substrate temperature less than 60 °C. When the film thickness is less than 60 nm, a negative β value was obtained. The noise driven Kuramoto-Sivashinsky model was used to explain their growth process. Hur et al.¹⁶⁷ characterized the evolution of surface roughness and strain relaxation of RF sputtered ZnO films grown on sapphire (0001) by *in situ* synchrotron X-ray scattering and atomic force microscopy at 550 °C. The relaxation of the lattice strain can be attributed to the surface roughening. They determined three growth stages as Lee et al.⁷¹: well-aligned 2D planar layer growth at the highly strained initial growth stage with a growth exponent β_1 of 0.12, followed by 3D island growth developing as a result of strain relaxation with very large β_2 of 1.579, and then reach the strain relaxed steady-state regime with smaller β_3 of 0.234 again.

Mohanty et al.²⁰⁷ investigated the evolution of surface morphology and surface roughness scaling of ZnO:Al films on glass substrate grown by RF magnetron sputtering from a ceramic target at room temperature. They presented a rough scaling behavior with β of 1.03 and α of 0.75 ± 0.06 which was related to shadowing effects and nonuniform flux

distribution arising due to a 30° tilt of the substrates with respect to the normal of the sputtering target, and the bombardment of energetic particles during the sputtering process.

The above reviewed experimental scaling exponents show that the exponents are varying from case to case, depending on the specific materials and the sputtering conditions such as temperature, sputtering pressure (with/without reactive gas), DC/RF modes, substrates, and the angular spread of the incident flux. According to the structure zone model for sputtered films^{17,18}, it is known that the adatom mobility is very low at the low substrate temperature (i.e. room temperature, low T_S/T_M), and the shadowing process dominates the film growth and leads to porous structures. With increasing the T_S/T_M , the adatom mobility increases and surface diffusion starts to compete with shadowing process which leads to denser and less rough surfaces. The bulk diffusion will be promoted to generate large equiaxed recrystallized grains when T_S/T_M is sufficiently high. In all these processes, reemission which is an unavoidable factor due to the high energetic ion bombardment in the sputtering, smoothes the surface and reduces the roughness. The significant discrepancy between experimental and theoretically predicted growth exponents suggest a complexity of the surface evolution during sputter deposition which is not yet covered by the theoretical models. It is still not clear, how these local (i.e. noise, surface diffusion, evaporation) and nonlocal effects (i.e. shadowing, grain growth, strain relaxation, reemission, bulk diffusion) determine the film growth at the atomic length scale and the scaling exponents at large growth time. In the present work, we present a systematic experimental investigation of the structure, the surface evolution and the scaling of different semiconducting oxides (ITO and AZO) and sulfides (CIGS) prepared by magnetron sputtering and try to get a better understanding of the growth mechanism. Simulations for the nucleation and growth of these sputtered materials are not performed in this work. Fortunately, we can compare our experimental results with these results simulated from theoretical models all described above under different boundary conditions and other reported related experimental results, and then analyze which physical processes are dominating in our film growth.

3 Deposition and Characterization of Thin Films

3.1 Magnetron sputtering deposition: DC and RF

Magnetron sputtering is a very versatile plasma deposition method that was invented by Penning in the 1930s.^{74,75} After the planar magnetron sputtering source in the present form was developed in the 1970s^{76,77}, magnetron sputtering was used to deposit metallic films and later for semiconductor and insulating films with tailored and enhanced properties such as high hardness, wear and corrosion resistance, low friction, and specific optical or electrical properties as well as decorative colors or complex combination of those properties.^{78,79} Compared to other thin film deposition techniques such as evaporation, chemical vapor deposition (CVD), or spray pyrolysis, etc, the fundamental difference is that magnetron sputtering can achieve much higher energy input into the growing film. While depending on the desired film requirements, the energy input into the substrate need to be adjusted to tailor the film properties.²⁰ Generally, magnetron sputtering has the advantage of (1) uniform and good adhesion of films on the substrate, (2) relatively high deposition rate, (3) low substrate temperature, (4) large scalability (up to $3 \times 6 \text{ m}^2$)⁸⁰, (5) possibility of good control and long-term stability, and (6) relatively cheap deposition. In this study, we therefore choose (reactive) magnetron sputtering technique for the deposition of semiconductor sulfide (Cu(In,Ga)S_2) and oxides (tin-doped indium oxide and Al-doped ZnO).

Sputtering is a process in which the vapor of atoms is ejected from a target which consists of the material to be deposited due to bombardment of the target by energetic particles. This bombardment comes from a series of collisions transferring energy and momentum from an accelerated ion to the atoms in the target. The collision process is shown schematically in Fig. 3.1. Incident gas ions (such as Ar^+) impinging the target produce sputtered species and reflected from the surface as neutrals through elastic collision effects. In addition, secondary electron emission, photon emission and heating of the target surface may result from inelastic process. Since the incident ions lead to collision cascades in the target, the energy of target atoms can be high enough to overcome the potential binding (U) in the surface, and also its momentum is directed outward from the surface, they will escape into the gas phase. Only the energy of the arriving particles is much higher than the surface binding potential then the sputtering process is possible.

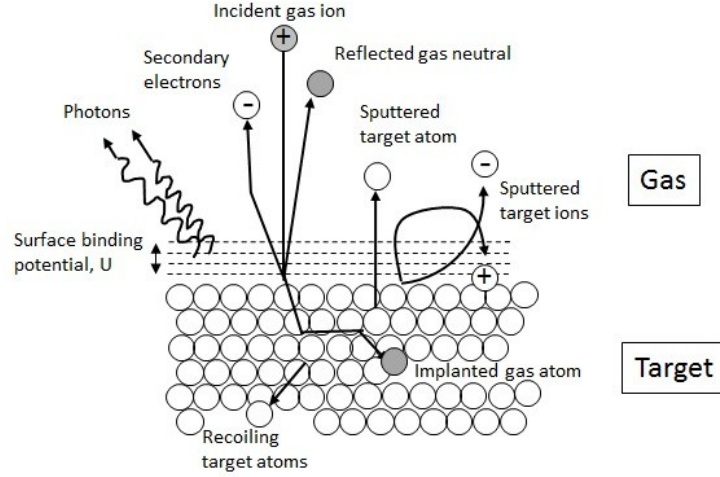


Fig. 3.1: Schematic drawing of the sputtering process. The surface binding potential results from the electronic bonding of the solid, symbolized by the dashes above the surface.⁸¹

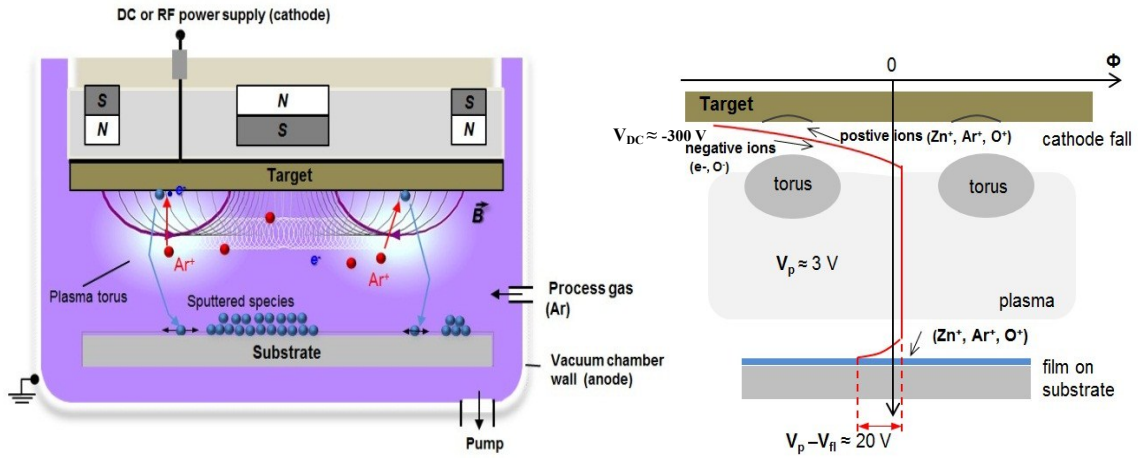


Fig. 3.2: (a) Schematic drawing of a magnetron sputtering configuration (after Ref. 82 and 83), and (b) potential distribution (red line) between the target and the substrate (in a magnetron sputtering discharge in Ar/O₂ with a ZnO target) for DC plasma excitation adapted from Ref.20.

In order to overcome low ionization efficiencies in the plasma, low deposition rates and high substrate heating effects in the sputtering process, magnetron sputtering was invented and developed continuously. The principle of a magnetron sputtering setup together with the potential distribution for a direct-current plasma excitation is displayed in Fig. 3.2. Magnetron sputtering is based on the plasma confinement in front of the target in contact with the cathode, while the substrate works as an anode. The confinement is obtained by combination of the electrical and magnetic fields in a high vacuum process. In present work, the balanced magnetrons were used in the setup. Due to the high energy transferring from impinging ions (such as Ar⁺), the neutral atoms from the target escape into the gas phase and then attract and accelerate to the anode-placed substrate, and afterwards

condense to a thin film. At the same time, emitted electrons are kept around the cathode due to the magnetic field near the cathode which is generated by magnets located behind the target. Therefore, the bombardment of the substrate with electrons which induces the main cause of defects of deposited film is strongly reduced. Moreover, the Ar ionizing electron density increases, leading to an enhanced Ar^+ density near the cathode. Consequently, the target bombardment and film deposition efficiencies are improved. The potential distribution in the discharge determines the energies of the ions and neutral species which contribute to the deposition process. Two sputtering modes: the direct-current (DC) sputtering and the radio-frequency (RF) sputtering are mainly used. The main difference between DC and RF magnetron sputtering is the power supply. For traditional DC sputtering, the plasma is excited by a constant voltage, usually in the range of 300 V~800 V, and only conductive targets can be sputtered. In this case, the torus-like plasma is essentially sustained upon the generation of ion-induced secondary electrons at the cathode (target) and the acceleration of the electrons in the cathode sheath. Therefore, large target voltages are necessary to sustain stable plasma as a result of the electron emission increasing almost linearly with the ion velocity. The positive ions bombardment of a low conductive target would lead to local charging up effects of the target surface and subsequently to a shielding of the electrical field, and then the ion current would break off. Therefore the DC excitation is restricted to conducting targets like metals or doped semiconductors. For low conductive targets (ceramics or insulators), RF excitation is used to avoid charging and discharging effect of the target. Very different with DC sputtering mechanism, the RF plasma is mainly maintained by the ionization attributed to oscillating movement electrons in the plasma body. Since the electrons can follow the RF oscillating electric field, while the ions cannot due to their large inertia, this excitation process is much more effective when compared to the ionization by non-oscillation secondary electrons. Therefore, target voltage in an RF discharge is lower than that of DC mode. Note that in the RF discharge, the target acts as anode during the positive half-cycle, so the magnetic confinement of the electrons is not as effective as in the DC excitation, which leads to a higher plasma density in front of the substrate.²⁰

The high discharge voltage in DC magnetron sputtering mode leads to much higher deposition rate in comparison with that of RF sputtering process under same discharge power. Deposition rate begin to increase from zero power in DC excitation. While low discharge voltage causes a certain threshold power (i.e., 10 W for ZnO target) for RF

sputtering process. Overcome the threshold value, the deposition rate in magnetron sputtering process is proportional to the discharge power.

3.2 Structure and Morphology characterization methods

The structure of sputtered films in this work has been characterized by X-ray diffraction (XRD). The surface and morphology were measured by atomic force microscopy (AFM) and scanning electron microscopy (SEM). The composition of the films in the bulk was accomplished by Rutherford backscattering spectrometry (RBS), energy dispersive X-ray fluorescence (EDXRF) and wavelength dispersive X-ray fluorescence (WDXRF) analysis. The electrical properties of the films were examined by Hall-effect measurements and conductive atomic force microscopy (CAFM). This chapter briefly presents the main principles of these characterization tools and typical measurement parameters employed for analyzing the sputtered films.

3.2.1 X-ray diffraction (XRD)

X-ray diffraction (XRD) is the most common technique for identification the crystalline phases present in materials and to measure the structural properties such as preferred orientation, crystallite size and defect structure of the phases. The advantage of this technique is non-contact, non-destructive and non-complex sample preparation requirement. The short wavelength of x-rays in the range of a few angstroms to 0.1 angstrom, comparable with the size of atoms, can probe the structural arrangement of atoms and molecules in a wide range of materials. A very detailed introduction of this technique, working principle and applications can be found in Ref.84.

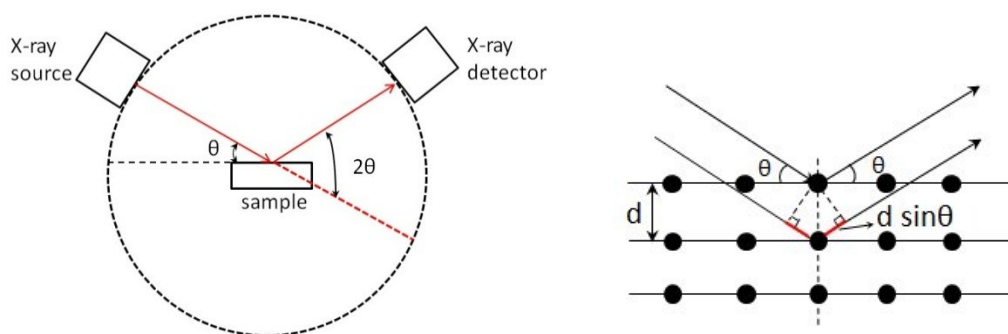


Fig. 3.3 (left) Schematic principle of XRD and (right) Bragg diffraction at the atomic layers.⁸⁴

Fig. 3.3 shows the basic operating principle of an XRD setup in Bragg-Brentano geometry where the diffraction angle 2θ is the angle between the incident and diffracted X-

rays. In θ -2 θ diffraction experiment, incident X-ray beams are impinging into a crystal surface which rotates about a goniometer axis. A detector is typically moved along the same axis as the sample but at twice the angular velocity of the latter to record the directions and intensities of the outgoing diffracted spectrum as a function of 2 θ . This allows to determine the orientation along the growth direction of polycrystalline films with respect to the substrate. The inter-planar spacing d , corresponding to each diffraction line is based on Bragg's law:

$$2d \sin \theta = n\lambda \quad (3.1)$$

where d is the spacing between consecutive diffracting planes, θ is Bragg's angle of diffraction, λ is the wavelength of the x-rays and n is integer denoting the order of diffraction. Experimentally obtained diffraction patterns of the sample are compared with the standard Joint Council on Powder Diffraction Standards (JCPDS) published by the International Centre for Diffraction Data. For a cubic crystal with lattice parameter a , the inter-planar spacing d_{hkl} of planes labeled by Miller indices (hkl) is,

$$d_{hkl} = \frac{a}{\sqrt{h^2 + k^2 + l^2}} \quad (3.2)$$

X-ray radiation generally has a large penetration depth into samples in conventional θ -2 θ scan mode which always generate an intense signal from the substrate and the surface sensitive property is poor. Grazing incidence X-ray diffraction (GIXRD) is used as a surface sensitive mode. In GIXRD, the incidence angle of the X-ray beam is fixed at a very small angle to maximize the signal from the thin layer and the detector was scanned to count the diffracted signals in a set 2 θ range.

In general, the XRD peak broadening is caused by instrumental and physical factors (finite crystallite size and lattice strain etc.). The peaks in the diffraction patterns need to be fitted to obtain useful information to analyze the crystal structure. The most popular function to model X-ray peaks is pseudo-Voigt function. The pseudo-Voigt function⁸⁵ is a convolution of Gaussian and Lorentzian functions with the same full width at half maximum B (FWHM), defined as:

$$\begin{aligned} I_{pV}(\Delta 2\theta, \eta, B) &= I_0 \left\{ \eta L(\Delta 2\theta, B) + (1 - \eta) G(\Delta 2\theta, B) \right\} \\ &= I_0 \left\{ \frac{2\eta}{\pi B} \cdot \left[1 + 4 \left(\frac{\Delta 2\theta}{B} \right)^2 \right]^{-1} + \frac{2(1 - \eta)}{B} \sqrt{\frac{\ln 2}{\pi}} \cdot e^{-4 \ln 2 \cdot \left(\frac{\Delta 2\theta}{B} \right)^2} \right\} \end{aligned} \quad (3.3)$$

where I_0 is the integrated intensity, $I(\Delta 2\theta)$ is the intensity of a point displaced by $\Delta 2\theta$ from the Bragg angle 2θ to centroid position $2\theta_0$ (corresponds to the peak maximum for symmetrical profiles). In experimental XRD measurement, instrumental broadening is unavoidable and has to be subtracted. The Lorentzian and Gaussian contributions to the instrumental broadening ($B_{L,ref}$ and $B_{G,ref}$, respectively) can be determined by measuring a reference material (LaB₆ powder). And then the breadth contributing to the peaks induced by the sample can be obtained by Lorentzian and Gaussian fitting ($B_{L,s}$ and $B_{G,s}$), respectively as:

$$B_{L,s} = B_{L,m} - B_{L,ref} \quad (3.4)$$

$$B_{G,s} = \sqrt{B_{G,m}^2 - B_{G,ref}^2} \quad (3.5)$$

where $B_{L,m}$ and $B_{G,m}$ is the measured FWHM of the peak fitting by Lorentzian and Gaussian functions, respectively. Therefore, the approximation used for B in pseudo-Voigt peak can be determined by:

$$B = \sqrt[5]{B_{G,s}^5 + 2.69269B_{G,s}^4B_{L,s} + 2.42843B_{G,s}^3B_{L,s}^2 + 4.47163B_{G,s}^2B_{L,s}^3 + 0.07842B_{G,s}B_{L,s}^4 + B_{L,s}^5} \quad (3.6)$$

Removing the instrumental broadening factor and assuming only broadening owing to the finite size of the crystals, the mean crystalline size (d_g) can be estimated by Scherrer's equation⁸⁶:

$$d_g = \frac{0.89\lambda}{\beta \cos \theta} \quad (3.7)$$

where β is the Full Width at Half Maximum of the diffraction peak in radians on the 2θ -scale.

In present study, X-ray diffraction in Bragg-Brentano geometry with a PANalytical X'Pert-MPD diffractometer (for oxides) and Bruker AXS D8 Advance X-ray diffractometer (for Cu(In,Ga)S₂) using copper K _{α} radiation ($\lambda=1.5408\text{\AA}$) and an X-ray tube voltage and current of 40 kV and 40 mA, respectively. A nickel filter was employed to suppress the intensity of K _{β} component. The XRD peaks were analyzed by the program FullProf⁸⁷ using pseudo-Voigt function.

3.2.2 X-ray Fluorescence (XRF)

X-ray fluorescence spectroscopy (XRF) is a non-destructive analytical technique to perform elemental analysis and chemical analysis in powder, solid and liquid materials.

Most of elements in the periodic table from beryllium to uranium in the concentration ranging from sub-ppm-level up to 100% can be measured by XRF. This method is based that each element has its unique characteristic energy spectrum (Fluorescence spectrum) consisted of the allowed transitions of the specific atom in the result of X-ray excitation. If the energy of X-rays is sufficient to dislodge a tightly-held inner shell electron, the atom becomes unstable and an outer shell electron replaces the missing inner electron. During this process, energy is released because the inner shell electron is more strongly bound in comparison with an outer one, as shown in Fig. 3.4. Since energy difference between electron shells are known and fixed, the emitted radiation always has characteristic energy, and the resulting fluorescent X-rays can be used to detect the abundances of elements that are present in the sample.

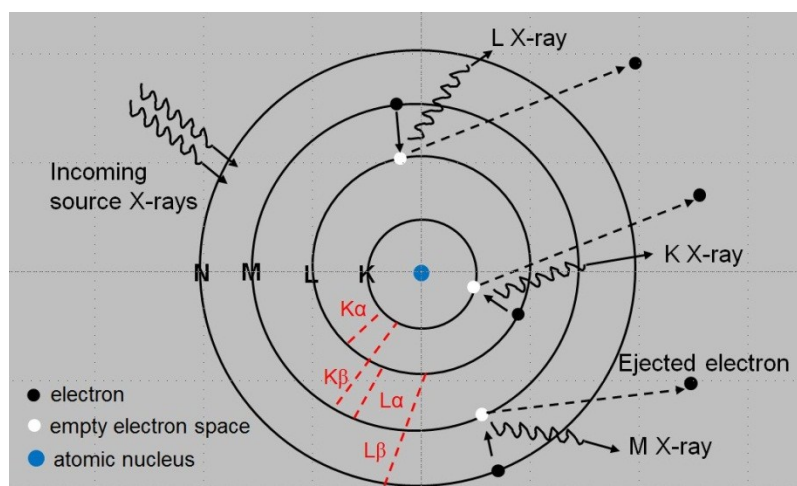


Fig. 3.4: Simple diagram showing incoming X-rays interact with inner-shell electrons and producing characteristic X-rays which is used in XRF.⁸⁸

Measurement of the spectrum of the emitted characteristic fluorescence radiation is performed by two methodologies: energy dispersive systems (EDXRF) and wavelength dispersive systems (WDXRF). EDXRF has a solid-state detector that is able to measure the different energies of the characteristic radiation coming directly from the sample. The result is X-ray energies as a function of intensity spectrum. In WDXRF, the result is an intensity spectrum of the characteristic lines versus wavelength measured with a Bragg single crystal as dispersion medium while records the diffracted X-Rays in different directions according to their wavelengths (energies). More detailed description of XRF principle, techniques and applications can be found for example in Ref. 88.

Compositional analysis of Cu(In, Ga)S₂ films was performed at an EDXRF system with a Si/Li detector from EDAX and a rhodium X-ray tube (30 kV, current 300 μ A, spot size 50 μ m). For the estimation of the atomic concentrations the CuK α , GaK α , and InL α signals

are evaluated in comparison with a reference sample: Cu(In,Ga)S₂ film on Mo/glass substrate and assuming 50 at. % of S in CIGS film. Since the MoL α (2.293 keV) and SK α (2.307 keV) lines are very close to each other, it is not possible to determine the S content for CIGS film on Mo/glass substrate by EDXRF. Therefore only the absolute composition of Cu, In, Ga with 16 points in the whole film from CuGa side to indium side is measured. To determine the S content and recalibrate the EDXRF results, the film composition is also checked by WDXRF (ZSW Primus II, Rigaku) with a rhodium X-ray tube (50 kV, current 60 mA, diaphragm size 1 cm). The average atomic element concentration of Cu, In, Ga, and S was measured at three positions from the CuGa side to the indium side.

3.2.3 Atomic force microscopy (AFM)

Atomic force microscopy (AFM) is a scanning probe technique which is very suitable for analyzing topography of a sample surface no matter its conductive or insulating. In present work, XEI-100 atomic force microscopy from Park System was used.⁸⁹ The schematic drawing of the setup is shown in Fig. 3.5(a). The basic components of an AFM are the probe tip, the laser, the mirrors, the scanner (X-Y scanner for the movement of sample stage in two-dimensional space and Z scanner for moving the tip in the Z direction), a position-sensitive photo detector (PSPD) and a data processor. The AFM works by scanning a probe over the sample surface, building up a map of the height or topography of the surface as it goes along. The probe is a sharp tip attached to a cantilever-type spring. When the tip approaches to the sample surface, forces between the tip and the sample lead to a deflection of the cantilever according to Hooke's law: $F = -kz$, where F is the force acting on the cantilever, k is the cantilever spring constant and z is the vertical displacement of the cantilever. Depending on the distance between the atoms at the tip and those at the sample surface, there exists either a repulsive or attractive force/interaction that may be utilized to measure the sample surface, as shown in Fig. 3.5(b). Therefore, according to the magnitude of tip-sample interaction, there are three primary imaging modes in AFM: contact mode, non-contact mode, and tapping mode which is a hybrid of contact and non-contact mode.

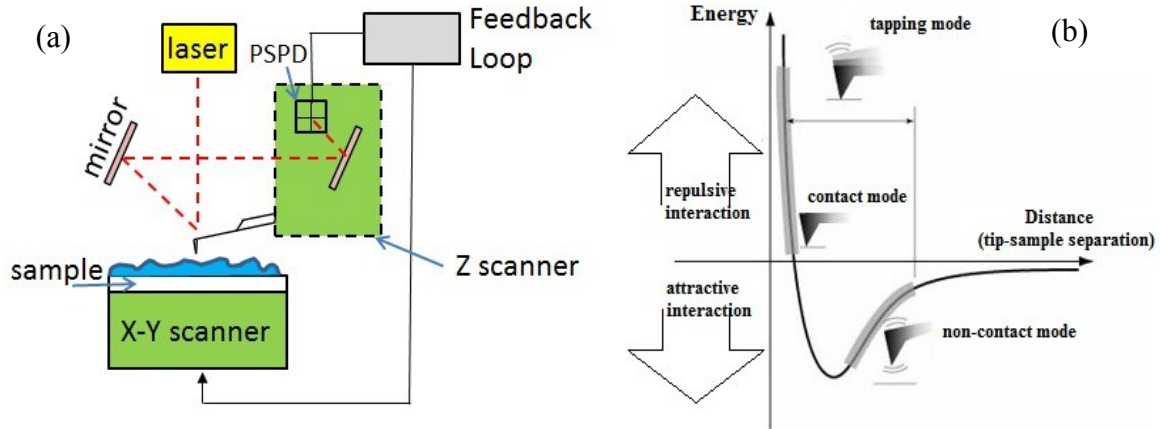


Fig. 3.5: (a) Principle of AFM and (b) Relation between the force and the tip/sample distance.⁸⁹

In contact mode, the distance between the tip and sample surface becomes very short, the interaction force is repulsive due to electrostatic repulsion. The forces between the tip and the sample remain constant by maintaining a constant cantilever deflection then an image of the surface is obtained. The imaging mode is good for rough samples and it can be used in friction analysis. The disadvantage is the high interaction force is easy to damage or deform soft samples.

In non-contact mode, the tip/sample distance gets relative longer than that of contact mode, the interatomic force becomes attractive due to the long-range van der Waals forces. Since the force is very weak there is no unexpected change in the sample surface during measurement, a cantilever is oscillated at a frequency a little bit higher than its resonant frequency (100~400 kHz with vibration amplitude of a few nanometers) near the sample surface experiences a shift in spring constant from its intrinsic spring constant (k_0). When attractive force is applied, the effective spring constant $k_{eff} = k_0 - F'$ will become smaller than k_0 since the force gradient $F' = \partial F / \partial z$ is positive. The effect is a damping of the cantilever oscillation which leads to a reduction in the frequency and amplitude of the oscillation. The oscillation can be monitored and the scanner controls the z height via the feedback loop and following the measurement of the force gradient to maintain the probe at a fixed distance from the sample. The advantages of this mode are low forces applied on the sample and can extend probe lifetime. However, the oscillation is easily interfered by the contamination layer on surface.

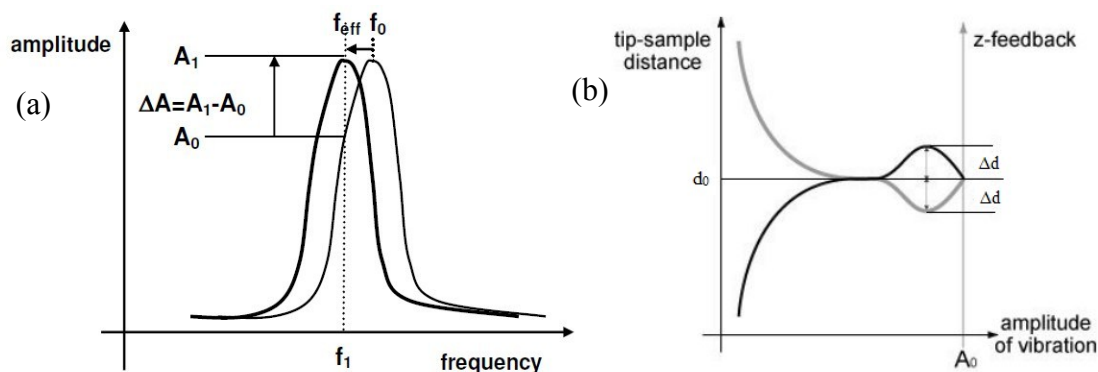


Fig. 3.6: (a) Resonant frequency shift and (b) Amplitude vs. Z-feedback in tapping mode.⁸⁹

The tapping mode is similar to non-contact mode in many ways such as the applied force and the measurement principle, but in this mode the cantilever makes intermittent contact with the surface in the vicinity of the resonant frequency. Since the vibrating cantilever get very close to the sample surface, it taps the surface repeatedly and the tip ‘contacts’ the sample surface as in contact mode. Tapping mode uses the non-contact mode feedback circuit with keeping the vibrating frequency (f_1) a little bit lower than the resonant frequency (f_0) while oscillating in free-space. When the tip comes closer to the sample surface, the attractive force becomes larger, and then the real spring constant reduces, as shown in Fig. 3.6(a). So the resonant frequency changes to effective frequency (f_{eff}) in non-contact regime and the amplitude at f_1 increases by $\Delta A = A_1 - A_0$. The non-contact mode feedback circuit decreases the distance Δd between the tip and sample surface, indicated in the Fig. 3.6(b). Therefore, the oscillating cantilever approaches the sample almost in contact or in collision with the surface. Tapping mode is usually suitable for soft samples (polymers or thin films) or samples with weakly bound structures to the surface. Topography of most sputtered films in this work is measured by tapping mode using an etched Si tip with a tip radius around 10 nm and a spring constant of 40 N/m and resonant frequency is 300 kHz. All scans gave the laterally resolved height information on a square array of 512×512 pixels.

AFM images do not only show how the surface structure looks like, but also contain a lot of detailed information about the surface structure. One of the most common analysis methods is the extraction of height profiles $h(r)$ from the topography, as describe in chapter 2. The AFM analysis software (XEI, Park System) allows the user to extract arbitrarily defined lines to obtain height information. By combine the height profiles of 512×512 pixels in X and Y direction, 3D images of the surface can be generated. In the present work, the height-height correlation functions were calculated from the data of AFM images with

512 × 512 pixels. Since the height data obtained by AFM in the fast scan direction are less affected by noise and tip artifacts, height-height correlation function using line-by-line averaging in the fast scan direction is calculated. For each scan line, the value of the height-height correlation function is given by:

$$H(md) = \frac{1}{N-m} \sum_{i=1}^{N-m} [h_{i+m} - h_i]^2 \quad (3.8)$$

where d is the distance between two adjacent pixels. h_{i+m} and h_i are the height at the sites $i+m$ and i on the scan line, respectively. $N = 512$ is the number of pixels in a scan line, $N-m$ is the number of data points contributing to the calculation of the height-height correlation function corresponding to correlation distance md . Then the value of height-height correlation function was averaged among 512 scan lines in vertical direction. In the present calculation, m was set to be 256.

3.2.4 Conductive atomic force microscopy (CAFM)

Conductive atomic force microscopy (CAFM) is a conventional AFM operating in a contact mode utilizing a conductive cantilever and tip. Fig. 3.7 shows a principle scheme of the CAFM setup. Besides conventional AFM scanner and cantilever detection technique, an external voltage source and a current amplifier are necessary. When applying an external bias to the sample, the current flows between the conductive tip and the sample allowing conductive AFM mode to measure the topography together with the electrical information of the sample. Contact topography image is generated by using feedback loop to maintain the constant tip deflection and conductive AFM image is generated by measuring the current flow. The current flow is measured by a highly sensitive amplifier as a current-to-voltage converter. The amplifier is very important for samples with low conductivity due to the current as low as femto-to picoampere range. A very detailed discussion related the working principle, experimental setup and some applications of conductive AFM can be found in Ref.90. The conductive AFM probe is also very important but is a kind of compromise between desired resolution and probe life time. In present work, conductive diamond-coated tip (CDT-NCHR from Park AFM, Schaefer Technologie GmbH) was used to maintain good electrical contact and resolution when measuring sputtered CIGS film. The force constant is 42 N/m and resonant frequency is 330 kHz.

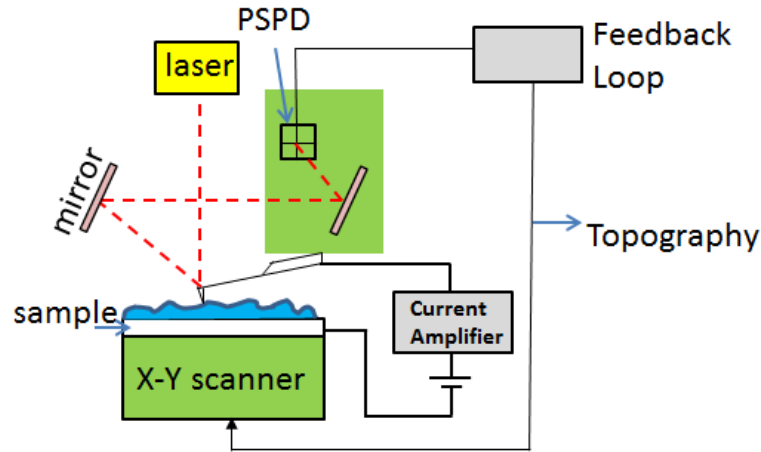


Fig. 3.7: Schematic drawing of the conductive AFM setup.⁸⁹

3.2.5 Scanning electron microscopy (SEM)

Scanning electron microscopy (SEM) is also used to check morphology of conductive samples. A convergent electron beam bombards a specimen and generates different types of signals such as secondary electrons, backscattered electrons, absorbed electrons, X-rays, cathodoluminescence etc. Those signals result from interactions of the electron beam with atoms at or near sample surface. Since the secondary electron signal depends on the surface undulation and has low energy (less than 50 eV), they are only emitted from a thin layer on the sample surface. The secondary electrons can be detected by a secondary electron detector and considered to be the most suitable signal for revealing detail information of the surface structures down to the order of 10 nm or better. In order to avoid charging problem the sample should be conductive or need to be coated by a very thin layer of gold or carbon without altering the surface features. Unlike 3D-AFM measurement, SEM image is a 2D intensity map. Each image pixel on the display corresponds to a point on the sample which is proportional to the signal intensity captured by the secondary electron detector at each measurement point.

A system LEO GEMINI 1530 (from the company Zeiss) equipped with a field-emission gun and an in-lens detector for secondary electron detection was used in present work. The accelerating voltage is 7 kV and the aperture size is 60 μm .

3.2.6 Rutherford backscattering spectrometry (RBS)

Rutherford backscattering spectrometry (RBS) is a very powerful technique for quantitative analysis of the composition, thickness and depth distribution of elements in thin solid films or solid samples near the surface region with film thickness up to a few

hundred nanometers. In RBS, a beam of monoenergetic helium ions of energy 0.5~2.5 MeV is directed at a target sample, and the energies of the ions which are scattered backwards by nuclei in the sample are analyzed. The higher the mass of an atom that is hit by a helium ion, the higher the energy of the ion will be after backscattering, which results in mass distinguish. By counting the helium ions as a function of energy, the number of atoms of each element present can be determined. Besides mass information, depth information is gained via the energy loss of the projectile on its inward and outward paths through the target. A detailed discussion can be found in Ref. 91.

The RBS measurements for sputtered oxide films on glassy carbon substrates were kindly performed by André Bikowski, at an accelerator available at the ‘Helmholtz-Zentrum Dresden-Rossendorf’ using 1.7 MeV He ions at an incidence and scattering angle of 0° and 170° , respectively. The ions have been accelerated by an energy stabilized van-de-Graaff accelerator. The resolution of the Si surface barrier detector by Canberra was in the range of 15 keV and the charge collected with the detector, covering a solid angle of 3.18 msr, was 10 μC . The analysis of the data was performed using the software SIMNRA version 6 by Dr. Matej Mayer from the ‘Max-Planck-Institut für Plasmaphysik’ in Garching, Germany.

3.2.7 Hall-Effect measurement

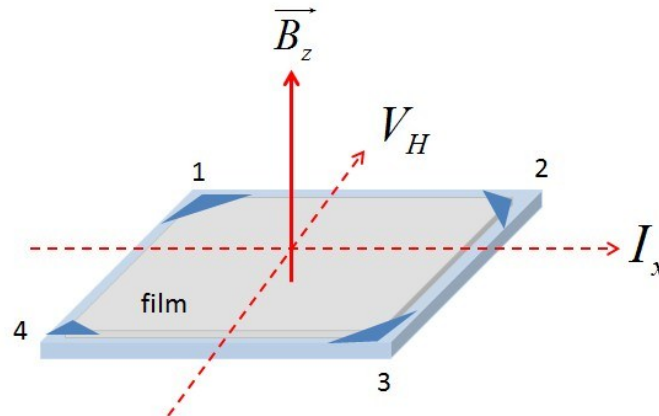


Fig. 3.8: Illustration of Hall-Effect on the van-der Pauw method: B_z is the applied magnetic field perpendicular through a sample, I_x is the applied current parallel along the surface, V_H is the measured Hall voltage.⁹²

The electrical property such as resistivity (ρ), carrier concentration (n) and Hall mobility of charge carriers (μ) of sputtered oxides (ITO, AZO) is determined by Hall-Effect measurement at room temperature using Van der Pauw four-point probe technique⁹².

According to Van der Pauw, the resistivity can be determined as a function of two resistances $R_{12,34}$ and $R_{23,41}$ and the film thickness d_f by:

$$\rho = \frac{\pi d_f}{\ln 2} \frac{(R_{12,34} + R_{23,41})}{2} f\left(\frac{R_{12,34}}{R_{23,41}}\right) \quad (3.9)$$

Where resistance $R_{12,34}$ is defined as the potential difference $V_4 - V_1$ between the contacts 4 and 3 per unit current through the contacts 1 and 2. Similarly with $R_{12,34}$, $R_{23,41}$ is defined as V when the current enters the film through the contact 1 and leaves it through the contact 2. The function f satisfies the relation:

$$\frac{R_{12,34} - R_{23,41}}{R_{12,34} + R_{23,41}} = f \cdot \arccos h\left[\frac{\exp(\ln 2 / f)}{2}\right] \quad (3.10)$$

In principle, the Hall effect can be observed when applying a magnetic field (B_z) perpendicular through a sample and a current (I_x) parallel along the surface of the sample with thickness d_f . Due to the Lorentz force on the electrons in the sample, an electrical current will be created perpendicular to both the applied magnetic field and current. And then a transverse voltage or Hall voltage (V_H) is created, as shown in Fig. 3.8. The obtained data contains information concerning carrier type and the carrier concentration (n) according to:

$$V_H = -\frac{1}{e \cdot n} \frac{I_x \times B_z}{d_f} = R_H \frac{I_x \times B_z}{d_f} \quad (3.11)$$

From the polarity of Hall voltage it can determine that the majority of charge carriers are electrons or holes. Carrier concentration also can be deduced from Eq.(3.11). The Hall mobility can be calculated by

$$\mu = \frac{d_f}{B_z} \frac{\Delta R_{24,13}}{\rho} \quad (3.12)$$

where $\Delta R_{24,13}$ is the change of the resistance $R_{24,13}$ due to the magnetic field B_z .

The measurement is performed at a home-built setup composed of a current source (220), a voltmeter (DMM 196) and a Hall card (7065) by Keithley Instruments with an operating program Igor Pro 5 (WaveMetrics, Lake Oswego, Oregon, USA). The film thickness was measured with a surface profilometer (Dektak 8, Veeco Instruments). The magnetic field is 0.86 T. Sample size is $1 \times 1 \text{ cm}^2$.

4 Transparent conductive oxides by DC/RF magnetron sputtering

4.1 Nucleation and growth of tin-doped indium oxide films

4.1.1 Introduction

The commercial value of thin films with high transparence and low electrical resistivity has been recognized and attracted great interest for their potential use in optoelectronic devices such as liquid crystal displays plasma displays and organic light emitting diodes (OLEDs) and for thin film solar cells.⁹³⁻⁹⁵ The first report on transparent conductive oxides (TCO) can be traced back to 1907 by Bädeker⁹⁶ on cadmium oxide films. Later on a list of potential TCO materials has expanded to include Tin oxide⁹⁷, Tin-doped indium oxide⁹⁸, Fluorine doped indium oxide⁹⁹, Aluminum doped zinc oxide¹⁰⁰, and Gallium-doped zinc oxide¹⁰¹ etc. Among those oxides, indium oxide (In_2O_3) is a very attracting semiconductor material on account of it behaving as an insulator in the stoichiometric form and as a highly conducting semiconductor with a wide direct band-gap $E_g > 2.6 \text{ eV}$ ¹⁰²⁻¹⁰⁵ in its non-stoichiometric form which also provide high transparency in the visible light range; Tin-doped indium oxides (ITO) show better properties owing to its superior electrical properties (as low as $1 \times 10^{-4} \Omega\text{cm}$) and optical properties (transmittance as high as $> 85\%$ in the visible and near-IR regions of the spectrum) in optoelectronics application.¹⁰⁶

To understand the reasons for those properties, it's necessary to investigate the structure and the morphology of the oxides/the doped oxides. The structure of indium oxide is generally known to crystallize in body-centered cubic (bixbyite type) structure^{107,108} which is in a cell of 16 molecules, i.e. 80 atoms which are 32 metallic atoms and 48 oxygen atoms with lattice constant $a = 10.117 \pm 0.001 \text{ \AA}$. O^{2-} ions occupy three- fourths of the tetrahedral interstices of a face-centered cubic In^{3+} ion array¹⁰⁹, as shown in Fig. 4.1. The calculated density is 7.12 gcm^{-3} . When small amount of tin is doped in indium oxide, the structure of tin-doped indium oxide retains bixbyite type. All the tin atoms enter substitutionally into the cation sublattice which will induce a slightly increase in the lattice constant ($10.117 \text{ \AA} < a < 10.31 \text{ \AA}$) depending on the deposition parameters¹¹⁰⁻¹¹³. ITO films normally exhibit a strong $\langle 111 \rangle$ or $\langle 100 \rangle$ orientation depending on the deposition conditions which was related to the amount of oxygen vacancies.^{108,110,111,114,115,116} However, the electrical and optical properties appear to be independent of the orientation effects^{112,115,117}.

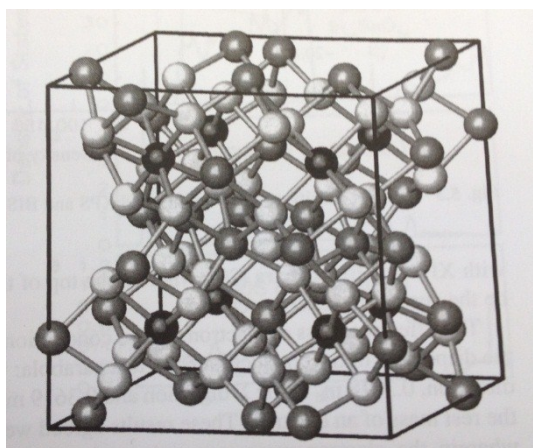


Fig. 4.1: Crystal structure of bixbyite In_2O_3 : black, shaded and white spheres represent 8b indium, 24d indium and 48e oxygen atoms, respectively.^{5,107}

In the application as a transparent electrode material, it is important not only to tailor the electrical or optical properties of ITO films, but also to precisely control the surface morphology and the film smoothness, which depend on the preparation method, such as electron beam evaporation^{118,123,131}, pulsed laser deposition^{119,124}, DC and RF magnetron sputtering^{125,126}, spray-pyrolysis¹²⁰ and so on. The surface morphology of these prepared ITO films directly affects the morphology of organic thin films which are deposited onto the ITO surface. For example, a critical requirement for ITO films for OLEDs is that the surface should be exceptionally smooth. There exists a strong correlation between the surface morphology of ITO film and its fractal properties which can be used as a fundamental parameter in determining the efficiency of the devices.^{121,122} Therefore, the characterization of surface morphology of ITO thin film and studying the fractal is one of the most serious problems which need to be solved. Recently, the evolution of morphology and surface roughness of ITO films was analyzed by Korobov et al.¹²³, who studied *in situ* the conductance of evaporated ITO films on glass substrate as a function of the surface coverage and found, that the growth model changed from anisotropic growth (three dimension, 3D) to isotropic planar (two dimension, 2D) growth at a critical island coalescence thickness, when substrate temperature is higher than 150°C. Sun et al.¹²⁴ observed a similar transition from Volmer-Weber growth (3D) at low temperature to the Frank-van der Merwe growth (2D) at higher temperature accompanied by a morphology transition from amorphous to polycrystalline in pulsed laser deposited ITO films. For room temperature depositions, Shigesato et al.^{125,126} investigated the early stages of ITO film growth on alkali-free glass by dc magnetron sputtering and observed Volmer-Weber-type

initial growth. However, they found that the island growth structure was not clearly observed for ITO films deposited at higher temperature ($>100\text{ }^{\circ}\text{C}$). Han et al.¹²⁷ studied the initial growth mode of ITO film on polycarbonate substrates prepared by ion-beam sputtering and observed initial part of the film growth transforming from a 3D-island growth to a 2D-like growth as a result of the formation of oxygen-bound functional groups in the polycarbonate substrate. They also demonstrated that ion-assisted reaction treatment could control the growth mode of ITO films on a polymer substrate. Zhang et al.^{128,129} studied the growth of In_2O_3 on different oriented Y-stabilized zirconia substrate surfaces at elevated temperature between $550\text{ }^{\circ}\text{C}$ and $1000\text{ }^{\circ}\text{C}$ by oxygen plasma assistance molecular beam epitaxy. They reported 3D-islands and continuous film incline to grow on (100) and (111) substrate surfaces, whereas highly aligned 1D-nanorods prefer growing on (110) surface which are attributed to different index surface energies (i.e. $\gamma(111) < \gamma(110) < \gamma(100)$) and minimization of surface energies during growth process. Bierwagen et al.¹³⁰ investigated nucleation of islands and continuous high-quality In_2O_3 (001) films during plasma-assisted molecular beam epitaxy on ZrO_2 (001). The surface they prepared is very rough with a root-mean square surface roughness w of above 30 nm for more than 4 nm-thick film. They observed that islanding is caused by a nucleation of the In_2O_3 with incomplete wetting of the substrate, i.e. 3D island nuclei, and not due to strain-induced breakup of the film. Moreover, this nucleation behavior can be controlled by the growth temperature and In/O ratio. So much work listed above were focused on the initial growth mode, but from the dynamic scaling view of this material, very few work related to the morphology evolution of ITO films has been done.^{131,132} Raoufi et al.¹³¹ characterized the surface morphology of ITO thin films deposited by electron beam evaporation onto glass substrates by atomic force microscope. In their work, the surface roughness w decreases from 25 nm to 6 nm when increasing the film thickness from 100 nm to 250 nm. They determined both spatial (described by the roughness exponent α) and temporal scaling (described by growth exponent β) for ITO films as 0.71 and -0.11, respectively, over a large variation of length scales and used a combination of Edwards-Wilkinson and Mullins diffusion local models to describe the growth process of ITO films. Wang et al.¹³² investigated the growth mechanism of ITO films prepared by direct current pulse magnetron sputtering and found the anomalous temporal scaling of roughness evolution (β) can be divided into three stages: 1.53, -0.85 and 1.25, which corresponds to the growth of island, coalescence of islands and the homogeneous growth, respectively.

The purpose of this study was to carry out a systematic investigation on the microstructure and morphology evolution of ITO films prepared by magnetron sputtering in different atmospheres, i.e. pure Ar or Ar/O₂/H₂ mixture, and by different excitation modes, i.e. RF and pulsed DC. It aims to understand the nucleation and growth mechanism of ITO films from the dynamic scaling view. Part of presented results has been published in Ref.133.

4.1.2 Experimental details

Tin-doped indium oxide thin films were deposited by magnetron sputtering from a 99.99% purity In₂O₃:SnO₂ (90 and 10 wt. %, respectively) target with a balanced three inch-diameter magnetron source at a constant power of 50 W and a total pressure of 0.3 Pa. The magnetron plasma can be excited by three possibilities: (1) 13.56 MHz RF generator RTX-600 combined with an ATX-600 matching network power supply by Advanced Energy, (2) 27.12 MHz RF power generator CESAR RF 276 by Dressler, and (3) pulsed DC power generator PMP-1 by Advanced Converters. The samples were prepared in a load-lock vacuum system with a process chamber base pressure better than 10⁻⁵ Pa. The target-to-substrate distance is fixed at 6.1 cm. The gas flows were adjusted by mass flow controllers before the ignition of the plasma and the total pressure was measured by a capacitance vacuummeter (Baratron). If no special mentioned, 13.56 MHz RF power supply is normally used. One interesting point of this study is to check the role of sputtering atmospheres on the microstructure of ITO film. For this purpose the mass flow ratio $F_{O_2 \text{ or } H_2} / (F_{Ar} + F_{O_2 \text{ or } H_2})$ was varied from 0% to 10% while keeping the total sputter pressure constant at 0.3 Pa. Another interesting point is to compare the influence of different discharge modes on the growth of ITO films. The substrate temperature can be heated to 600°C by a boron nitride-encapsulated graphite heater during the deposition. As substrates, silicon substrate, glassy carbon or borosilicate substrate with a size of 10 × 10 × 1.1 mm³ were used. The silicon substrates with a native oxide layer were cleaned in an ultrasonic bath for 20 min using organic solvents (ethanol, acetone, and isopropyl alcohol). After each sonication step, substrates were rinsed with deionized water (Millipore[®] 18.2 MΩcm). Finally, they were heated on a hot plate at 130°C for 20 min. The glassy carbon and borosilicate substrates were cleaned at isopropanol in an ultrasonic bath at 80 °C for 10 min and rinsed with deionized water, and then dried by a N₂ flow. After the cleaning process, the substrates were transported to the vacuum chamber directly.

4.1.3 Growth of ITO films in different sputtering atmospheres

Tin-doped indium oxide thin films were deposited onto glassy carbon substrates by 13.56 MHz RF magnetron sputtering at room temperature in different atmospheres: pure argon or a mixture of Ar/O₂ or Ar/H₂ which the mass flow ratio $F_{O_2 \text{ or } H_2}/(F_{Ar}+F_{O_2 \text{ or } H_2})$ was varied from 0 to 10%. The stoichiometry (oxygen-to-metal ratio: O/(In+Sn)) derived from RBS for different ITO films are shown in Fig. 4.2. Be aware of that the indium and tin elements could not be separated due to the limited mass resolution when using 1.7 MeV helium ions as projectiles. It can be found with increasing O₂ or H₂, the O-to-metal atomic ratio increases and varies from 1.57 to 1.78, higher than the stoichiometric ratio (~1.55) of corresponding mixture of In₂O₃ and SnO₂. Overstoichiometric ITO films have been reported for reactive magnetron sputtering from a metallic alloy target or ceramic target when increase the oxygen partial pressure.^{134,135} The additional oxygen was assumed to reside on interstitial sites in the ITO lattice.¹³⁵ The film composition was also measured by Energy dispersive X-ray spectroscopy, the atomic ratio of In/Sn is 10.3, close to the target composition (In/Sn ratio of 9.8).

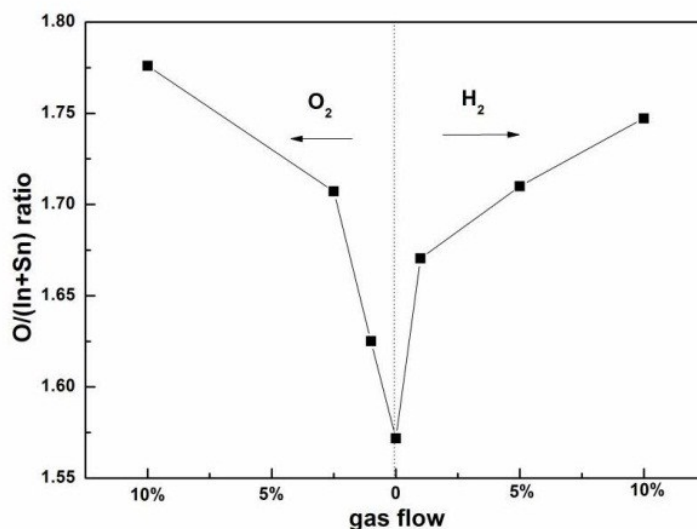


Fig. 4.2: O/(In+Sn) ratio of ITO films prepared at room temperature as a function of O₂ and H₂ flow: sputtering power: 50 W, total gas pressure 0.3 Pa.

4.1.3.1 Growth of ITO films in pure Ar

X-ray diffraction patterns of ITO films deposited on Si (100) substrate in pure Ar (40 sccm, 0.3 Pa) at room temperature for different film thicknesses (d_f) are presented in Fig. 4.3. The assigned peaks are related to the crystalline indium oxide with a body-centered cubic structure (JCPDS card no. 06-0416) and the tetragonal rutile tin oxide structure (JCPDS card no. 41-1445). For the 60 nm-thick film, the XRD pattern shows a broad

feature and a single (222) diffraction peak. The broad feature is mainly due to the amorphous part in the ITO film, often reported in literature^{125,136,137}. For room temperature depositions, ITO forms amorphous layers or a combination of a polycrystalline top layer and an amorphous bottom layer close to the substrate surface for ITO films¹³⁷, which is also confirmed later by TEM analysis for a 400 nm-thick film, kindly performed by Dr. Mythili Rengachari. With increasing d_f , the integrated broad peak intensity increases and additionally the (211) diffraction peak appears and its peak intensity increases faster, than that of the (222) peak. A transition of the orientation of the ITO films from (111) to (211) orientation can be observed when the film thickness is larger than 200 nm. The integrated intensity ratio of (211) peak to (222) peak was 1.38 and 2.15 for 200 nm and 400 nm-thick ITO films, respectively, whereas the values for the standard In_2O_3 powder in JCPDS_06-0416 is 0.14, which indicates a preferred (211) orientation. The size of the (211) oriented crystallites obtained from Scherrer's formula is 38 nm and 43 nm for the 200 nm- and 400 nm-thick films, respectively. In a GIXRD measurement ($\theta = 0.3^\circ$, orange line in Fig. 4.3), we did not observe the (211) peak which due to the fact that the GIXRD technique probes the material structure near to the surface. Therefore, Bragg-Brentano geometry XRD is prior for us to check the crystallinity.

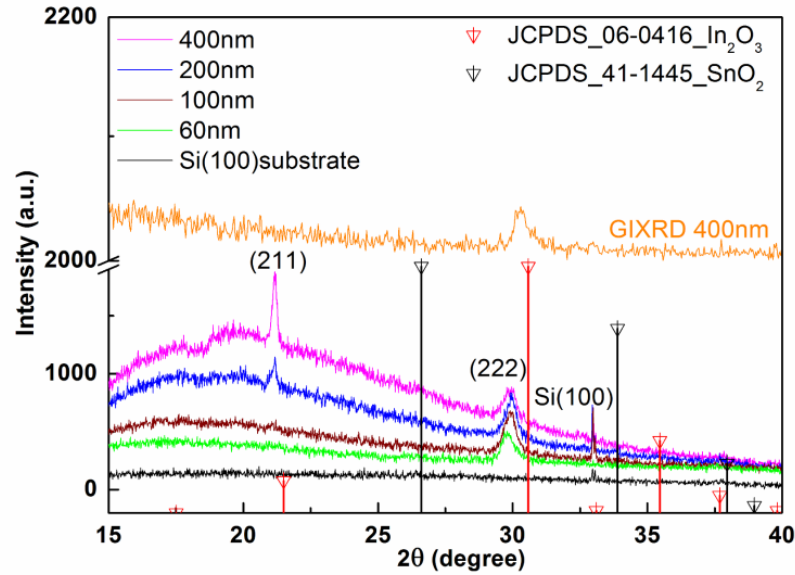


Fig. 4.3: XRD patterns for ITO films prepared in pure Ar with various film thicknesses.

The surface morphology of the ITO thin films prepared in pure Ar was characterized by atomic force microscopy (AFM). Fig. 4.4 shows AFM images over a scan area of $2 \times 2 \mu\text{m}^2$ of the ITO thin films for different film thicknesses. In order to see the grain shape, the insets display $200 \times 200 \text{ nm}^2$ scan areas. The height scale for different images is indicated by

the height profiles, shown in Fig. 4.4(right). The ITO film surfaces show isotropic, homogenous and continuous island-like structures, and with increasing film thickness, these irregular islands become bigger in both lateral and vertical directions, as can be seen from the height profiles of these films shown in Fig. 4.4(right).

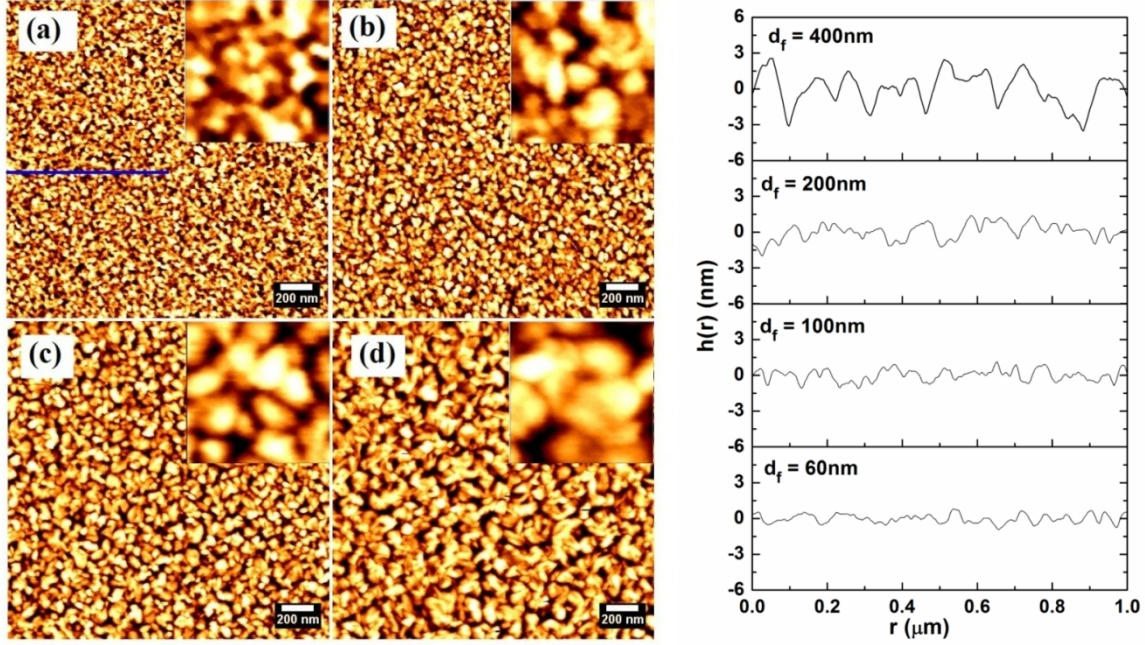


Fig. 4.4: (left) AFM images of ITO films on Si substrate prepared in pure Ar for different film thicknesses $d_f =$ (a) 60 nm, (b) 100 nm, (c) 200 nm, and (d) 400 nm, and (right) the corresponding height profiles along the blue line. The insert AFM image sizes are $200 \times 200 \text{ nm}^2$.

In order to obtain an insight into the dynamic behavior and the detailed growth processes for the evolution of ITO films, the height-height correlation functions $H(r)$ as a function of lateral distance r on a log-log scale for the Si substrate and ITO films deposited in pure Ar with various film thicknesses are displayed in Fig. 4.5. According to Sinha et al.²⁶ for the short distance $r \ll \xi$, the surface is fractal and $H(r)$ scales as $r^{2\alpha}$. Then in the logarithmic plot, the slope of the linear part in the curve is 2α . The intercept of the fitting linear line with the vertical axis gives a measure of the average magnitude of the local surface slope m . For longer distances $r \gg \xi$, $H(r)$ tends to saturate to the value $2w^2$. The evolution of the roughness exponent α as a function of film thickness, i.e. growth time is summarized in Fig. 4.6(a). It is found that in the early growth regime α is time-invariant with a value around 0.67, and then increases with the growth time till 0.75. The short-range behavior of $H(r)$ varies with growth time t which is characterized by the increase of the local slope m with t , indicating that the deposition process is non-stationary³. Such a phenomenon is induced during the growth over short distances by the balance between random fluctuations in the

deposition rate and local smoothening effects such as surface diffusion which cannot easily reach a balance, and then the scaling behavior of ITO films belongs to anomalous dynamic scaling. The correlation lengths ξ range from ≈ 12 –56 nm for film thicknesses between 10 nm and 400 nm and also follow a power law dependence with film thickness $\xi \sim$, where $1/z = 0.44 \pm 0.05$.

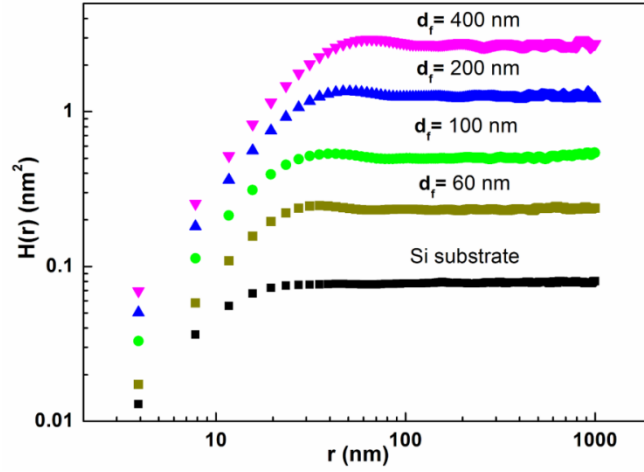


Fig. 4.5: The height-height correlation functions $H(r)$ of ITO films prepared in pure Ar in dependence of the lateral position r as log-log plots for different film thicknesses.

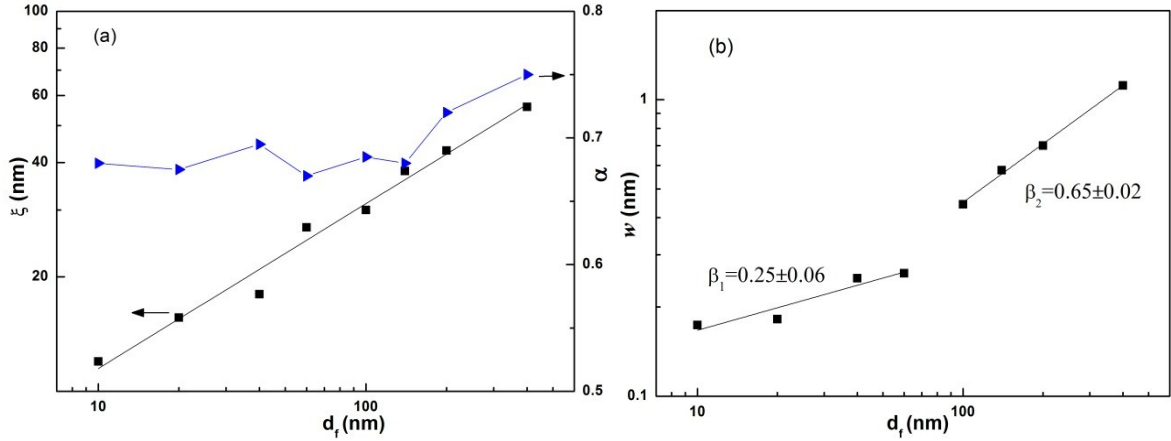


Fig. 4.6: (a) roughness exponent α and correlation length ξ and (b) surface roughness w of ITO films prepared in pure Ar as a function of the film thicknesses.

To characterize the vertical surface morphology, the obtained surface roughness w as a function of the film thickness d_f is displayed in Fig. 4.6(b). It can be seen that the surface width w values increase from 0.17 nm to 1.12 nm with increasing film thickness from 10 nm to 400 nm, i.e. deposition time from 0.5 min to 20 min. By fitting a power law behavior to the surface roughness as $w \sim d_f^\beta$, two growth exponents can be obtained: $\beta_1 = 0.25 \pm 0.06$ for $10 \text{ nm} < d_f < 60 \text{ nm}$ and 0.65 ± 0.02 for $100 \text{ nm} < d_f < 400 \text{ nm}$. The roughness evolution is comparable with Shigesato et al.'s work^{125,126}, where the average roughness of the ITO

films on glass deposited by DC planar magnetron sputtering, increased with increasing film thickness and then, quite remarkably, decreased at a thickness of 10~14 nm corresponding to the island nucleation and coalescence thickness, and then the roughness increased again due to continuous film growth processes, i.e., Volmer-Weber-type initial growth. In Shigesato's work^{125,126}, the initial growth of ITO nucleating islands is mainly affected by the roughness of glass substrate and higher ion bombardment by DC sputtering compared to RF sputtering retreating the substrate surface before a continuous ITO film is formed. However, in the present work, very smooth silicon substrates ($w = 0.14$ nm) are used and the dynamics of surface morphology is independent on the initial substrate, which is probably the reason why we did not observe the obvious roughness up and down behavior. The growth exponent obtained here is smaller than $\beta=1$ (for $12 \text{ nm} < d_f < 180 \text{ nm}$) reported by Wang et al.¹³² who prepared ITO films by pulsed DC magnetron sputtering at 245°C . Our smaller β can be caused by the lower deposition rate (nearly one half of Wang's), lower ion bombardment and lower deposition temperature which results in poorly crystallized films, lowering the β . But for our pulsed DC characterization, it is similar to their result which will be introduced in detail in section 4.1.4.2.

4.1.3.2 Growth of ITO films in Ar/10%O₂ atmosphere

Fig. 4.7 displays XRD patterns obtained for the ITO films on Si substrates deposited in an Ar/10%O₂ gas mixture (36 sccm Ar and 4.4 sccm O₂) at room temperature for different film thicknesses. The ITO films show a very strong (111) texture with additional weak (211) peaks, which are related to the cubic In₂O₃ crystal structure which has a (222) close-packed plane. The broad halo pattern between 15° and 28° still exists indicating the film contains an amorphous part. The (222) peak is predominant and much higher than that for the Ar deposition indicating a strong $\langle 111 \rangle$ -oriented crystal growth under excess O₂ flow. The weak (211) diffraction did not appear until the film thickness reached 400 nm. With increasing film thickness from 38 nm to 400 nm, the full width at half maximum of the (222) peak decreases and the crystallite size obtained from the (222) peak increases from 19 nm to 33 nm, as displayed in Fig. 4.7 (b).

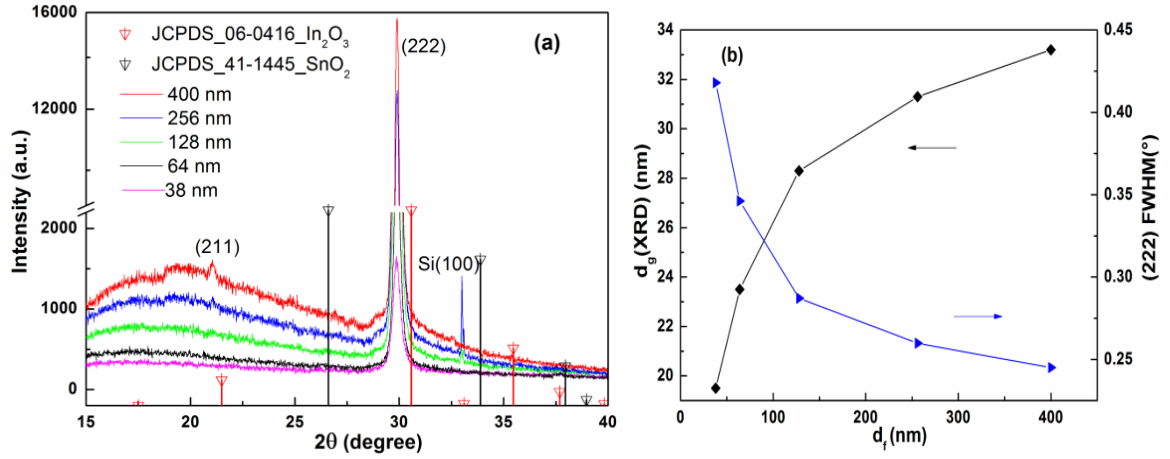


Fig. 4.7: (a) XRD patterns of ITO films prepared in Ar/10%O₂ atmosphere, and (b) FWHM of (222) peak and crystallite size $d_g(\text{XRD})$ as a function of film thickness.

The significant difference of the crystalline structure of ITO films deposited without and with 10% O₂ flow suggests a different surface morphology evolution. AFM images of ITO films prepared at Ar/10% O₂ mixture for different film thicknesses are shown in Fig. 4.8. Insets, measured with a 200 × 200 nm² scan areas are displayed to show the grain shape. The height scale for different images is indicated by the height profiles, shown in Fig. 4.8 (e). The surface of these samples is much smoother and exhibits smaller nanosized grains in comparison to films deposited in pure Ar in previous section 4.1.3.1.

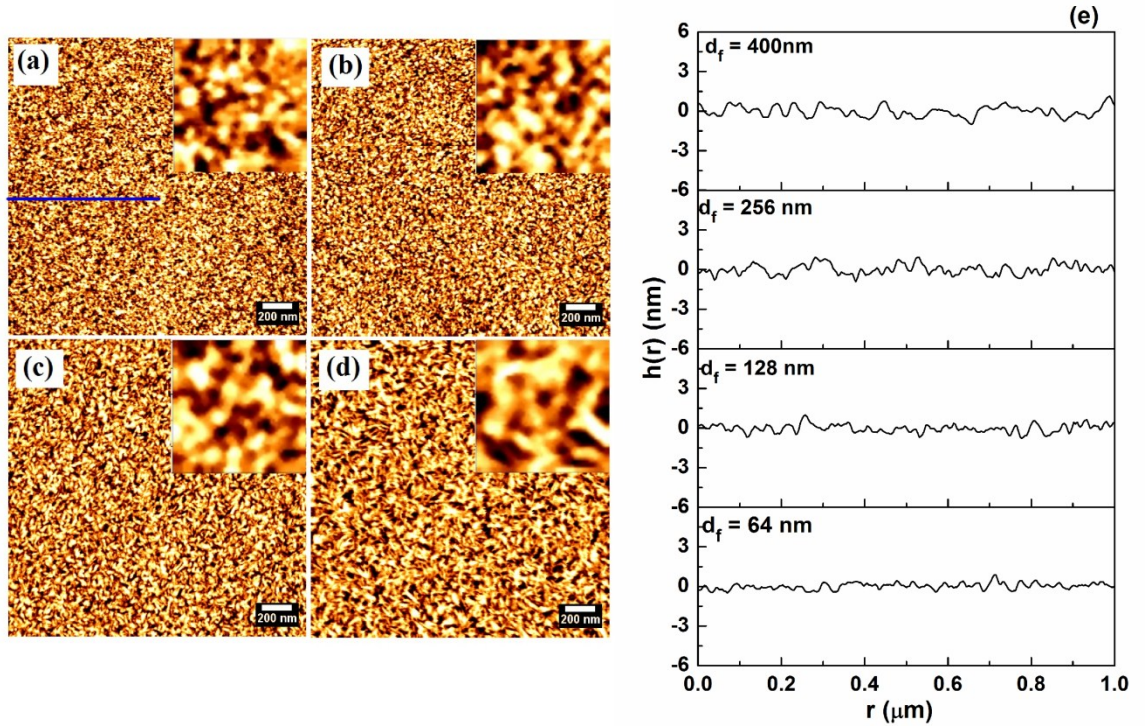


Fig. 4.8: AFM images of ITO films prepared in an Ar/10%O₂ mixture for different thicknesses $d_f =$ (a) 64 nm, (b) 128 nm, (c) 256 nm, (d) 400 nm, and (e) line height profiles $h(r)$ for these films. Insert AFM image sizes are 200 × 200 nm². The blue lines show the positions of the line scans, displayed in (e).¹³³

From the line height profiles shown in Fig. 4.8(e), it can be seen that the lateral size grows and the surface height slightly increases with increasing film thickness. The height-height correlation functions $H(r)$ of these ITO films are displayed in Fig. 4.9. The surface roughness w as a function of film thickness (d_f) is shown in Fig. 4.10. The roughness increases from 0.21 nm to 0.47 nm with increasing film thickness from 38 nm to 400 nm. By fitting a power law behavior to the surface roughness as $w \sim d_f^\beta$, a growth exponent β of 0.35 ± 0.02 is obtained. The roughness becomes smaller when the films are sputtered in Ar/10% O₂ atmosphere. For a 400 nm-thick ITO film, the surface roughness is 1.12 nm and 0.47 nm in pure Ar and Ar/10%O₂ atmosphere, respectively. The average roughness exponent α calculated from $H(r)$ ranges from 0.65 to 0.78 with increasing thickness, which are very close to pure Ar deposition. The correlation length increases with increasing film thickness with a power law exponent of $1/z = 0.36 \pm 0.04$. When the film thickness reaches 400 nm, ξ is about 32 nm, still much smaller than 56 nm for the deposition in pure Ar.

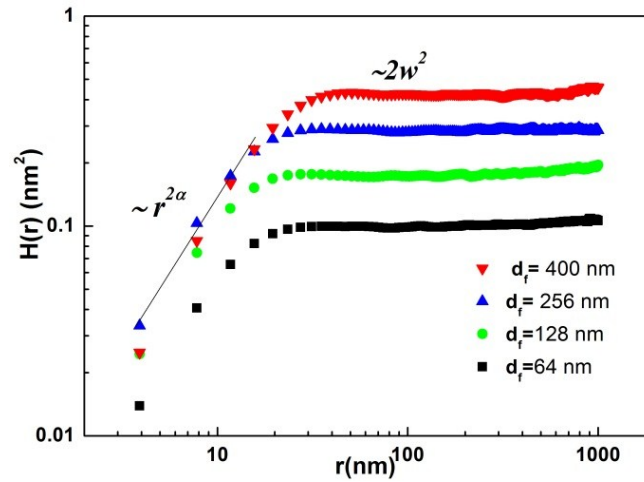


Fig. 4.9: The height-height correlation function of ITO films prepared in Ar/10%O₂ mixture dependence of the distance r as log-log plots for different film thicknesses.

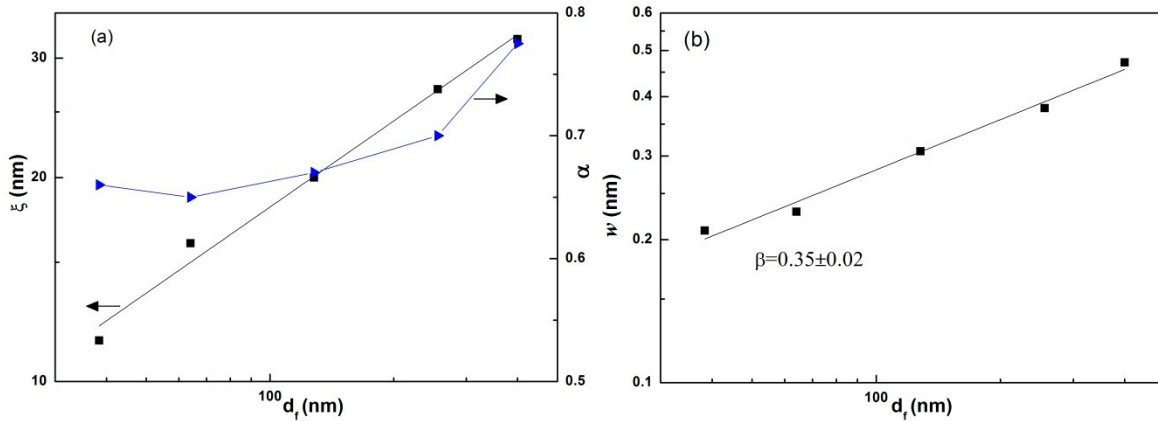


Fig. 4.10: (a) roughness exponent α and correlation length ξ and (b) surface roughness w of ITO films prepared in Ar/10%O₂ mixture as a function of the film thicknesses.

4.1.3.3 Growth of ITO films in Ar/10% H_2 Atmosphere

Fig. 4.11 displays XRD patterns obtained for the ITO films on Si substrates deposited in an Ar/10% H_2 gas mixture at room temperature for different film thicknesses. These ITO films display an amorphous structure when the film thickness is less than 100 nm. Increasing the thickness to 200 nm results in the development of the (400) diffraction peak together with the broad peak, and later a weak (222) peak appears, when the film thickness reaches 420 nm. The preferential orientation along (100) plane becomes pronounced in ITO films when the films are prepared in a state of oxygen deficiency.¹³⁸ The crystallite size obtained from the (400) peak is 28 nm and 36 nm for 210 nm- and 420 nm-thick films, respectively. From X-ray texture analysis, it is clear that there is a significant variation of the crystallite orientation with respect to the substrate plane for films prepared in different gas atmospheres. As the fraction of oxygen is decreased, the (222) peak disappears and the (100) peak becomes dominant. The driving force of this change in preferred orientation can be speculated to relate to the concentration of oxygen vacancies and their subsequent diffusion. The crystal growth in the (100) plane is explained as a stress-induced grain growth due to oxygen deficiency also affecting the electronic environment of the crystallites¹³⁹; it was reported the formation of an additional electronic level resulting from the creation of an oxygen vacancy excess.^{140,141} However, the almost (111)-oriented growth is explained by a reduction of oxygen vacancies¹⁴² when using 10% O_2 during the deposition.

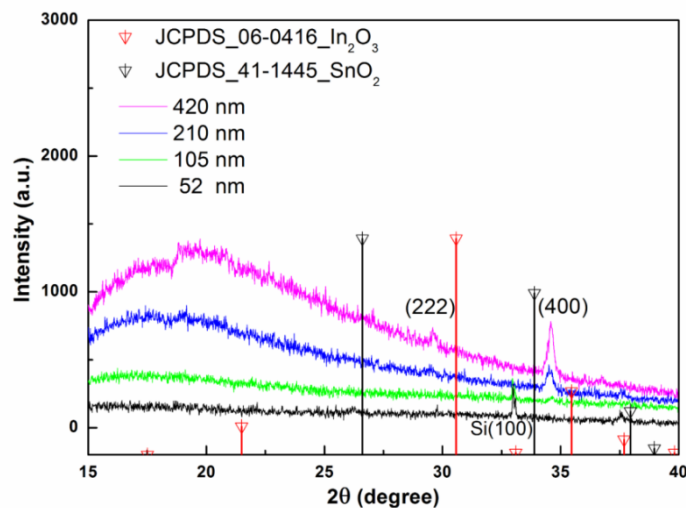


Fig. 4.11: XRD patterns of ITO films prepared in an Ar/10% H_2 atmosphere.

Fig. 4.12 shows the AFM images of ITO films prepared in an Ar/10% H_2 mixture as a function of the film thickness. The height scale for different images is indicated by the

height profile, shown in Fig. 4.12e. Obviously, the surface morphology is very different compared to the depositions in pure Ar or Ar/10%O₂ atmosphere. Small spherical grains appear in the initial growth stage, i.e., for film thicknesses less than 50 nm. At the very beginning of the growth, the roughness changes only slightly from 0.18 nm to 0.15 nm when film thickness is less than 50 nm. With increasing film thickness, i.e. deposition time, the ITO clusters aggregate and larger islands are formed which increase in size, due to coalescence until large polygonal grains are observed. When the film thickness further increases from 52 nm to 420 nm, the roughness increases from 0.38 nm to 2.1 nm and with a growth exponent β of 0.98 ± 0.06 . With increasing film thickness, the lateral correlation length increases with a power law exponent of $1/z = 0.57 \pm 0.10$ while the average roughness exponent α calculated from $H(r)$ is in the range from 0.56 to 0.78, shown in Fig. 4.14.

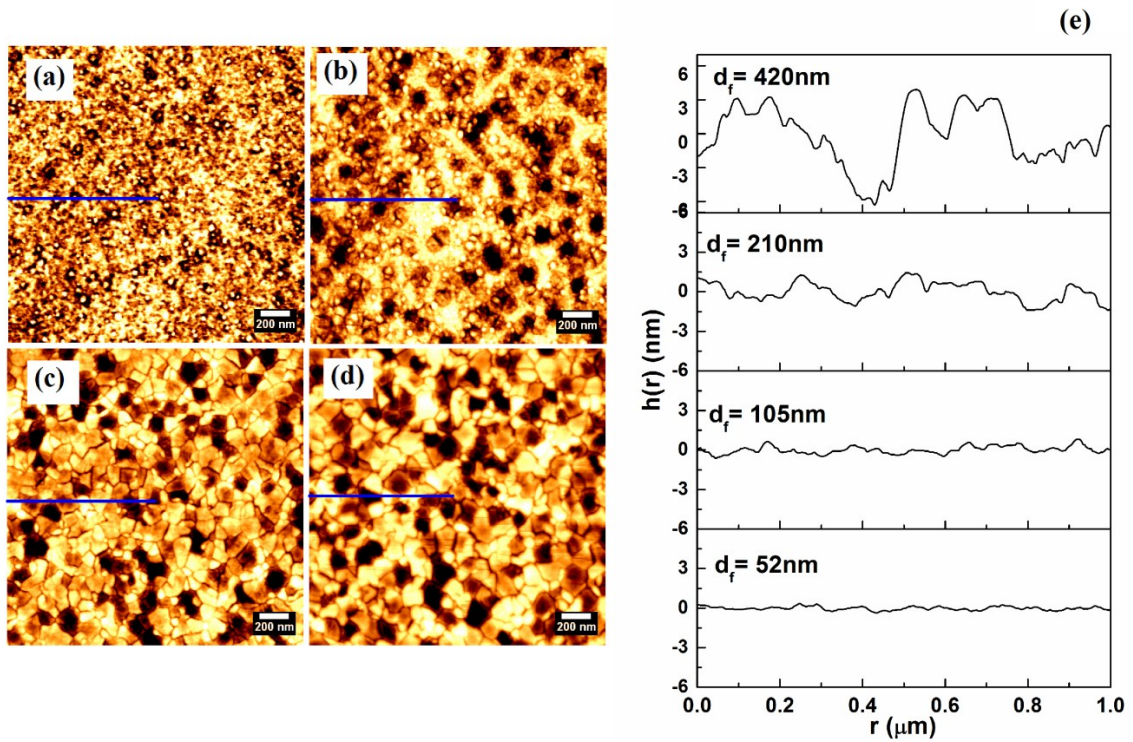


Fig. 4.12: AFM images of ITO films prepared in Ar/10%H₂ mixture for different thicknesses $d_f =$ (a) 52 nm, (b) 105 nm, (c) 210 nm, (d) 420 nm, and (e) line height profiles $h(r)$ of these films. Insert AFM image sizes are 200×200 nm². The blue lines show the positions of the line scans, displayed in (e).¹³³

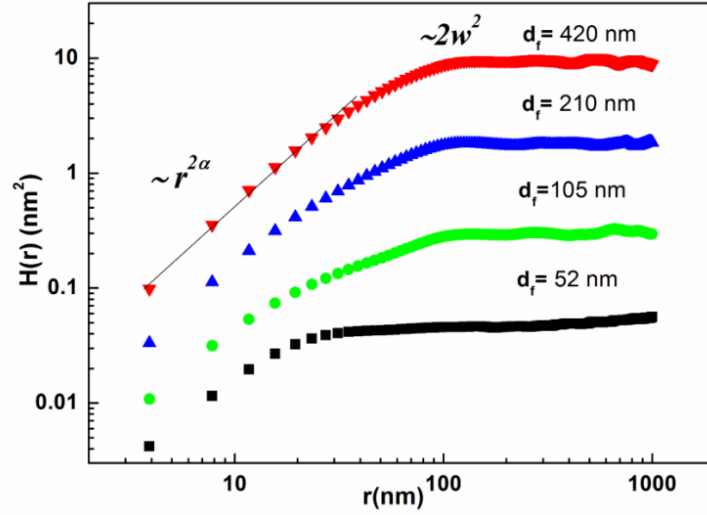


Fig. 4.13: The height-height correlation function of ITO films prepared in an Ar/10% H_2 atmosphere in dependence of the distance r as log-log plots for different film thicknesses.

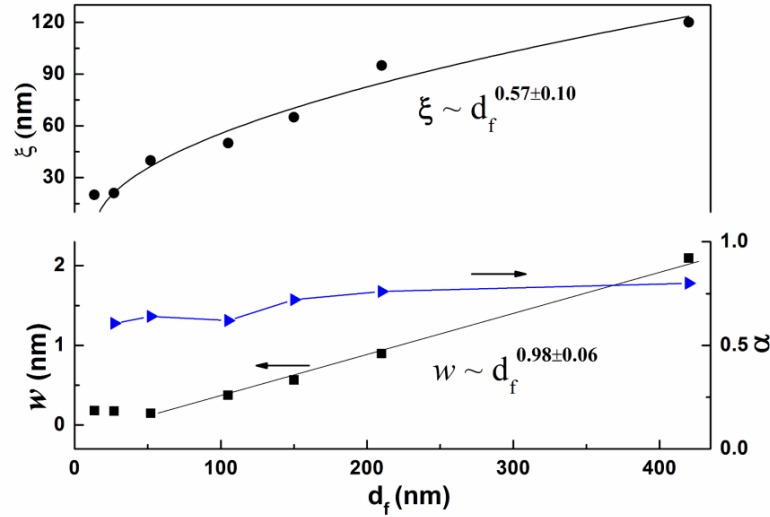


Fig. 4.14: Surface roughness w , roughness exponent α and correlation length ξ of ITO films prepared in an Ar/10% H_2 atmosphere as a function of the film thickness.

4.1.3.4 Growth of ITO films in different Ar/ O_2 or H_2 atmospheres

The influence of oxygen or hydrogen incorporation on the microstructure of the films was studied by depositing ITO films on Si (100) substrates at various oxygen or hydrogen partial pressures at room temperature. The sputtering RF power was 50 W and the sputtering pressure was fixed at 0.3 Pa. 400 nm-thick ITO films were also prepared in Ar/ O_2 and Ar/ H_2 atmospheres with varying O_2 or H_2 flows from 0 to 10% relative to the Ar flow. XRD patterns obtained for the ITO films deposited at various oxygen and hydrogen partial pressures are displayed in Fig. 4.15. XRD pattern (Fig. 4.15a) show a (211) preferred orientation when applying no additional oxygen, while they show a preferred

orientation (222) peak when applying 1% O₂. The increase in O₂ content causes a strong increase in the (222) peak intensity and a slight decrease in (211) peak intensity. It has to be noted that the deposition rate is 0.2 nm/s in Ar/10%O₂ atmosphere which is smaller than the 0.33 nm/s for deposition in pure Ar. This suggest that the oxygen addition to the plasma during the film deposition enhanced the (222) orientation independent on the deposition rate. XRD patterns (Fig. 4.15b) show only (211) peaks and no (222) peaks for ITO film prepared in Ar/1%H₂ atmosphere. When increasing H₂ to 2.5%, the (400) peak was observed. By further increasing the H₂ content, the (400) peak intensity increased and the (211) peak disappeared while a very weak (222) peak was observed when applying 10% H₂. With decreasing the oxygen content, the preferred orientation changes from (222) to (211). With increasing the hydrogen content, the texture transition switches from (211) to (100) plane. The change in orientation of the films from (111) to (100) texture results from the incorporation of oxygen into the films. The crystal growth in the (100) and (111) plane is characterized by an excess or reduction of oxygen vacancies¹⁴², respectively, and low-index surface energy $\gamma(111) < \gamma(211) < \gamma(100)$ ^{128,143}. The (211) surface of ITO is unstable with respect to oxygen-rich or hydrogen-rich deposition which can be explained by a mixed (111) and (100) character structure¹⁴³.

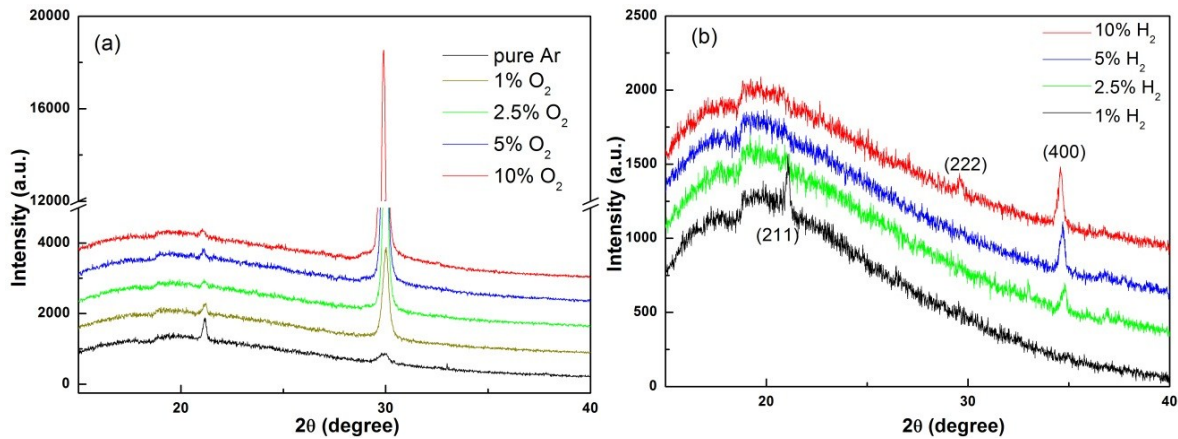


Fig. 4.15: XRD patterns of ITO films prepared in (a) different Ar/O₂ and (b) Ar/H₂ atmospheres.

The roughness evolution as a function of the reactive gas flows (O₂ or H₂) is displayed in Fig. 4.16. The surface roughness w and the lateral grain size ξ decrease with increasing O₂ flow while both quantities increase with increasing H₂ flow. This can be explained by surface smoothing due to surface diffusion when there is more O₂ flow during the deposition. With increasing H₂ flow, increased voids are observed in between the larger clusters. The surface roughness increases which is due to the increased shadowing effect

(see the height profile for $d_f = 420$ nm in Fig. 4.12e, where much deeper valleys are observed) and increased oriented (100) grain growth.

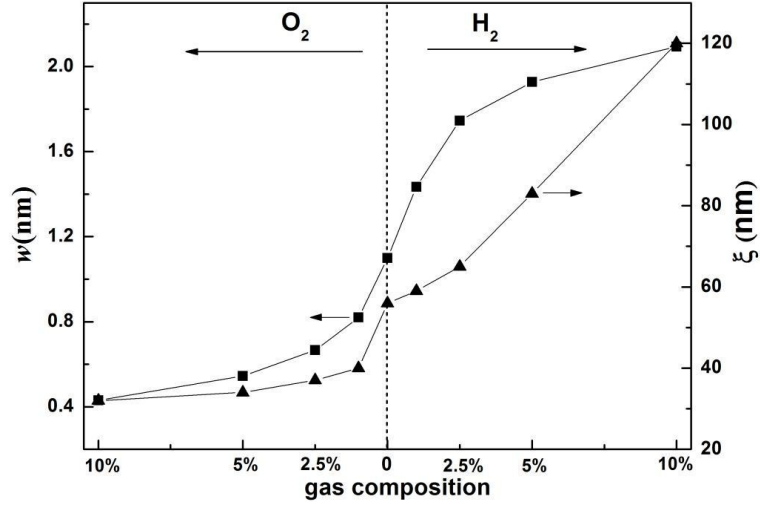


Fig. 4.16: Surface roughness w and correlation length ξ of 400 nm thick ITO films as a function of O_2 and H_2 flow.

In the above four sections, the surface roughness w of ITO films prepared by 13.56 MHz RF magnetron sputtering in different Ar/ O_2 or Ar/ H_2 atmospheres at room temperature is less than 2.1 nm for film thicknesses less than 420 nm. These roughness values are small and comparable with those reported for other DC or RF magnetron sputtering methods^{125,126, 144}, and much smaller than those of ITO films prepared by plasma-assisted molecular beam epitaxy method¹³⁰ ($w > 30$ nm for more than 4 nm-thick film) and for electron-beam evaporated films¹³¹ ($w=6\sim 25$ nm for 100~250 nm-thick film). In general, during non-equilibrium thin film growth, three competing processes occur: random fluctuations (noise) of the incoming particle flux, local smoothing/roughening effects, and non-local smoothing/roughening effects which influence the evolution of the surface morphology.⁶³ Raoufi et al.¹³¹ used a local growth model which combines the diffusion

model of Mullins⁴⁵ ($\frac{\partial h}{\partial t} = -D'\nabla^4 h + \eta$) and the Edwards-Wilkinson model⁴⁴ ($\frac{\partial h}{\partial t} = v\nabla^2 h + \eta$) to describe the smoothening mechanism with random fluctuations for their evaporated ITO film growth. The combined models can be described by the general linear equation:

$$\frac{\partial h(\mathbf{x}, t)}{\partial t} = -D'\nabla^4 h(\mathbf{x}, t) + v\nabla^2 h(\mathbf{x}, t) + \eta(\mathbf{x}, t) \quad (4.1)$$

where the $-D'\nabla^4 h$ term accounts for smoothing by surface diffusion due to the curvature-induced chemical potential gradient with D' proportional to the surface diffusion constant,

the second term $\nu \nabla^2 h$ is related to the relaxation of the surface by the surface tension ν , and the third term $\eta(\mathbf{x}, t)$ represents a white noise by random fluctuation in the flux of arriving species. This combined local growth model leads to roughness exponents in the range of $0 \leq \alpha \leq 1$ and growth exponents of $0 \leq \beta \leq 0.25$ in 2+1 dimensions, which fits to their result of $\alpha=0.71$ and $\beta = 0.11$. In the present work, however, the growth exponents β of 0.35, 0.65 and 0.98 for Ar/10% O₂, pure Ar and Ar/10% H₂ mixture deposition, respectively, are larger than these predicted values² (shown in Table 4.1). Obviously, the combined Mullins diffusion model and the Edwards-Wilkinson model in 2+1 dimensions are inappropriate to explain our results which have much higher growth exponents than that of the local growth model. Nonlocal effects such as shadowing, bulk diffusion etc. should exist in our system.

Karunasiri, Bruinsma, and Rudnick (KBR)⁵⁶ and Bales et al.⁵⁷ developed a continuous nonlocal model with a shadowing instability for sputter deposition in 2+1 dimensions which is given by:

$$\frac{\partial h(\mathbf{x}, t)}{\partial t} = -D \nabla^4 h(\mathbf{x}, t) + R \theta(\mathbf{x}, t) + \eta(\mathbf{x}, t) \quad (2.18)$$

where only the second term is different in comparison to Eq.(4.1). Here the second term is the deposition rate R with the exposure angle $\theta(\mathbf{x}, t)$ measuring the amount of particle flux that each point receives. They predicted that the surface develops into a self-similar mountain-like landscape for small diffusion lengths while flat, compact films can be grown up to a critical thickness when the surface diffusion length is high. Further deposition leads to surface roughening due to the shadowing effect. Yao and Guo⁶⁰ extended the KBR model to sputter growth in three dimensions when the shadowing instability leads to the development of a mounded surface where the surface roughness w increases linearly with time ($\beta = 1.0 \pm 0.04$) and that column width ξ grows as $\xi \sim t^{0.33 \pm 0.02}$. Later, Drotar et al.⁶¹ used a pure shadowing model to calculate by Monte Carlo simulations in 2+1 dimensions a roughness growth exponent of $\beta = 1$. They also suggested that the competition between surface diffusion which lowers the growth exponent and shadowing which roughens the surface and generates a higher dynamic scale could result in exponents β between 0.5 and 1. Drotar et al.⁵³ also performed a numerical analysis of the noise-driven KS model in 2+1 dimensions, which can describe the growth process by the non-linear Langevin equation:

$$\frac{\partial h(\mathbf{x}, t)}{\partial t} = -\nu \nabla^2 h(\mathbf{x}, t) - D \nabla^4 h(\mathbf{x}, t) + \frac{\lambda}{2} |\nabla h(\mathbf{x}, t)|^2 + \eta(\mathbf{x}, t) \quad (4.2)$$

They obtained α values from 0.75~0.85 and β values of 0.22~0.25. Note that these simulations are done for amorphous films and did not consider crystalline growth effect which also roughens the surface. In this work, the roughness growth exponents are around 0.6-0.8 which is in the range of the noise-driven KS model in 2+1 dimensions. The growth exponents increase with decreasing oxygen content in the sputtering atmosphere. For the Ar/10%O₂ deposition, a high kinetic energy of the impinging species, mostly negative oxygen ions¹⁴⁵ will lead to a significant bombardment-induced mobility of the adatoms which generates a higher density of the deposit and a reduced surface roughness. Then, the surface diffusion is strong enough to smoothen the surface while the grain growth along (111) plane roughens the surface leading to β of 0.35. In pure Ar and Ar/10% H₂ deposition, the negative ion bombardment by oxygen ions is reduced accompanied by a lower surface mobility and crystallite growth is weaker in comparison to the Ar/10%O₂ deposition which can be seen from the XRD analysis. Our observed growth exponents β of 0.65 and 0.98 for the depositions in pure Ar and in Ar/10% H₂ respectively, are close and very close to $\beta=1$. Thus, we can conclude that shadowing is the dominating effect during our film growth.^{60,61} If a surface obeys dynamic scaling³, the growth exponents are related in a specific way according to $z = \alpha / \beta$. However, such a relation no longer holds for surfaces growing under the influence of shadowing³. For the deposition in pure Ar, $z=2.27$ is far from $\alpha/\beta= 1.03\sim 1.15$. For the deposition in Ar/10%O₂, $z=2.78$ does not equal to $\alpha/\beta= 1.86\sim 2.23$, but get closer. For the deposition in Ar/10% H₂, $z=1.75$ is also not in the range of $\alpha/\beta= 0.61\sim 0.82$. Tentatively, our results can be explained by a combination of local and non-local growth models in 2+1 dimensions where the shadowing effect plays a crucial role and noise and oriented grain growth cannot be neglected in the morphology evolution during different gas atmospheres deposition.

Table 4.1: Surface parameters roughness exponent α , growth exponent β , and z for ITO films deposited in different gas atmospheres.

| | pure Ar | Ar/10% O ₂ | Ar/10% H ₂ | Combined linear growth ⁵⁴ | Random depositon ^{2,61} | Surface diffusion ² | Noisy KS model ⁵³ | Shadowing ^{39,61} |
|----------------|-----------|-----------------------|-----------------------|--------------------------------------|----------------------------------|--------------------------------|------------------------------|----------------------------|
| α | 0.67~0.75 | 0.65~0.78 | 0.6~0.8 | 0~1 | - | 1 | 0.75~0.8 | - |
| β | 0.65 | 0.35 | 0.98 | 0~0.25 | 0.5 | 0.25 | 0.22~0.25 | 1 |
| α/β | 1.03~1.15 | 1.86~2.23 | 0.61~0.82 | - | - | 4 | - | - |
| $1/z$ | 0.44 | 0.36 | 0.57 | 0.25~1 | - | 0.25 | 0.25~0.33 | - |
| z | 2.27 | 2.78 | 1.75 | 2~4 | - | 4 | 3~4 | 0.33, 0.93 |

4.1.4 Influence of different discharge modes on the growth of ITO films

DC and RF magnetron sputtering are the most attractive techniques and widely used for the deposition of thin films in general and also ITO films due to the high deposition rate, good reproducibility on large substrate areas, and good film performances even at low substrate temperatures, as mentioned in the previous chapter. In terms of the role of the plasma parameters, i.e. ion flux and ion energy to the substrate, some research groups have performed systematic investigations^{135, 146, 147}. Song et al.¹⁴⁶ investigated the effect of deposition pressure and sputtering gas species on the crystallinity of ITO films prepared by DC magnetron sputtering using oxide ceramic (ITO, doped with 10 wt.% SnO₂) or alloy (IT, indium-tin alloy with 10 wt.% tin) targets at low temperature. They reported that the crystallinity of ITO films was not only strongly affected by the kinetic energy of the sputtered In particles arriving at the substrate surface, which was shown to be closely related to the transport processes between the target and substrate, but also dominated by the O₂ partial pressure during reactive sputtering using an IT alloy target. Bender et al.¹⁴⁷ presented a RF-superimposed DC-magnetron sputter process which improved the resistivity of ITO films prepared from an ITO target. They measured the ion energy distribution function of the positively charged ions approaching the substrate surface and showed that the mean energy of the ions increases with increasing RF portion of the total power. Mientus and Ellmer¹³⁵ studied systematically the influence of the sputtering pressure and the plasma excitation mode (DC, pulsed DC and RF) on the structure and electrical properties of ITO films deposited from IT target. They found that the RF excitation (13.56 MHz) of a magnetron discharge is the most effective mode with respect to the usage of the oxygen for oxidizing the sputtered metal atoms on the substrate surface. RF or combined DC/RF excitation is propitious to good ITO growth process. In the present work, the aim is

to study systematically the influence of different plasma excitation modes, i.e. of the negative ion bombardment on the microstructural and morphology of ITO films.

Tin-doped indium oxide thin films were deposited onto borosilicate glass substrates by magnetron sputtering at low temperature (RT, less than 70 °C) and high temperature (300 °C). The magnetron plasma was excited by different discharge modes (27.12 MHz RF, 13.56 MHz RF and pulsed DC power supply) at a constant power of 50 W in an atmosphere of pure argon at a total pressure of 0.3 Pa, resulting in a target voltage of about -100 V, -210 V and -340 V (during the duty cycle), respectively. The pulsed DC sputtering was done with a frequency of 40 kHz and a duty cycle of 60%.

4.1.4.1 *Low temperature ITO film growth under different discharge modes*

Fig. 4.17(a) shows the XRD pattern of the ITO films deposited at 27.12 MHz RF discharge mode with various film thicknesses at room temperature. From the XRD pattern, only a broad peak can be observed when the film thickness is 15 nm, indicating that the film was an amorphous structure. When the film thickness is between 30 nm and 100 nm, only one peak around $2\theta=30^\circ$ can be observed which is related to the (222) peak of the cubic structure of In_2O_3 . A weak (211) peak begins to appear when the film thickness is larger than 200 nm. For 13.56 MHz RF deposition, similar preferred orientation is observed, shown in Fig. 4.17 (b). When film thickness is less than 30 nm, no peaks appear in the XRD pattern. When the film reaches to 36 nm -thick, only a small intensity of (222) peak can be measured which indicates the film is almost X-ray amorphous or has a nanocrystalline texture.¹⁴⁸ When the film thickness is less than 90 nm, only the (222) peak can be seen. When the film thickness is higher than 180 nm, the (211) peak begins to appear. The intensity ratio of (211)/(222) is 0.96 and 1.43 for 180 nm and 360 nm-thick ITO films, respectively, indicating that (211) plane grows faster than (222) plane and becomes the preferred orientation. This behavior is very similar with the structure evolution of ITO film on Si substrates described in section 4.1.3.1. XRD patterns of the films deposited in the pulsed DC discharge mode are also very similar with that in 13.56 MHz RF mode except the increasing growth of (440) peak. However, in the 27.12 MHz RF discharge mode, (222) always keep the dominate growth orientation. None of the films showed (400) plane texturing in these three different discharge mode depositions. The average grain size derived from XRD measurements with Scherrer analysis is 32.3 nm, 40.1 nm and 47 nm for 27.12 MHz RF, 13.56 MHz RF and pulsed DC, respectively, as shown in Table 4.2.

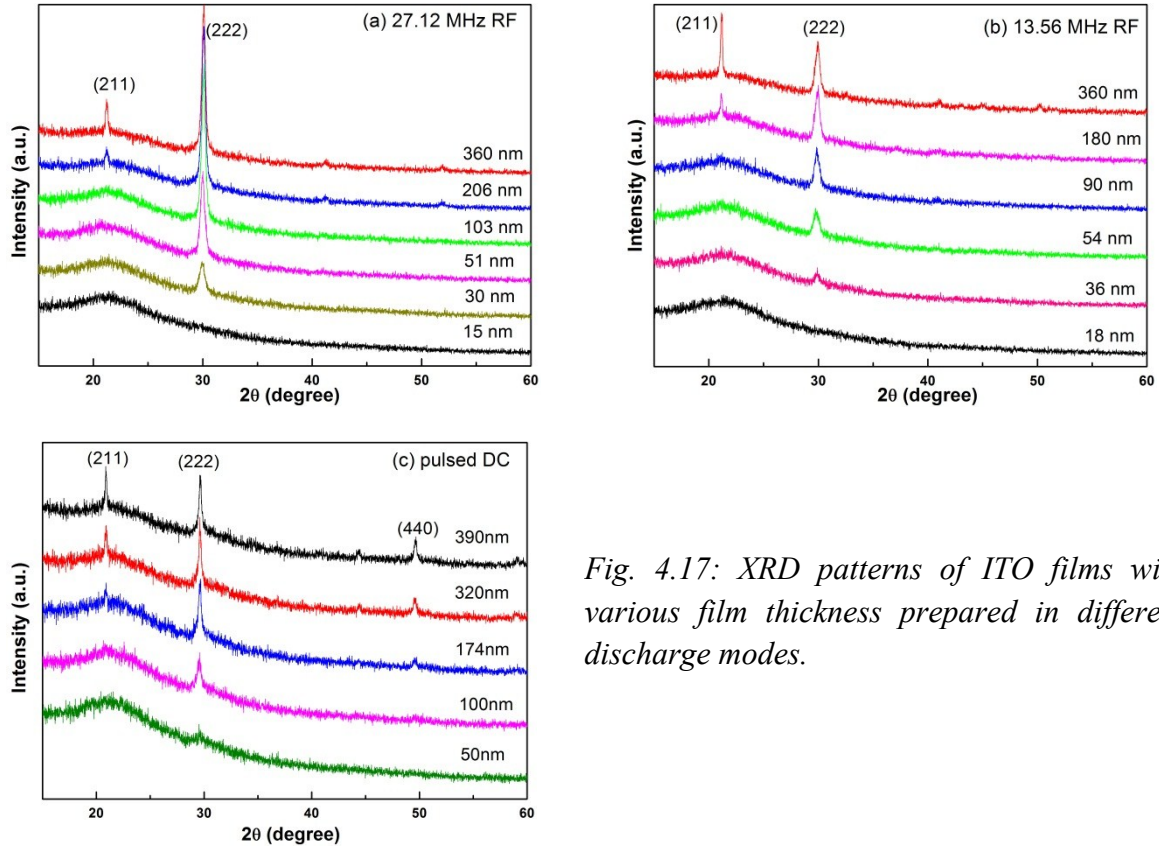


Fig. 4.17: XRD patterns of ITO films with various film thickness prepared in different discharge modes.

Table 4.2: Structure information of ITO films prepared in different discharge modes obtained from XRD patterns. In JCPDS_06-0416: $I(211)/I(222)=0.14$.

| Discharge mode | Thickness/nm | Orientation | Peak intensity ratio $I(211)/I(222)$ | FWHM/ $^{\circ}$ | dg(XRD) /nm |
|----------------|--------------|-------------|--------------------------------------|------------------|-------------|
| 27.12 MHz RF | 360 | (222) | 0.47 | 0.356 | 32.3 |
| | 206 | (222) | 0.36 | 0.367 | 26.8 |
| 13.56 MHz RF | 360 | (211) | 1.43 | 0.126 | 40.1 |
| | 180 | (211) | 0.96 | 0.131 | 38.7 |
| Pulsed DC | 390 | (211) | 1.06 | 0.109 | 55.6 |
| | 320 | (211) | 0.99 | 0.151 | 47 |

Fig. 4.18 shows SEM images of 320~360 nm-thick ITO thin films prepared in different discharge modes at room temperature. It is clear that all the films are compact uniform and consist of agglomeration of the densely populated grains with grain size of 30 ~100 nm.

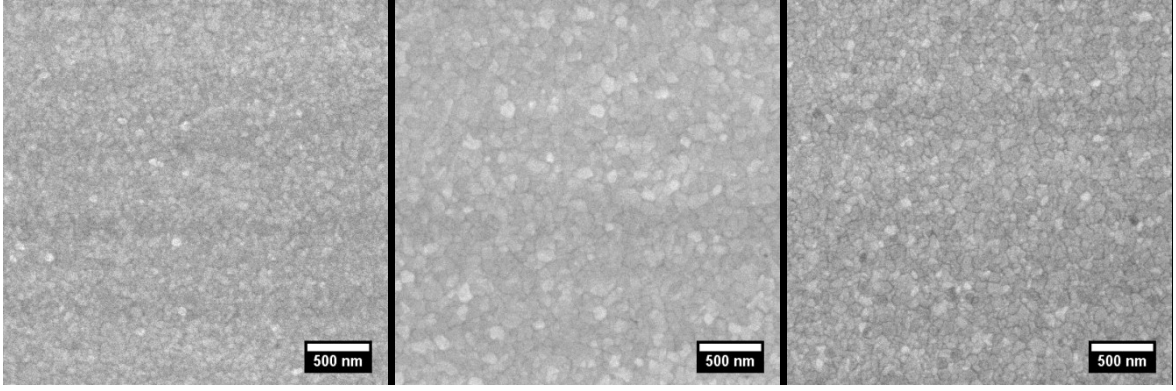


Fig. 4.18: SEM images of 320~360 nm-thick ITO prepared at room temperature with different discharge modes (a) 27.12 MHz RF, (b) 13.56 MHz RF and (c) pulsed DC.

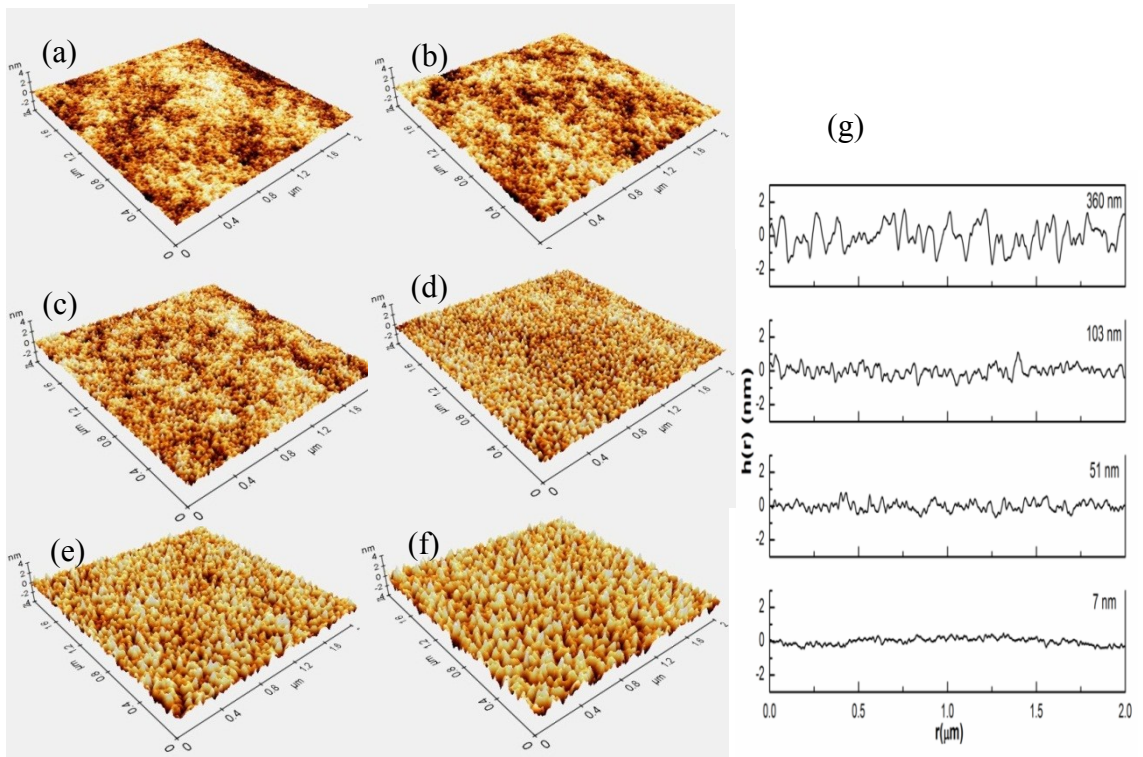


Fig. 4.19: 3D-AFM images of ITO prepared at 27.12 MHz RF mode (a) 7 nm, (b) 30 nm, (c) 51 nm, (d) 103 nm, (e) 206 nm, and (f) 360 nm, and (g) height profiles $h(r)$ for different film thicknesses.

Fig. 4.19 shows 3D-AFM images of ITO films prepared with the 27.12 MHz RF mode with various film thicknesses from 7 nm to 360 nm, which display surface morphologies in island growth mode with mound-like structure. All images are sized $2 \times 2 \mu\text{m}^2$ with the same vertical scale. 1D cross-section scans in the middle position of surface profiles from 7 nm, 51 nm, 103 nm and 360 nm thick films are plotted in Fig. 4.19(g), respectively. As can be seen in Fig. 4.19, the lateral size grows with increasing film thickness. The surface height (peak to valley) showed in the height profile also markedly increases with increasing

thickness. For ITO films prepared with 13.56 MHz RF and pulsed DC discharge modes, it is observed that all film surfaces are of the island growth type. Their surface morphology (not shown here) is similar with ITO films prepared in 27.12 MHz RF mode, but the grains grow bigger and rougher. The grain sizes obtained from AFM images vary with film thickness by a power law $d_g(AFM) \sim d_f^{1/z}$ with $1/z$ of 0.31, 0.39, and 0.42 for 27.12 MHz RF, 13.56 MHz RF and pulsed DC discharge mode, respectively.

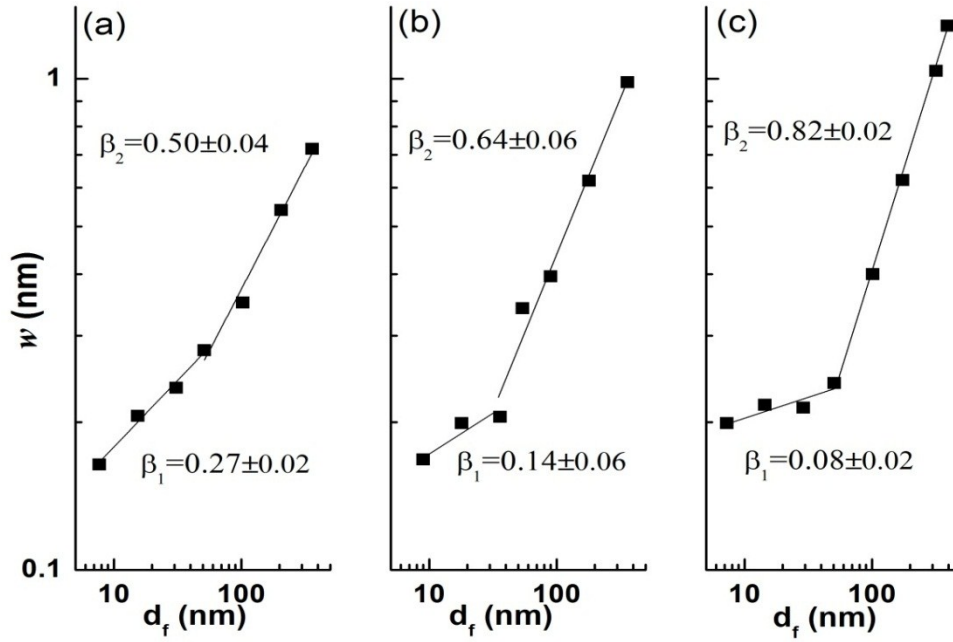


Fig. 4.20: Surface roughness w of ITO films prepared at (a) 27.12 MHz RF, (b) 13.56 MHz RF and (c) pulsed DC discharge mode at room temperature as a function of film thickness.

Fig. 4.20 shows, on a log-log scale, the root-mean-square surface roughness of ITO films prepared with different discharge modes as a function of film thickness. The line on the plots represents the best fits to the data. The roughness evolution can be divided into two regions for all discharge modes. For 27.12 MHz RF discharge mode, as shown in Fig. 4.20(a), in the initial growth stage, the roughness increases slightly from 0.16 nm to 0.28 nm when the film thickness increases from 7 nm to 53 nm thick. By linear fitting, a growth exponent of $\beta_1 = 0.27 \pm 0.02$ was obtained. Then there is a roughness transition. In the later growth stage, the roughness increases more quickly than the initial growth stage. The roughness increases from 0.35 nm to 0.78 nm as the film grows from 103 nm to 360 nm, and a growth exponent of $\beta_2 = 0.5 \pm 0.04$ was obtained which is larger than that in initial growth stage.

For 13.56 MHz RF discharge mode, as shown in Fig. 4.20(b), the roughness increases only marginally from 0.17 nm to 0.20 nm as the film thickness increases from 9 nm to 36

nm. The obtained growth exponent β_1 is 0.14 ± 0.06 which is smaller than 0.27 ± 0.02 for 27.12 MHz RF deposition in the initial growth stage. In the later growth stage, the roughness increases from 0.34 nm to 0.98 nm as the film grows from 54 nm to 360 nm, and a growth exponent of $\beta_2 = 0.64 \pm 0.06$ was obtained which is larger than that in initial growth stage, and also larger than $\beta_2 = 0.5 \pm 0.04$ obtained for the 27.12 MHz RF deposition.

For pulsed-DC discharge mode, as shown in Fig. 4.20(c), at the beginning of the growth from 7 nm to 50 nm-thick, the roughness of the surface gradually increases from 0.20 nm to 0.24 nm with a growth exponent $\beta_1 = 0.08 \pm 0.02$, which is smaller than the growth exponent $\beta_1 = 0.27 \pm 0.02$ and 0.14 ± 0.06 in the initial growth stage for 27.12 MHz RF and 13.56 MHz RF deposition indicating stronger surface diffusion compared to the other two modes. Further growth leads to a strong increase in roughness. When film grows from 100 nm to 390 nm, the roughness increases from 0.4 nm to 1.3 nm with a larger exponent $\beta_2 = 0.82 \pm 0.02$.

Table 4.3: Growth exponent β , roughness exponent α and $1/z$ parameters of ITO films prepared with different discharge modes at room temperature.

| Discharge mode | $V_{\text{dis}}(\text{V})$ | β_1 | β_2 | $1/z$ | α |
|----------------|----------------------------|-----------|-----------|-------|----------|
| 27.12 MHz RF | 100 | 0.27 | 0.50 | 0.31 | 0.7~0.85 |
| 13.56 MHz RF | 210 | 0.14 | 0.64 | 0.39 | |
| Pulsed DC | 340 | 0.08 | 0.82 | 0.42 | |

In this section, the crystallinity and the morphology of ITO films prepared with different excitation modes at room temperature were studied. The discharge voltages were about -100 V, -210 V and -340 V for 27.12 MHz RF, 13.56 MHz RF and pulsed DC discharge mode, respectively. According to the XRD analysis, the excitation mode of the magnetron discharge does not influence significantly the structure of the ITO films at room temperature. Based on the morphology investigations, it is found that the excitation mode does not change the island growth type for ITO films, but plays an important role in the non-equilibrium film growth. Growth exponents β and roughness exponents α were obtained, as shown in Table 4.3. The above experimental results show that the roughness evolution of ITO films deposited by the three discharge modes all can be divided into two regions. The critical transition thickness is in the range of 30~ 50 nm. With increasing discharge voltage (changing the excitation mode from RF to DC), in the initial growth

stage, the growth exponent β_1 of the ITO films is small and decreases. However, the growth exponent β_2 is much larger and increases in the later growth stage. As discussed in the previous section 4.1.3, the competitions among surface diffusion, shadowing and oriented growth determine the surface morphology and the scaling exponents. The surface diffusion, smoothing the surface, will only lower the exponents, but the shadowing effect and oriented grain growth will roughening the surface and increase the exponents³. In the initial growth stage, the films are almost amorphous so there will be no grain growth roughening effect. The growth exponent β is 0.27, 0.14 and 0.08 for 27.12 MHz RF, 13.56 MHz RF and pulsed DC discharge mode, respectively. Surface diffusion dominates the film growth. With increasing discharge voltage, the average kinetic energy of the negative ions also increase¹⁴⁵ which will increase the adatoms mobility causing a smooth surface. Therefore, the surface diffusion effect is strongest in the pulsed DC deposition and weakest in the 27.12 MHz RF deposition in the initial growth stage. In the later growth stage, due to the increased deposition rate, atoms have no time to move and covered by new impinging particles which reduced the adatom mobility. The oriented grain growth and shadowing effect dominate the film growth and rough the surface leading to larger growth exponents.

4.1.4.2 High temperature ITO film growth with different discharge modes

The substrate temperature was kept at 300 °C while keeping the other sputtering parameters the same as for the room temperature deposition in section 4.1.4.1 to investigate the influence of the substrate temperature on the morphology evolution of ITO films prepared at different discharge modes.

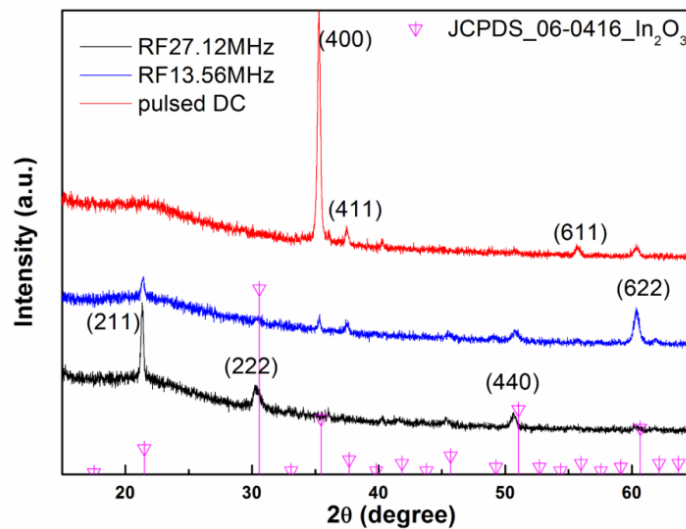


Fig. 4.21: XRD patterns of 360 nm- thick ITO films prepared in different discharge modes.

Fig. 4.21 shows XRD spectra of 360 nm-thick ITO films sputtered with the same power of 50 W but different discharge mode, 27.12 MHz RF, 13.56 MHz RF and pulsed DC, respectively. The growth of the films showed different preferred orientations depending on the discharge mode, which is not observed for the room temperature depositions. The film deposited with the 27.12 MHz RF discharge showed reflections corresponding to the (211), (222) and (440) planes. The normalized peak intensities for these peaks are 100, 38 and 16, respectively. In the 13.56 MHz RF discharge mode, the XRD peaks are small and broad indicating growth in (211), (400), (411), (440) and (622) orientations. The normalized peak intensities for these peaks are 100, 47, 39, 26 and 56, respectively. The pulsed-DC discharge mode resulted in a very sharp (400) peak together with small broad peaks for (411), (611) and (622) orientation. The reason for (400) preferred orientation might be related to that the concentration of oxygen vacancies in the ITO film prepared at pulsed DC mode at high temperature sputtering is higher than that of room temperature sputtering and other RF discharge modes due to the reduced sticking coefficient of oxygen at higher temperatures.¹³⁸ On the other hand, ITO films deposited by RF discharge modes at high temperature show (211) or (622) preferred plane indicating that films accommodate fewer oxygen vacancies compared to that of the pulsed DC discharge mode.

The morphology of the 360 nm-thick ITO films deposited at 300°C with different discharge modes was characterized by SEM and AFM. Fig. 4.22(a, b, c) and (d, e, f) display SEM and 3D-AFM images of ITO films prepared at 27.12 MHz RF, 13.56 MHz RF and pulsed DC discharge modes, respectively. The corresponding surface roughness is 3.0 nm, 2.4 nm and 3.2 nm which are bigger than these of room temperature depositions (0.72 nm for 27.12 MHz RF, 1.12 nm for 13.56 MHz RF and 1.28 nm for pulsed DC discharge mode). Big grooves can be seen for all the films from the AFM results. Elongated grain structures are observed for the films deposited in the RF discharge mode. For the pulsed DC discharge mode, small clusters of conical grains distributed uniformly on the substrate were grown; grains 150~250 nm in size consist of highly oriented small clusters 20~50 nm in diameter. Comparing the morphology of low temperature and high temperature depositions, it can be found that the thermal activation enlarges the grains and increases the grooves.

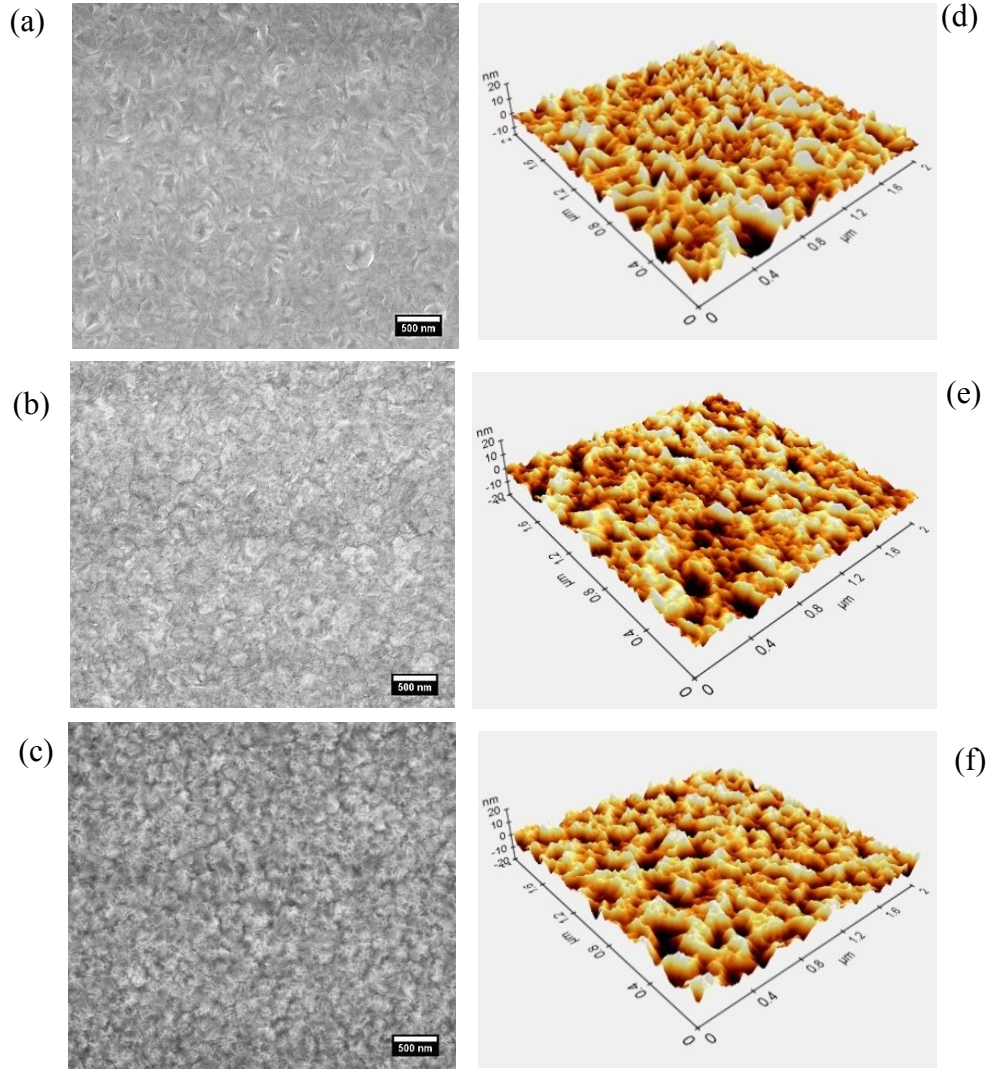


Fig. 4.22: SEM morphology and 3D-AFM images of ITO films prepared with different discharge modes (a, d) 27.12 MHz RF, $w = 3.0$ nm (b, e) 13.56 MHz RF, $w = 2.4$ nm and (c, f) pulsed DC, $w = 3.2$ nm. The size of the AFM images is $2 \times 2 \mu\text{m}^2$.

Fig. 4.23 displays the variation of the surface roughness w of ITO films deposited with different discharge modes as a function of the film thickness d_f in a log-log scale. The analysis of Fig. 4.23 shows that the roughness evolution of three series ITO films can be divided into two regions with a crossover at 100 nm for RF discharge mode and 200 nm for pulsed DC deposition. In the first region, for $d_f \leq 100$ nm, growth exponents β_1 for 27.12 MHz RF and 13.56 MHz RF deposition is very close and are 0.90 ± 0.08 and 0.89 ± 0.03 , respectively. Whereas for the second region, for $d_f > 100$ nm, β_2 is 0.17 ± 0.06 and 0.22 ± 0.04 , respectively. For pulsed DC discharge mode, β_1 and β_2 are 0.80 ± 0.04 and 0.04 ± 0.1 . All β_1 obtained at high temperature are larger than 0.5 and smaller than 1 indicating that the shadowing and oriented grain growth dominates the film growth.

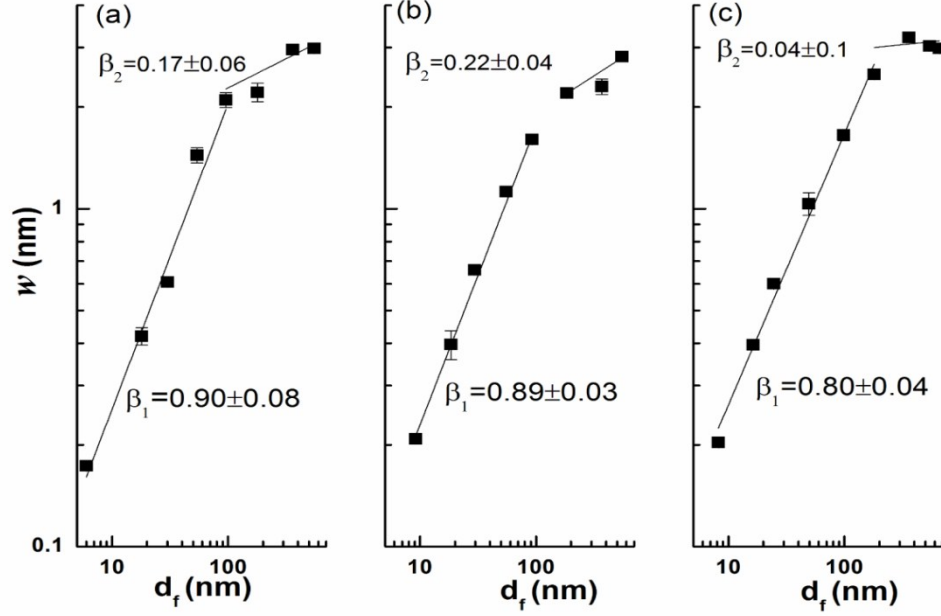


Fig. 4.23: Surface roughness w of ITO films prepared at (a) 27.12 MHz RF, (b) 13.56 MHz RF and (c) pulsed DC discharge mode at 300°C as a function of film thicknesses.

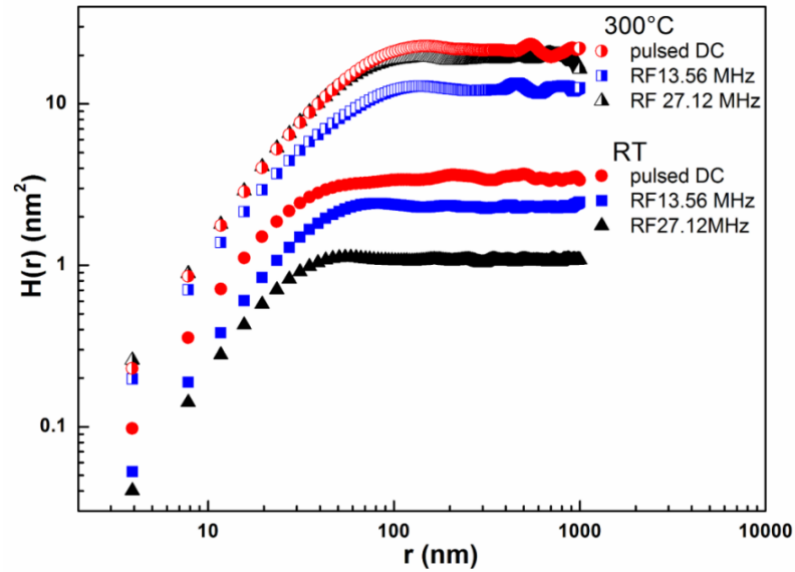


Fig. 4.24: The height-height correlation functions $H(r)$ of ITO films prepared with different discharge modes at room temperature and 300 °C.

The height-height correlation functions $H(r)$ as a function of the lateral distance r for 360~390 nm- thick ITO films deposited with different discharge modes at RT and 300 °C are shown in Fig. 4.24. The roughness exponent α can be extracted from the fitting of $H(r)$ for the short distance (slope= 2α), α ranges from 0.77 to 0.81, which are very close to these of room temperature deposition ($\alpha=0.79\sim0.83$). There is much more fluctuation in longer-

range behavior of $H(r)$ which is due to voids and grooves contributing to the roughening of the surface.

According to the revised structure zone models¹⁷⁻¹⁹, the microstructure of sputtered metal thin films can be described as a function of the substrate homologous temperature (T_s/T_m), sputtering pressure and discharge voltage. In this model, shadowing, surface diffusion, bulk diffusion and desorption are the factors determining the microstructure of sputtered films with increasing substrate temperature. The T_s/T_m for ITO at a T_s of RT and 300 °C is about 0.15 and 0.28, respectively, which corresponds to the transition zone where shadowing and surface diffusion both are active and the structure of the films consists of densely packed fibrous grains. This matches with the microstructural observations at all depositions at RT and RF deposition at 300 °C, but does not account for the subgrain characteristics for pulsed DC deposition at 300 °C. Kamei and Shigesato et al.^{149,150} explained that {400} planes are most stable against resputtering and prefer to expose at the surface of each grain, resulting in the subgrain boundaries consisting of small- angle grain boundaries due to the bombardment by energetic particles during DC sputtering growth of ITO films. In present work, only ITO film prepared with pulsed DC discharge at 300 °C shows preferential <400> orientation normal to the substrate subgrain structure. Comparing the roughness evolution of ITO films prepared with different discharge modes at RT and 300 °C, higher temperature results in rougher surfaces. For low temperature depositions, a very clear transition from surface diffusion to shadowing/grain growth effect can be observed which caused two distinguished growth exponents: small β_1 in the initial growth and large β_2 in later growth. The important role of kinetic energy of negative ions which affects the adatom mobility is much more obvious. For high temperature depositions, the film properties, i.e. crystallinity and surface morphology, are more dominated by the temperature, which is a more beneficial effect than the kinetic energy inducing the film growth with big grains and hence rough surface. It coincides with the results reported by Sittinger et al.¹⁵¹, who reported the beneficial effect of target material ionization for high charge voltages (here $V_{RF27.12MHz} < V_{RF13.56MHz} < V_{pulsed\ DC}$) for low temperature ITO deposition but no clear effect of varying discharge voltage can be observed for high substrate temperature depositions where the temperature dominate the film growth and properties. Therefore, the growth exponents are very close for RF and pulsed DC deposition in high temperature depositions.

4.1.5 Conclusions

Tin-doped indium oxide (ITO) films have been prepared by magnetron sputtering from a ceramic target. The film morphology is affected by the sputtering atmosphere, the excitation mode and the substrate temperature, but not the type of the substrate used in this work: Si or borosilicate glass. For room temperature depositions, sputtering atmospheres play an important role for the surface evolution from oxygen deficient to oxygen excess conditions. The preferred orientation of ITO films prepared without O₂ addition to the argon sputtering gas changed from (211) to (111) with increasing O₂ flow, while the crystallites grow with a (100) texture with increasing H₂ content of the sputtering atmosphere. The morphology changes from densely nanosized grains to voided large polygonal grains. The surface becomes rougher and the growth exponent increases with increasing the oxygen vacancies by tuning the O₂ and H₂ content. The dynamic scaling is explained tentatively by a combination of local and non-local growth modes in 2+1 dimensions where the shadowing effect plays a crucial role and noise and oriented grain growth cannot be neglected in the morphology evolution during low-ion-bombardment deposition in Ar/H₂ atmospheres compared with a Ar/O₂ deposition. The effect of the excitation modes on the growth of ITO films were also checked for pure Ar deposition. The excitation modes, i.e., from RF to pulsed-DC have a smaller effect on the crystallite growth at room temperature deposition compared to high temperature deposition. For room temperature deposition, the preferred orientation changes very slowly and the roughness evolution all composed of two transition stage: ion-bombardment induced surface diffusion dominates and then transfer to shadowing and crystallite growth leading the growth. However, for high temperature deposition, the kinetic energy of negative ions which affects the adatom mobility is less obvious than the thermal dynamics induced by the temperature. Distinct crystallite growth and morphology can be observed.

4.2 Nucleation and growth of Al-doped zinc oxide films

4.2.1 Introduction

When considering the practical use of transparent conducting oxide films, not only their optical and electrical properties should be considered, but also environmental stability, work function and compatibility with substrate or contact layer and other parameters of devices, as appropriate for the application. Although ITO films are still the best performing transparent conductors, the potential use of this material is considered to be reduced due to the rare and expensive element Indium. Some of the properties of In_2O_3 and ZnO are listed in Table 4.4. Transparent conducting oxides composed of doped zinc oxide have found great interest and chosen as an alternative to replace bixbyite structured ITO as transparent conducting electrodes owing to its cheap and abundant resources, chemical stability and also the high visible transparent and electrical conductivity (as low as $2.4 \times 10^{-4} \Omega\text{cm}$) in photovoltaic window and display technology applications. The electrical and optical properties of pure and also doped- ZnO have been extensively studied and reviewed.^{20,152} In the undoped state, pure ZnO has very high resistivity because the native point defects are not efficient donors which is different with In_2O_3 . Fortunately, the electrical properties of ZnO can be improved by substitutional doping with group III element (B, Al, Ga or In)¹⁵²⁻¹⁵⁴. However, the general performance of doped- ZnO is still not as good as that of ITO. In the present work, the microstructure and morphology of Al-doped zinc oxide (AZO) prepared by RF magnetron sputtering in different atmospheres are investigated. And we also tried to compare the structure evolution and electrical properties of AZO films with ITO films to figure out why the property of AZO is inferior to ITO.

ZnO is a direct wide band-gap ($E_g=3.37$ eV at room temperature) II-VI binary compound semiconductor and crystallizes in three forms: hexagonal wurtzite, cubic zinc-blende, and cubic rocksalt structure, in which wurtzite structure is the most thermodynamically stable and common phase at ambient conditions.⁵ The zinc-blende ZnO structure can be stabilized only by growth on substrates with a cubic lattice structure and the rocksalt structure can only be prepared at relatively high pressures (10 GPa) or when it is alloyed with a high amount of magnesium. The wurtzite structure of ZnO , schematically shown in Fig. 4.25, consists of two interpenetrating hexagonal close-packed sublattices, each of which is composed of one type of atoms displaced with respect to each other along the threefold c -axis.¹⁵⁵ The bulk lattice parameters reported in literature for wurtzite ZnO , i.e., that of in hexagonal unit cell are: $c=0.52066$ nm and $a=0.32498$ nm (JCPDS 36-1451)

and the ratio of $c/a = 1.6$. ZnO belongs to the space group $P6_3mc$ in the Hermann-Mauguin notation. However, the lattice parameters for ZnO thin films strongly depend on the doping and the deposition conditions. The wurtzite ZnO structure lacks an inversion plane perpendicular to the c -axis which means that the surfaces have either Zn polarity with a designation of (0001) plane or O polarity with a designation of $(000\bar{1})$ plane. The distinction between these two directions is essential due to their polarization charge. The polar surface of ZnO is metastable in nature and is responsible for some unique properties including piezoelectricity, spontaneous polarization, and a strongly anisotropic etching behavior.⁵ The Al-doped zinc oxide films exhibit in all cases the wurtzite structure of ZnO.

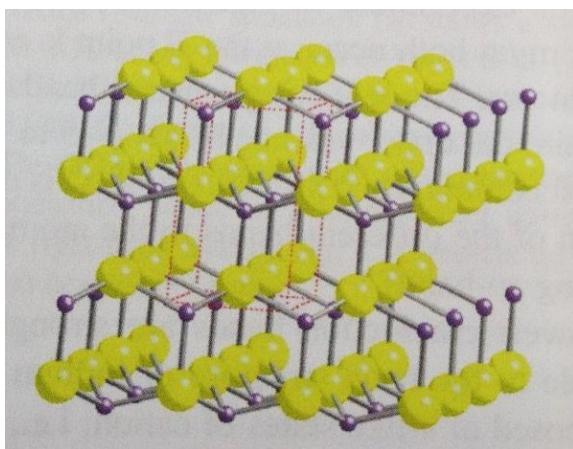


Fig. 4.25: the crystal structure of wurtzite ZnO: perspective view perpendicular to the c -axis. Large yellow balls and small gray balls denote O and Zn atoms, respectively. Dotted lines show the unit cell.⁵

Table 4.4: Properties of In_2O_3 and ZnO.²⁰ ΔH_f is the heat of formation per formula unit of indium oxide and zinc oxide. T_{vp} is the temperature at which the metal has a vapor pressure of 10^{-3} Pa.

| Property | In_2O_3 | ZnO |
|--|-------------------------|--------------------------------------|
| Crystal structure, lattice parameters (nm) | cubic, a: 1.0117 | hexagonal, a: 0.32498; c: 0.52066 |
| Density (gcm^{-3}) | 7.12 | 5.67 |
| Band gap E_g (eV) | >2.7 | 3.37 |
| Melting point ($^{\circ}\text{C}$) | 1910 | 1975 |
| Melting point of the metal ($^{\circ}\text{C}$) | 157 | 420 |
| ΔH_f (eV) | 9.6 | 3.6 |
| T_{vp} ($^{\circ}\text{C}$) | 670 | 208 |
| Average amount of the metal in the earth' crust (ppm) | 0.1 | 40 |

4.2.2 Experimental details

The depositions were performed in the same load-lock sputtering system in which the ITO preparation has been performed (see chapter 4.1.2). Aluminum doped zinc oxide (AZO) thin films were deposited by RF magnetron sputtering from a ZnO/Al₂O₃ (98/2 wt.%) target at a total pressure of 0.3 Pa. The target-to-substrate distance is fixed at 6.1 cm. The magnetron plasma was excited by a 13.56 MHz RF generator RTX-600 combined with an ATX-600 matching network power supply by Advanced Energy at a constant power of 50 W. Borosilicate glass with dimensions of 10×10×1.1 cm³ was used as substrates, which was kept at room temperature or 300 °C by a boron nitride-encapsulated graphite heater during the deposition. According to section 4.1.3, we know that the sputtering atmosphere plays an important role in determining the microstructure and morphology evolution of ITO thin films. Therefore, AZO films were also prepared at room temperature (RT) in different atmospheres: pure Ar, a mixture of Ar/O₂ or Ar/H₂, while keeping the total sputtering pressure constant. With changing the additional gas from O₂ to H₂, the deposition rate was found to decrease. Moreover, the influence of substrate temperature on the microstructure and morphology evolution of AZO thin films was analyzed by depositing a thickness series onto preheated substrates of 300 °C in pure Ar. The electrical properties of 300°C- AZO films were also measured and compared to that of ITO films.

4.2.3 Growth of AZO films in different sputtering atmospheres

4.2.3.1 Growth of AZO films in pure Ar

Fig. 4.26(a) shows the XRD patterns of AZO films prepared at RT in pure Ar with various film thicknesses ranging from 6.5 nm to 420 nm. The XRD spectra only show peaks of the {0002} peak family of hexagonal wurtzite ZnO (JCPDS_36-1451). No secondary phase (e.g. Zn, Al, Al₂O₃, and ZnAl₂O₄) was detected, suggesting efficient incorporation of Al dopants on Zn sites or too small grains. When the film thickness is 6.5 nm, a weak and broad peak near 34.0° was observed, suggesting the film has poor crystallinity. The structure of the thicker AZO films was polycrystalline with preferred *c*-axis orientation perpendicular to the substrate surface, which is due to the fact that the lowest surface free energy of the most densely packed (0001) planes in wurtzite ZnO¹⁵⁶. With increasing film thickness, the peak position of the (0002) peak does not change significantly, however the peak becomes sharper, indicating an improved *c*-axis orientation of the AZO films. The full width at half maximum (FWHM) of the (0002) peak, the crystallite size, the *c*-axis lattice constant and the mechanical stress of AZO films are

displayed in Fig. 4.26(b). With increasing film thickness from 6.5 nm to 105 nm, the FWHM decreases from 1.53° to 0.26° and the grain size increases from 5.4 nm to 33.1 nm. By further increasing the film thickness to 420 nm, a tendency for a thickness independent with grain size was observed, changing slightly from 33 nm to 35 nm. The crystallite sizes obtained here are of the same order of magnitude as reported by other authors¹⁵⁷⁻¹⁵⁹. The c -axis lattice constant shows the same tendency as the crystallite size. The lattice constant is 0.5249 ± 0.0005 nm and 0.5267 ± 0.0005 nm for 6.5 nm and 420 nm-thick films, respectively which corresponds to a relative change of 0.4%. All lattice constant are larger than that in pure ZnO (JCPDS_36-1451) suggesting a strong compressive stress. On the basis of the biaxial strain model¹⁶⁰, the film stress σ_{film} can be calculated from the following formula, which is valid for a hexagonal lattice:

$$\sigma_{\text{film}}^{\text{XRD}} = \frac{2c_{13}^2 - c_{33}(c_{11} + c_{12})}{2c_{13}} \times \frac{c_{\text{film}} - c_{\text{bulk}}}{c_{\text{bulk}}} \quad (4.3)$$

where c_{bulk} is the unstrained lattice parameter for ZnO powder (0.52066 nm, JCPDS_36-1451). For the elastic constant c_{ij} , data of single crystalline ZnO have been used: $c_{11} = 208.8$ GPa, $c_{33} = 213.8$ GPa, $c_{12} = 119.7$ GPa, $c_{13} = 104.2$ GPa.¹⁶¹ The calculated film stress is displayed in Fig. 4.26(b). The result shows AZO films were in a state of compressive stress and the stress increases with increasing film thickness, and then only slightly decrease.

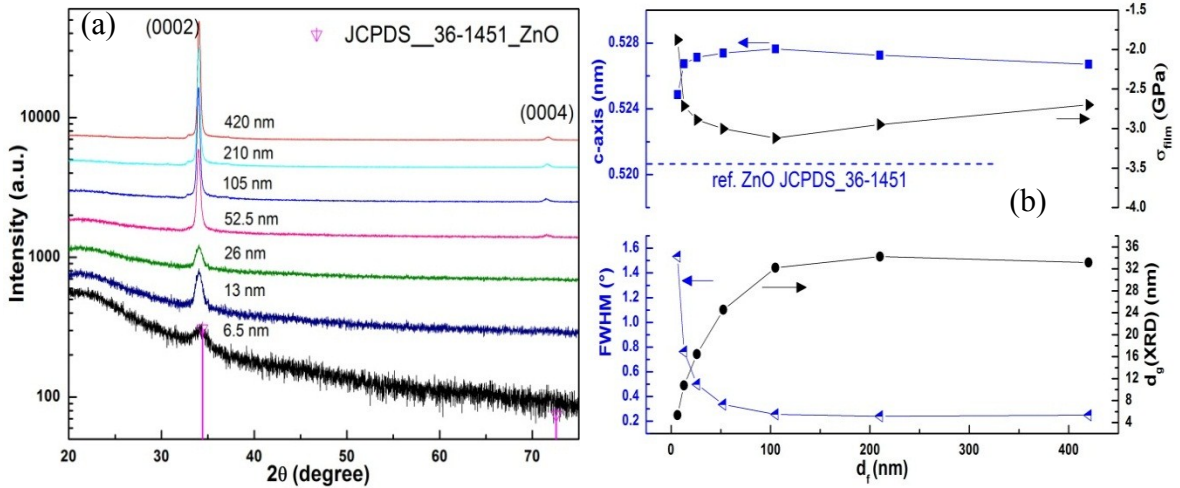


Fig. 4.26: (a) XRD patterns for AZO films prepared in pure Ar at room temperature, and (b) the FWHM, crystallite size, c -axis lattice constant and stress derived from the (0002) peak parameter as a function of film thicknesses.

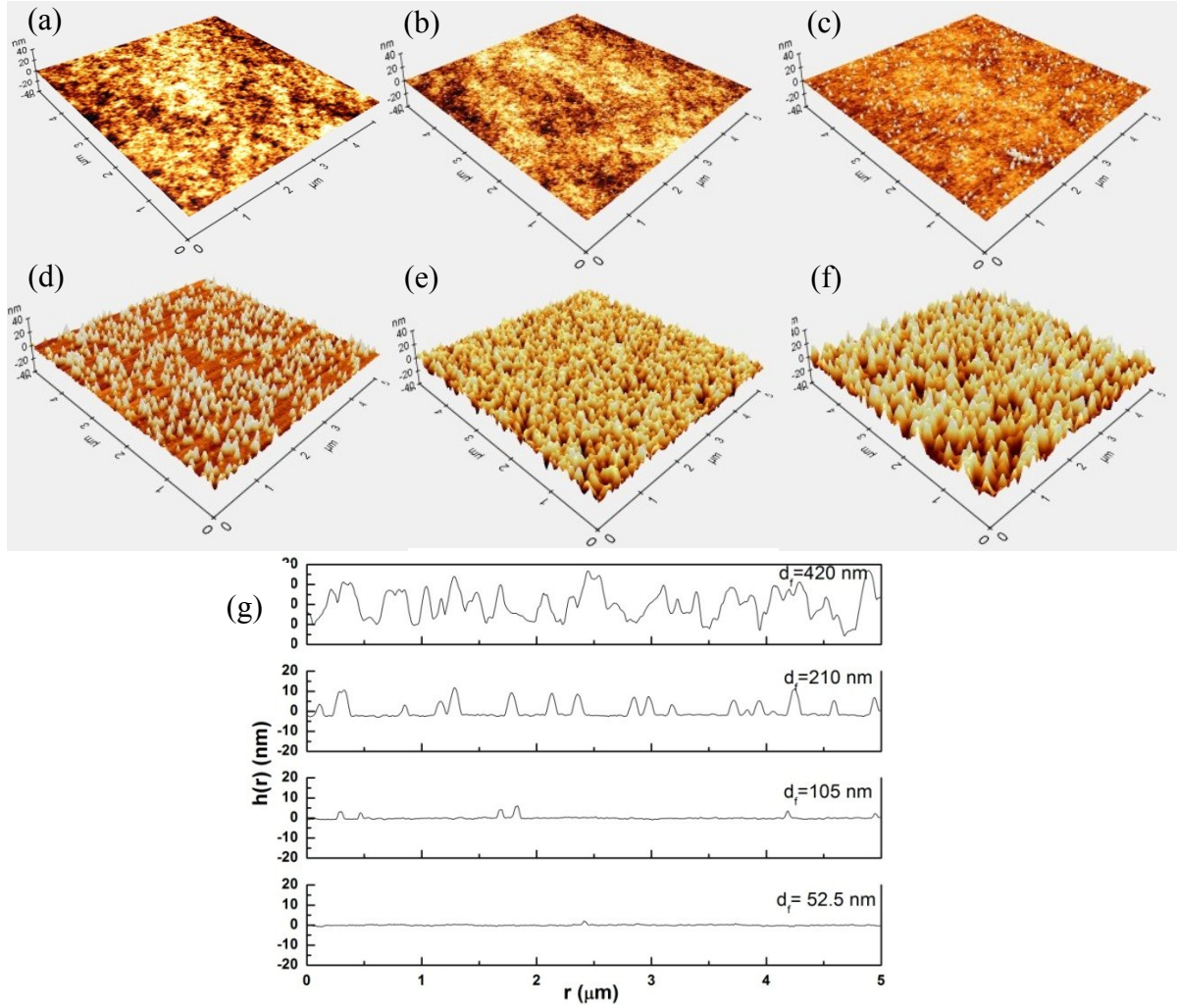


Fig. 4.27: 3D-AFM measurements of AZO films prepared in pure Ar at room temperature with nominal thicknesses (a) 6.5 nm, (b) 52.5 nm, (c) 105 nm, (d) 210 nm, (e) 315 nm and (f) 420 nm. (g) Height profiles $h(r)$ at middle position for the different AZO films.

The film composition was measured by Rutherford backscattering spectrometry (RBS) method. The portions of Zn, Al and O are 44.4 at.%, 2.2 at.% and 53.4 at.%. The Al dopant content in the film is close to the Al content in the target. 3D-AFM images with a scan size of $5 \times 5 \mu\text{m}^2$ of AZO films are shown in Fig. 4.27. Different morphologies can be observed for the different film thicknesses. Height profiles $h(r)$ at the middle position along x -axis of different thickness films are displayed in Fig. 4.27(g). From the height profiles, two length scales can be seen: the first one formed by small aggregates of grains and the second one defined by the height fluctuation of the different grains. When comparing different height profiles in Fig. 4.27(g), it is possible to see the initial stages of development of the surface morphology. When film thickness is less than 52.5 nm, very smooth surface with a subnanoscale corrugation appears. When the film thickness is above 105 nm, hillock-like particles grow along the $\langle 0001 \rangle$ direction on the first smooth layer. The hillock structures

have been reported for ZnO or doped ZnO by magnetron sputtering¹⁶², PLD¹⁶³, MOCVD¹⁶⁴ and vapor phase transport process¹⁶⁵. With increasing film thickness, these hillocks grow bigger and denser due to the increased compressive stress and form a continuous film covering the first smooth layer. The evolution of double layer can be clearly observed when the film thickness is over 52.5 nm. The rough 3D-columnar structure grows both on lateral and perpendicular directions. Hayamizu et al.¹⁶⁶ investigated the mechanism of the growth of ZnO films on glass substrates by pulsed laser deposition and found two stages of the growth process of ZnO films. They suggested an amorphous layer around 5 nm formed at the first stage of deposition which plays an important role in the *c*-axis orientation of the ZnO film deposited on top of it. Subsequently, first a polycrystalline layer (5~10 nm) followed by a *c*-axis oriented layer (>10 nm) begins to grow on the amorphous ZnO layer. Obviously, according to previous XRD analysis, there is a transition from nanocrystalline to *c*-axis oriented polycrystalline structure which is related to the evolution of smooth to rough layer.

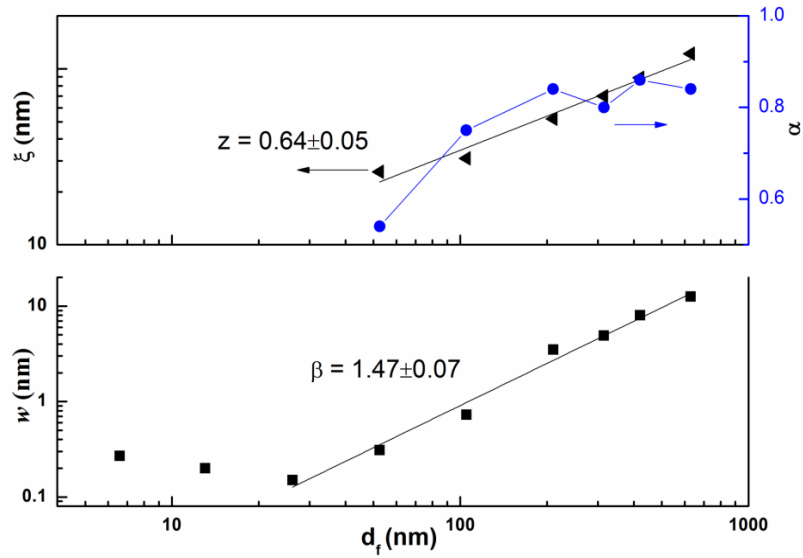


Fig. 4.28: Surface roughness w , correlation length ξ and roughness exponent α of AZO films prepared in Ar at room temperature as a function of the film thickness.

By using the height-height correlation function $H(r,t)$, the root-mean square surface roughness w , the lateral correlation length ξ , and the roughness exponent α can also be calculated. The surface roughness w as a function of the film thickness d_f in a log-log scale is plotted in Fig. 4.28. The variation of the surface roughness can be divided into two regions. The evolution of roughness can be described as $w \sim d_f^\beta$ with the growth exponent $\beta > 0$ in the dynamic scaling theory.^{2,3} However, as shown in Fig. 4.28(below), the roughness is slightly decreasing from 0.26 nm to 0.16 nm with increasing film thickness

from 6.5 nm to 26 nm in the early growth stage. A negative growth exponent β can be obtained which is an anomalous value. The development of the flat surface is caused by the surface diffusion of the initial ZnO nuclei. A crossover to $\beta > 0$ follows in the later growth stage. The roughness increases monotonically from 0.31 nm to 12.6 nm when the film thickness increases from 52.5 nm to 630 nm with a growth exponent $\beta = 1.47 \pm 0.07$. Such a large growth exponent does not fit to any growth model described in Ref. 2 and 3, in which the largest dynamical scaling exponent β of 1 can only be simulated for a pure shadowing effect^{60,61}. Therefore, it can be expected that the shadowing plays an important role during our sputtering process, and there should exist another roughening mechanism to generate $\beta > 1$. The intrinsic material properties such as polarity, surface free energy should play an important role. In this thickness range the correlation length ξ increases from 26 nm to 120 nm and can be fitted by a power law $\xi \sim d_f^{0.64}$. The lateral correlation length is close to the vertical crystallite size estimated from XRD when the film is thinner than 105 nm, but a factor of 2 to 4 larger when the film is over 105 nm thick. The roughness exponent α increases from 0.54 to 0.75 with increasing the film thickness from 52.5 nm to 105 nm. For even larger thicknesses the exponent stays constant at a value of about 0.84 with further deposition. Zhu et al.³⁶ reported similar result during ion-beam-assisted growth of amorphous diamondlike carbon films. They attributed the film growth involving substrate surface process to the ion bombardment during the deposition. This means that the substrate surfaces have an important influence on the film roughening in the initial growth stage. In our deposition process, the negative ion bombardment also should have a very strong effect on the film growth. Vasco et al.¹⁶³ observed that the roughness evolution of ZnO films deposited on InP(100) substrates at 350°C by PLD is characterized by two different growth regimes: the first regime is dominated by shadowing effects owing to the angular spreading of the incident material flux under high-pressure deposition condition which results in β values of 1. The second regime is characterized by smaller β value of 0.6 due to the competition between the step-edge barrier effect induced by the development of a pyramidal structure surface and the shadowing effect. Hur et al.¹⁶⁷ studied the evolution of surface roughness and strain relaxation versus the film thickness of ZnO films grown on sapphire (0001) at 550 °C by RF magnetron sputtering deposition with a deposition rate 0.6 nm/min. They found three regimes of the film growth: 2D planar layer-by-layer growth for the highly-strained first growth stage with $\beta_1 = 0.12$ when the film thickness is less than 9.2 nm, the lattice strain is 0.1% for the 9.2 nm-thick film. In the second growth stage 3D island growth occur due to strain relaxation characterized by $\beta_2 = 1.579$ ($9.2 \text{ nm} < d_f < 34$

nm). Continuing the growth to reach the strain relaxed steady-state regime leads to $\beta_3=0.234$. In the present work, the deposition rate is more than 20 times higher compared to the value reported by Hur et al.¹⁶⁷. The compressive stress in our film takes longer time to relax. The microstrain of 420 nm-thick AZO film prepared at room temperature is 1.16%, which is still very high indicating the fully strain relaxation might take place only for even thicker film. Therefore, the shadowing effect and increased crystallinity plus the high compressive stress lead to the highly abnormal growth behavior in our case.

4.2.3.2 Growth of AZO films in Ar/1%O₂

AZO films with different thicknesses were deposited in an Ar/1%O₂ atmosphere at room temperature. X-ray diffraction analysis revealed that all films exhibit the typical hexagonal wurtzite ZnO phase only showing {0002} family peaks, i.e. *c*-axis preferred orientation. Though, the borosilicate glass is amorphous, the AZO films present strong *c*-axis-oriented. This means these AZO films develop to a self-textured structure due to minimization of the surface energy¹⁶⁸. With increasing film thickness from 31 nm to 250 nm, as shown in Fig. 4.29, the lattice constants decrease from 0.5265 nm to 0.5260 nm, but they still all larger than 0.52066 nm, the value of the unstrained ZnO (JCPDS_36-1451), suggesting that the film contains compressive stress. The compressive stress varies in the same way as the lattice constant and it is smaller than that in pure Ar deposition. The FWHM decreases and the crystallite size derived from XRD increases from 19 nm to 35 nm.

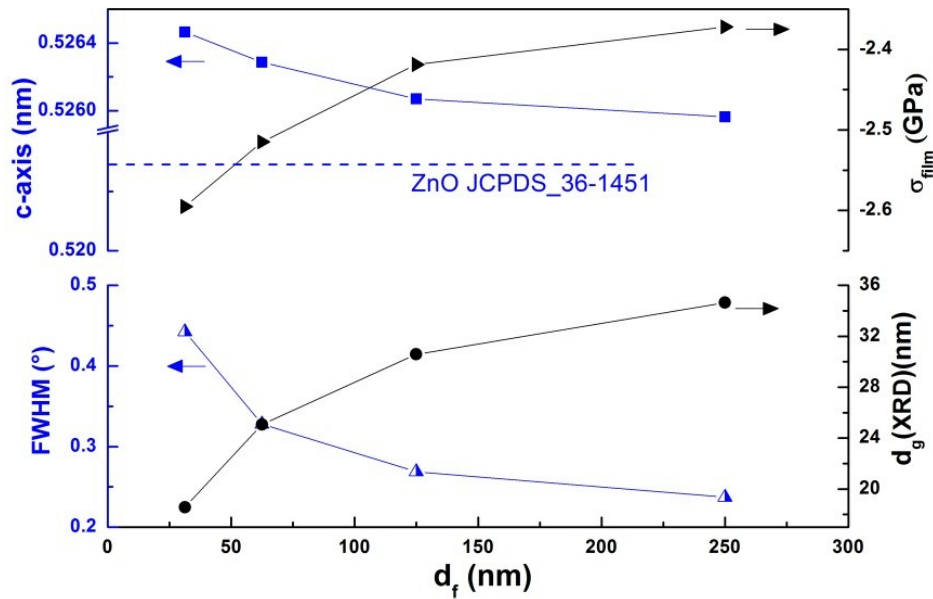


Fig. 4.29: The FWHM, lattice constant *c*, and grain size of AZO films prepared in Ar/1%O₂ atmosphere at room temperature as a function of film thickness.

Fig. 4.30 displays the surface morphology of these AZO films measured by AFM. The morphology of the AZO films prepared in Ar/1%O₂ atmosphere is very similar to that prepared in pure Ar, shown in Fig. 4.27. It can also be seen that a first smooth layer grows and later rough 3D-islands develop. These hillock mounds become larger in both lateral and vertical direction. The evolution of the hillock structure can be more clearly observed from the height profiles of these films in Fig. 4.31(inset).

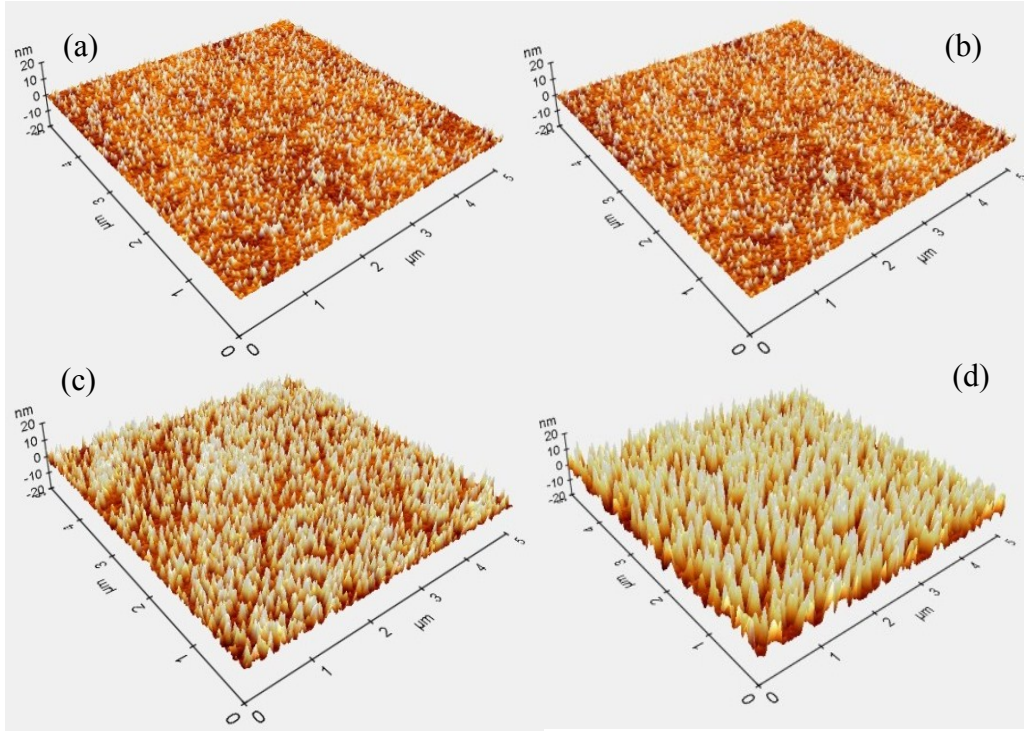


Fig. 4.30: 3D-AFM measurements for AZO films prepared in Ar/1%O₂ atmosphere at room temperature with various nominal thickness (a) 31 nm, (b) 62.5 nm, (c) 125 nm and (d) 250 nm.

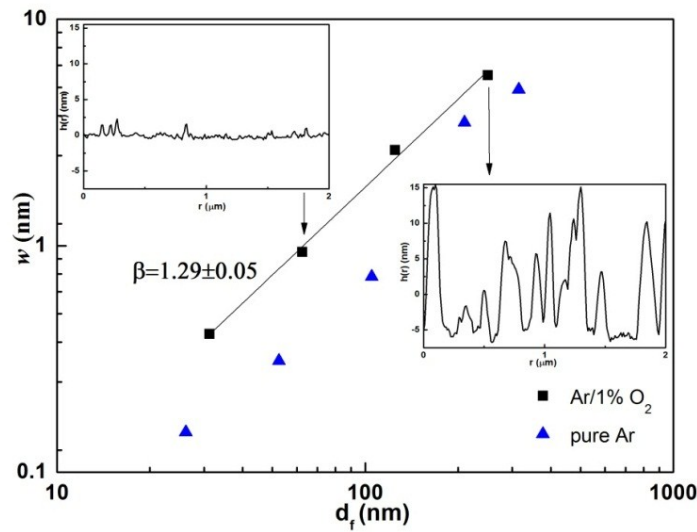


Fig. 4.31: Surface roughness w of AZO films prepared in Ar/1%O₂ (black ■) and pure Ar (blue ▲) atmosphere as a function of the film thickness. The inset shows the height profiles for 62.5 nm and 250 nm-thick films respectively.

From Fig. 4.31, it can be seen that with increasing film thickness from 31 nm to 250 nm, the roughness increases from 0.4 nm to 5.7 nm, which is bigger than that in pure Ar deposition when comparing the roughness of similar thickness film. The fitting growth exponent $\beta=1.29\pm0.05$ which is slightly smaller than $\beta=1.47\pm0.07$ in pure Ar deposition at room temperature. Kajikawa¹⁶⁸ investigated comprehensively the texture development of polycrystalline ZnO films and pointed out that the preferred orientation growth of ZnO is affected by preferential nucleation, preferential crystallization, sticking process, surface diffusion and grain growth. In the initial nucleation stage, random orientation nuclei are formed on the non-epitaxial substrates. At the same time, there exists another process where preferential nuclei form with a specific crystallographic direction normal to the substrate when the preferred orientation is the lowest surface energy plane parallel to the substrate. With initial preferential nuclei growth, the film develops an equiaxed columnar structure. Obviously, our AZO films show a non-equiaxed columnar structure. It means even though the initial nuclei have random orientation on the glass substrate, the *c*-axis strong orientation has a fast development in the growth stage which dominates the film morphology. Here it involves the 3D hillock structure. Kajikawa¹⁶⁸ also pointed out that the surface diffusion along grains would restrain the surface with higher energy and assist lower energy surface growth which will reduce the surface texture character and smoothen the surface. In the present work, by O₂ addition to the sputtering atmosphere, more Zn-Al-O nucleation sites are formed and the sticking probability of Zn-Al-O species increases causing increasing *c*-axis preferred orientation¹⁶⁹ and then roughens the surface. And surface diffusion among grains, i.e. mobility of Zn and Al atoms which smooth the surface is reduced which are probably the reasons the roughness is higher than in pure Ar deposition. Note that the roughness is mostly contributed by these 3D hillocks which are the result of *c*-axis orientation growth and high compressive stress parallel to the film surface, that increases the shadowing and generate the abnormal growth exponent.

4.2.3.3 Growth of AZO films in Ar/H₂ atmosphere

Van de Walle¹⁷⁰ presented a theoretical investigation on the formation of a shallow donor level in ZnO by hydrogen, which was confirmed experimentally by different groups¹⁷¹⁻¹⁷³. Therefore, adding hydrogen to the magnetron sputtering process or post annealing in hydrogen atmosphere can be used to improve the conductivity of aluminum or gallium doped ZnO films.¹⁷⁴⁻¹⁷⁶ With increasing hydrogen content, the resistivity of doped/undoped ZnO films decreases due to an increase of the electron concentration and Hall mobility but the crystallinity deteriorates. In this work, we also prepared Al-doped ZnO film in hydrogen containing atmosphere during the sputtering process and investigate the dynamic scaling behavior.

AZO films with various thicknesses were deposited at room temperature in different Ar/H₂ atmospheres with H₂ contents of 5% and 10%. The deposition rate was 8.3 nm/min and 7.8 nm/min for Ar/5% H₂ and 10% H₂ atmosphere deposition, respectively, lower than that in pure Ar deposition (~14 nm/min). According to the XRD patterns, shown in Fig. 4.32 for 45 min-depositions in both atmospheres, it can be clearly seen that the hydrogen strongly deteriorates the film crystallinity when comparing with pure Ar and Ar/O₂ deposition in the previous two sections. Only a very broad and weak peak can be observed for Ar/5%H₂ deposition indicating the film presents almost X-ray amorphous or nanocrystallite structure.

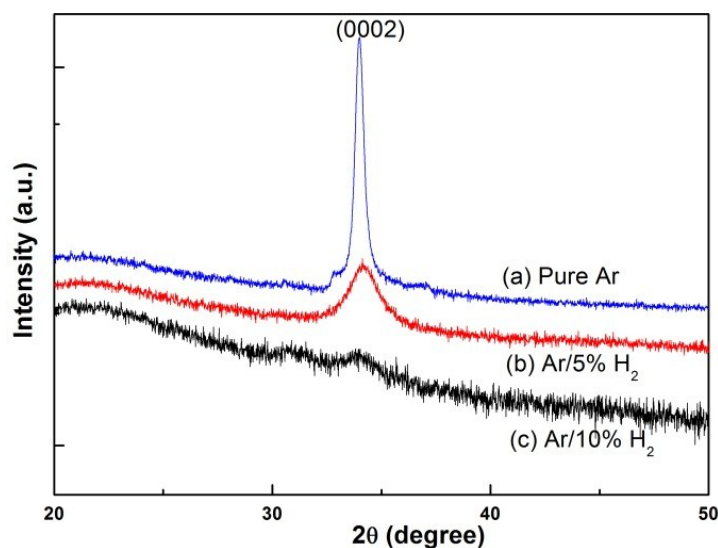


Fig. 4.32: XRD patterns of AZO films prepared in (a) pure Ar for $t=15$ min, (b) Ar/5% H₂ and (c) Ar/10%H₂ for $t=45$ min at room temperature. The respective film thicknesses are 210 nm, 351 nm and 370 nm.

4.2 Nucleation and growth of Al-doped zinc oxide films

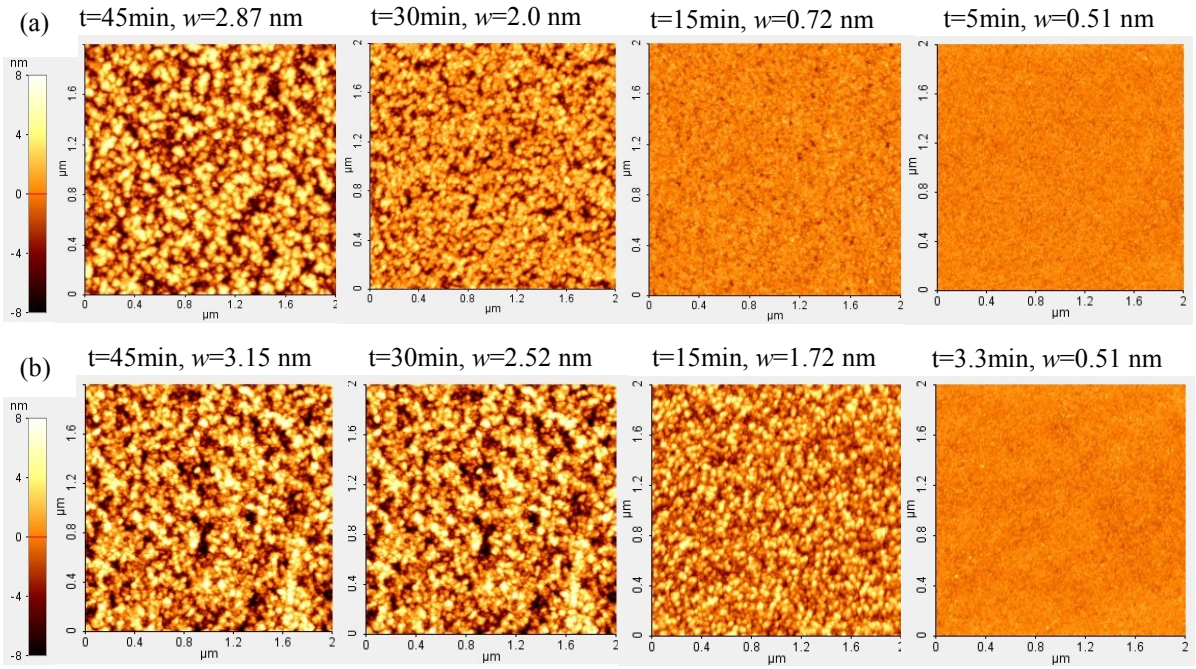


Fig. 4.33: Evolution of the surface microstructure for AZO films prepared at room temperature with various nominal thicknesses in (a) Ar/5% H_2 and (b) Ar/10% H_2 .

The evolution of the surface morphology of AZO films characterized by AFM is illustrated in Fig. 4.33 (a) Ar/5% H_2 and (b) 10% H_2 atmosphere respectively. All the images have lateral scan sizes of $2 \times 2 \mu m^2$ and the same height scale displayed on the left side of the graphs. It can be seen that all the films exhibit similar surface topographies consisting of globular grains that become larger as the film thickness, i.e. deposition time, increases. The morphology evolution of these films is different from that of the films sputtered in pure Ar and Ar/ O_2 atmospheres, which show a layer plus island growth type. By quantitative analysis of the growth interface, the statistical characteristics such as surface roughness w , roughness exponent α and correlation length ξ are checked from height-height correlation functions. Fig. 4.34 shows the height-height correlation functions in the log-log scale for two thickness series deposited in (a) Ar/5% H_2 and (b) 10% H_2 atmosphere. The general behavior of $H(r)$ for different hydrogen contents is very similar. It increases linearly as a function of the lateral position in the short range and then reaches to a plateau for longer distance. Obviously, $H(r)$ of 15 min-sample jump to higher in 10% H_2 deposition than low hydrogen deposition indicating a rougher surface. The roughness exponent α can be extracted by linear fitting of $H(r)$ in the short-range part, displayed in Fig. 4.35(a). With increasing film thicknesses, α increases for the depositions with 5% H_2 but shows a saturation trend for large film thicknesses for the high hydrogen content deposition which is in the range of 0.65~0.84, indicating the growth of AZO films in

hydrogen is non-stationary. The correlation length ξ for Ar/10%H₂ deposition is slightly larger than lower hydrogen deposition and increases with film thickness as $\xi \sim d_f^{0.44 \pm 0.04}$.

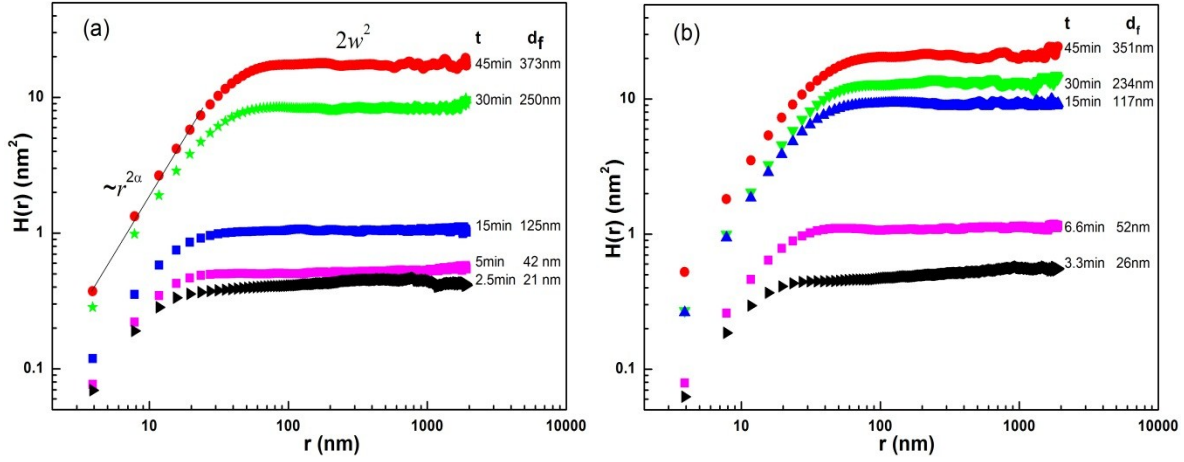


Fig. 4.34: The height-height correlation function of AZO films prepared at room temperature in different atmospheres: (a) Ar/5% H₂ and (b) Ar/10% H₂.

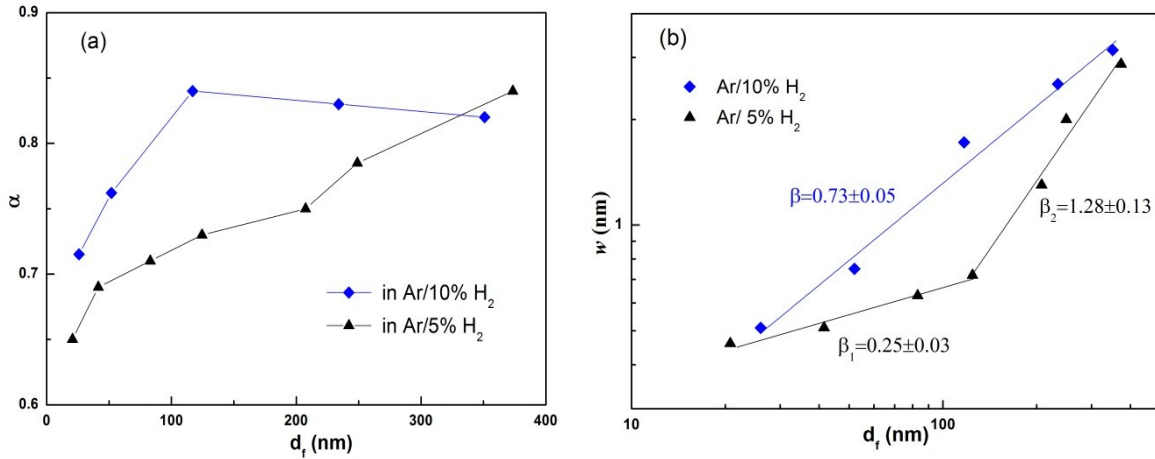


Fig. 4.35: (a) Roughness exponent α obtained from the height-height correlation functions and (b) surface roughness w of AZO films prepared in different atmospheres as a function of the film thickness.

The variation of the surface roughness with the film thickness for AZO films prepared in Ar/5%H₂ and 10%H₂ atmospheres is plotted in Fig. 4.35(b). The surface roughness for the low hydrogen content is smaller than for the higher hydrogen content, but both are more than two times smaller in comparison to the depositions without hydrogen. Two regions with different values of the growth exponent β can be distinguished for the films deposited in Ar/5% H₂ atmosphere. At low film thicknesses, i.e. deposition times, the increase of roughness is slow with small β of 0.25 ± 0.03 . Then a transient regime appears. With further increasing film thickness, the value of the growth exponent changes to 1.28 ± 0.13 . However, no transient regime can be observed for Ar/10% H₂ deposition films. In the whole thickness range from 26 nm to 351 nm, the surface roughness increases from 0.51

nm to 3.15 nm with a growth exponent β of 0.73 ± 0.05 . The competition between shadowing effects and surface diffusion dominates the film morphology. The incorporation of hydrogen in the film mostly influences the dynamics behavior of the grain growth, i.e. diffusion of material along the grains. By successive introduction of hydrogen during the sputtering process, H plasma can remove the O atoms and then the surface mobility of Zn atom increases. Therefore strong surface diffusion induces a small growth exponent for the Ar/5% H₂ deposition. When more material is deposited on the substrate surface, the increased nanocrystallinity and continuously depleting small grains growing at the grain boundaries by H plasma deepen the valley and help to roughen surface. With increasing hydrogen content till 10% during the deposition, the crystal growth roughening effect can be ignored due to the amorphous structure. The increased roughness is probably due to the decreased nuclei size in the initial growth stage by the lack of O atoms, and continuous H plasma depleting the increased grain boundaries at the later growth stage.

4.2.4 Temperature effect of the growth of AZO films

In order to study the effect of the substrate temperature on the AZO film growth, the structure and the morphology of AZO films prepared in pure Ar at a substrate temperature of 300 °C were investigated. XRD patterns of AZO films with various thicknesses are shown in Fig. 4.36(a). When the film grows to 33 nm-thick, a broad (0002) peak around 34.35° can be observed. The FWHM is 0.8° and the crystallite size is 10 nm. With increasing film thickness from 55 nm to 515 nm, the FWHM decreases from 0.33° to 0.18° and crystallite size of (0002) peak increases from 25 nm to 47 nm, as displayed in Fig. 4.36(b). The lattice constant changes from 0.5220 nm to 0.5204 nm (relative change 0.3%) with increasing film thickness. The stress nearly relaxes for high temperature deposition.

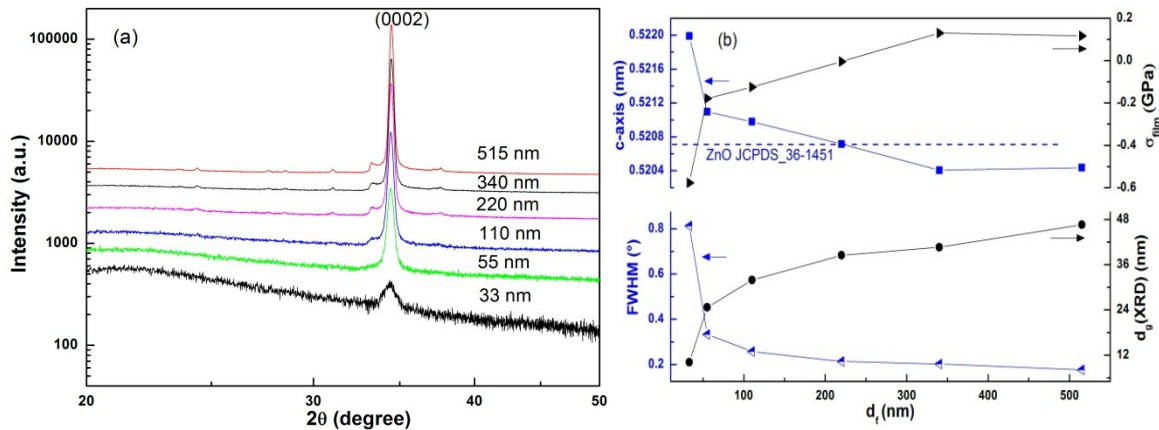


Fig. 4.36:(a) XRD patterns of AZO films prepared in pure Ar at 300 °C, and (b) the FWHM, lattice constant, stress and grain size derived from the (0002) peak as a function of the film thickness.

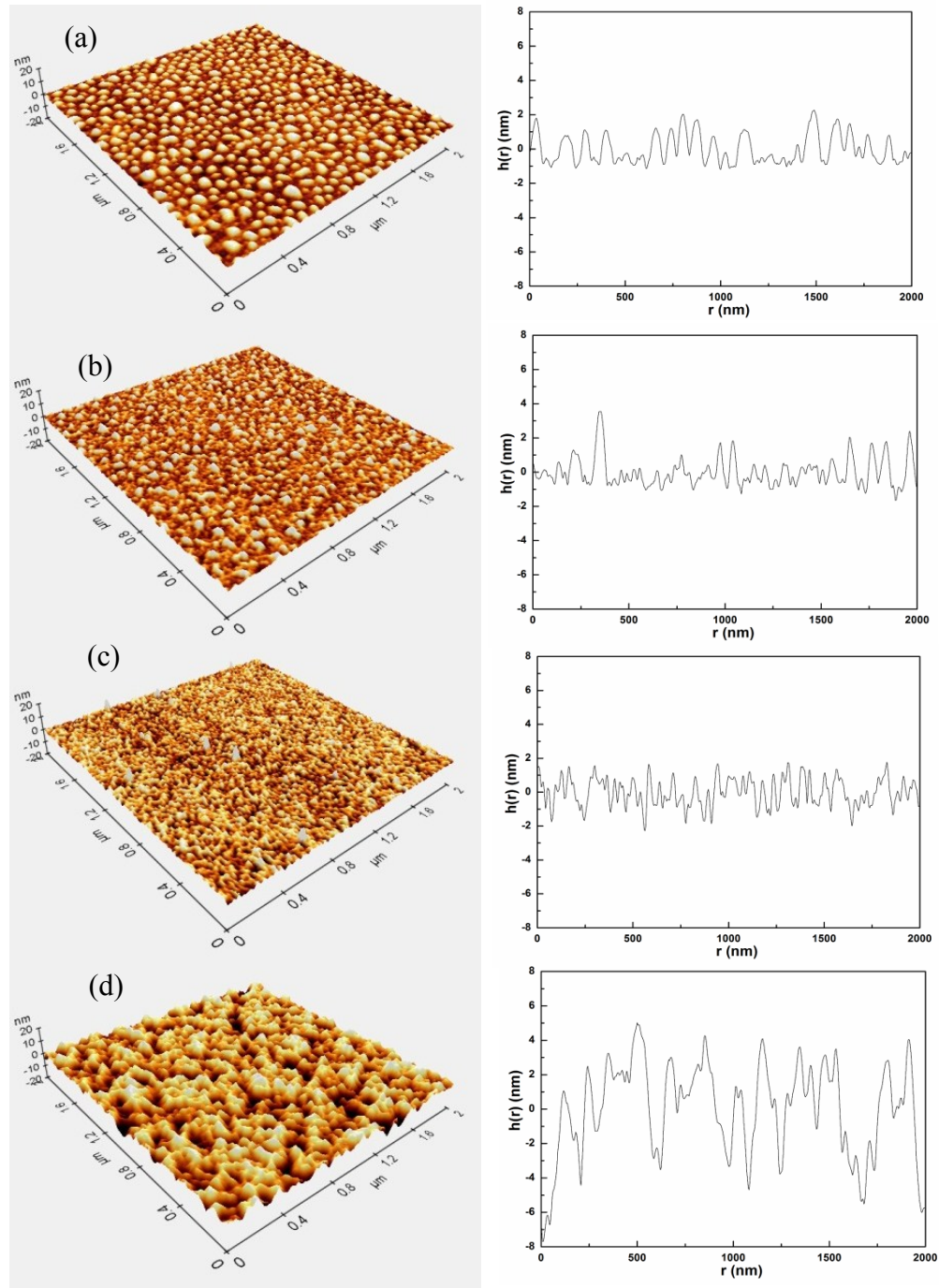


Fig. 4.37: 3D-AFM images and corresponding height profiles $h(r)$ for AZO films prepared in pure Ar at 300 °C with various nominal thicknesses (a) 6 nm, (b) 11 nm, (c) 33 nm, and (d) 515 nm.

The surface morphology of the 300 °C AZO films was also characterized by AFM. Some typical 3D-AFM images and the corresponding height profiles $h(r)$ are shown at Fig. 4.37. When the film thickness is 6 nm, mounded grain features with the size varying from 10 nm to 80 nm are dispersive distributed on the substrate surface, suggesting a typical 3D-island growth. According to transmission electron microscopy and atom probe tomography results on AZO films prepared in the same sputtering system and same target from André

Bikowski¹⁷⁶, an enrichment of the aluminum layer i.e. Al_2O_3 or ZnAl_2O_4 is prone to form in the interface region to the substrate, especially at high temperature since Zn atoms re-evaporate from the substrate. By X-ray photoelectron spectroscopy measurement (kindly performed by Xin Song, not shown here) and RBS analysis, the atomic ratio of Al/Zn in 6-nm thick film is 0.18, four times higher than the value of 0.045 in thicker bulk films, which also confirms the Al enrichment layer, very likely composed of these 3D mounds in Fig. 4.37 (a). When less Zn atoms are incorporated in the initial nuclei, it is also hard for crystallization hence the (0002) peak does not show up. 11 nm-thick AZO film shows similar behavior as the 6 nm-thick film, but the distribution of the grain size slightly becomes smaller as indicated from Fig. 4.37(b). With depositing more material on the surface, the mounds continuously coarsen and the lateral grain size decreases first and then increases when the film becomes continuous. Then the preferred c -axis orientation growth can be observed.

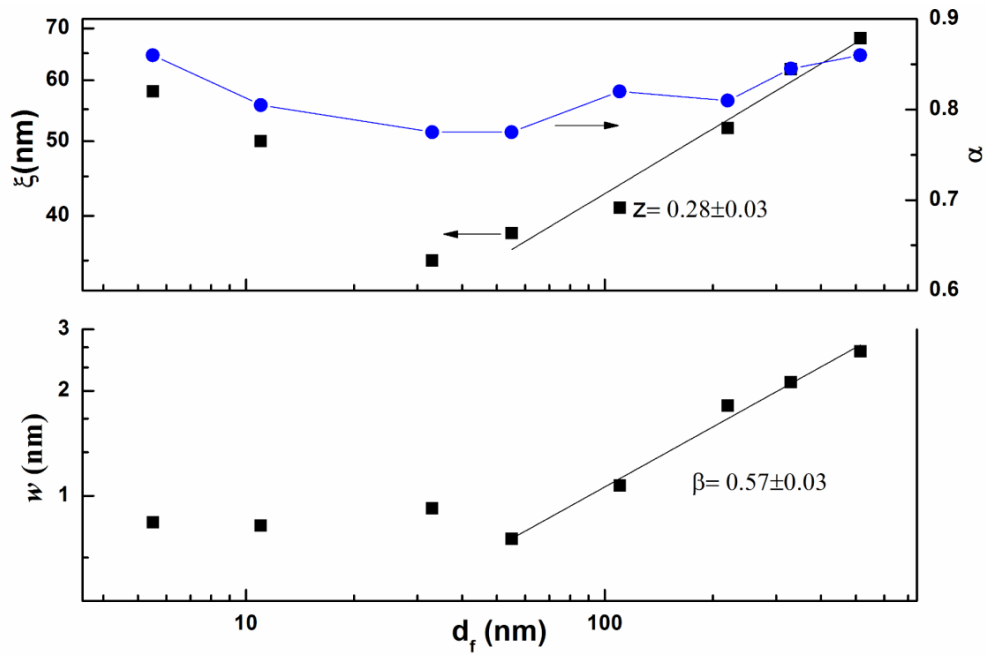


Fig. 4.38: Surface roughness w , correlation length ξ and roughness exponent α of AZO films prepared in Ar at 300 °C as a function of the film thickness.

The surface roughness w of AZO films prepared at 300 °C is plotted at Fig. 4.38(below) in a log-log scale as a function of film thickness d_f . The roughness evolution can be also divided into two regions. In the first initial stage, with increasing film thickness from 6 nm to 33 nm the roughness shows no apparent increases from 0.84 nm to 0.92 nm, much higher than roughness (0.21 nm) of pure substrate, i.e., with a growth exponent nearly to zero. By looking at the roughness exponents obtained from height-height correlation functions,

shown in Fig. 4.38(above), it appears that it does not remain constant for different film thickness, i.e. deposition time as it is predicted by the conventional dynamic scaling theory²⁴ while the values are very close to these of RT deposition. The correlation length, displayed in Fig. 4.38 (above) decreases from 58 nm to 35 nm. For larger film thicknesses when the film grows continuously, there is a roughness evolution transition. The roughness increases from 0.75 nm to 2.59 nm with increasing film thickness from 55 nm to 515 nm in the second growth stage with a much higher growth exponent β of 0.57 ± 0.03 . And the correlation length also increases with a power law $\xi \sim d_f^{0.28 \pm 0.03}$. The roughness exponents α also show first a decrease and then increase tendency in the whole thickness range. Comparing the roughness behavior for 300°C and RT deposition films, the roughness is larger in the initial growth stage but much smaller in the later growth stage which due to the different growth mechanism, i.e. first smooth 2D growth then transforming to 3D growth for RT deposition, but typical 3D growth for 300°C deposition which account for the high adatom mobility and a faster strain relaxation.

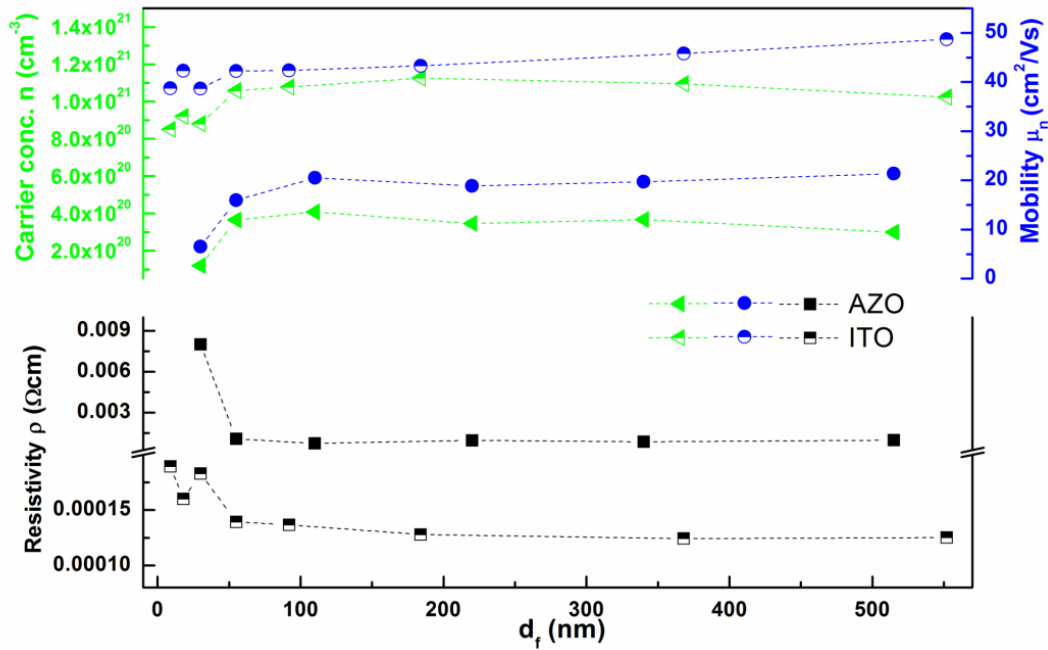


Fig. 4.39: Electrical resistivity ρ , free carrier concentration n and Hall mobility μ_n of AZO films and ITO films prepared at 300 °C as a function of film thickness.

The electrical properties, i.e., the resistivity ρ , free carrier concentration n and Hall mobility μ_n of AZO films prepared in pure Ar at 300 °C as a function of film thickness d_f for $d_f \geq 33$ nm are displayed in Fig. 4.39. For thinner AZO films (6 nm and 11 nm), the electrical resistivity is too high to be measured, caused by the discontinuous surface. It reveals that the resistivity is $8.0 \cdot 10^{-3} \Omega\text{cm}$ and $1.0 \cdot 10^{-3} \Omega\text{cm}$ measured for 33 nm and 55 nm-thick films, respectively. The resistivity decreases significantly by one order of

magnitude with increasing film thickness from 33 nm to 55 nm. Further increasing the film thickness, the resistivity of the AZO films decreases very slightly compared to the earlier drop, down in the range of $7.5 \cdot 10^{-4} \Omega\text{cm}$. The evolution of the resistivity for AZO films is attributed to the inverse trend of carrier concentration n and Hall mobility μ , shown in Fig. 4.39. With increasing thickness from 33 nm to 55 nm, n and μ increase by a factor of 3.5 and 2, respectively, and then a weaker variation is observed for thicker films. Similarly, the dependence of the electrical properties on roughness exponent is not evident in the present experiment. For comparison, the electrical properties of ITO films prepared at 300°C (section 4.1.4.2: 13.56 MHz RF deposition) are plotted in Fig. 4.39 too. Similar but slowly drop-down transition behavior of resistivity can be observed with increasing film thickness. Interestingly, the resistivity of an ITO film only 9 nm-thick is $1.9 \cdot 10^{-4} \Omega\text{cm}$, already four times lower than that of the best performance AZO film prepared here, attributed to higher carrier concentration and mobility. Therefore, low resistivity of very thin ITO film indicates the high density of nuclei. With increasing ITO film thickness to 550 nm, ρ is only improved by a factor of two.

The transition region for the resistivity of the AZO films is in correspondence with the roughness evolution (Fig. 4.38). When the film thickness is less than 55 nm, after the islands grow and coalesce to form a continuous film, the continuous conduction paths build up and the resistivity decreases whereas the roughness varies slightly with increasing film thickness, and then after the transition region (33nm~55nm), the roughness increases with a growth exponent β of 0.57 but resistivity only slightly decreases, suggesting an independence of the resistivity on the film thickness and the surface roughness in the later growth stage. In terms of the relation between roughness evolution and electrical properties of ITO films, the roughness of ITO films first increases with a growth exponent β of 0.89 ($d_f \leq 50$ nm) and then increases slowly with a smaller β of 0.22. The transition of roughness around 50 nm is also linked to reaching the steady state region of resistivity evolution. Note that when $d_f \leq 50$ nm, the roughness of AZO film is higher than that of the ITO films. Only after the transition stage, the roughness of ITO film becomes larger due to the higher growth rate normal to the substrate. Zhang et al.¹²⁹ performed a thickness variation for In_2O_3 epitaxial films on Y-stabilized ZrO_2 substrates and observed that the change in morphology from thin film to thick film is accompanied by a progressive relax atom of the tensile strain and an increase in the carrier mobility. The drop-down transition in resistivity (or jump-up of mobility) of AZO and ITO films can be also assigned to the release of stress with increasing film thickness.

4.2.5 Conclusions

The evolution of the microstructure and the morphology of aluminum-doped zinc oxide (AZO) films deposited by RF magnetron sputtering in different atmospheres: pure Ar, Ar/O₂ and Ar/H₂ at room temperature, was investigated as a function of the film thickness by XRD and AFM. From the XRD results, c-axis orientation of hexagonal wurtzite AZO was observed for pure Ar and Ar/O₂ deposition. This growth can be described by the Stranski-Krastanov model, i.e. layer growth plus island growth. Additional hydrogen in the sputtering atmosphere deteriorates the crystallinity of the films and makes it even X-ray amorphous. This growth regime can be described by the Volmer-Weber model, i.e. island growth was observed. The dynamic scaling behavior of the AZO film growth in different deposition process is listed in Table 4.5. The roughness exponents do not vary significantly when changing the sputtering atmosphere and are independent on the film thickness. The abnormal growth exponents $\beta > 1$ are observed in pure Ar and Ar/1%O₂ depositions at room temperature which may be most likely ascribed to the presence of shadowing effects and the compressive stress parallel to the substrate induced preferred c-axis grain growth. The reduced growth exponent for hydrogen deposition at room temperature and pure Ar deposition at high temperature is dominated by shadowing effect and relaxation of stress. The electrical properties of AZO and ITO were also measured. The performance of very thin ITO film (~9 nm) is already much better than thick AZO films due to the much higher density of ITO nuclei. The resistivity of AZO and ITO films decreases and reaches a steady-stage after a transition region (~50 nm). For AZO films, the electrical performance can be correlated with the evolution of the surface morphology, i.e. 3D islands aggregate and then form continuous films to form the conduction paths, but is not suitable for the evolution of ITO film due to the high density of nuclei.

Table 4.5: Growth exponent β and roughness exponent α for AZO films prepared in different sputtering atmospheres and different temperatures.

| T_s | 300 °C | RT | RT | RT | |
|----------------------------|-----------|-----------|----------------------|----------------------|-----------------------|
| Atmosphere | pure Ar | pure Ar | Ar/1% O ₂ | Ar/5% H ₂ | Ar/10% H ₂ |
| α | 0.78~0.86 | 0.54~0.75 | 0.56~0.76 | 0.65~0.84 | 0.71~0.82 |
| β | 0.57 | 1.47 | 1.29 | 0.25, 1.28 | 0.73 |

5 One-stage deposition of Cu(In,Ga)S₂ films by dc reactive magnetron sputtering

The chalcopyrite semiconductors Cu(In, Ga)S(e)₂ have attracted great scientific and technical interest owing to their exceptional optoelectronic properties for photovoltaic applications. Cu(In,Ga)S(e)₂ belong to the I-III-VI₂ semiconductor material class and they exhibit tetrahedrally bonded chalcopyrite structure. Cu(In,Ga)Se₂ (CIGSe) based thin film solar cells exhibit the world record efficiency for polycrystalline absorber materials of 20.8% on laboratory scale.^{177,178} While so far, the highest efficiency of Cu(In,Ga)S₂ (CIGS) solar cells is less than 13% when prepared by reactive magnetron sputtering¹⁷⁹ or other deposition techniques¹⁸⁰. The three-stage co-evaporation process, which was mostly used for the absorbers with the highest efficiencies, is generally considered to be inadequate for cheap, large-scale production because of its complicated processing steps. Scientific and technological research efforts have started to focus on exploring cost-effective and large-scale one-step processes for CIGS(e) absorber film preparation.^{3, 181 - 184} Among them, reactive magnetron sputtering is characterized by several advantages like its large-area scalability, one-step deposition and low temperature processing attributed to the ion-assisted film growth. It was reported that the main defects of magnetron-sputtered CIGS solar cells are microscopic pin holes and crevices which lead to short circuits.¹⁸⁵ In order to reach higher efficiencies with high reproducibility, the microstructure and morphology of the CIGS films have to be optimized and a detailed understanding of their nucleation and growth mechanisms is needed. For CIGS(e) films grown by co-evaporation or molecular beam deposition, grain growth models and substrate roughness effects have been studied by different groups¹⁸⁶⁻¹⁹⁰. Gossila et al.¹⁸⁶ grew CuInS₂ films on (100) Si and glass by three-source molecular beam deposition. They characterized the properties of room-temperature (RT) grown films and subsequently discussed how the annealing, substrate temperature and deposition rates affect the crystallinity and the surface morphology. Their films prepared at RT were planar with a surface roughness ($w \sim 4$ nm) well below 10% of the total film thickness (~ 60 nm) which was not affected by deviations from stoichiometry and amorphous structure was insensitive to the deposition rate. Films prepared at high temperature showed island growth and a much rougher surface ($w \sim 17$ nm) compared to the RT-deposition due to the increased crystal quality, whereas the crystallinity was not affected strongly by the deposition rate which only influenced the surface morphology.

Walter and Schock¹⁸⁷ studied the crystal growth and diffusion process in four source co-evaporated polycrystalline CIGSe thin films on glass. They found epitaxial effects and interdiffusion of indium and gallium closely linked to the existence of Cu_xSe on the surface which has a big impact on the growth of CIGSe films with large crystallites. Liao and Rockett¹⁸⁸ studied the epitaxial growth of CIGSe films on (110)-oriented GaAs substrates by a hybrid sputtering and evaporation process. They reported the epitaxial growth temperature for the (220)/(204)-oriented layers was lower than (112) and other textured surfaces which was suggested to be due to the higher facet density and consequently to shorter diffusion distances. The polar {112} surfaces have much lower energies than the nonpolar (220)/(204) surfaces and couple with surface reconstructions. Schlenker et al.¹⁸⁹ investigated the initial growth stage of CIGSe on Mo films on glass prepared by thermal evaporation. They observed three-dimensional island growth, i.e. Volmer-Weber growth mode and the density of the CIGSe nuclei were controlled by the deposition rate (0.6~8.2 Ås⁻¹) and the substrate temperature (400~600 °C). Schlenker et al.¹⁹⁰ studied the grain growth of co-evaporated CIGSe films on the basis of a kinetic growth model. Grain growth with a (112) texture is energetically preferred and these grains grow at the expense of other orientations. Higher Cu-contents induce the growth of larger grains attributed to lower activation energies. However, for CIGS(e) films deposited by one-step reactive magnetron co-sputtering (RMS), only few work focused on their grain growth and surface evolution. Thornton et al.¹⁹¹⁻¹⁹³ first demonstrated that single phase CuInSe₂ films can be deposited by reactive co-sputtering from Cu and In planar magnetron sources in a mixed working gas of Ar/H₂Se already in the 1980's. They suggested the following formation reaction of CuInSe₂: $Cu + In + 2H_2Se \rightarrow CuInSe_2 + 2H_2$. At that time they achieved solar efficiencies of about 6% even though they observed an indium-rejection behavior during the film growth. Later probably due to the toxic gas (H₂Se and H₂S) complexity, reactive sputtered CIGSe was out of research focus and co-evaporated CIGSe was more concentrated. About two decades later, Meyer's group¹⁹⁴ and Ellmer's group^{179,185,195-198} made efforts to develop an one-step RMS process attributed to the basic advantages of the sputtering process concerning the scalability which already mentioned in section 3.1. Meyer's group focuses on the CuInS₂ films on float glass and sapphire substrates by RF reactive sputtering method and still performing sulfurization during annealing process. Ellmer's group were able to make Cu(In, Ga)S(e)₂ based solar cell with a competitive efficiency around 12.2% by one-step RMS without sulfurization. They also investigated the nucleation and growth morphology of CIGS films prepared with different recipes by in-situ energy dispersive X-

ray diffraction and ex-situ X-ray diffraction and microscopic characterization and tried to provide a good model system on CIGS to analyze the growth of chalcopyrites prepared by one-step RMS. Part of the presented results was already published in ref. 195.

In this work, the evolution of the roughness scaling properties was studied for CIGS thin films prepared by one-step RMS. The purpose of this investigation is firstly to understand the scaling behavior of these CIGS films as a function of both deposition time (i.e. film thickness) and scale of the measurement. Secondly, to correlate further information with the deposition process this involved in the kinetic roughening mechanism by negative ions bombardment during sputtering. The aim is also to contribute to the general understanding of the processes controlling the growth of semiconductor films prepared by RMS which is a unique and relative cheap one-step procedure for CIGS absorber preparation.

5.1 Experiments details

The deposition of the Cu(In,Ga)S₂ thin films were performed in a magnetron sputtering system, specially designed for the deposition of sulfides by sputtering in Ar-H₂S mixtures and equipped with a load lock vacuum system (LESKER chamber) with a process chamber base pressure better than 10⁻⁴ Pa. This system is operated in the co-sputtering mode with two rectangular planar magnetron sputtering sources with a copper-gallium alloy (Cu85Ga15 with 15 wt.% Ga) target and an indium target, each with a size of 10.4 × 5.4 cm². The two targets are mounted with an inclination angle of 142° against each other. The average target-to-substrate distance was about 8 cm. The plasmas of both magnetrons were excited independently by two DC power supplies (Advanced Energy, MDX 1K). The sputtering pressure was fixed at 1 Pa with different Ar/H₂S ratios. The Ar and H₂S gas supplies were controlled by mass flow controllers from MKS instruments. The base pressure was measured with a full range gauge from Pfeiffer vacuum and the process pressure by a capacitance gauge (Baratron). A LabVIEW program was used to control the whole deposition system. Molybdenum-coated float glass substrates (Mo/glass), the usual back contact for chalcopyrite thin film solar cells, were used as substrates (5×1.25×0.2 cm³). The deposition area in the used sputtering equipment was about 5×5 cm². The substrates could be heated up to temperatures of up to 600 °C by a pyrolytic graphite heater encapsulated by boron nitride.

Before the deposition of the CIGS film, pre-sputtering was usually performed with Ar gas (51 sccm results of 1 Pa) for at least 10 min to clean the target and stabilize the

discharge voltages for the CuGa target and the In target. Since the deposition parameters i.e. sputtering pressure, temperature, etc. play an important role on the film growth, in the following subchapters, these influences on the CIGS film growth will be discussed separately. Table 5.1 summarizes the general deposition parameters used in this work. Some as-deposited CIGS films were chemically etched in diluted potassium cyanide (KCN, 3%, 3 min) to remove a Cu-rich layer from the surface (CuS, covellite).

Table 5.1: Summary of typical deposition parameters for sputtered CIGS films.

| T _s (°C) | P(CuGa)(W) | P(In)(W) | Pressure/Pa | F _{Ar} /F _{H₂S} | Deposition rate(nm/min) |
|---------------------|------------|----------|-------------|--|-------------------------|
| RT | 70 | 70 | 0.5~1.5 | 2 | ~100 |
| 200 ~ 400 | 70 | 70 | 1 | 2 | |

5.2 Influence of sputtering parameters on the nucleation and growth of CIGS films

5.2.1 Influence of deposition pressure

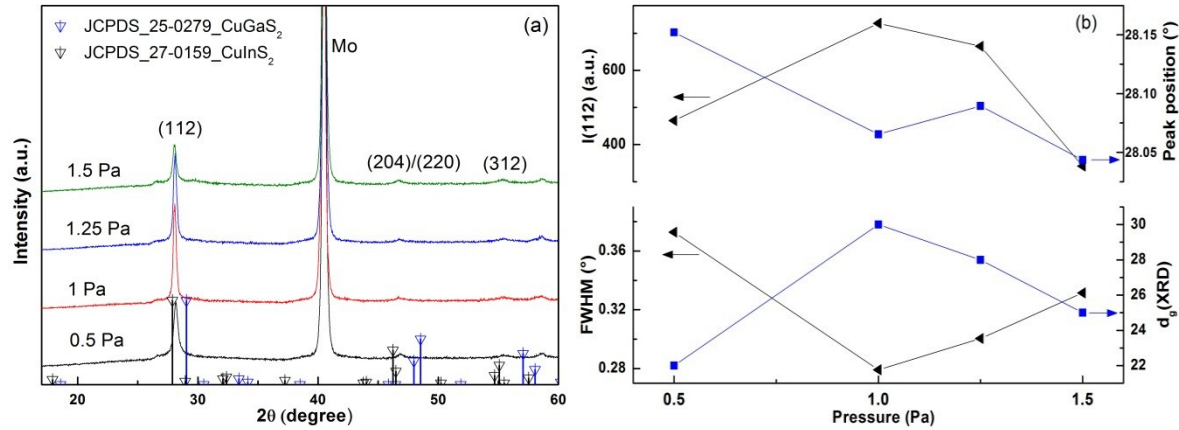


Fig. 5.1: (a) XRD spectra of CIGS films on Mo/glass deposited at room temperature at different sputtering pressures, and (b) FWHM, peak position, peak height intensity of the (112) diffraction peak and crystallite size: P(CuGa)=P(In)=70 W, F_{Ar}/F_{H₂S}=2, t=5 min.

The Cu(In,Ga)S₂ films on Mo/glass were prepared by the one-step RMS at room temperature for different sputtering pressure varying from 0.5 Pa to 1.5 Pa while keeping the Ar/H₂S ratio of 2 constant. Fig. 5.1(a) shows the X-ray diffraction spectra of four CIGS films prepared at room temperature for 5 min with different sputtering pressures. Only the chalcopyrite phase with a preferential (112) texture around 28° is detected with additional diffraction peak from Mo back contact. The other chalcopyrite peaks as (204)/(220) around 46.7° and (312) around 55.4° are very weak. As can be seen from Fig. 5.1(b), with increasing sputtering pressure from 0.5 Pa to 1 Pa, the intensity of the (112) peak increases and then decreases with further increasing the pressure up to 1.5 Pa. The full widths at half

maximum (FWHM) and crystallite size obtained from (112) peak have an inverse trend compared to the evolution of the peak intensity. When the sputtering pressure is 1 Pa, crystallite size is the biggest around 30 nm.

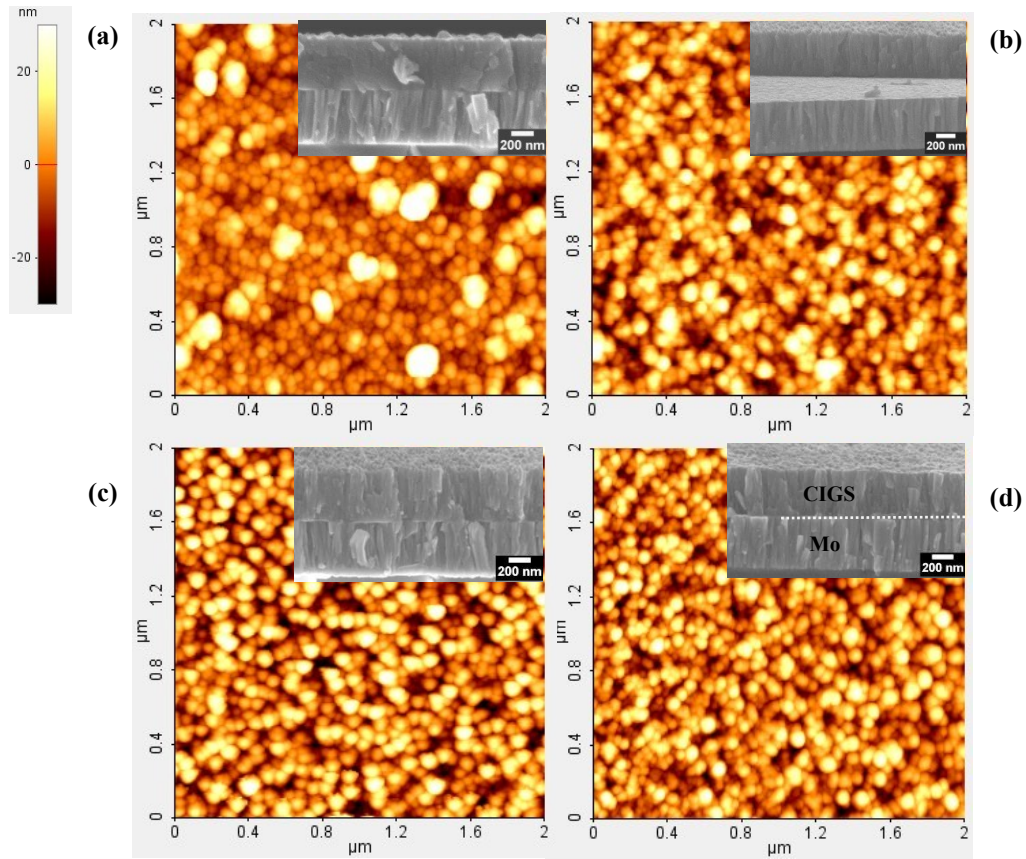


Fig. 5.2: AFM topography and SEM cross-sections for CIGS films prepared at different sputtering pressures (a) 0.5 Pa, (b) 1 Pa, (c) 1.25 Pa and (d) 1.5 Pa for $t=5\text{min}$. The dashed line is a guide to see the two layers.

Fig. 5.2 displays the surface morphology as $2 \times 2 \mu\text{m}^2$ AFM images and corresponding cross-sectional SEM micrographs for CIGS films. It can be clearly seen that the surface of CIGS films prepared at 0.5 Pa is inhomogeneous and consists of dispersed big aggregates (100~160 nm) on the top than those of higher pressure. It can be explained by the mean free path for sputtered species (Cu, In, Ga, S) is longer in lower pressure and the surface mobility of these species increases and hence form the big clusters.⁷⁷ This result does not fit to the XRD analysis described above due to the fact that the grain size obtained from XRD is the size of the coherently diffracting regions normal to the substrate and the grain size obtained from AFM is parallel to substrate surface. Clear columnar structures appear when the pressure is over 0.5 Pa. The film thicknesses for all samples are very close which seems independent on the pressure, indicating the growth normal to the substrate is dominant by other sputtering parameters, i.e. substrate temperature, growth time and direction, sputter

power, etc. Hence, 1 Pa was used to prepare other CIGS films in the following CIGS chapters.

5.2.2 Influence of deposition time

The effect of deposition time, i.e. film thickness, on the microstructure of CIGS films prepared by one-step RMS in a sputtering pressure 1 Pa with Ar/H₂S ratio of 2. The substrate temperature (T_s) was kept at room temperature (RT) for the first 5 min and afterwards was increased during the deposition. For the 7 min and 10 min depositions, T_s at the end was 95 °C and 200 °C. The deposition rate was around 100 nm/min. The film composition for 5min-sample is measured by WDXRF, which the Cu, In, Ga and S contents are 26.2, 22.8, 4.3 and 46.7 at. %, respectively. Nearly stoichiometric CIGS film is obtained with Cu/(In+Ga)=0.97.

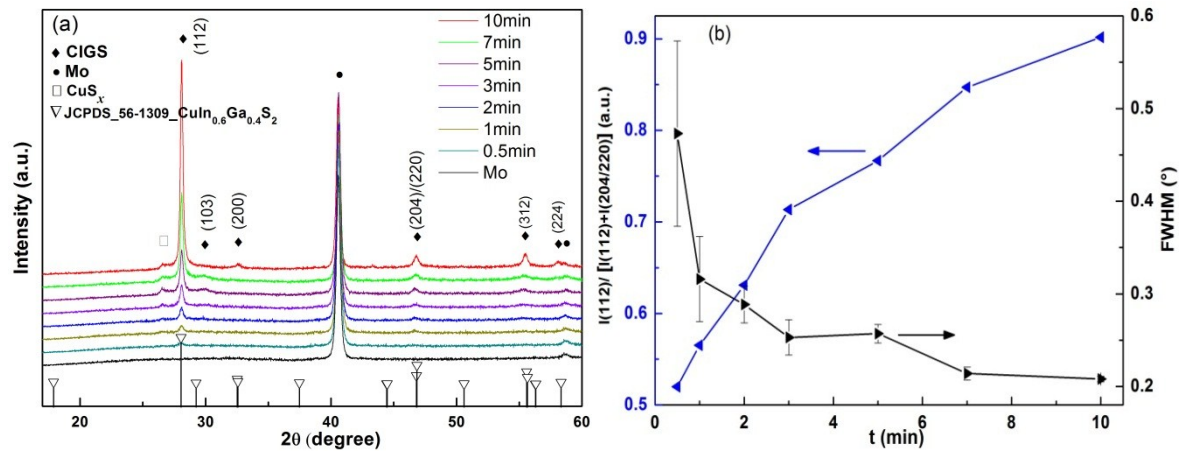


Fig. 5.3: (a) XRD patterns of the CIGS films on Mo/glass substrates at different deposition times, and (b) FWHM of the (112) diffraction peak and (112), [(112)+(204/220)] diffraction peak height intensity ratio of CIGS films $I(112)/[I(112)+I(204/220)]$ as a function of deposition time.¹⁹⁵

Fig. 5.3a shows a series of XRD patterns of CIGS films on Mo/glass deposited for different times. The chalcopyrite phase with (112) preferred orientation is mainly found with additional diffraction peaks from the Mo back contact. A weak diffraction peak around 26.5° left to the (112) chalcopyrite diffraction peak can be tentatively assigned to the covellite phase (CuS_x), since it decreases in intensity after selectively etching the covellite in a diluted KCN solution. The FWHM of (112) peak decreases from 0.47° to 0.21° and the XRD peak height intensity ratio $I(112)$ to $[I(112)+I(204/220)]$ increases from 0.52 to 0.90 with increasing film thickness from 50 nm (0.5 min) to 1000 nm (10 min), as displayed in Fig. 5.3b indicating stronger preferred orientations along the (112) direction at longer deposition times and higher deposition temperatures. For $t=0.5$ min, the weak and broad (112) peak suggests poor crystallinity and a small grain size. From former investigations in

our group¹⁷⁹ the CuInS₂ films prepared by one-step RMS exhibit only low intrinsic stress values, significantly below 300 MPa, which agree well with the tensile strain values derived from X-ray diffraction¹⁹⁹ and Raman measurements²⁰⁰ for evaporated CuInS₂ films. Therefore the variation of the Ga content induces shift of the chalcopyrite diffraction peak. Also, for the calculation of the grain size from the XRD peak width, no microstrain was taken into account. The $d_g(\text{XRD})$ which will be discussed together with the grain size obtained from AFM in the following part.

The surface evolution as a function of the growth time, as $2 \times 2 \mu\text{m}^2$ AFM images of the pure Mo and CIGS films on top for different deposition times is shown in Fig. 5.4. Although the surface of the Mo film (Fig. 5.4a) displays elongated grain structures, all CIGS surfaces exhibit spherical grain morphology. With increasing deposition time, the CIGS clusters aggregate and ramified islands were formed which grew bigger and denser to coalescence and form a continuous film covering the Mo substrate surface. This growth type is very similar to the growth of co-evaporated CIGSe films as investigated by Schlenker et al.¹⁸⁹ who found island growth in the very early stages for their CIGSe films. Only their island density is much smaller than ours attributed to the slower deposition rate (a factor of 3) by evaporation. Additional higher kinetic energy by the negative bombardment from RMS process could induce a high density of nuclei. The height profiles of these structures, displayed in Fig. 5.4g, show that the lateral size grows and the surface corrugation increases significantly with increasing film thickness.

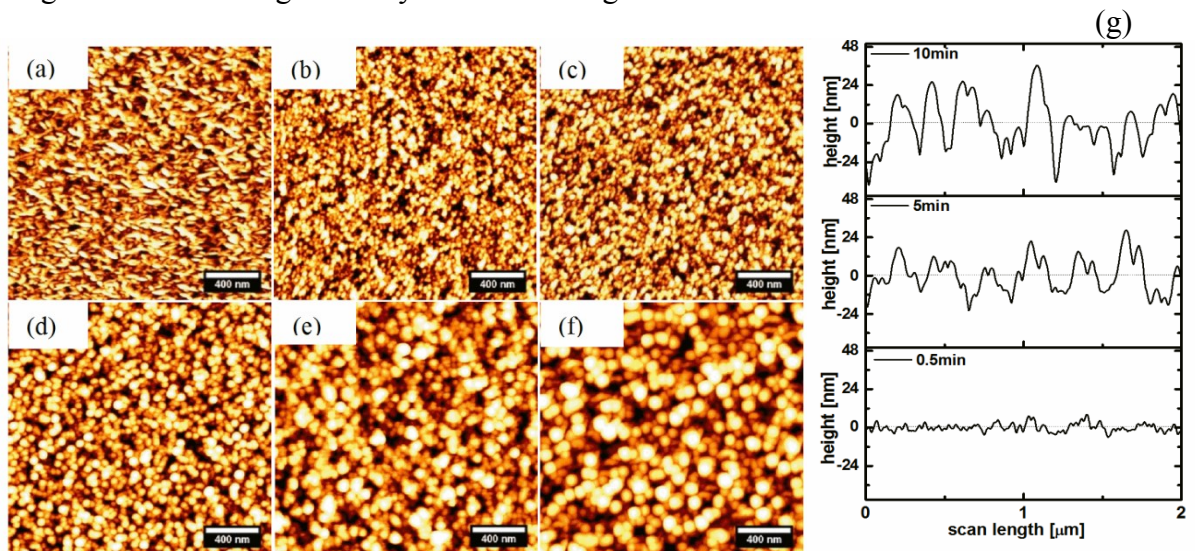


Fig. 5.4: (a-f) AFM images of CIGS films on Mo coated glass substrates for $t =$ (a) 0, (b) 0.5, (c) 1, (d) 3, (e) 5, (f) 10 min. (g) Line height profiles for the films with $t =$ 0.5, 5, and 10 min.

Fig. 5.5 displays the cross-sectional SEM micrographs of CIGS films on Mo/glass. A clear columnar growth can be seen for CIGS films of sufficiently large thickness (≥ 300 nm, $t \geq 3$ min), comparable to the columnar morphology of the Mo layers, visible in the same SEM pictures. For growth times over 5 min (corresponding also to a rising substrate temperature) the CIGS columns develop much sharper pyramidal tops, which are related to the (112) texture growth of the CIGS films. The larger roughness (~ 11 nm) of the CIGS films in comparison to the Mo surface (roughness around 3 nm for comparable thickness) can be deduced from Fig. 5.5c, deposited for 5 min, showing both surfaces. For thicker CIGS films also some porosity between the columns can be observed, especially, when comparing with the packing of the columns in the underlying Mo films. This porosity is accompanied by a separation of the columns also in vertical direction.

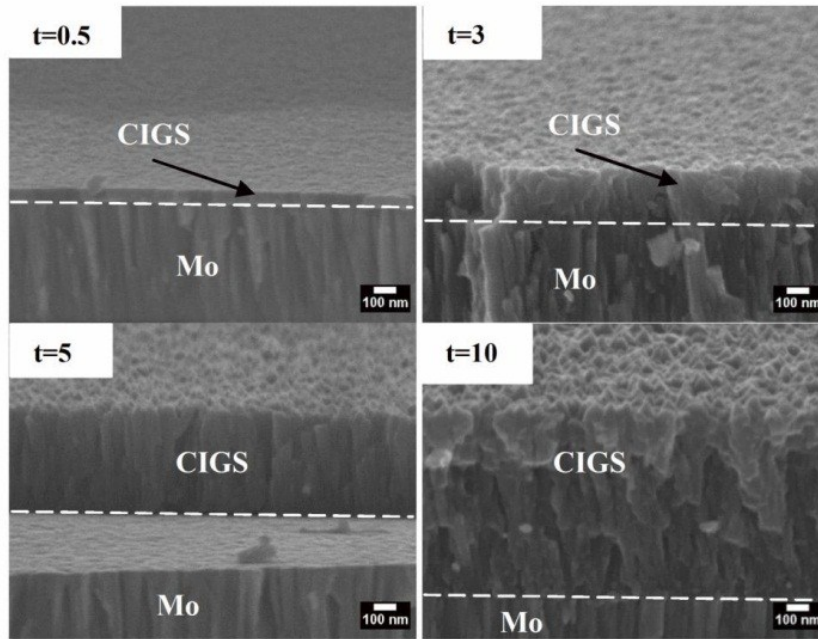


Fig. 5.5: Cross-sectional SEM micrographs of CIGS films on Mo/glass at different deposition times: $t = 0.5, 3, 5$, and 10 min. (The dashed lines mark the interfaces between CIGS layer and Mo layer).¹⁹⁵

By AFM measurements, the growth process can be analyzed by measuring the evolution of the lateral grain size. Fig. 5.6(a) displays the grain size $d_g(\text{AFM})$ of the CIGS films versus the film thickness d_f . For comparison, we also plot the grain size $d_g(\text{XRD})$ calculated from the FWHM of the (112) diffraction peak using the Scherrer equation. The lateral $d_g(\text{AFM})$ is more than twice larger than the vertical $d_g(\text{XRD})$. Such a difference is not rare and was also reported by other researchers who derived the grain size from electron microscopy and XRD for CuInS₂¹⁹⁴ and other materials^{201, 202}. They attributed their observed difference to the domain structure of the grains, twinning of the grains and the

tendency to overlook smaller particles in electron microscopy. The grain size obtained from AFM and XRD can be fitted by a power law $d_g(\text{AFM}) \sim d_f^{1/z}$ with $1/z=0.33$ and 0.24 , respectively. These exponents are close to the experimental value for gold films reported by Ruffino et al.²⁰³ and match with a theoretical study of Novikov²⁰⁴ for normal grain growth, where the atomic diffusion at grain boundaries dominates the grain growth. Up to a film thickness of 100 nm, the surface of the CIGS film is relatively smooth. For thicker films, a part of the grains grows faster leading to larger aggregates, which increases the total average grain size and roughness.

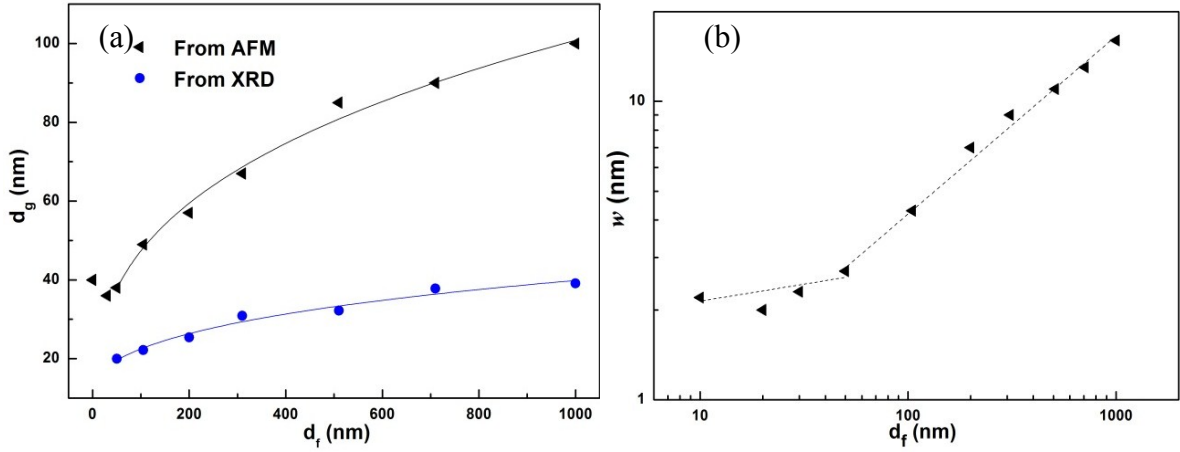


Fig. 5.6: (a) Mean grain sizes d_g of CIGS films on Mo/glass, calculated with the Scherrer equation from the FWHM of the (112) diffraction peaks (•), and obtained from AFM measurements (◄) and (b) surface roughness w derived from AFM scans as a function of the film thickness d_f . The lines are fitting curves.

The advantage of AFM measurement is that the vertical morphology can also be characterized by the mostly used surface roughness. Fig. 5.6(b) shows the root-mean-square roughness w of CIGS films on Mo/glass as a function of the film thickness d_f on a log-log scale. In conventional dynamic scaling theory, the roughness exponent α and growth exponent β are independent of the film thickness, i.e. deposition time. However, for our Cu(In,Ga)S₂ films there is a transition between different growth mechanisms, characterized by different β values. The roughness evolution of the CIGS films can be divided into two regions, as shown in Fig. 5.6(b). In the initial growth regime, w changes only slightly from 2.2 nm to 2.7 nm for $d_f \leq 50$ nm with a growth exponent $\beta_1=0.13\pm0.09$. Such a small growth exponent indicates surface diffusion as the dominant mechanism which smoothes the surface. By increasing the surface diffusion effect, the exponent will become even smaller which was proven by the application of electron cyclotron resonance plasma.¹⁹⁷ Further increasing the film thickness, the roughness increases monotonically from 4.3 nm to 16 nm with a much bigger growth exponent $\beta_2=0.56\pm0.03$. The increased growth

exponent is related to the oriented crystallite growth which enhances the shadowing effect and leads to surface roughening.

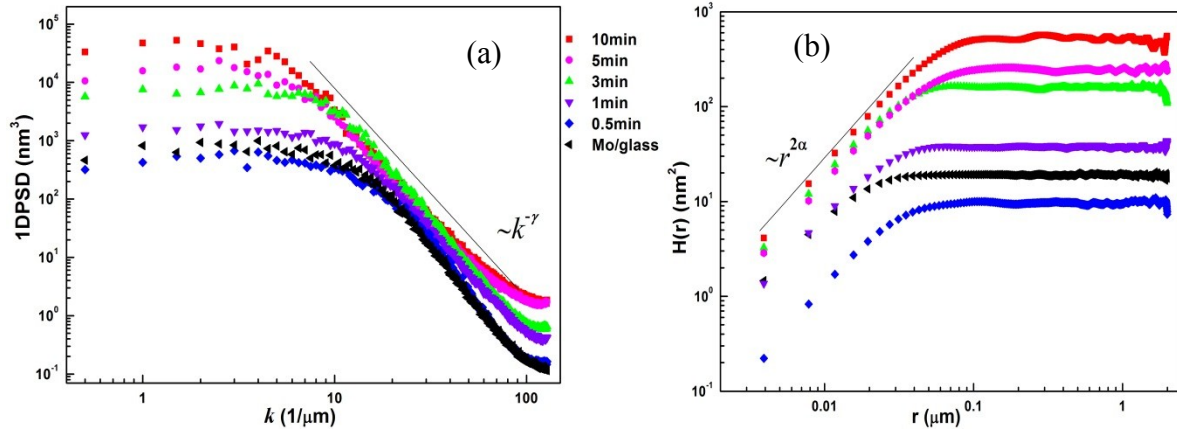


Fig. 5.7: (a) 1D-power spectral density functions and (b) height-height correlation functions of CIGS films on Mo/glass obtained for different deposition times.

As described in chapter 2.4, some growth processes does not follow the Family-Vicsek scaling relation and show an anomalous scaling behavior which was explained in terms of more complex scaling relations. The dynamic scaling derived from power spectral density function and height-height correlation function shows a difference. Here we will use both functions to derive the corresponding roughness exponents. Fig. 5.7 plots 1D-power spectral density functions (1DPSD) and height-height correlation functions (HHCF, $H(r)$) of CIGS films on Mo/glass obtained for different deposition times. It is clear that all 1DPSD spectra are consisted two regions: (a) for high spatial frequency (large k values, small length scales), a negative slope presents and indicates the existence of kinetic roughening for these length scales; (b) for low spatial frequency (small k values, large length scales), the spectra are nearly saturated suggesting the lack of any lateral correlation in the surface roughness in these length scale range. The 1DPSD spectra are shifted upwards as the deposition time increasing up to 1 min for the initial growth region, which is also in accordance with the upward shifting for HHCF, as shown in Fig. 5.7(b). Thus, it can be concluded that there are two growth regimes with a crossover time close to 1 min, as already reflected from the roughness evolution in Fig. 5.6(b). Based on the scaling theory introduced in chapter 2.4, the roughness exponent α can be calculated from the slope γ of the linear fit in the high frequency region (or low length scales, guided by the straight line from Fig. 5.7(a) as $\alpha=(\gamma-1)/2$). By fitting the linear slopes of the 1DPSD curves in Fig. 5.7, the evaluated value of α for different deposition times are shown in Fig. 5.8(above). Obviously it displays a changing α with growth time as it is predicted by the conventional dynamic scaling theory²⁴. And all the roughness exponents α are bigger than 1 which is an

anomalous dynamic scaling behavior described in linear diffusion models^{51, 205, 206}, indicating competition between roughening fluctuations and smoothing effects, suggesting that the local surface slope increases with growth time.

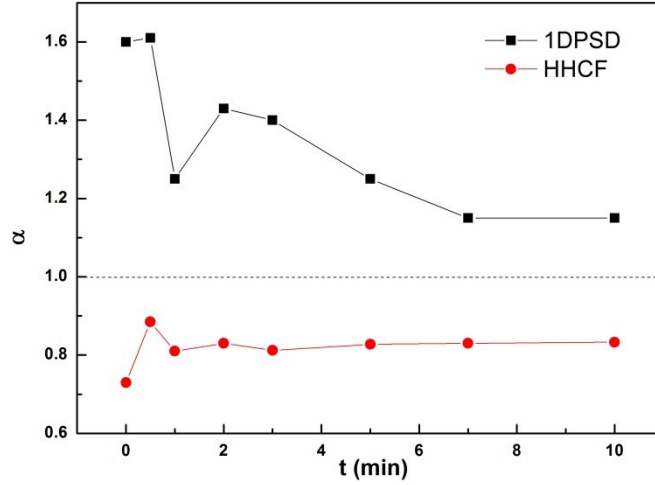


Fig. 5.8: Roughness exponent α of CIGS films on Mo/glass obtained from 1DPSD (■) and the height-height correlation function (HHCF, ●), respectively.

Fig. 5.8(below) depicts the roughness exponent α obtained from one half of the linear fitting slope at small length scales in the height-height correlation functions. This result shows that the calculated α values (0.73~0.89) are nearly two times smaller than those obtained from 1DPSD (1.15~1.61). Similar results have been reported by Yanguas-Gil et al.³³ and Mohanty et al.²⁰⁷ who studied SiO₂ and ZnO:Al thin films, respectively. Such a difference was explained by the longer length scale using to obtain the roughness exponent by 1DPSD than that by HHCF which corresponds to the global and local exponent respectively, and attributed to a situation of an anomalous scaling.²⁹ According to Fig. 5.7, the length scale which was used to evaluate the roughness exponent from 1DPSD is 10~100 nm, indeed bigger than the analysis range (4~50 nm) in HHCF. Actually, such an anomalous scaling derived from these two methods can be also observed for sputtered TCO materials in this work. The evolution of α obtained from height-height correlation functions is more independent with time, i.e., α nearly keeps constant for 0.82 ± 0.01 for $t > 0.5$ min.

5.2.3 Effect of substrate temperature

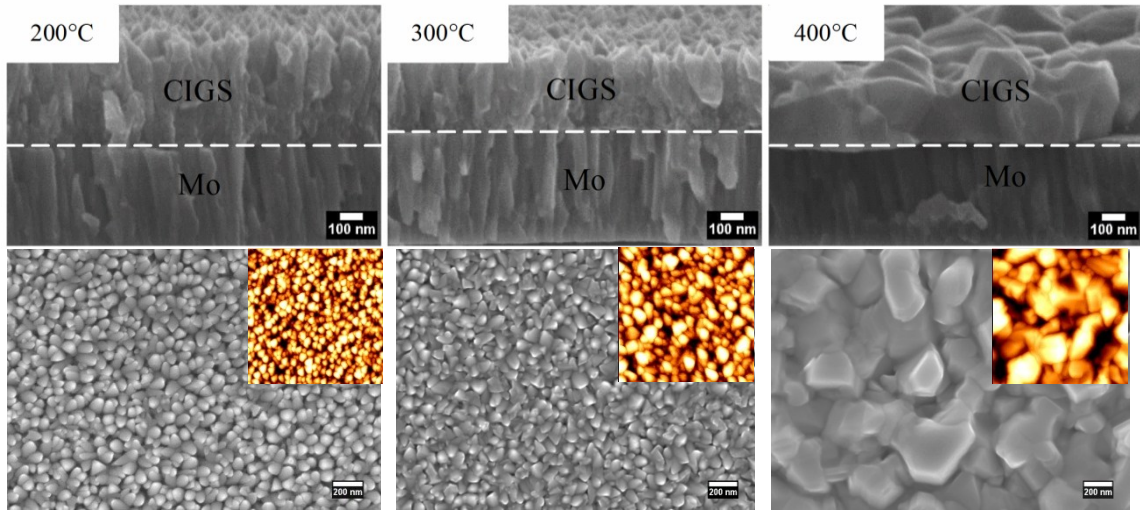


Fig. 5.9: (above) Cross-sectional SEM images and (below) SEM topography for CIGS films prepared at $T_s = 200\text{ }^\circ\text{C}$, $300\text{ }^\circ\text{C}$ and $400\text{ }^\circ\text{C}$, respectively, $t = 5\text{ min}$. Below also inset corresponding AFM images with scan size of $2 \times 2\text{ }\mu\text{m}^2$.

The Mo/glass substrates were heated to different temperatures while keeping other deposition parameters constant. Fig. 5.9 shows SEM images (cross section and topography) for CIGS films prepared at different substrate temperatures. The topography obtained by SEM and AFM has identical views to analyze the surface morphology. With increasing substrate temperature up to $300\text{ }^\circ\text{C}$, columnar grains can be observed. While for $T_s = 400\text{ }^\circ\text{C}$, very dense and large polyhedrally-shaped grains form with average grain size around 270 nm which are comparable to the film thickness (400 nm) and nearly more than three times bigger than those prepared at lower temperatures.

By analyzing 1DPSD spectra of CIGS films prepared at different temperatures, shown in Fig. 5.10, it can be seen that all 1DPSD curves overlap in high frequency region indicating the same global roughness exponent. The calculated roughness exponent α of 1.3 is still in the region of anomalous scaling implying roughening fluctuations and surface diffusion smoothing effects cannot reach a balance, leading to a local surface slope increase in high frequency region, i.e. small length scale. In low frequency region, 1DPSD curve for $300\text{ }^\circ\text{C}$ -sample is slightly higher than that of $200\text{ }^\circ\text{C}$ -samples, while, both are much lower than $400\text{ }^\circ\text{C}$ -sample. The surface roughness is 12 nm and 14 nm for $200\text{ }^\circ\text{C}$ and $300\text{ }^\circ\text{C}$ depositions which is a little bigger than that of RT deposition (11 nm). But, the roughness of 38 nm for $400\text{ }^\circ\text{C}$ deposition is more than three times bigger than RT deposition, due to the pronounced (112) texture growth of large polyhedral-shaped grains. Obviously, the temperature effect on the morphology of CIGS film growth is prominent when $T_s > 300\text{ }^\circ\text{C}$.

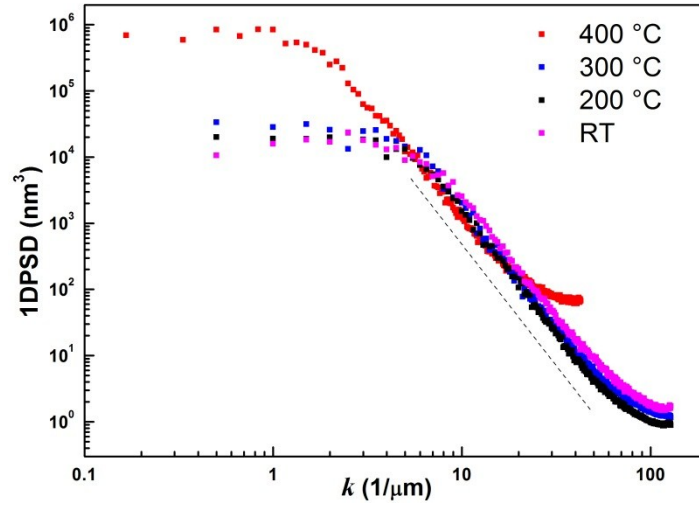


Fig. 5.10: 1DPSD spectra of CIGS films on Mo/glass at different substrate temperatures, $t=5\text{min}$. Note that for the 400 °C-sample, 1DPSD was obtained from AFM measurement with scanning size of $6\times 6\text{ }\mu\text{m}^2$. Other two are $2\times 2\text{ }\mu\text{m}^2$ due to the smaller grains.

5.2.4 Intrinsic electrical properties: CAFM

The grain boundaries (GB) have been identified as beneficial for high efficiency polycrystalline CIGSe based solar cell.^{208 - 211} GBs can enhance the minority carrier collection and build a current pathway for minority carriers to reach the n-type buffer layer and window layer and be collected, which is normally bad for optoelectronic or transistor applications. The microstructure and electrical properties related to GBs are important issues to consider in terms of improving the chalcopyrite based solar cell performance. Topography together with local electrical transport behavior of Cu(In,Ga)S₂ thin films on Mo/glass prepared by one-step RMS with a substrate temperature of 450 °C were examined by conductive atomic force microscopy. Fully coated diamond tips (CDT-NCHR) were used for C-AFM (XE-100, Park System). The current signal was recorded simultaneously during the contact-mode topography mapping. Current maps were obtained at a constant DC voltage by applying 0 V, 0.5 V and 1.0 V sample bias. The contact force of about 500 nN was applied onto the tip and a scanning area of 2×2 μm² at a scan rate of 0.6 Hz was used.

Fig. 5.11 displays XRD spectra of the CIGS films prepared at different times $t = 1, 5$, and 15 min. All the films show the chalcopyrite phase with a (112) preferential texture. With increasing deposition time, the (112) peak becomes sharper and narrower, indicating an improved crystallization. The FWHM of (112) peak is 0.26°, 0.14° and 0.11° for 1min, 5 min and 15 min samples, respectively. And the corresponding crystallite sizes are 31 nm, 58 nm and 71 nm.

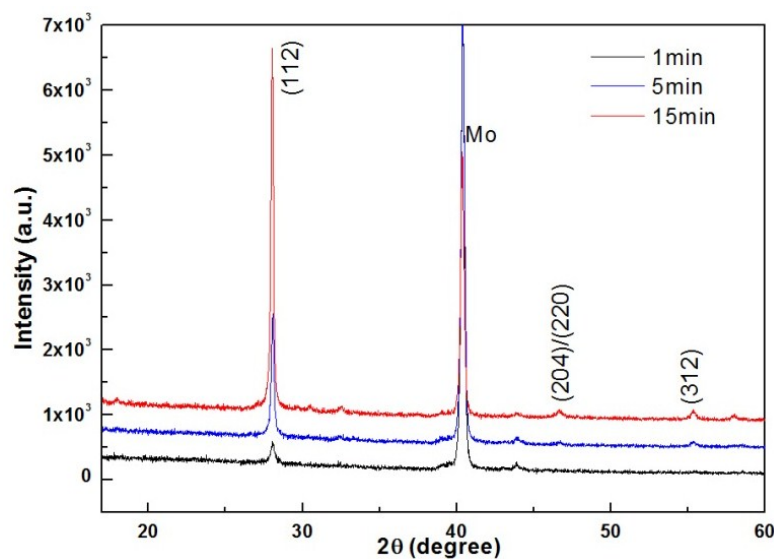


Fig. 5.11: XRD spectra of the CIGS films on Mo/glass substrate for different deposition times, $T_s = 450$ °C.

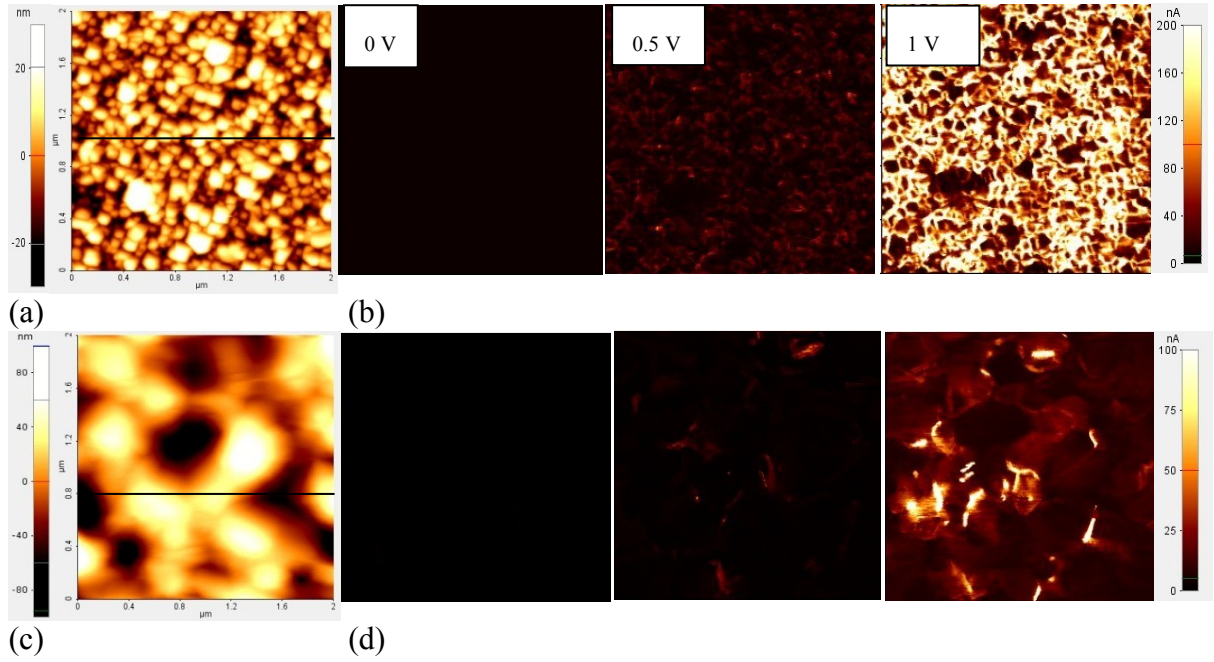


Fig. 5.12: (a), (c) Topography and (b), (d) current maps of CIGS films on Mo/glass for $t=1$ min and 15 min, respectively. Current maps were taken at sample bias of 0 V, 0.5 V and 1 V.

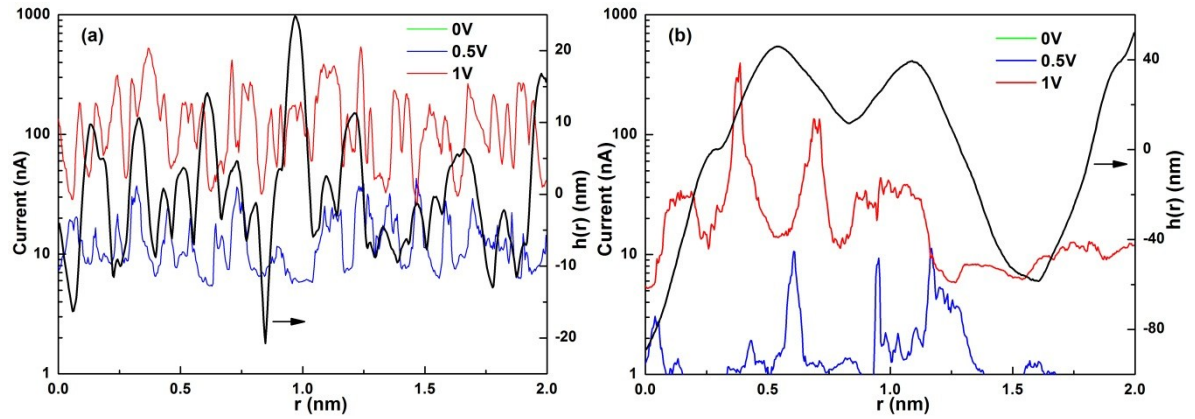


Fig. 5.13: Height and current profiles for (a) 1 min and (b) 15 min-CIGS films derived from Fig. 5.12. The black lines give the height profiles; color lines give the current profiles.

Fig. 5.12 (a) and (c) display the topography of CIGS films deposited at 1 min and 15 min, respectively. The lateral grains for 1minute-sample (~ 100 nm) are three times smaller than for 15min-sample which is consistent with the XRD results. Current images of these CIGS films, shown in Fig. 5.12 (b) and (d), were obtained simultaneously with the scanning of the topography by applying a sample bias of 0 V, 0.5 V and 1 V. Note that for two samples, the height scale bar and current scale bar are different. The whole measurements were performed without external light source but with a red light laser to maintain the contact mode scanning. The dark state was confirmed from the current maps at 0 V, therefore photocurrent effect can be excluded. In general view of these current images, the

conduction area was increased with increasing the sample bias for both samples. The current profiles plotted in Fig. 5.13 can give more detailed information. For the 1min-sample, a relative small current was observed when applying voltage of 0.5 V. A dramatically increased current appears for most of the scanning area when the voltage is increased to 1 V. While the increased amplitude for 15min-sample is smaller. Azulay et al.²¹¹ reported that high current flow of polycrystalline CuInSe₂ and Cu(In,Ga)Se₂ was observed mainly through grain boundaries which pointed to inversion at the GBs. Under different laser illumination, they also found that the current cannot always be detected along the entire GB but varied between GBs which was due to different crystallographic orientations, contaminants, tip-GB contact quality, etc. Shin et al.²¹² compared the local electrical behavior of (112) preferentially and randomly textured Cu(In,Ga)Se₂ films. They found, with increasing high bias to 1V, the conducting region was invariant for preferentially textured films since the downward energy band was dominant at GB. However, the conducting area was dramatically increased due to the randomly formed energy band bending at GBs in the randomly textured films. The current did not flow along the GB but at the adjacent regions of the GB. Li et al.²¹⁰ further demonstrated that current flowed in the vicinity of the GB core rather than in the GBs for CIGSe films attributed to lower electron mobility of GB core resulting higher conductivity compared to surrounding regions. Similar phenomenon occur for our CIGS films prepared by one-step RMS. The 1min-sample is randomly textured in comparison with 15 min-sample. High current flew almost through the whole region (i.e. GB, near GB, grains) for the 1min-sample. But current was only detected near GB for 15min-sample, which is probably due to much lower number of GBs. If the root-mean square current ($R_{cur.}$) is defined as the distribution of electrical conductivity on the surface, $R_{cur.}$ is 89.57 nA, 53.85 nA, 18.76 nA for 1min, 5 min and 15 min sample, respectively, revealing the surface conductivity increases with increasing number of GBs (i.e. decreasing growth time).

5.3 Conclusions

In conclusion, Cu(In,Ga)S_2 thin films can be successfully deposited by one-step DC reactive magnetron co-sputtering from a copper-gallium alloy target (Ga15 wt.%) and an indium target in argon-hydrogen sulfide gas mixtures. The microstructural and morphological properties of CIGS films have been investigated with respect to the influence of sputtering pressure, deposition time, substrate temperature etc. by XRD, AFM and SEM. XRD results reveal a (112) preferential orientation for over 100 nm thick CIGS films. AFM and SEM were used to characterize the morphology. In terms of growth type, Volmer-Weber model, i.e. 3D island growth was determined for CIGS films on Mo coated glass substrates. The dynamic scaling behavior of CIGS films was analyzed by the 1D power spectral density function and by the height-height correlation function. The critical transition stage from surface diffusion to grain growth and shadowing effects was determined. The intrinsic electrical properties of sputtered CIGS films were investigated by conductive AFM. It was shown that the surface conductivity increases with increasing the number of grain boundaries.

6 Summary and Outlook

6.1 Main Conclusions of this Thesis

The objective of this thesis was the systematic investigation of the evolution of surface morphology and scaling of roughness of semiconducting oxides such as tin-doped indium oxide (ITO) and Al-doped zinc oxide (AZO) films and semiconducting sulfides such as Cu(In,Ga)S₂ (CIGS) films grown by the magnetron sputtering process. The influence of the deposition parameters, i.e., sputtering atmosphere, sputtering pressure, substrate temperature, and plasma excitation mode on the kinetic roughening of those semiconductor thin films has been explored in detail to understand the exact growth mechanism for the observed morphological features and the dominant process of film growth during magnetron sputtering process. The obtained growth exponent β for ITO, AZO and CIGS films was shown in Fig. 6.1.

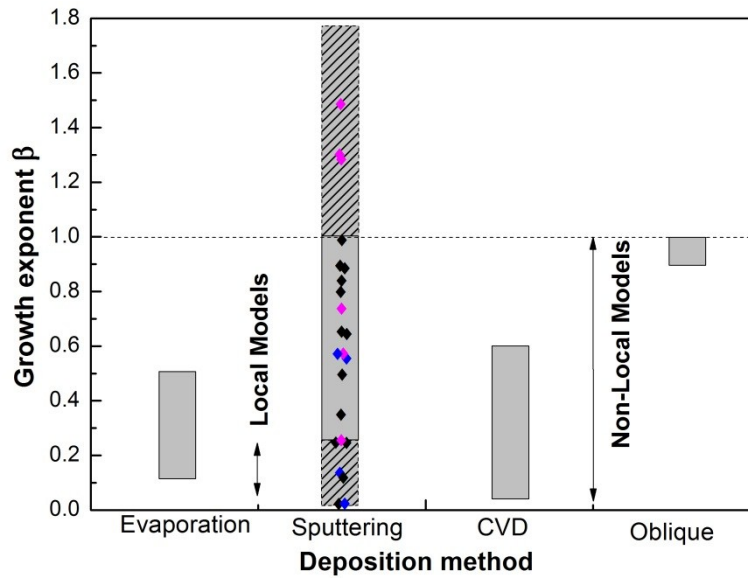


Fig. 6.1: Fitting of the growth exponent β from this work with literature values based on Fig.2.15. Inserting symbols \blacklozenge , \blacklozenge , and \blacklozenge represents the obtained β values for ITO, AZO and CIGS films, respectively, from this work.

Evolution of structure and surface roughness in ITO thin films

The evolution of microstructure and morphology of tin-doped indium oxide (ITO) films prepared from an In₂O₃:SnO₂ (90 and 10 wt. %, respectively) target was investigated under different sputtering atmospheres (pure Ar, mixtures of Ar with O₂ or H₂), and different plasma excitation modes (from 27.12 MHz via 13.56 MHz RF to pulsed DC) at low and high temperatures.

The crystallinity and the surface morphology of ITO films depend on the sputtering atmospheres. For ITO films on Si (100) substrates prepared by 13.56 MHz RF mode at room temperature, the body-centered cubic (bixbyite type) structure of ITO films remains, but the preferred orientation changed from (111) via (211) to (100) texture with decreasing O₂ addition and then increasing H₂ to the argon sputtering gas related to an excess or reduction of oxygen vacancies. The roughness of the ITO films prepared in this work is less than 3 nm. The surface roughness w increases as a power law of the film thickness d_f as $w \sim d_f^\beta$. The roughness decreases with increasing O₂ flow, while it increases with increasing H₂ flow. The growth exponent β was found to be 0.35, 0.65 and 0.98 for depositions in Ar/10%O₂, pure Ar and Ar/10%H₂ atmosphere, respectively. The lateral correlation length ξ grows as $\xi \sim d_f^{1/z}$, with $1/z=0.36$, 0.44, and 0.57 for these three different gas atmospheres, respectively. The roughness exponent α obtained from the height-height correlation functions is in the same range of 0.6~0.8. Similar morphology of ITO films prepared at borosilicate glass substrate was observed, i.e. island growth.

It is well known that films prepared by magnetron sputtering process are bombarded by high energetic species, such as high energetic negative ions or sputtered and reflected atoms. By decreasing the energy of the bombarding particles at the growing films, the electrical and structural properties can be improved.¹⁷⁶ A part of the present work demonstrated the effect of the particle energy on the morphology and structure properties of ITO films prepared at room temperature and 300 °C in pure Ar under different excitation modes: 27.12 MHz RF, 13.56 MHz and pulsed DC, i.e. increasing the discharge voltage and deposition rate and the mean energy of the negative oxygen ions. It was found that varying the excitation mode from RF to pulsed DC has a small influence on the crystallite growth of the ITO films at room temperature compared to elevated temperature depositions. For RT deposition, with increasing film thickness up to 400 nm, the roughness is less than 1.3 nm. ITO films prepared with different excitation modes show two growth regimes without a saturation stage. The critical transition thickness is in the range of 30~50 nm. With increasing discharge voltage (changing the excitation mode from RF to pulsed DC), the growth exponent β decreases from 0.27 via 0.14 to 0.08 in the initial growth stage. Such small β indicate surface diffusion dominating the film growth mechanism corresponding to nearly amorphous structure. Obviously, the surface diffusion effect is weakest in 27.12 MHz RF and strongest in the pulsed DC deposition. It could be related to the higher negative ion bombardment in DC induced higher adatoms mobility than that of

RF mode in the initial growth stage. However, β increases from 0.50 via 0.64 to 0.82 in the later growth stage. When the film grows thicker, the deposition rate increases when changing from RF to DC mode ($R_{27.12\text{MHz}} < R_{13.56\text{MHz}} < R_{\text{pulsed DC}}$). The adatoms on the surface have not enough time to move and are covered by new impinging atoms at higher deposition rates, which decrease the smoothing effect. Moreover, high deposition rates lead to increasing stress in the polycrystalline ITO films¹³⁵. The mechanical strain in the ITO films, obtained from the shift of the (222) diffraction lines, yield compressive strain values of 1.6%, 2% and 3% at room temperature for 27.12 MHz RF, 13.56 MHz RF and pulsed DC deposition respectively. Therefore, the pulsed DC mode can generate the highest β value. Note that the strain obtained from the shift of the dominant diffraction line decreases to 0.7%, 0.5% and 0.6%, respectively, for the 300 °C deposition. In the literature reported compressive stress value for ITO films sputtered from ceramic target in pure Ar are less than 0.2 GPa for room temperature deposition and even smaller for 250°C deposition.^{213,214} The roughness evolution of ITO films prepared at 300 °C with different excitation modes shows two growth stages but with a nearly steady stage when the film thickness is over 100 nm. The growth exponent β is 0.9, 0.89 and 0.80 for 27.12 MHz RF, 13.56 MHz RF and pulsed DC deposition, respectively. The roughness is less than 3.2 nm when the film thickness is less than 400 nm. A subgrain structure is only observed for ITO films prepared with pulsed DC at 300 °C which shows pronounced preferential $\langle 400 \rangle$ orientation normal to the substrate surface. The roughness exponent is in the range of 0.70~0.85 and 0.77~0.81 for RT and 300 °C depositions, respectively. Unfortunately, all of the scaling exponents of ITO films do not obey the well-known dynamic scaling relation²⁴, i.e. $\alpha / \beta \neq z$, suggesting that nonlocal growth effects such as crystal growth enhanced shadowing instability, resputtering, and bulk diffusion are mainly responsible for the kinetic roughening. Because only local growth effect such as noise, surface diffusion and relaxation can generate $0 \leq \beta \leq 0.25$.^{2, 3} Note that for room temperature deposition (~25 °C), considering the continuous sputtering bombardment effect, the final substrate temperature was increased but less than 70 °C. The effect of bulk diffusion should be insignificant under $T_s/T_m \leq 0.16$. For the 300 °C deposition, the surface diffusion was enhanced by the increased thermal activation, but the surface smoothing by the enhanced diffusion cannot compete with the enhanced shadowing due to the increased crystallite growth which generates high β values close to 1.

Table 6.1: Calculated scaling parameters for the investigated materials in the present work.

| ITO | Atmosphere | $V_{\text{dis}}(\text{V})$ | β_1 | β_2 | $1/z$ | α |
|--------------------------|-----------------------|---|-----------|-----------|-----------|-----------|
| RT 13.56 MHz RF | Ar/10% O ₂ | ~210 | - | 0.35 | 0.36 | 0.65~0.78 |
| | pure Ar | ~210 | 0.25 | 0.65 | 0.44 | 0.67~0.75 |
| | Ar/10% H ₂ | ~210 | - | 0.98 | 0.57 | 0.60~0.80 |
| ITO | Discharge mode | $V_{\text{dis}}(\text{V})$ | β_1 | β_2 | $1/z$ | α |
| RT Pure Ar | 27.12 MHz RF | ~100 | 0.27 | 0.50 | 0.31 | 0.70~0.85 |
| | 13.56 MHz RF | ~210 | 0.14 | 0.64 | 0.39 | |
| | Pulsed-DC | ~340 | 0.08 | 0.82 | 0.42 | |
| 300°C Pure Ar | 27.12 MHz RF | ~100 | 0.90 | 0.17 | 0.34 | 0.77~0.81 |
| | 13.56 MHz RF | ~210 | 0.89 | 0.22 | 0.25 | |
| | Pulsed DC | ~340 | 0.80 | 0.04 | 0.33 | |
| AZO | Atmosphere | $V_{\text{dis}}(\text{V})$ | β_1 | β_2 | $1/z$ | α |
| RT 13.56 MHz RF | Ar/1% O ₂ | ~155 | - | 1.29 | 0.55 | 0.56~0.76 |
| | pure Ar | ~155 | < 0 | 1.47 | 0.64 | 0.54~0.75 |
| | Ar/5% H ₂ | ~155 | 0.25 | 1.28 | 0.29,0.66 | 0.65~0.84 |
| | Ar/10% H ₂ | ~155 | - | 0.73 | 0.44 | 0.71~0.82 |
| 300°C 13.56 MHz RF | Pure Ar | ~155 | ~0 | 0.57 | 0.28 | 0.78~0.86 |
| CIGS | Atmosphere | $V_{\text{dis,CuGa}}/$ $V_{\text{dis,In}}(\text{V})$ | β_1 | β_2 | $1/z$ | α |
| RT, DC | Ar/H ₂ S | ~630/615 | 0.13 | 0.56 | 0.33 | 0.73~0.89 |

Evolution of structure and surface roughness in AZO thin films

The surface roughness scaling of Al-doped zinc oxide (AZO) thin films deposited by 13.56 MHz RF magnetron sputtering from a ZnO/Al₂O₃ (98/2 wt.%) target was investigated for different atmospheres (Ar/O₂, pure Ar or Ar/H₂ mixture), pressures and temperatures. It was found that the *c*-axis orientation of the hexagonal wurtzite of AZO was observed for pure Ar and Ar/O₂ deposition at room temperature. The growth can be described by the Stranski-Krastanov model, i.e. layer growth plus island growth. An abnormal growth exponent $\beta > 1$ was observed for film thicknesses larger than 20 nm. Additional hydrogen in the sputtering atmosphere deteriorates the crystallinity of the films and makes it even X-ray amorphous, corresponding to the Volmer-Weber model, i.e. island growth. The growth exponent β is decreased to 0.73 in the Ar/10%H₂ atmosphere. AZO films are roughened by additional O₂, whereas smoothed by additional H₂, which is opposite to the ITO films. By using the biaxial strain model, compressive stress of AZO films prepared in Ar/1%O₂, pure Ar and Ar/5%H₂ atmospheres have been calculated to be about 2.5 GPa, 3 GPa and 1.8 GPa respectively, which is much larger than that in ITO films. With increasing sputtering pressure of pure Ar (not shown details in this work), the growth exponent β decreases, i.e. β of 1.47, 0.90, 0.56 for 0.3 Pa, 0.6 Pa, and 1 Pa-depositions, respectively, which is attributed to the decreased deposition rate and reduced ion bombardment as a result of collisional thermalization. When increasing the substrate temperature to 300 °C, as expected, the stress of AZO films prepared in pure Ar relaxed to 0.1 GPa, which smoothens the surface. In the initial growth stage, very typical 3D island growth can be observed for film thicknesses below 50 nm. β was ~ 0 for this region. In the later growth stage, an ordered hillock structure grew with a growth exponent β of 0.57. The overall roughness of AZO films is much larger than that of ITO films which is due to the stronger self-nucleation and *c*-axis preferential growth of ZnO film.

The electrical properties, i.e., resistivity ρ , free carrier concentration n and Hall mobility μ_n of ITO and AZO films prepared in pure Ar at 300 °C as a function of film thickness d_f were also compared. The resistivity of an only 9 nm- thick ITO film ($\rho = 1.9 \cdot 10^{-4} \Omega\text{cm}$) was already much lower than that of the best performance AZO films ($\rho = 7.5 \cdot 10^{-4} \Omega\text{cm}$) prepared in the present work, due to the higher carrier concentration and mobility. The resistivity ρ of AZO films decreases significantly with increasing film thickness up to 55 nm and then shows a weaker variation with further growth, as a result of the inverse trend of n and μ_n . A similar, but weaker reduction of the resistivity for ITO films with further increasing film thickness was also observed. But the electrical properties of ITO are better

than that of AZO films. The higher resistivity of thin AZO films can be explained by the low nuclei density and the formation of discontinuous films which cannot build up the continuous conduction paths, corresponding to the roughness evolution in the initial growth stage ($\beta \sim 0$). The low resistivity of very thin ITO films indicates a high nucleation density. The drop-down transition in resistivity of AZO and ITO films can be assigned to the release of compressive stress with increasing film thickness. After the stress is released, the resistivity is not affected significantly by the thickness.

Growth and morphology evolution of CIGS thin films

The roughness and morphology of chalcopyrite $\text{Cu(In,Ga)}\text{S}_2$ (CIGS) thin films grown on Mo coated glass substrates by a one-step DC reactive magnetron co-sputtering from a copper-gallium alloy (Ga 15 wt.%) target and an indium target in Ar- H_2S gas mixtures was investigated. Spherical granular growth and Volmer-Weber island growth model were observed for CIGS films. In the initial growth stage, a small growth exponent β of 0.13 was obtained which indicates the surface diffusion as the dominant growth mechanism. With increasing surface diffusion effect, β becomes even very small, i.e. ~ 0 .¹⁹⁷ After the transition stage ($d_f > 50$ nm), a larger growth exponent $\beta = 0.56$ was obtained for $50 \text{ nm} < d_f \leq 1000$ nm for room temperature depositions, suggesting an oriented crystallite growth enhanced shadowing effect leading to rough surface. The intrinsic stress, determined by curvature measurements, was around 120 MPa for a 1000 nm thick film. The mean grain size ξ increases with film thickness with a power law relationship: $\xi \sim d_f^{0.33}$. The roughness exponent α obtained from height-height correlation functions and 1D-power spectral density functions is in the range of 0.73~0.89 (local) and 1.15~1.61 (global), respectively.

The formation of a thin film grown by magnetron sputtering starts when the atoms from the vapor phase impinge onto the substrate surface (adsorption/condensation). And then the absorbed atoms may gain enough energy to move across the surface (surface diffusion) or reemission. During the diffusion process, the adatoms will encounter other adatoms/nucleus to form stable islands (nucleation). Lots of distinct islands will grow by incorporating more adatoms and the vapor phase species to coarsen with other islands (crystal growth) and form continuous films with single crystalline or polycrystalline structure (grain growth). The final structure and morphology of the thin film depends on the dominant mechanisms in the nucleation and growth process. For example, the surface diffusion is determined by thermodynamics (i.e. temperature effect) and kinetics (energetic particle energy transfer). The reemission process is depending on the sticking coefficient of the impinging species.

The shadowing effect is generated by the height difference of the initial surface implying that higher surface positions grow faster at the expense of lower positions, which could be the native substrate feature or induced by surface diffusion between grains, or preferential crystal growth which grows faster than other textures. In our sputtering process, different species (i.e. In and Sn for ITO; Zn and Al for AZO; Cu, In and Ga for CIGS) were sputtered from the target and subsequently deposited on the substrate. Besides, negative O ions for oxides and negative S ions for CIGS were also present in the plasma and impinged onto the substrate surface with higher bombardment energy than positive species. And the average energy of the high energetic negative O or S ions is determined by the target voltage, as shown in Table 6.1, i.e., for the 13.56 MHz RF deposition in pure Ar, ~210 eV for ITO target and ~155 eV for AZO target. The discharge voltage in (pulsed) DC is much higher than that in RF mode. Note that higher energetic ion bombardment of the surface increases the surface mobility but also creates more defects on the film and even disturb the film growth. Although the activation energy of surface diffusion for different species is relative low (<0.4 eV), they are very easily trapped in these defect sites. The diffusion barrier becomes higher. It is known that the flux of sputtered target particles follows a cosine distribution in sputtering process which leads to a shadowing effect during growth. The dynamical scaling behavior of 1+1 dimensional ballistic deposition with shadowing has been theoretically studied in terms of uniform angular distribution and cosine distribution of the impinging particles.²¹⁵ Uniform angular distribution condition (standard setting used in the models of shadowing) corresponds to an anisotropic flux of particles on the growing surface and generates β of 1. In contrast, for the ballistic deposition with a cosine distribution implying an isotropic flux which is similar with the condition in sputtering deposition, smaller β value (0.52~0.64) was obtained. Unfortunately, dynamic scaling of 2+1 dimensional ballistic deposition has not been reported yet which can be used to directly compare with the experimental exponents and obtain better understanding of the role of shadowing effect in low temperature sputtering deposition. But the trend of smaller β values than 1 for a cosine distribution should be also present in 2+1 dimensions deposition. The scaling relation of ITO, AZO and CIGS films prepared by DC or RF magnetron sputtering does not obey the traditional dynamic theory and all show anomalous scaling behavior (high β values). Basically, high growth exponents indicate the existence of a destabilizing growth mechanism due to nonlocal effects in the surface dynamics. For our room temperature deposition, even though the substrate temperature increased due to continuous bombardment by high energetic ions, it was still relative low (less than 70 °C).

The effect of bulk diffusion should be insignificant for three different materials. With changing the sputtering atmospheres, the β value increases with increasing the intrinsic stress (i.e. very high stress in ZnO films generates β value as high as 1.47 at RT). With increasing temperature, the stress starts to relax and the adatom diffusion is enhanced and then generates smaller β values than that at low temperature. With increasing discharge voltage, i.e. changing from RF to DC mode, the sputtering rate increases and high energetic bombardment generates high β value. The obtained local roughness exponent (<1) and global roughness exponent (>1) is independent with growth time and sputtering conditions. And we deduced that it is probably due to the crystallinity growth and enhanced shadowing effects plus high bombardments during the sputtering process for the nonlocal effects. Multiscaling and anomalous scaling are very often observed in different materials under different deposition conditions indicating they most probably are characteristic features for polycrystalline thin films grown by magnetron sputtering.

6.2 Outlook

Through the above investigations, a better understanding of the structure and morphology evolution of semiconductor oxides (ITO and AZO) and sulfides (CIGS) prepared by magnetron sputtering process could be achieved. But due to the complexity of different materials and experimental process, a lot of open questions could not be answered. For example, surface diffusion and relaxation normally as local effect smooth the surface and generate small growth exponent. The crystallite growth and shadowing effect as the nonlocal dominant roughening mechanism generate large growth exponent, which only can be qualitatively described through comparison of different β values. It is very hard to quantify the surface diffusion, reemission/resputtering effect induced by negative ion bombardment in the sputtering process. If theoretical works focusing on the simulation of scaling properties in sputtering processes can consider the crystallite growth effect and overcome the computation difficulties in large scales would be a great advantageous to understand the surface scaling for different polycrystalline materials and sputtering process itself. It would be also very interesting to relate other film properties to the different morphologies and the surface scaling.

References

- ¹ S. M. Sze, K. K. Ng: Physics of Semiconductor Devices, 3rd Edition. (John Wiley & Sons, Inc., New Jersey 2007).
- ² A. L. Barabasi, H.E, Stanley: Fractal concepts in surface growth. Cambridge University Press, 0-521-48318-2 Cambridge (1995).
- ³ M. Pelliccione, T. -M. Lu, Evolution of Thin Film Morphology Modeling and Simulations (Springer Series in Materials Science, Vol. 108, 2008).
- ⁴ Y. -P. Zhao, G. -C. Wang, T. -M. Lu: Characterization of Amorphous and Crystalline Rough Surface: Principles and Applications (academic Press, New York 2001).
- ⁵ D. S. Ginley, H. Hosono, D.C. Paine (editors): Handbook of Transparent Conductors. (Springer, New York, 2010).
- ⁶ A. Goetzberger, V. U. Hoffmann: Photovoltaic Solar Energy Generation. (Springer, Berlin, 2005).
- ⁷ P. M. Martin: Introduction to surface engineering and functionally engineered materials. (Wiley 2011, ISBN: 978-0-470-63927-6).
- ⁸ Oura, K., V.G. Lifshits, A.A. Saranin, A.V. Zotov, M. Katayama: Surface Science: An Introduction. (Springer, Berlin 2003, ISBN3-540-00545-5).
- ⁹ J. Venables (2000): Introduction to Surface and Thin Film Processes. Cambridge: Cambridge University Press.2 Pimpinelli, Alberto; Jacques Villain (1998). *Physics of Crystal Growth*. Cambridge: Cambridge University Press, 3.Oura.
- ¹⁰ I. Petrov, P. B. Barna, L. Hultman, J. E. Greene: Microstructural evolution during film growth. *Journal of Vacuum Science & Technology A* **21**, S117 (2003).
- ¹¹ C. V. Thompson: Structure Evolution During Processing of Polycrystalline Films. *Annual Review of Materials Science* **30**, 159 (2000).
- ¹² P. Bruschi, P. Cagnoni, A. Nannini: Temperature-dependent Monte Carlo simulations of thin metal film growth and percolation. *Physical Review B* **55**, 7955 (1997).
- ¹³ L. Xu, C. T. Campbell, H. Jonsson, G. Henkelman: Kinetic Monte Carlo simulations of Pd deposition and island growth on MgO (100). *Surface Science* **601**, 3133 (2007).
- ¹⁴ M. Ohring: The Materials Science of Thin Films, 2nd ed. (Academic Press Inc., San Diego, 2002).
- ¹⁵ J. Bøttiger, J. Chevallier, P. Kringhøj, K. O. Schweitz: Stresses in thin films. *Adhesion Aspects of Thin Films* **1**, 1 (2001).

-
- ¹⁶ B. A. Movchan, A. V. Demchishin: Investigation of the structure and properties of thick vacuum- deposited films of nickel, titanium, tungsten, alumina and zirconium dioxide. *Fizika Metallov i Metallovedenie (Physics of Metals and Metallography)* **28**, 653 (1969).
- ¹⁷ J. A. Thornton: High rate thick film growth. *Annual Review of Materials Science* **7**, 239 (1977).
- ¹⁸ J. A. Thornton, Influence of apparatus geometry and deposition conditions on the structure and topography of thick sputtered coatings. *Journal of Vacuum Science & Technology A* **11**, 666 (1974).
- ¹⁹ R. Messier, A. P. Giri, R. A. Roy: Revised structure zone model for thin film physical structure. *Journal of Vacuum Science & Technology A* **2**, 500 (1984).
- ²⁰ K. Ellmer: Magnetron sputtering of transparent conductive zinc oxide: relation between the sputtering parameters and the electronic properties. *Journal of Physics D-Applied Physics* **33**, R17 (2000).
- ²¹ E. Mirica, G. Kowach, H. Du: Modified Structure Zone Model to Describe the Morphological Evolution of ZnO Thin Films Deposited by Reactive Sputtering. *Crystal Growth & Design* **4**, 157 (2004).
- ²² G. Palasantzas, J. Barnas: Surface-roughness fractality effects in electrical conductivity of single metallic and semiconducting films. *Physical Review B* **56**, 7726 (1997).
- ²³ U. Diebold: The surface science of titanium dioxide. *Surface Science Reports* **48**, 53 (2003).
- ²⁴ F. Family, T. Vicsek: Scaling of the active zone in the Eden process on percolation networks and the ballistic deposition model. *Journal of Physics A - Mathematical and General* **18**, L75 (1985).
- ²⁵ K. Ellmer, in: R. Hippler, H. Kersten, M. Schmidt, K.H. Schoenbach (Eds.), *Low Temperature Plasmas: Fundamentals, Technologies and Techniques*, Wiley-VCH, Berlin, 2008, p. 675, (2).
- ²⁶ S. K. Sinha, E. B. Sirota, S. Garoff, H. B. Stanley: X-ray and neutron scattering from rough surfaces. *Physical Review B* **38**, 2297 (1988).
- ²⁷ J. M. López, M. A. Rodriguez, R. Cuerno: Superroughening versus intrinsic anomalous scaling of surfaces. *Physical Review E* **56**, 3993 (1997).
- ²⁸ J. M. López: Scaling Approach to Calculate Critical Exponents in Anomalous Surface Roughening. *Physical Review Letters* **83**, 4594 (1999).
- ²⁹ J. M. López, Mario Castro, R. Gallego: Scaling of Local Slopes, Conservation Laws, and Anomalous Roughening in Surface Growth. *Physical Review Letters* **94**, 166103 (2005).

- ³⁰ S. Huo, W. Schwarzacher: Anomalous Scaling of the Surface Width during Cu Electrodeposition. *Physical Review Letters* **86**, 256 (2001).
- ³¹ J. J. Ramasco, J.M. López, M.A. Rodriguez: Generic dynamic scaling in kinetic roughening. *Physical Review Letters* **84**, 2199 (2000).
- ³² F. Ojeda, R. Cuerno, R. Salvarezza, L. Vázquez: Dynamics of Rough Interfaces in Chemical Vapor Deposition: Experiments and a Model for Silica Films. *Physical Review Letters* **84**, 3125 (2000).
- ³³ A. Yanguas-Gil, J. Cotrino, A. Walkiewicz-Pietrzykowska, A. R. González-Elipe: Scaling behavior and mechanism of formation of SiO₂ thin films grown by plasma-enhanced chemical vapor deposition. *Physical Review B* **76**, 075314 (2007).
- ³⁴ J. H. Jeffries, J. -K. Zuo, M. M. Craig: Instability of Kinetic Roughening in Sputter-Deposition Growth of Pt on Glass. *Physical Review Letters* **76**, 4931 (1996).
- ³⁵ S. Huo, W. Schwarzacher: Anomalous Scaling of the Surface Width during Cu Electrodeposition. *Physical Review Letters* **86**, 256 (2001).
- ³⁶ X. D. Zhu, H. Naramoto, Y. Xu, K. Narumi, K. Miyashita: Coarsening dynamics and surface instability during ion-beam-assisted growth of amorphous diamondlike carbon. *Physical Review B* **66**, 165426 (2002).
- ³⁷ J. M. Kim, J. M. Kosterlitz: Growth in a restricted solid-solid model. *Physical Review Letters* **62**, 2289 (1989).
- ³⁸ M. J. Vold: Computer simulation of floc formation in a colloidal suspension. *Journal of Colloidal Science* **18**, 684 (1963).
- ³⁹ D. Y. K. Ko, Flavio Seno: Simulations of deposition growth models in various dimensions: The possible importance of overhangs. *Physical Review E* **50**, R1741 (1994).
- ⁴⁰ P. Meakin, P. Ramanlal, L. M. Sander, R. C. Ball: Ballistic deposition on surfaces. *Physical Review A* **34**, 5091 (1986).
- ⁴¹ R. Baiod, D. Kessler, P. Ramanlal, L. Sander, R. Savit: Dynamical scaling of the surface of finite-density ballistic aggregation. *Physical Review A* **38**, 3672 (1988).
- ⁴² M. Eden, in Proceedings of the Fourth Berkeley Symposium on Mathematical Statistics and Probability, Volume 4: Biology and Problems of Health, edited by J. Neyman (University of California Press, Berkeley 1961), pp.223-239.
- ⁴³ S. T. Chui, J. D. Weeks: Dynamics of the roughening transition. *Physical Review Letters* **40**, 733 (1978).
- ⁴⁴ S. F. Edwards, D. R. Wilkinson: The surface statistics of a granular aggregate. *Proceedings of the Royal Society of London Series A* **381**, 17 (1982)
- ⁴⁵ W. W. Mullins: Theory of Thermal Grooving. *Journal of Applied Physics* **28**, 333 (1957).

-
- ⁴⁶ L. -H. Tang, T. Nattermann: Kinetic roughening in molecular-beam epitaxy. *Physical Review Letters* **66**, 2899 (1991).
- ⁴⁷ A. Zangwill, C.N. Luse, D.D. Vvedensky, M. R. Willby: Equations of motion for epitaxial growth. *Surface Science* **274**, 529 (1992).
- ⁴⁸ T. M. Lu, H. -N. Yang, G. C. Wang: When interface gets rough....*Material Research Society Symposium Proceedings* **367**, 283 (1995).
- ⁴⁹ M. Kardar, G. Parisi, Y.C.Zhang: Dynamic scaling of growing interfaces. *Physical Review Letters* **56**,889(1986).
- ⁵⁰ M. Plischke, Z.Racz: Dynamic scaling and the surface structure of Eden clusters. *Physical Review A* **32**, 3825 (1985).
- ⁵¹ D. E. Wolf, J. Villain: Growth with Surface Diffusion. *Europhysics Letters* **13**, 389 (1990).
- ⁵² Z. -W. Lai, S. Das Sarma: Kinetic Growth with Surface Relaxation: Continuum versus Atomistic Models. *Physical Review Letters* **66**, 2348 (1991).
- ⁵³ J. T. Drotar, Y. -P. Zhao, T. -M. Lu, G. C. Wang: Numerical analysis of the noisy Kuramoto-Sivashinsky equation in 2+1 dimensions. *Physical Review E* **59**, 177 (1991).
- ⁵⁴ S. Majaniemi, T. Ala-Nissila, J. Krug: Kinetic roughening of surfaces: Derivation, solution, and application of linear growth equations. *Physical Review B* **53**, 8071 (1996).
- ⁵⁵ Y. -P. Zhao, J. T. Drotar, G. -C. Wang, T.-M. Lu: Morphology Transition during Low-Pressure Chemical Vapor Deposition. *Physical Review Letters* **87**,136102 (2001).
- ⁵⁶ R. P. U. Karunasiri, R. Bruinsma, J. Rudnick: Thin-film growth and the shadowing instability. *Physical Review Letters* **62**, 788 (1989).
- ⁵⁷ G. S. Bales, R. Bauinsma, E. A. Eklund, R.P.U. Karunasiri, J. Rudnick, A. Zangwill: Growth and erosion of thin solid films. *Science* **249**, 264 (1990).
- ⁵⁸ C. Tang, S. Alexander, R. Bruinsma: Scaling theory for the growth of amorphous film. *Physical Review Letters* **64**, 772 (1990).
- ⁵⁹ G. S. Bales, A. Zangwill: Growth Dynamics of Sputter Deposition. *Physical Review Letters* **63**, 692 (1989).
- ⁶⁰ J. H. Yao, H. Guo: Shadowing instability in three dimensions. *Physical Review E* **47**, 1007 (1993).
- ⁶¹ J. T. Drotar, Y.-P. Zhao, T.-M. Lu, G.-C. Wang: Surface roughening in shadowing growth and etching in 2+1 dimensions. *Physical Review B* **62**, 2118 (2000).
- ⁶² T. -M. Lu, Y. -P. Zhao, J.T. Drotar, T. Karabacak, G. -C. Wang: Novel mechanisms on the growth morphology of films. In: Morphological and Compositional Evolution of Thin

- Films, ed by M. J. Aziz, N.C. Bartelt, I. Berbezier, J. B. Hannon, S.J. Hearne. *Material Research Society Proceedings* **749**, W1.2 (2003).
- ⁶³ M. Pelliccione, T. Karabacak, C. Gaire, G.-C. Wang, T.-M. Lu: Mound formation in surface growth under shadowing. *Physical Review B* **74**, 125420 (2006).
- ⁶⁴ A. E. Lita, J. E. Sanchez, Jr.: Effects of grain growth on dynamic surface scaling during the deposition of Al polycrystalline thin films, *Physical Review B* **61**, 7692 (2000).
- ⁶⁵ J. J. Yang, K. W. Xu: Characterization of multiscale surface evolution of polycrystalline copper thin films. *Journal of Applied Physics* **101**, 104902 (2007).
- ⁶⁶ J. Santamaria, M. E. Gomez, J. L. Vicent, K M. Krishnan, I. K. Schuller: Scaling of the Interface Roughness in Fe-Cr Superlattices: Self-Affine versus Non-Self-Affine, *Physical Review Letters* **89**, 190601 (2002).
- ⁶⁷ J. -P. Schlomka, M. Tolan, W. Press: In situ growth study of NiMnSb films on MgO (001) and Si (001), *Applied Physics Letters* **76**, 2005 (2000).
- ⁶⁸ M. A. Auger, L. Vázquez, R. Cuerno, M. Castro, M. Jergel, O. Sánchez: Intrinsic anomalous surface roughening of TiN films deposited by reactive sputtering. *Physical Review B* **73**, 045436 (2006).
- ⁶⁹ B. W. Karr, I. Petrov, P. Desjardins, D. G. Cahill, J. E. Greene: InCtu scanning tunneling microscopy studies of the evolution of surface morphology and microstructure in epitaxial TiN (001) grown by ultra-high-vacuum reactive magnetron sputtering, *Surface and Coating Technology* **94-95**, 403 (1997).
- ⁷⁰ J. H. Xu, L. H. Yu, I. Kojima: Surface evolution of nanostructured CrN and Si₃N₄ films, *Journal of Applied Physics* **94**, 6827 (2003).
- ⁷¹ I. J. Lee, J. W. Kim, T. B. Hur, Y. H. Hwang, H. K. Kim, Synchrotron x-ray scattering study on the evolution of surface morphology of the InN/Al₂O₃(0001) system, *Applied Physics Letters* **81**, 475 (2002).
- ⁷² B. Q. Li, I. Kojima, J. M. Zuo: Surface evolution of ultrahigh vacuum magnetron sputter deposited amorphous SiO₂ thin films, *Journal of Applied Physics* **91**, 4082 (2002).
- ⁷³ H. J. Qi, L. H. Huang, Z. S. Tang, C. F. Cheng, J. D. Shao, Z. X. Fan: Roughness evolution of ZrO₂ thin films grown by reactive ion beam sputtering, *Thin Solid Films* **444**, 146 (2003).
- ⁷⁴ F. M. Penning, J. H. A. Moubis: Cathode Sputtering in a Magnetic Field. *Proceedings of the Koninklijke Nederlandse Akademie van Wetenschappen* **43**, 41 (1940).
- ⁷⁵ F. M. Penning: Rectifying device. *US Patent* No. 2,182,736 (1939).
- ⁷⁶ S. Schiller, U. Heisig, K. Goedicke: Electron-beam evaporation and high-rate sputtering with plasmatron-magnetron systems-comparison. *Vakuum-Technik* **27**, 51 (1978).

- ⁷⁷ S. Schiller, U. Heisig, K. Goedicke: Electron-beam evaporation and high-rate sputtering with plasmatron-magnetron systems-comparison.2. *Vakuum-Technik* **27**, 75 (1978).
- ⁷⁸ P. J. Kelly, R. D. Arnell: Magnetron sputtering: a review of recent developments and applications. *Vacuum* **56**, 159 (2000).
- ⁷⁹ J. L. Vossen, W. Kern: Thin Film Processes II. Academic Press 1991, ISBN 978-0-08-052421-4.
- ⁸⁰ J. Szczyrbowski, A. Dietrich, K. Hartig: Bendable silver-based low emissivity coating on glass. *Solar Energy Materials* **19**, 43 (1989).
- ⁸¹ A. Rochkett: The Materials Science of Semiconductors. Springer Science, 2008, ISBN 978-0-387-25653-5.
- ⁸² S. Seeger, PhD thesis, Technische Universität Berlin, 2006.
- ⁸³ B. Szyszka: Magnetron Sputtering of ZnO Films, in Transparent Conductive Zinc Oxide: Basics and Applications in Thin Film Solar Cells, edited by K. Ellmer, A. Klein and B. Rech (Springer, Berlin, 2008), pp. 187-233.
- ⁸⁴ H. P. Klug, L. E. Alexander: X-ray Diffraction Procedures for Polycrystalline and Amorphous Materials (John Wiley & Sons, New York, 1974).
- ⁸⁵ P. Thompson, D. E. Cox, J. B. Hastings: Rietveld Refinement of Debye-Scherrer Synchrotron X-ray Data from Al_2O_3 . *Journal of Applied Crystallography* **20**, 79 (1987).
- ⁸⁶ P. Scherrer: Bestimmung der Gröss Kolloidteilchen und der Inneren Skruktur von Kolloidterlchen Mittels Röntgenstrahlen, Nachrichten von der Gesellschaft der Wissenschaften, Göttingen. *Mathematisch-Physikalische Klasse* **2**, 98, (1918).
- ⁸⁷ Rodriguez-Carvajal: FULLPROF: A program for rietveld refinement and pattern matching analysis in: Abstracts of the satellite meeting on powder diffraction of the XV congress of the IUCr, Toulouse, France, (1990) p. 127
- ⁸⁸ B. Bechhoff, B. Kanngießer, N. Langhoff, R. Wedell, H. Woff (Eds.): Handbook of Practical X-Ray Fluorescence Analysis, Springer-Verlag Berlin Heidelberg 2006.
- ⁸⁹ XE-100, User's Manual, Park System, 2002.
- ⁹⁰ C. Teichert, I. Beinik: Conductive Atomic-Force Microscopy Investigation of Nanostructure in Microelectronics in 'Scanning Probe Microscopy in Nanoscience and Nanotechnology', Vol.2, Edited by B. Bhushan, (Springer Berlin 2011), 691-721.
- ⁹¹ T. G. Finstad, E. -K. Chu: Rutherford Backscattering Spectrometry on Thin Solid Films in Analytical Techniques For Thin Films, Edited by K. N. Tu, R. Rosenberg, *Treatise on Materials Science and Technology* **27**, 392 (1988).
- ⁹² L. van der Pauw: A Method of Measuring Specific Resistivity and Hall Effect of Discs of Arbitrary Shape. *Philips Research Reports* **13**, 1 (1958).

- ⁹³ S. Ishibashi, Y. Higuchi, Y. Ota, and K. Nakamura: Low resistivity indium–tin oxide transparent conductive films. II. Effect of sputtering voltage on electrical property of films. *Journal of Vacuum Science & Technology A* **8**, 1403 (1990).
- ⁹⁴ H. Kim, A. Piqué, J. S. Horwitz, H. Mattoussi, H. Murata, Z. H. Kafafi, D. B. Chrisey: Indium tin oxide thin films for organic light-emitting devices. *Applied Physics Letters* **74**, 3444 (1999).
- ⁹⁵ J. Yang, A. Banerjee, S. Guha: Triple-junction amorphous silicon alloy solar cell with 14.6% initial and 13.0% stable conversion efficiencies. *Applied Physics Letters* **70**, 2975 (1997).
- ⁹⁶ K. Bädcker: Über die elektrische Leitfähigkeit und die thermoelektrische Kraft einiger Schwermetallverbindungen. *Annalen der Physik* **22**, 749 (1907).
- ⁹⁷ K. Ishiguro, T. Sasaki, T. Arai, I. Imai: Optical and Electrical Properties of Tin Oxide Films. *Journal of Physical Society of Japan* **13**, 296 (1958).
- ⁹⁸ Y. Shigesato, S. Takaki, T. Haranou: Crystallinity and electrical properties of tin-doped indium oxide films deposited by DC magnetron sputtering. *Applied Surface Science* **48/49**, 269 (1991).
- ⁹⁹ Y. Shigesato, N. Shin, M. Kamei, P. K. Song, I. Yasui: Study on fluorine-doped indium oxide films deposited by RF magnetron sputtering. *Japanese Journal of Applied Physics* **39**, 6422 (2000).
- ¹⁰⁰ T. Minami, H. Nanto, S. Takata: Highly Conductive and Transparent Aluminum Doped Zinc Oxide Thin Films Prepared by RF Magnetron Sputtering. *Japanese Journal of Applied Physics* **23**, L280 (1984).
- ¹⁰¹ B. H. Choi, H. B. Im, J. S. Song: Electrical Properties of Gallium-Doped Zinc Oxide Films Prepared by RF Sputtering. *Journal of the American Ceramic Society* **73**, 1347 (1990).
- ¹⁰² H. K. Muller: Electrical and Optical Properties of Sputtered In_2O_3 Films. *Physica Status. Solidi* **27**, 723 (1968).
- ¹⁰³ I. Hamberg, C. G. Granqvist, K. F. Berggren, B. E. Sernelius, L. Engström: Band-gap widening in heavily Sn-doped In_2O_3 . *Physical Review B* **30**, 3240 (1984).
- ¹⁰⁴ A. Walsh, J. L. F. Da Silva, S. H. Wei, C. Körber, A. Klein, L. F. J. Piper, A. DeMasi, K. E. Smith, G. Panaccione, P. Torelli, D. J. Payne, A. Bourlange, R. G. Egdell: Nature of the band gap of In_2O_3 revealed by first-principles calculations and x-ray spectroscopy. *Physical Review Letters* **100**, 167402 (2008).
- ¹⁰⁵ P. D. C. King, T. D. Veal, F. Fuchs, Ch. Y. Wang, D. J. Payne, A. Bourlange, H. Zhang, G. R. Bell, V. Cimalla, O. Ambacher, R. G. Egdell, F. Bechstedt, C. F. McConville: Band

gap, electronic structure, and surface electron accumulation of cubic and rhombohedral In_2O_3 . *Physical Review B* **79**, 205211 (2009).

¹⁰⁶ K. L. Chopra, S. Major, D. K. Pandya, "Transparent Conductors - A Status Review". *Thin Solid Films* **102**, 1 (1983).

¹⁰⁷ M. Marezio: Refinement of the Crystal Structure of In_2O_3 at two Wavelengths. *Acta Crystallographica* **20**, 723 (1966).

¹⁰⁸ P. Nath, R. F. Bunshah: Preparation of In_2O_3 and tin-doped In_2O_3 films by a novel activated reactive evaporation technique. *Thin Solid Films* **69**, 63 (1980).

¹⁰⁹ R. W. G. Wyckoff: Crystal Structures, 2nd ed. (Wiley, New York, 1964), vol. 2, p.2.

¹¹⁰ H. W. Lehmann, R. Widmer: Preparation and properties of reactively co-sputtered transparent conducting films. *Thin Solid Films* **27**, 359 (1975).

¹¹¹ J. L. Vossen: RF Sputtered Transparent Conductors System In_2O_3 - SnO_2 . *RCA Review* **32**, 289 (1971).

¹¹² J. C. C. Fan, F. J. Bachner, G. H. Foley: Effect of O_2 pressure during deposition on properties of rf-sputtered Sn-doped In_2O_3 films. *Applied Physics Letters* **31**, 773 (1977).

¹¹³ S. Kulaszewicz: Electrical optical and structural properties of thin films of In_2O_3 :Sn deposited by hydrolysis. *Thin Solid Films* **76**, 89 (1981).

¹¹⁴ D. B. Fraser, H. D. Cook: Highly Conductive, Transparent Films of Sputtered $\text{In}_{2-x}\text{Sn}_x\text{O}_{3-y}$. *Journal of the Electrochemical Society* **119**, 1368 (1972).

¹¹⁵ J. C. C. Fan, F. J. Bachner: Properties of Sn-Doped In_2O_3 Films Prepared by RF Sputtering. *Journal of the Electrochemical Society* **112**, 1719 (1975).

¹¹⁶ K. Itoyama: Properties of Sn-Doped Indium Oxide Prepared by High Rate and Low Temperature RF Sputtering. *Japanese Journal of Applied Physics* **17**, 1191 (1978).

¹¹⁷ M. Kamei, T. Yagami, S. Takaki, Y. Shigesato: Heteroepitaxial growth of tin-doped indium oxide films on single crystalline yttria stabilized zirconia substrates. *Applied Physics Letters* **64**, 2712 (1994).

¹¹⁸ H. R. Fallah, M. Ghasemi, A. Hassanzadeh, H. Steki: The effect of annealing on structural, electrical and optical properties of nanostructured ITO films prepared by e-beam evaporation. *Materials Research Bulletin* **42**, 487 (2007).

¹¹⁹ T. -K. Yong, S. -S. Tan, C. -H. Nee, S. -S. Yap, Y. -Y. Kee, G. Safran, Z.E. Horvath, J. Moscatello, Y. -K. Yap, T. -Y. Tou: Pulsed laser deposition of indium tin oxide nanowires in argon and helium. *Materials Letters* **66**, 280 (2012).

- ¹²⁰ H. El Rhaleb, E. Benamar, M. Rami, J. P. Roger, A. Hakam, A. Ennaoui: Spectroscopic ellipsometry studies of index profile of indium tin oxide films prepared by spray pyrolysis. *Applied Surface Science* **201**, 138 (2002).
- ¹²¹ C. Jonda, ABR Mayer, U. Stolz, A. Elschner, A. Karbach: Surface roughness effects and their influence on the degradation of organic light emitting devices. *Journal of Materials Science* **35**, 5645 (2000).
- ¹²² KB. Kim, YH. Tak, YS. Han, KH. Baik, MH. Yoon, MH. Lee: Relation between surface roughness of Indium tin oxide and leakage current of organic light-emitting diode, *Japanese Journal of Applied Physics* **42**, L438 (2003).
- ¹²³ V. Korobov, M. Leibovitch, Y. Shapria: Structure and conductance evolution of very thin indium oxide films, *Applied Physics Letters* **65**, 18 (1994).
- ¹²⁴ X. W. Sun, H. C. Huang, H. S. Kwok: On the initial growth of indium tin oxide on glass. *Applied Physics Letters* **68**, 19 (1996).
- ¹²⁵ Y. Shigesato, R. Koshi-ishi, T. Kawashima, J. Ohsako: Early stages of ITO deposition on glass or polymer substrates. *Vacuum* **59**, 614 (2000).
- ¹²⁶ Y. Sato, M. Taketomo, N. Ito, A. Miyamura, Y. Shigesato: Comparative study on early stages of film growth for transparent conductive oxide films deposited by dc magnetron sputtering. *Thin Solid Films* **516**, 4598 (2008).
- ¹²⁷ Y. G. Han, DW. Kim, J. S. Cho, Y. W. Beag, S. K. Koh, V.S. Chernysh: Effects of substrate treatment on the initial growth mode of indium-tin-oxide films. *Journal of Applied Physics* **97**, 024910 (2005).
- ¹²⁸ K. H. L. Zhang, A. Walsh, C. R. A. Catlow, V. K. Lazarov, R. G. Egdell: Surface Energies Control the Self-Organization of Oriented In_2O_3 Nanostructures on Cubic Zirconia. *Nano Letters* **10**, 3740 (2010).
- ¹²⁹ K. H. L. Zhang, V. K. Lazarov, T. D. Veal, F. E. Oropeza, C. F. McConville, R. G. Egdell A. Walsh: Thickness dependence of the strain, band gap and transport properties of epitaxial In_2O_3 thin films grown on Y-stabilised $\text{ZrO}_2(111)$. *Journal of Physics-Condensed Matter* **23**, 334211 (2011).
- ¹³⁰ O. Bierwagen, J.S. Speck: Nucleation of islands and continuous high-quality $\text{In}_2\text{O}_3(001)$ films during plasma-assisted molecular beam epitaxy on Y-stabilized $\text{ZrO}_2(001)$. *Journal of Applied Physics* **107**, 113519 (2010).
- ¹³¹ D. Raoufi, F. Hosseinpanahi: The effect of film thickness on surface morphology of ITO thin films. *Journal of Theoretical and Applied Physics* **7**, 21 (2013).
- ¹³² H. Wang, H. Liu, W.Y. Ding, W.P. Chai: Study on the growth mechanism of tin-doped indium oxide films deposited by direct current pulse magnetron sputtering. *Thin Solid Films* **542**, 415 (2013).

- ¹³³ M. Nie, T. Mete, and K. Ellmer: Morphology and structure evolution of tin-doped indium oxide thin films deposited by radio-frequency magnetron sputtering: The role of the sputtering atmosphere. *Journal of Applied Physics* **115**, 154905 (2014).
- ¹³⁴ D. Mergel, W. Stass, G. Ehl, D. Barthel: Oxygen incorporation in thin films of $\text{In}_2\text{O}_3\text{:Sn}$ prepared by radio frequency sputtering. *Journal of Applied Physics* **88**, 2347 (2000).
- ¹³⁵ R. Mientus, K. Ellmer: Reactive magnetron sputtering of tin-doped indium oxide (ITO): influence of argon pressure and plasma excitation mode. *Surface and Coatings Technology* **142-144**, 748 (2001).
- ¹³⁶ Y. J. Kim, S. B. Jin, S. I. Kim, Y. S. Choi, In S. Choi, J. G. Han: Effect of oxygen flow rate on ITO thin films deposited by facing targets sputtering. *Thin Solid Films* **518**, 6241 (2010).
- ¹³⁷ K. Ellmer, R. Mientus, V. Weiß, H. Rossner: In situ energy-dispersive x-ray diffraction system for time-resolved thin-film growth studies. *Measurement Science & Technology* **14**, 336 (2003).
- ¹³⁸ S. Jun, T. E. McKnight, M. L. Simpson, P. D. Rack: A statistical parameter study of indium tin oxide thin films deposited by radio-frequency sputtering. *Thin Solid Films* **476**, 59 (2005).
- ¹³⁹ P. Thilakan, C. Minarini, S. Lorei, E. Terzini: Investigations on the crystallization properties of RF magnetron sputtered indium tin oxide thin films. *Thin Solid Films* **388**, 34 (2001).
- ¹⁴⁰ M. Mizuhashi: Electrical Properties of Vacuum-Deposited Indium Oxide and Indium Tin Oxide Films. *Thin Solid Films* **70**, 91 (1980).
- ¹⁴¹ M. Mizuno, T. Miyamoto, T. Ohnishi, H. Hayashi: Effects of Tin Doping and Oxygen Vacancies on the Electronic States of Indium Oxide. *Japanese Journal of Applied Physics* **36**, 3408 (1997).
- ¹⁴² T. Nagatomo, V. Maruta, O. Omoto: Electrical and optical properties of vacuum-evaporated indium-tin oxide films with high electron mobility. *Thin Solid Films* **192**, 17 (1990).
- ¹⁴³ P. Agoston, K. Albe: Thermodynamic stability, stoichiometry, and electronic structure of bcc- In_2O_3 surfaces. *Physical Review B* **84**, 045311 (2011).
- ¹⁴⁴ S. H. Kim, C. Yoon: Comparison of ITO prepared by capacitive RF magnetron sputtering and DC facing target sputtering as an anode on the organic light emitting diode. *Physica Status Solidi A* **206**, 2206 (2009).

- ¹⁴⁵ T. Welzel, K. Ellmer: Negative oxygen ion formation in reactive magnetron sputtering processes for transparent conductive oxides. *Journal of Vacuum Science & Technology A* **30**, 061306 (2012).
- ¹⁴⁶ P. K. Song, Y. Shigesato, I. Yasui, C.W. Ow-Yang, D.C.Paine: Study of Crystallinity of Tin-Doped Indium Oxide Films Deposited by DC Magnetron Sputtering. *Japanese Journal of Applied Physics* **37**, 1870 (1998).
- ¹⁴⁷ M. Bender, J. Trube, J. Stollenwerk: Characterization of a RF/dc-magnetron discharge for the sputter deposition of transparent and highly conductive ITO films. *Applied Physics A* **69**, 397 (1999).
- ¹⁴⁸ F. Horstmann, V. Sittinger, B. Szyszka: Heat treatable indium tin oxide films deposited with high power pulse magnetron sputtering. *Thin Solid Films* **517**, 3178 (2009).
- ¹⁴⁹ M. Kamei, Y. Shigesato, S. Takaki: Origin of characteristic grain-subgrain structure of tin-doped indium oxide films. *Thin Solid Films* **259**, 38 (1995).
- ¹⁵⁰ Y. Shigesato, D. C. Paine: A microstructural study of low resistivity tin-doped indium oxide prepared by d.c. magnetron sputtering. *Thin Solid Films* **238**, 44 (1994).
- ¹⁵¹ V. Sittinger, F. Ruske, W. Werner, C. Jacobs, B. Szyszka, D. J. Christie: High power pulsed magnetron sputtering of transparent conducting oxides. *Thin Solid Films* **516**, 5847 (2008).
- ¹⁵² E. Fortunato, D. Ginley, H. Hosono, D. C. Paine: Transparent conducting oxides for photovoltaics. *Materials Research Society Bulletin* **32**, 242 (2007).
- ¹⁵³ H. J. Ko, Y.F. Chen, S. K. Hong, H. Wenisch, T. Yao: Ga-doped ZnO films grown on GaN templates by plasma-assisted molecular-beam epitaxy. *Applied Physics Letters* **77**, 3761 (2000).
- ¹⁵⁴ Ü. Özgür, Ya. I. Alivov, C. Liu, A. Teke, M. A. Reshchikov, S. Doğan, V. Avrutin, S.-J. Cho, H. Morkoç: A comprehensive review of ZnO materials and devices. *Journal of Applied Physics* **98**, 041301 (2005).
- ¹⁵⁵ G. Heiland, P. Kunstmann, H. Pfister: Polare Eigenschaften von Zinkoxyd-Kristallen, *Zeitschrift für Physik* **176**, 485 (1963).
- ¹⁵⁶ Y. E. Lee, Y. J. Kim, H. J. Kim: Thickness dependence of microstructural evolution of ZnO films deposited by rf magnetron sputtering. *Journal of Material Research* **13**, 1260 (1998).
- ¹⁵⁷ M. Chen, Z.L. Pei, X. Wang, C. Sun, L. S. Wen: Dependence of structural, electrical, and optical properties of ZnO: Al films on substrate temperature. *Journal of Material Research* **16**, 2118 (2001).
- ¹⁵⁸ B. Szyszka: Transparent and conductive aluminum-doped zinc oxide films prepared by mid-frequency reactive magnetron sputtering. *Thin Solid Films* **351**, 164 (1999).

- ¹⁵⁹ A. Bikowski, K. Ellmer: Influence of the deposition temperature on electronic transport and structural properties of radio frequency magnetron-sputtered $\text{Zn}_{1-x}\text{Mg}_x\text{O}:\text{Al}$ and $\text{ZnO}:\text{Al}$ films. *Journal of Material Research* **27**, 2249 (2012).
- ¹⁶⁰ A. Segmüller, M. Murakami, in *Analytical Techniques for Thin Films*, edited by K. N. Tu & R. Tosenberg (Academic, Boston, 1988), p. 143.
- ¹⁶¹ E. Mollwo, in *Landoldt-Börnstein. Zahlenwerte und Funktionen aus Naturwiss. u. Technik. Neue Serie*, edited by O. Madelung, M. Schulz, and H. Weiss (Springer, Berlin, 1982), p.35.
- ¹⁶² C. G. Ching, S. C. Lee, S.S. Ng, Z. Hassan, H. Abu Hassan: Infrared reflectance studies of hillock-like porous zinc oxide thin films. *Thin Solid Films* **539**, 70 (2013).
- ¹⁶³ E. Vasco, C. Zaldo, L. Vazquez: Growth evolution of ZnO films deposited by pulsed laser ablation. *Journal of Physics Condense Matter* **13**, L663 (2001).
- ¹⁶⁴ D. C. Kim, B. H. Kong, S. O. Jun, H. K. Cho, D. J. Park, J. Y. Lee: Pressure dependence and micro-hillock formation of ZnO thin films grown at low temperature by MOCVD. *Thin Solid Films* **516**, 5562 (2008).
- ¹⁶⁵ M. H. Huang, S. Mao, H. Feick, H.Q. Yan, Y.Y. Wu, H. Kind, E. Weber, R. Russo, P. D. Yang: Room-Temperature Ultraviolet Nanowire Nanolasers. *Science* **292**, 1897 (2001).
- ¹⁶⁶ S. Hayamizu, H. Tabata, H. Tanaka, T. Kawai: Preparation of crystallized zinc oxide films on amorphous glass substrates by pulsed laser deposition. *Journal of Applied Physics* **80**, 787 (1996).
- ¹⁶⁷ T. B. Hur, Y.H. Hwang, H.K. Kim: Study of the structural evolution in ZnO thin film by in situ synchrotron x-ray Scattering. *Journal of Applied Physics* **96**, 1740 (2004).
- ¹⁶⁸ Y. Kajikawa: Texture development of non-epitaxial polycrystalline ZnO films. *Journal of Crystal Growth* **289**, 387 (2006).
- ¹⁶⁹ N. Fujimura, T. Nishihara, S. Goto, J. Xu, T. Ito: Control of preferred orientation for ZnO_x films- control of self-texture. *Journal of Crystal Growth* **130**, 269 (1993).
- ¹⁷⁰ C. G. Van de Walle: Hydrogen as a cause of doping in zinc oxide. *Physical Review Letters* **85**, 1012 (2000).
- ¹⁷¹ D. G. Thomas, J. J. Lander: Hydrogen as a donor in zinc oxide. *Journal of Chemical Physics* **25**, 1136 (1956).
- ¹⁷² D. M. Hofmann, A. Hofstaetter, F. Leiter, H. Zhou, F. Henecker, B. K. Meyer, S. B. Orlinskii, J. Schmidt, P. G. Baranov: Hydrogen: A relevant shallow donor in zinc oxide. *Physical Review Letters* **88**, 045504 (2002).
- ¹⁷³ S. F. J. Cox, E. A. Davis, S. P. Cottrell, P. J. C. King, J. S. Lord, J. M. Gil, H. V. Alberto, R. C. Vilao, J. Piroto Duarte, N. Ayres de Campos, A. Weidinger, R. L. Lichti, S.

J. C. Irvine: Experimental confirmation of the predicted shallow donor hydrogen state in zinc oxide. *Physical Review Letters* **86**, 2601 (2001).

¹⁷⁴ J. Jia, A. Takasaki, N. Oka, Y. Shigesato: Experimental observation on the Fermi level shift in polycrystalline Al-doped ZnO films. *Journal of Applied Physics* **112**, 013718 (2012).

¹⁷⁵ D. -H. Kim, S. -H. Lee, G. -H. Lee, H. -B. Kim, K. H. Kim, Y. -G. Lee, T. -H. Yu: Effects of deposition temperature on the effectiveness of hydrogen doping in Ga-doped ZnO thin films. *Journal of Applied Physics* **108**, 023520 (2010).

¹⁷⁶ A. Bikowski, PhD thesis, Humboldt-Universität Berlin, 2013.

¹⁷⁷ P. Jackson, D. Hariskos, E. Lotter, S. Paetel, R. Wuerz, R. Menner, W. Wischmann, M. Powalla: New world record efficiency for Cu(In,Ga)Se₂ thin-film solar cells beyond 20%. *Progress in Photovoltaics: Research and Application* **19**, 894 (2011).

¹⁷⁸ ZSW: press release (23.10.2013) [http://www.zsw-de/infoportal/presseinformationen/presse-detail/zsw-stellt-weltrekord-solarzelle-her.html](http://www.zsw.de/infoportal/presseinformationen/presse-detail/zsw-stellt-weltrekord-solarzelle-her.html).

¹⁷⁹ T. Unold, I. Sieber, K. Ellmer: Efficient CuInS₂ solar cells by reactive magnetron sputtering. *Applied Physics Letter* **88**, 213502 (2006).

¹⁸⁰ S. Merdes, D. Abou-Ras, R. Mainz, R. Klenk, M. Ch. Lux-Steiner, A. Meeder, H. W. Schock, J. Klaer: CdS/Cu(In,Ga)S₂ based solar cells with efficiencies reaching 12.9% prepared by a rapid thermal process. *Progress in Photovoltaics: Research and Application* **21**, 88 (2013).

¹⁸¹ CH. Chen, TY. Lin, CH. Hsu, SY. Wei, CH. Lai: Comprehensive characterization of Cu-rich Cu(In,Ga)Se₂ absorbers prepared by one-step sputtering process. *Thin Solid Films* **535**, 122 (2013).

¹⁸² A. J. Zhou, D. Mei, X. G. Kong, X. H. Xu, L. D. Feng, X. Y. Dai, T. Gao, J. Z. Li: One-step synthesis of Cu(In,Ga)Se₂ absorber layers by magnetron sputtering from a single quaternary target. *Thin Solid Films* **520**, 6068 (2012).

¹⁸³ JH. Moon, HW. Choi, KH. Kim, JH. Kim, SJ. Park: Preparation of Mo/Cu(In, Ga)Se₂ Thin Films by One-Step Sputtering. *Journal of Nanoscience and Nanotechnology* **12**, 656 (2012).

¹⁸⁴ L. Ribeaucourt, E. Chassaing, G. Savidand, D. Lincot: Synthesis of Cu(In,Ga)Se₂ absorber using one-step electrodeposition of Cu-In-Ga precursor. *Thin Solid Films* **519**, 7241 (2011).

¹⁸⁵ S. Seeger, K. Ellmer: Reactive magnetron sputtering of CuInS₂ absorbers for thin film solar cells: Problems and prospects. *Thin Solid Films* **517**, 3143 (2009).

¹⁸⁶ M. Gossila, Th. Hahn, H. Metzner, J. Conrad, U. Geyer: Thin CuInS₂ films by three-source molecular beam deposition. *Thin Solid Films* **268**, 39 (1995).

- ¹⁸⁷ T. Walter, H. W. Schock: Crystal growth and diffusion in Cu(In, Ga)Se₂ chalcopyrite thin films. *Thin Solid Films* **224**, 74 (1993).
- ¹⁸⁸ D. Liao, A. Rockett: Epitaxial growth of Cu(In,Ga)Se₂ on GaAs(110). *Journal of Applied Physics* **91**, 1978 (2002).
- ¹⁸⁹ T. Schlenker, H. W. Schock, J. H. Werner: Initial growth behavior of Cu(In,Ga)Se₂ on molybdenum substrates. *Journal of Crystal Growth* **259**, 47 (2003).
- ¹⁹⁰ T. Schlenker, M. L. Valero, H.W. Schock, J.H. Werner: Grain growth studies of thin Cu(In,Ga)Se₂ films. *Journal of Crystal Growth* **264**, 178 (2004).
- ¹⁹¹ J. A. Thornton, D. G. Cornog, R. B. Hall, S. P. Shea, J. D. Meakin: Reactive sputtered copper indium diselenide films for photovoltaic applications. *Journal of Vacuum Science&Technology A* **2**, 307 (1984).
- ¹⁹² J. A. Thornton: Fundamental Processes in Sputtering of Relevance to The Fabrication of Thin-film solar-cells. *Solar Cells* **21**, 41 (1987).
- ¹⁹³ J. A. Thornton, T. C. Lommasson, H. Talieh, B. –H. Tseng: Reactive Sputtered CuInSe₂. *Solar Cells* **24**, 1 (1988).
- ¹⁹⁴ Y. B. He, PhD thesis, Justus-Liebig-Universität Gießen, 2003 (PhD work done in Prof. B. K. Meyer' group).
- ¹⁹⁵ M. Nie, K. Ellmer: Growth and morphology of thin Cu(In,Ga)S₂ films during reactive magnetron co-sputtering. *Thin Solid Films* **536**, 172 (2013).
- ¹⁹⁶ J. Schulte, S. Brunken, K. Ellmer: Nucleation and phase formation during reactive magnetron co-sputtering of Cu(In,Ga)S₂ films, investigated by in situ EDXRD. *Journal of Crystal Growth* **384**, 114 (2013).
- ¹⁹⁷ M. Nie, K. Ellmer: Morphology and structure evolution of Cu(In,Ga)S₂ films deposited by reactive magnetron co-sputtering with electron cyclotron resonance plasma assistance. *Journal of Applied Physics* **115**, 084902 (2014).
- ¹⁹⁸ J. Schulte, PhD thesis, Technical University Berlin, 2014.
- ¹⁹⁹ J. Álvarez-García, Ph.D. thesis, Universitat de Barcelona, 2002.
- ²⁰⁰ C. Camus, E. Rüdiger, D. Abou-Ras, N.A.Allsop, T. Unold, Y. Tamm, S. Schorr, S. E. Gledhill, T. Köhler, J. Klaer, M. C. Lux-Steiner, Ch.-H. Fischer: Phonon confinement and strain in CuInS₂. *Applied Physics Letter* **92**, 101922 (2008).
- ²⁰¹ K. Ishikawa, K. Yoshikawa, N. Okada: Size effect on the ferroelectric phase transition in PbTiO₃ ultrafine particles. *Physical Review B* **37**, 5852 (1988).
- ²⁰² W. L. Zhong, Y. G. Wang, D. S. Kong, P.L. Zhang, B. D. Qu: Microstructure and composition analysis of PbTiO₃ films. *Thin Solid Films* **237**, 160 (1994).

- ²⁰³ F. Ruffino, M. G. Grimaldi, C. Bongiorno, F. Goammazzo, F. Roccaforte, V. Raineri, C. Spinella: Normal and abnormal grain growth in nanostructured gold film. *Journal of Applied Physics* **105**, 054311 (2009).
- ²⁰⁴ V.Y. Novikov: Grain growth controlled by mobile particles on grain boundaries. *Scripta Materialia* **55**, 243 (2006).
- ²⁰⁵ J. G. Amar, P. -M. Lam, F. Family: Groove instabilities in surface growth with diffusion. *Physical Review E* **47**, 3242 (1993).
- ²⁰⁶ H. -N. Yang, Y.-P. Zhao. G. -C. Wang, T. -M. Lu: Noise-induced roughening evolution of amorphous Si films grown by thermal evaporation. *Physical Review Letter* **76**, 3774 (1996).
- ²⁰⁷ B. C. Mohanty, H. R. Choi, Y. S. Cho: Scaling of surface roughness in sputter-deposited ZnO:Al thin films. *Journal of Applied Physics* **106**, 054908 (2009).
- ²⁰⁸ C. H. Champness, Proceeding of the 29th IEEE Photovoltaic Specialist Conference, New Orleans, 2002 (IEEE, Piscataway, 2002), p. 732.
- ²⁰⁹ C. -S Jiang, R. Noufi, K. Ramanathan, J. A. AbuShama, H. R. Moutinho, M. M. Al-Jassim: Does the local built-in potential on grain boundaries of Cu(In,Ga)Se₂ thin films benefit photovoltaic performance of the device? *Applied Physic Letter* **85**, 2625 (2004).
- ²¹⁰ J. B. Li, V. Chawla, B. M. Clemens: Investigating the Role of Grain Boundaries in CZTS and CZTSSe Thin Film Solar Cells with Scanning Probe Microscopy. *Advanced Materials* **24**, 720 (2012).
- ²¹¹ D. Azulay, O. Millo, I. Balberg, H.-W. Schock, I. Visoly-Fisher, D. Cahen: Current routes in polycrystalline CuInSe₂ and Cu(In,Ga)Se₂ films. *Solar Energy Materials and Solar Cells* **91**, 85 (2007).
- ²¹² R. H. Shin, W. Jo, D. -W. Kim, J. H. Yun, S. Ahn: Local current-voltage behaviors of preferentially and randomly textured Cu(In,Ga)Se₂ thin films investigated by conductive atomic force microscopy. *Applied Physics A-Materials Science & Processing* **104**, 1189 (2011).
- ²¹³ H. Y. Yeom, N. Popovich, E. Chason, D.C. Paine: A study of the effect of process oxygen on stress evolution in d.c. magnetron-deposited tin-doped indium oxide. *Thin Solid Films* **411**, 17 (2002).
- ²¹⁴ T. J. Vink, W. Walrave, J.L.C. Daams, P.C. Baarslag, J. E.A.M. van den Meerakker: On the homogeneity of sputter-deposited ITO films Part I. Stress and microstructure. *Thin Solid Films* **266**, 145 (1995).
- ²¹⁵ J. G. Yu, J. G. Amar: Dynamical scaling behavior in two-dimensional ballistic deposition with shadowing. *Physical Review E* **66**, 021603 (2002).

Publications

Parts of Mrs. Nie's PhD work have already been published:

- [1] **M. Nie** and K. Ellmer: Growth and morphology of thin Cu(In,Ga)S₂ films during reactive magnetron co-sputtering. *Thin Solid Films* **536**, 172-178 (2013).
- [2] **M. Nie** and K. Ellmer: Morphology and structure evolution of Cu(In,Ga)S₂ films deposited by reactive magnetron co-sputtering with electron cyclotron resonance plasma assistance. *Journal of Applied Physics* **115**, 084902 (2014).
- [3] **M. Nie**, T. Mete, and K. Ellmer: Morphology and structure evolution of tin-doped indium oxide thin films deposited by radio-frequency magnetron sputtering: The role of the sputtering atmosphere. *Journal of Applied Physics* **115**, 154905 (2014).
- [4] F. Bozheyev, D. Friedrich, **M. Nie**, M. Rengachari and K. Ellmer: Preparation of highly (001)-oriented photoactive tungsten diselenide (WSe₂) films by an amorphous solid-liquid-crystalline solid (aSLcS) rapid- crystallization process. *Physica Status Solidi A*, 1-7 (2014). DOI: 10.1002/pssa.201400016

Publication during Mrs. Nie's master study:

- [5] **M. Nie**, C. Wang, Y. C. Wen, Y. Sun, Y. Y. Na, L. H. Chu, and M. B. Tang: Magnetic phase transitions of antiperovskite Mn_{3-x}Fe_xSnC (0.5 ≤ x ≤ 1.3). *Solid State Communications* **151**, 377-381 (2011).
- [6] E. Metwalli, **M. Nie**, V. Köstgens, J. Perlich, S.V. Roth, and P. Müller-Buschbaum, Morphology of lithium-containing diblock copolymer thin films. *Macromolecular Chemistry and Physics* **212**, 1742-1750 (2011).
- [7] Y. C. Wen, C. Wang, **M. Nie**, Y. Sun, L. H. Chu and C. Dong: Influence of carbon content on the lattice variation, magnetic and electronic transport properties in Mn₃SnC_x. *Applied Physics Letters* **96**, 041903 (2010).

Acknowledgments

The three years, during which this work was performed, have become an invaluable experience of my life. It is a great fortune for me to do this doctoral work in Dr. Klaus Ellmer's group at the Helmholtz-Zentrum Berlin für Materialien und Energie. I would like to express my special gratitude to Dr. Ellmer, who introduced me to the world of material preparation with magnetron sputtering and material analysis with experimental and theoretical tools. I not only benefited from his invaluable knowledge, but also learned from him how proper science should be done. His generous guidance and support has given me confidence to complete my doctoral thesis. When my thesis topic was modified to another aspect in the middle of my study, I almost felt lost and had no idea how to build connections among those different sample materials. It is Dr. Ellmer who supervised me to the right direction and stay in the track. He always tries every possibility and encourages me not only stay in my own research, but open more my mind to embrace new topics and ideas.

Furthermore, I would like to thank Prof. Dr. Bernd Szyszka for being my first supervisor at the Technical University Berlin and for the helpful suggestions on my thesis. I still remember when we had a meeting he insisted to discuss with me first even though he just came back to office after a long lecture and had no lunch. His word “discussing interesting work and gaining new ideas are much enjoyable than the hamburger” made me so moved. I also want to thank Prof. Dr. Norber Kaiser from the Fraunhofer Institute for Applied Optics and Precision Engineering to be my second examiner in the procedure of my doctoral thesis and the defense afterwards.

I had the pleasure of working with André Bikowski, Jonas Shulte and Karsten Harbauer who introduced me into different equipment for sample preparation. I also enjoyed the time with Dr. LiChao Jia who has good sense to science and positive attitudes to life that affected me a lot.

Besides my colleagues in the institute, I want to express my deepest gratitude and love to my husband Mr. Xin Song who always supports and believes me all the time. I appreciate the endless love from my parents. Although I only visited you twice in China during the last three years abroad, I always miss you so much in my deep heart.

Finally, I would like to thank China Scholarship Council and Helmholtz-Zentrum Berlin for the financial support during my doctoral studies.